

High-Resolution Retinal Imaging with a Compact Adaptive Optics Ophthalmoscope

Ibolya Edit Kepiro

Imperial College
London

Imperial College of Science, Technology and Medicine
The Blackett Laboratory, Physics Department

Thesis submitted in partial fulfilment of the requirements for the degree of
Doctor of Philosophy

London 2013

I certify that this thesis, and the research to which it refers, are the product of my own work, and that any ideas or quotations from the work of other people, published or otherwise, are fully acknowledged.

Copyright

The copyright of this thesis rests with the author and is made available under a Creative Commons Attribution Non-Commercial No Derivatives licence. Researchers are free to copy, distribute or transmit the thesis on the condition that they attribute it, that they do not use it for commercial purposes and that they do not alter, transform or build upon it. For any reuse or redistribution, researchers must make clear to others the licence terms of this work.

Abstract

This thesis presents work on the development of a compact adaptive optics ophthalmoscope to visualize microscopic details of the human fovea. Conventional ophthalmoscopes currently employed in retinal imaging for diagnostic purposes help to detect disorders in real-time; however, their resolution is limited by the optical quality of the last focusing lens, the human eye. In recent years there has been a significant increase in studying retinal alterations, including the complication of non-ophthalmic diseases. In a number of cases, especially for visually impaired and elderly people, when the ocular media become less transparent, fixation is hard for the patients. It is often difficult to repeat the measurements during the usual clinical diagnostic routine; the dynamic changes and imperfection in the optics of the eye also significantly degrade the retinal image quality. In order to resolve cellular level details and hence detect ocular diseases in their infancy, dynamic correction of ocular aberrations is required. Developments in ophthalmoscopy have extended its application to high-resolution imaging using adaptive optics. This technology enables the *in-vivo* study of finer microscopic structures by dynamically correcting higher-order ocular aberrations. To date, such systems have been large and confined to research laboratory conditions. This thesis investigates the performance of a compact adaptive optics ophthalmoscope built in a cost effective way to provide a diagnostic tool that is more affordable and usable in a general clinical environment. It also highlights some of the problems associated with retinal imaging and discusses the limitations of retinal imaging systems. The results obtained with this system suggest that it is possible to non-invasively detect structural and functional changes of the retina in their early phases of development and enable precise monitoring of the effect of therapies in later clinical research.

Acknowledgements

First I have to express my gratitude to my supervisor Dr Carl Paterson for offering me the opportunity to come to Imperial and do this exciting research. Over the years I gained skills to become an independent researcher and this PhD helped my integration into the research community of this innovative subfield of ophthalmology for which I am especially grateful. I also sincerely appreciate the effort and comments of my examining committee which supported the evolution of the thesis to a more comprehensive study.

I thank Dr Mihaly Vegh, my PhD advisor in ophthalmology and Dr Laszlo Szalay, ophthalmologist for the stimulating discussions and their critical comments on my work. I also acknowledge the contribution of the following people: special thanks have to go to Ara for all the support and for his sincere friendship, Gordon for his help in the labs at the start, Cliff and Carlos for providing microscopic samples, Carl and David for their assistance in performing real eye tests. When it came to Linux problems and coding Laszlo-Stephan was always there and willing to lend a hand. I am fortunate enough to have such a good friend; I am grateful for his encouragement, support and patient in the stressful times. Ara and Sunil were also kind enough to accept my request for proofreading of the thesis. Some images were taken of my eyes by Dr Kester Nahen, Heidelberg Engineering and by Dr Laszlo Szalay for which I thank them both. I also thank the Department of Ophthalmology, University of Szeged and Dr David Lara for their permissions to publish retinal images for illustration.

I want to thank the members of the mechanical and optics workshop, Martin and Simon for all the pieces they made for my system, even when the time was tight towards the end. I especially thank the anonymous volunteers for participating in the eye tests; their help was very important but ethical regulations prevent me from mentioning their names.

I also thank the friends and colleagues that made the environment of Blackett Laboratory a pleasant place to work in. The work was not easy sometimes at Imperial since I had no group members to share the problems or success; I was fortunate enough to be an 'honourable' member of the Damzen Group. I am grateful for the welcome distractions the Group members offered, coffee-breaks and after-work programs with Ara, Mike, Gabs, Sunil, Sanja and Jake - showing me that there is life outside the lab.

Finally and most of all, I am deeply thankful for the help and encouragement of my parents, to whom I dedicate this thesis, and I am grateful for their continued support throughout my lengthy education; without their love and support this PhD would not have been possible to complete.

Substantial financial support of this research was provided by EPSRC and partial support from Imperial College HSF at the late stages of the work.

For my parents

Journal publications and conference presentations

The following research papers and contributions related with this work have been presented or being under publication:

Conference / congress presentations

- [1] *Improved non-invasive cell death detection by adaptive optics ophthalmoscopy*, IE Kepiro and C Paterson. 4th World Congress on Controversies in Ophthalmology, Budapest, Hungary. Book of abstracts, p.61, p-6-7 (2013)
- [2] *Preliminary results from a compact adaptive optics laser scanning ophthalmoscope for in-vivo imaging the cellular structures*, IE Kepiro and C Paterson. Annual Congress of the Hungarian Ophthalmological Society on Ophthalmic diseases of elderly people, Hungary. Ophthalmol. Suppl. / Ophthalmologia Hungarica **148**(S1), 112 (2011)
- [3] *A compact scanning laser ophthalmoscope with adaptive optics*, IE Kepiro, GT Kennedy and C Paterson. 4th European Meeting in Visual and Physiological Optics, Greece. Book of abstracts, p.62 (2008)
- [4] *A CMOS camera for pyramid wavefront sensors*, KN Modha, IM Stockford, IE Kepiro, C Paterson, RA Light and B Hayes-Gill. Proc. SPIE 7015, 70155R1-9 (2008)

Publications in preparation

- [5] *Adaptive optics ophthalmoscope findings in photoreceptor loss*, IE Kepiro and C Paterson (*in preparation*)
- [6] *Progress for early diagnosis of ophthalmic diseases: Improved non-invasive evaluation of human retina structures using a compact adaptive optics ophthalmoscope*, IE Kepiro and C Paterson (*in preparation*)
- [7] *Characterization of phantom retina samples for optimization in adaptive optics ophthalmoscopy*, IE Kepiro and C Paterson (*in preparation*)

Table of Contents

Copyright	3
Abstract	4
Acknowledgements	5
Journal publications and conference presentations	7
Table of figures	10
List of tables	12
Glossary of medical terms	13
List of abbreviations	16
I. Introduction	19
I.1 General introduction to retinal imaging	19
I.1.1 Current retinal imaging methods in clinical practice	20
I.1.2 Limitations of retinal imaging systems	22
I.1.3 Adaptive optics in ophthalmology	24
I.2 Motivation of thesis	26
I.3 Thesis outline	27
II. Biological aspects of retinal imaging	30
II.1 The human eye as a living adaptive optics system	30
II.1.1 Physiological and functional optics of the main components	32
II.1.2 Anatomical structures and physiology of the retina	39
II.1.3 Change of optics with aging and abnormal ocular conditions	48
II.2 Ocular aberrations and dynamical effects performed in the eye	54
II.3 The human eye as a biological sample	59
II.3.1 Radiation sensitivity of the ocular cells	59
II.3.2 Ocular scattering and stray light	60
II.4 Summary and discussion	62

III. Technical issues in retinal imaging	66
III.1 HRT as a confocal scanning laser ophthalmoscope	66
III.2 Wavefront sensing for ophthalmic application	69
III.2.1 Shack-Hartmann wavefront sensor	70
III.2.2 Pyramid wavefront sensor	74
III.2.3 Centroiding at low light levels in AO systems	76
IV. The compact adaptive optics ophthalmoscope	83
IV.1 Design consideration of an adaptive optics system	84
IV.2 Construction of a compact adaptive optics system	86
IV.2.1 Light delivery and optical layout of the system	86
IV.2.2 Wavefront sensor and deformable mirror	91
IV.3 Operation of the adaptive optics ophthalmoscope	97
IV.3.1 Optimization of the system	98
IV.3.2 Summary and discussion	111
V. Retinal imaging with the compact AO ophthalmoscope	113
V.1 Objective of non-invasive retinal investigations	113
V.1.1 Retinal imaging protocol	114
V.1.2 Method and subjects	117
V.1.3 High-resolution retinal imaging with adaptive optics	117
V.2 Morphology of human photoreceptor populations	122
V.2.1 Mosaic structure of the photoreceptors in the central field	122
V.2.2 Photoreceptor mosaic regularity	123
V.2.3 Discontinuities in photoreceptor mosaic structure	124
V.2.4 Comparison of cAO-HRT imaging results with histological data	125
V.3 Discussion: Limits of the current configuration	127
VI. Summary and conclusion: Progress for non-invasive cellular imaging	131
Bibliography	135
Appendix A: The decomposition of the waveform into Zernike polynomials	163
Appendix B: Java Codes	171
Appendix C: Python Codes	172
Copies of permission documents	174

Table of figures

Fig. 1.1 The eye as a microscope objective	21
Fig. 1.2 Schematic of a Shack-Hartmann aberrometer	24
Fig. 2.1 Schematic representation of the human eye in cross-section	31
Fig. 2.2 Typical ocular temperature distribution	35
Fig. 2.3 Ophthalmoscopic view of a healthy retina and regional structures	41
Fig. 2.4 Varying thickness of a healthy retina in central field	42
Fig. 2.5 Cross section of a healthy retina	43
Fig. 2.6 Retinal layers and histology of normal adult human retina	44
Fig. 2.7 Non-uniform structure of a healthy retina at the optic disc	45
Fig. 2.8 Fundus photography and OCT images in dry and wet AMD	51
Fig. 2.9 Fundus photography in early phase of diabetic retinopathy	52
Fig. 2.10 Fundus photography in progressed diabetic retinopathy	53
Fig. 2.11 Velocity distribution in anterior chamber when gravity is applied	57
Fig. 2.12 Stable fixation and blinking during SLO/OCT image acquisition	58
Fig. 2.13 Thickness of human retinal layers during development and maturation	63
Fig. 3.1 Schematic optical layout of the modified HRT	67
Fig. 3.2 Schematic representation of a SHS in geometrical optics approximation	70
Fig. 3.3 Limited dynamic range of a conventional Shack-Hartmann sensor	73
Fig. 3.4 Schematic representation of the knife edge test	74
Fig. 3.5 Schematic representation of a pyramid sensor	75
Fig. 3.6 Wavefront-slope measurement	77
Fig. 3.7 Error propagation illustrating wavefront map changes in cAO-HRT	81
Fig. 4.1 Estimated light budget in the ocular media for imaging	84
Fig. 4.2 Optical layout of the compact AO scanning laser ophthalmoscope	87
Fig. 4.3 The movement of the scanners as they cross the field	89
Fig. 4.4 Schematic of the HRT for beam alignment of the pinhole	90
Fig. 4.5 Schematic diagram of the cAO-HRT for beam alignment of the pinhole	91

Fig. 4.6 Schematic for the sensitivity of a Shack-Hartmann sensor	93
Fig. 4.7 Schematic for the dynamic range of a Shack-Hartmann sensor	93
Fig. 4.8 Schematic representation of the 37 channel OKO membrane mirror	95
Fig. 4.9 Aberrated and corrected images using a microscope target	104
Fig. 4.10 Corrected images after optimization using highly reflective samples	105
Fig. 4.11 Aberrated and corrected images using thin film with regular structure	106
Fig. 4.12 Aberrated and corrected images using photographic film	106
Fig. 4.13 Intensity profile for sharpness metric (low gain) in photographic film	107
Fig. 4.14 Intensity profile for sharpness metric (medium gain) in photographic film ..	107
Fig. 4.15 Intensity profile for sharpness metric (high gain) in photographic film	108
Fig. 4.16 Relative intensity taken through corrected images with optimization	108
Fig. 4.17 Relative intensity taken through uncorrected values	109
Fig. 4.18 Comparison of metrics for removal of non-common path errors	109
Fig. 4.19 Average actuator arrays using metric S_3 for photographic film	110
Fig. 4.20 Average actuator arrays metric S_3 for sand paper sample	110
Fig. 5.1 Surface and cross section of fundal locations under investigation	114
Fig. 5.2 Location of high-resolution images on the centre of the retina	118
Fig. 5.3 Images of the macula obtained with a fundus camera and cAO-HRT	119
Fig. 5.4 Plot profile taken from Figure 5.3 at $\sim 1.5^\circ$ field of view	119
Fig. 5.5 Retinal image at about 4.5° from the centre of the fovea	120
Fig. 5.6 Non-invasive images of the nerve fibre layer of a human volunteer	121
Fig. 5.7 Retinal image at about 4.5° from the centre of the fovea	121
Fig. 5.8 Image of the macula at about 3.5° from the centre of the fovea	122
Fig. 5.9 Images of the fovea in the central field	123
Fig. 5.10 Images of the centre of the retina; gray scale and color coded	123
Fig. 5.11 Image of the macula at about 2° from the centre of the fovea	124
Fig. 5.12 Cone density map in comparison to histological study	125
Fig. 5.13 Photoreceptor densities in comparison to histological data	126
Fig. 6.1 Comparison of retinal images taken by a fundus camera and cAO-HRT	133

List of tables

Table 1.1 Clinical and anatomical terms for retinal imaging	40
Table 3.1 Error sources of CCD-based centroiding and their distribution	79
Table 4.1 Definition of image sharpness metrics	100
Table 4.2 Selection of list of targets used as artificial samples	103
Table 5.1 Common eye drops used for mydriasis and cycloplegia	115

Glossary of medical terms

Amacrine cell: a retinal neuron that is located in the inner nuclear layer and modulates signals in the inner plexiform layer. *Amacrine cells* are distinguishable from other cell types due to their larger size, around 10 μm in diameter, and oval shape.

Avascular tissue: a kind of tissue that has no blood vessels or receives no supply of blood.

Emmetropic eye: an eye which has no significant refractive error

Bowman's membrane: in adults an approximately 8 to 12 μm thick acellular and slightly irregular layer of the cornea towards the epithelium containing randomly oriented collagen fibrils.

Ciliary: used particularly in reference to certain eye structures such the *ciliary body* or *ciliary muscle*

Ciliary body: the thickened part of the tunic of the eye, an approximately 5-6 mm wide ring of tissue, connecting the choroid and the iris. Histologically it can be divided into the *ciliary epithelium*, *ciliary body stroma* and *ciliary muscle*. Its principal functions are: accommodation and aqueous humour formation.

Ciliary muscle: a smooth muscle that forms the main part of the *ciliary body* and functions to alter the refractive power of the lens

Ciliary epithelium: containing two layers, an inner non-pigmented and an outer pigmented layer. It is responsible for the aqueous humour formation.

Collagen fibril: a minute fibre of collagen in *connective tissue*; these unit fibrils are aggregated in bundles to form larger fibrils or fibres

Connective tissue: stromatous tissue

Corneal dystrophy: term includes a large group of inherited developmental conditions that causes bilateral, slowly progressive corneal opacification

Crystallines / crystalline granules: make up 90% of water soluble proteins of the lens; there are three different types (α , β , γ) mainly on the basis of their molecular weight in the range from 20,000 - 800,000 Da in average. The structure of the *crystallines* in the lens allows the light entering the eye to pass through unimpeded. If some pathologic change occurs that results in clumping together of the molecules causing loss of clarity of the lens. As light passes through the lens, the newly formed molecule structure scatters the light; at later stages the result is cataract formation.

Cycloplegia: paralysation of the ciliary muscle which inhibits accommodation

Descemet's membrane: basement membrane (basal lamina) of the corneal endothelium

Edinger-Westphal nucleus: contains small preganglionic parasympathetic neurones located in the midbrain and a centre for coordination of oculomotor activity

Endothelium / endothelial layer: a tissue consisting of a single layer of cells that line the blood

Epithelium / epithelial layer: membranous single or multi-layered tissue of cells forming the covering of most internal and external surfaces of organs

Fluorescein angiography / fluorescein angiogram: FLAG (or FG) is a dilated eye test in clinical diagnosis to investigate the status of the retinal and choroidal vascular systems. FLAG administers sodium fluorescein dye intravenously which travels through the retinal vessels with blood flow. The dye is tracked in the following way: the dye absorbs photons when the retina is illuminated in the 465-490 nm region of the spectrum and fluoresces yellow-green (520-530 nm in wavelength); the illumination is band pass filtered at the camera and only the fluorescence light is detected. The resulting high contrast image of the retinal vessel is the *fluorescein angiogram*. This diagnostic method is used to visualize the dynamics of the flowing blood and the alterations of the blood-retinal barrier which can be useful in cases of inflammation, blood circulation problems, and diabetic retinopathy or AMD.

Fovea (*lat. fovea centralis*): the area of diameter about 1.85 mm in the centre of the retina where the photoreceptors are densely populated; the central 0.35 mm diameter region of the fovea is the foveola.

Fundus (*lat. fundus oculi*): term used for the back of the eye

Ganglion cell: a nerve cell whose axon is located in the nerve fibre layer of the retina

Glial cell: a cell of the supportive tissue of the nervous system

Haemorrhage: profuse bleeding from ruptured blood vessels

Horizontal cell: a neural cell located in the inner nuclear layer of the retina connected to the outer plexiform layer that provides inhibitory feedback to photoreceptor cells

Hypermetropia: condition of farsightedness (also called: hyperopia)

Macula (*lat. macula lutea retinae*): a small, yellow pigmented spot or region on the retina; this is the location of sharp vision in the central retina.

Melanin: dark pigment in the retinal pigment epithelium

Microaneurysm: protruded blood vessel wall; characteristic of for example progressed diabetic retinopathy.

Mydriasis: prolonged abnormal dilatation of the pupil due to disease, trauma or drugs

Myopia: condition of short-sightedness, inability to see distant objects clearly

Neovascularisation: abnormal or excessive formation of blood vessels or formation of new blood vessels in the tissue

Programmed cell death (*lat. apoptosis*): a mechanism that allows cells to self-destruct when stimulated by an appropriate trigger

Stroma: supporting tissues of an organ, including nervous and *connective tissues* and blood vessels. Stromal elements perform a protective role and are capable of reproduction.

Tapetum: a reflecting layer in the choroid behind the neural retina in nocturnal mammals

Vascular: of, or relating to, or having vessels

List of abbreviations

AHF: aqueous humour flow

AMD / ARMD: age-related macular degeneration

AO: adaptive optics

(c)AO-HRT: (compact) adaptive optics Heidelberg Retina Tomograph

AOSLO: adaptive optics scanning laser ophthalmoscope

BM: Bruch's membrane

CH: choroid

CNV: choroid neovascularisation

CRA: central retinal artery

ELM: external limiting membrane

FC: foveola or centre of fovea (*lat.* fovea centralis)

FLAG: fluorescein angiography

GCL: ganglion cell layer

INA: inferior nasal artery

INF: inferior

INL: inner nuclear layer

IOL: intraocular lens

IOP: intraocular pressure

I/OPJ: inner/outer photoreceptor junction

IPL: inner plexiform layer

ITA: inferior temporal artery

ITV: inferior temporal vein

NAS: nasal

NFL: nerve fibre layer

OCT: optical coherence tomography

OPD: optic disc

OD: right eye (*lat. oculus dexter*)

ONL: outer nuclear layer

OPL: outer plexiform layer

OS: left eye (*lat. oculus sinister*)

PaF: parafovea

PE: retinal pigment epithelium

PeF: perifovea

PE/BM: retinal pigment and Bruch's membrane complex

POS: photoreceptor outer segments

PPI: parafovea-perifovea interface

PR: peripheral retina

PRL: photoreceptor layer

R/C-IS: rod/cod inner segments

S: sclera

(c)SLO: (confocal) scanning laser ophthalmoscope

SNA: superior nasal artery

STA: superior temporal artery

STV: superior temporal vein

SUP: superior

TEMP: temporal

Chapter I

Introduction

I. Introduction

I.1 General introduction to retinal imaging

Developments in ophthalmic instrumentation have resulted in unprecedented progress over the last 10 years. However, detection of progressive retinal diseases is extremely difficult and none of the currently used imaging methods fulfil the requirement for an accurate and reproducible diagnostic technique in a clinical setting. Ophthalmologists are often faced with clinical challenges in routine retinal examination, both in terms of proper diagnosis as well as treatment for patients, as only major tissue alterations ($>25\ \mu\text{m}$ Sarks *et al.*, 1999) can be detected by conventional ophthalmoscopes (Staurenghi *et al.*, 2007). In most severe cases of retinal disease, photoreceptor cells are affected (Carroll *et al.*, 2004; Wolfing *et al.*, 2006; Choi *et al.*, 2006; Duncan *et al.*, 2007; Baraas *et al.*, 2007; Yoon *et al.*, 2009; Torti *et al.*, 2009; Ooto *et al.*, 2011; Lombardo *et al.*, 2012a) and cell death is the final irreversible event in many blinding conditions.

Most investigations on the optical (Franze *et al.*, 2007) and mechanical properties (Lindqvist *et al.*, 2010; Franze *et al.*, 2011) of retinal tissues to date are based on studies of retina donor samples (Lindqvist *et al.*, 2010; Franze *et al.*, 2007) and animal tissues (Franze *et al.*, 2007; Gray *et al.*, 2006; Hunter *et al.*, 2010). A major current focus in ocular imaging development is to provide a high-resolution *in-vivo* retinal imaging device for potential clinical intervention to prevent photoreceptor cell death. This thesis aims to address the development of adaptive optics in compact ophthalmological instrumentation.

This chapter gives an overview of retinal imaging and adaptive optics ophthalmoscopy to place the results presented in this thesis into context. This section focuses on technological advances in retinal imaging and the limitations of such configurations. Recent clinical findings using high-resolution *non-invasive* imaging modalities will also be discussed. Finally, at the end of this chapter, an explanation of the motivation for this thesis will be presented.

I.1.1 Current retinal imaging methods in clinical practice

Retinal imaging, including optical coherence tomography (OCT) and confocal scanning laser ophthalmoscopy (cSLO), are increasingly used in clinical routines for diagnosis and assessment of effectiveness of treatments. Some of the advances in practical ophthalmology (Holz & Spaide, 2007; Staurenghi *et al.*, 2007; Issa *et al.*, 2007; Johansson *et al.*, 2008) and adaptive optics ophthalmoscopy (Krueger *et al.*, 2004; Doble, 2005; Porter *et al.*, 2006; Roorda *et al.*, 2006; Podoleanu & Rosen, 2008; Williams, 2011) have been recently published in books and review papers.

The major recent technological development in ophthalmology (Pawley, 1995; Doble, 2005; Roorda, 2006) was the invention of a confocal laser system to obtain images of the fundus developed by Webb & Hughes (1981) and Webb *et al.* (1987). The first conventional scanning laser ophthalmoscope (SLO) was introduced to clinical practice by Rodenstock in 1989. The difference between a conventional ophthalmoscope and an SLO is in the method of illuminating the retina. An SLO essentially works as a scanning laser microscope, the important difference being that in SLO systems, the optics of the human eye ($NA_{\text{eye}} = 0.23$ with a normal 3.5 mm pupil diameter) serve as the objective lens (Figure 1.1), a doublet in which the cornea (f_1) and the crystalline lens (f_2) are separated by the aqueous humour and the space between the lens (f_2) and the retina is the vitreous humour (n_{VH}). The sample is always the retina at a fixed position $d_{\text{OR}}=16$ mm (in the relaxed case: Atchison & Smith, 2002); in an analogous way to microscopy where the distance is measured from the front lens of the objective to the sample, and in ophthalmoscopy it is the distance between the posterior surface of the lens and the retina.

Confocal imaging in ophthalmology (Staurenghi, 2007) was obtained by introducing a pinhole (in a plane conjugate to the focal plane) in front of the detector (Elsner *et al.*, 1996). This confocal optical setup allows spatial filtering of the light, i.e. only light which is reflected from the focal plane of the source is detected. This was the first high-resolution imaging technique applied to the eye (Webb, 1990), providing improved signal-to-noise ratio and good contrast compared to conventional fundus photography, where objects outside the plane of interest contribute to the image formation, resulting in low resolution and a blurred image.

There is intensive research on the development of instruments for imaging the cross-section of the living retina (Wu & Evans, 2007). OCT was the first such imaging method, derived from interferometry in the 1990s that provided a non-invasive and non-contact high-resolution imaging method for cross-sectional investigations. OCT uses low coherence interferometry, which is a sensitive method to detect weak signals from the retina due to the increased gain provided by heterodyne detection (Brezinski, 2006; Williams, 2011). One of the early applications of this method in biomedical optics was the measurement of eye length (Fercher *et al.*, 1988).

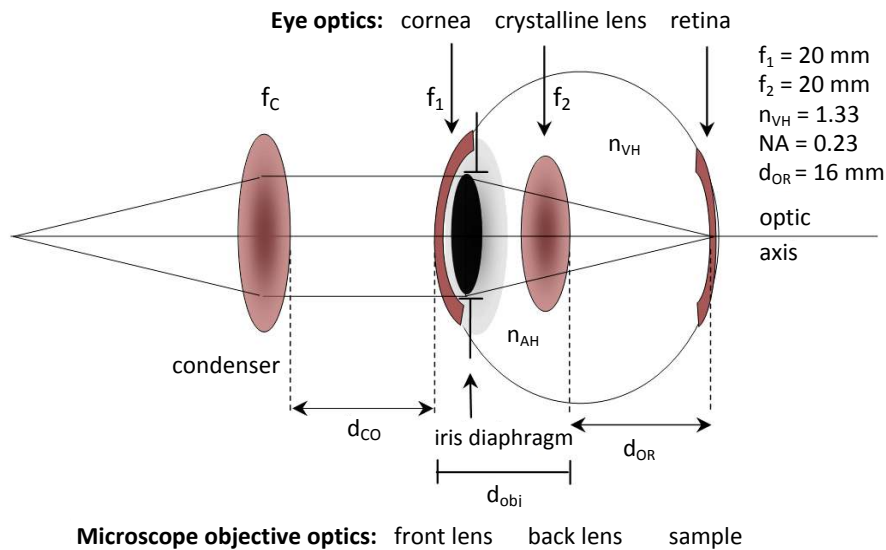


Fig. 1.1 The eye as a microscope objective

The diagram shows the schematic of the eye as a microscope objective. Notations: cornea/front lens (f_1), crystalline lens/back lens (f_2), n_{VH} refractive index of vitreous humour, n_{AH} refractive index of aqueous humour ($n_{AH} = n_{VH}$); condenser lens (f_c), d_i referring to distances of surfaces as indexed. (Figure drawn by the author, 2012.)

OCT has the potential of achieving high axial resolution which is determined by the coherence length of the source. Early OCT systems provided a theoretical resolution of 10-15 μm , which was significantly improved by the use of broad band sources, giving an axial resolution of 3 μm in the eye (Drexler *et al.*, 1999). New combined imaging instruments have also been introduced, allowing the study of retinal regions of interest with quasi *non-invasive* histology in high resolution OCT and cSLO images simultaneously. The combination of these techniques allows a more accurate monitoring of pathological changes compared to the early and single modality techniques, but retinal imaging has limitations partly due to the limited range of wavelengths the instruments use in clinical applications, and partly due to the aberrations present both in the ocular media and the imaging systems.

I.1.2 Limitations of retinal imaging systems

Imaging quality of the retinal tissue is limited mainly by the imaging method and the applied wavelength for retinal illumination, the optical quality of the eye and the configuration of the imaging instrument. For some of these issues, biological and technological tools have provided improvements.

For fundus imaging applications, a range of wavelengths is available depending on the retinal structure of interest (Delori & Pflibsen, 1989; Van Norren & Tiemeijer, 1986). Near-IR imaging has been tested to provide improved visualization and diagnosis of vascular diseases for subretinal features (Leibowitz *et al.*, 1980; Webb & Delori, 1988). IR images have been used to detect pathological change despite the presence of opaque tissues (Elsner *et al.*, 1991 and 1993); the effect of other wavelengths on imaging in the human retina has been also investigated (Elsner *et al.*, 1994; Ducrey *et al.*, 1979; Delori *et al.*, 1977; Snodderly *et al.*, 1984; Wyszecski & Stiles, 1982). The applied wavelength is limited by the permitted exposure of light for retinal illumination and the transmission properties of the ocular media. Ocular media are relatively transparent biological tissues, and some of the layers absorb significant amount of light, making the retina a weak reflector.

The precise expression for the peak irradiance (I_{peak}) obtainable from the eye (Sheppard & Larkin, 1994) as an objective lens can be estimated from the following equation:

$$I_{\text{peak}} = \frac{\pi}{2} P T \left(\frac{\eta}{\lambda}\right)^2 (1 - \cos \alpha) (3 + \cos \alpha), \quad (1.1)$$

where P is the input power in Watts, $\alpha = \sin^{-1} NA/\eta$ is the semi-aperture angle of the objective, η is the refractive index of the immersion medium, and T is the transmission factor of the objective. The overall transmittance of the ocular media is about 90% according to Alguere *et al.* (1993). This is particularly important since the amount of laser illumination is limited due to safety hazards, and since the microscope is used in reflection mode in retinal imaging, any losses occur twice, thus significantly reducing the signal detected from the retina. In practice, only 10^{-4} - 10^{-6} of the entering photons returns for detection (Delori & Pflibsen, 1989); this imposes an unavoidable constraint.

The effectiveness of diagnosis in retinal diseases can be improved through increased contrast by using angiography (Fine *et al.*, 2007; Friberg & Labriola, 2007). This is a

commonly used method to provide insight into vascular abnormalities by injecting dye into the blood stream of the patient, followed by standard confocal imaging. This is a more sensitive method suitable for refined classification of early and late stages of retinal diseases.

Some of the limitations have been investigated to enable the development of more sophisticated diagnostic methods. However, using the eye as the objective of the ophthalmoscope imposes one of the most serious constraints on any retinal imaging system, since the imaging quality is limited by the optical quality of the human eye. The eye exhibits diffraction limited optical performance for a pupil diameter of up to 2-3 mm (Campbell & Gubisch, 1966; Donnelly & Roorda, 2003; Walsh *et al.*, 1984); for larger pupil sizes significant amounts of aberration occurs (Campbell & Gubisch, 1966).

The theoretical diffraction limited resolution of the human eye can be estimated from the following equation:

$$r_{\text{Airy}} = 0.61 \frac{\lambda}{\text{NA}_{\text{eye}}}, \quad (1.2)$$

where r_{Airy} is expressed as distance in the retinal plane, NA_{eye} is related to the ratio of the focal length of the eye to the diameter of the entrance pupil, and λ is the imaging wavelength. This expression shows that as the pupil diameter is increased, the size of the resolvable cell structures in the retina decreases due to the smaller point-spread-function. The first minimum of the Airy pattern in the plane of the sample can be approximated by:

$$z_{\text{min}} = \frac{2\lambda\eta_{\text{eye}}}{(\text{NA}_{\text{eye}})^2}, \quad (1.3)$$

where η_{eye} is the refractive index of the eye. Eq. 1.2 gives an estimate for the illuminated spot diameter (Cogswell & Larkin, 1995) on the retina of 2 μm (approximately the diameter of one photoreceptor at the centre of the fovea). In comparison to this, the transverse resolution (at $\lambda=670$ nm) of an ophthalmoscope is limited to 10 μm in practice (Doble, 2005) and the axial resolution is limited to approximately 200 μm by ocular aberrations (Donnelly & Roorda, 2003). The transverse resolution can be generally improved by using a higher NA objective lens if aberrations are not significant, which is not the case in ophthalmoscopy, hence the resolution can be only improved by compensating for the optical aberrations.

Optical aberrations have substantially greater impact on the overall performance of any ophthalmoscope than diffraction. The phase distortions that limit the performance of the optical system can originate both in the device and in the ocular media, and diffraction limited performance can be achieved only by correction of these aberrations.

I.1.3 Adaptive optics in ophthalmology

Adaptive optics (AO) with sophisticated wavefront sensing modalities (Liang *et al.*, 1994; Williams *et al.*, 1999) offers a tool that enables compensation of the optically induced distorting effects in retinal imaging by dynamically correcting the aberrations (Tyson, 1997; Hardy, 1998; Porter *et al.*, 2006). In an AO system the optical distortions are first measured by a wavefront sensor, usually a Shack-Hartmann (Prieto *et al.*, 2000; Neal, 2007; Porter *et al.*, 2006; Tyson 1997, Hardy 1998) or pyramid sensor in vision science. The most widely used wavefront sensor is the Shack-Hartmann sensor, which has an increasing number of applications, including its integration into aberrometers in routine clinical tests (Prieto *et al.*, 2000; Neal, 2007). Figure 1.2 shows the optical arrangement of a Shack-Hartmann aberrometer.

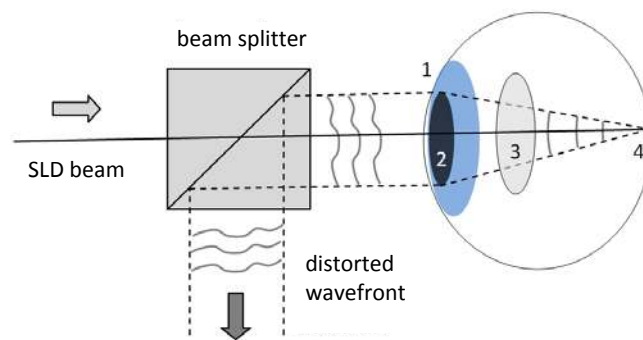


Fig. 1.2 Schematic of a Shack-Hartmann aberrometer

The optical arrangement of a Shack-Hartmann aberrometer (after Neal, 2007) is similar to the architecture of a guide star (diagram drawn by the author, 2012). Notations: cornea (1), pupil (2), crystalline lens (3) and retina (4).

The light entering the eye that is scattered from the retina is collected by the sensor to analyze the aberration of the eye through the use of a lenslet array. Then the deformable mirror (Vdovin *et al.*, 2008; Doble *et al.*, 2002; Fernandez *et al.*, 2006; Shirai, 2002; Dalmier & Dainty, 2005; Vargas-Martin *et al.*, 1998, Paterson *et al.*, 2000) provides the conjugate correction to the optical distortions.

The stroke requirements of the DM for imaging in the eye is $>10 \mu\text{m}$ for correcting astigmatism and higher modes (Doble *et al.*, 2003); in ophthalmic applications the speed of the closed loop is a few Hz. The continual process of measuring the residual wavefront aberration and feeding back the correction to the mirror is termed “closed loop adaptive optics”.

During AO imaging of the retina, the optics of the instrument and the eye (objective) temporarily form a single optical system. This configuration of the instrument / eye combination contains two adaptive optics components (deformable mirror / eye) and two controlling systems (computer control / brain with neural sensors). When dynamic correction is performed in a closed loop, this procedure requires the optimisation of the behaviour of the adaptive objective lens of the ophthalmoscope. Since the eye has highly adaptive characteristics in its optics, it is able to operate in an antagonistic fashion to counter the effects of the deformable mirror. Hence, the eye must be prepared for AO imaging by dilating the pupil to maximise the amount of light entering the eye, and by paralysing the ciliary muscle which inhibits accommodation. This allows manipulation of the wavefront with no biological adaptive optics effects induced by the crystalline lens working against the deformable mirror.

Adaptive optics in a human subject was first tested (Dreher *et al.*, 1989) by correcting astigmatism. The use of AO in the eye was later extended to the integration of a Shack-Hartmann sensor by Liang, Williams & Miller (1997) in a closed loop, and then dynamically correcting systems were introduced (Fernandez *et al.*, 2001; Hofer *et al.*, 2001a). The first results taken from an AO system with clinical relevance were published by Roorda & Williams (1999) and Roorda *et al.* (2001) on the trichromatic cone mosaic using AO with retinal densitometry; analytical studies showed that the distribution of different photopigments in cones is random (Hofer *et al.*, 2005).

Over the last 10 years, great advances in developing sophisticated high resolution retinal imaging modalities were made by Roorda *et al.* (2006), Bigelow *et al.* (2007), Burns *et al.* (2007), Dreher *et al.* (1989), Fernandez *et al.* (2008) and Zawadzki *et al.* (2005) using OCT. The first generation of AO ophthalmoscopes (Roorda, 2000; Roorda *et al.*, 2002) confirmed the capability of this technology in non-invasive diagnosis in ophthalmology. Adaptive optics has been used to study the foveal dynamics (Martin & Roorda, 2005 and 2009, Zhong *et al.*, 2008), the waveguiding properties of cones (Roorda & Williams,

2002), retinal pigment epithelium cell mosaics (Gray *et al.*, 2006; Morgan *et al.*, 2009), ganglion cell functions (Gray *et al.*, 2006), including study of cone-rod dystrophies (Choi *et al.*, 2006, Roorda *et al.*, 2007) and confirmation of genetic defects in the living eye have been made (Yoon, Roorda *et al.*, 2009) using an AO ophthalmoscope (Roorda, 2010).

Adaptive optics ophthalmoscopy recently provided imaging results of the nerve fibre layer (Takayama *et al.*, 2012). The cone photoreceptors associated with retinal diseases have begun to be studied *in-vivo* (Carroll *et al.*, 2004; Wolfing *et al.*, 2006; Choi *et al.*, 2006; Duncan *et al.*, 2007; Baraas *et al.*, 2007; Yoon *et al.*, 2009; Torti *et al.*, 2009; Ooto *et al.*, 2011; Lombardo *et al.*, 2012a), and this was recently followed by the first real-time images of human rods (Dubra *et al.*, 2011).

The high resolution capability of adaptive optics ophthalmoscopy allows it to resolve the finer cell structures in the retina and detect retinal disease in its infancy. However, there are constraints on the use of these imaging systems in clinical applications; namely the high cost of deformable mirrors, and that fact that most AO instruments have been designed and constructed for use in laboratory conditions, using complex control instruments. These have all slowed the transition of AO ophthalmoscopy to clinical practice.

I.2 Motivation of thesis

Although adaptive optics has undergone substantial advancement since its first application in ophthalmic instruments, compact AO ophthalmoscopes for clinical studies have not yet been demonstrated. Further to this, in addition to the great advances made in developing optical forms, design techniques and manufacturing methods that minimize fixed and time-varying aberrations, the achievement of diffraction limited performance of the ophthalmoscopes is usually limited by the optical-mechanical characteristics of the human eye, the low light conditions due to safety hazards in the living cells and the high manufacturing cost of deformable mirrors in development. One of the goals of this work is to investigate the performance of a modified version of the Heidelberg Retina Tomograph in providing an instrument for high-resolution imaging developments.

Given the great potential of adaptive optics with wavefront sensing, it is the aim of this thesis to examine the feasibility of using this technology in a cost effective way for compensating the dynamic aberrations caused by the eye and for correcting the static aberrations in the compact optical layout of an ophthalmoscope suitable for integration into clinical research.

I.3 Thesis outline

Retinal imaging system definition and aim of this work:

1. Construction of a compact adaptive ophthalmoscope in a cost effective way
2. Achieving diffraction limited performance by
 - a) Removal of static aberrations of the ophthalmoscope
 - b) Correction of dynamic ocular aberrations
3. Resolving individual photoreceptors in the centre field of the human retina

The thesis is structured as follows:

Chapter I gives a general introduction of ophthalmic imaging and highlights some problems associated with retinal imaging. The first part of this chapter presents an introduction to the field of adaptive optics along with the potential applicability of this technology in ophthalmologic research. Finally, recent developments and research challenges are presented as an introduction to this field.

Development of instruments capable of producing high-resolution fundus images promises a means for the early detection of pathological changes and will allow more precise characterization of retinal diseases. Since difficulties in imaging are mostly due to the anatomical features and adaptive behaviour of the eye in response to external changes, the understanding of the eye and its complex mechanism is essential in the design consideration of any optical system in ophthalmology.

Chapter II summarizes the biological aspects of retinal imaging. The chapter opens with a detailed description of the physiological optics and aberrations of the human eye. This is followed by a description of dynamic effects and abnormal ocular conditions including estimation of the structural changes contributing to ocular distortion effects.

This chapter concludes with a short summary of the human eye as a highly scattering biological sample.

Chapter III gives an overview of the technological issues of retinal imaging including a description of the Heidelberg Retina Tomograph. It introduces the two main wavefront sensing methods, the Shack-Hartmann and the pyramid sensor, the most frequently used techniques in ophthalmic applications, and gives an overview of centroiding to estimate the theoretical limitations of wavefront sensing.

Chapter IV presents the experimental realisation of the compact adaptive optics ophthalmoscope including design considerations for, and optical lay-out of, the imaging system. This chapter gives an overview of the construction and operation of the ophthalmoscope and examines the removal of non-common path errors, including the characterization of phantom retina samples in fake eye models.

Chapter V discusses the retinal imaging protocols and methods, it shows the first imaging results of the compact AO ophthalmoscope on human volunteer subjects; finally retinal images are analysed and compared to histological findings and a discussion of the current system limitations along with the possible improvements.

Chapter VI concludes with a summary and potential impact of this work for future developments.

Chapter II

Biological aspects of retinal imaging

II. Biological aspects of retinal imaging

The human eye is a sophisticated biological image-forming system which allows *in-vivo* study of the nervous system by providing an objective method for non-invasive investigation of microscopic structures of the retina. The performance of ophthalmological instruments is limited by the last focusing optical element, which is the human eye in this case, it being an active part of the ophthalmic imaging system. Therefore, a better understanding of the function and operation of the optical components of the eye is necessary in construction of new state-of-the-art diagnostic instrumentation in order to achieve higher spatial resolution for studying the structures in the back of the eye at a cellular level. This chapter summarizes the basic principles of the human eye as a living optical system (Freeman *et al*, 2003) and from a clinical viewpoint (Tasman & Jaeger, 2006); a more detailed treatment of the eye can be found in (Bennett & Rabbetts, 2007) or (Atchison & Smith, 2002).

II.1 The human eye as a living adaptive optics system

The human eye is a complicated adaptive optical image forming system having positive refractive power for focusing incoming light rays onto an array of photosensitive detectors, which all fit inside the approximately spherical orbit. In addition to its physiological and optical complexity, the eye provides our primary sense. A cross-section of a human eye is given in Figure 2.1, which shows the most relevant optical elements and dynamic components which have a role in the visual process. The eye uses a flexible crystalline lens of variable focal length, operated by muscular power and controlled by nerve signals as a closed loop system. The optics of the visual system comprises several refractive interfaces, the anterior and posterior surfaces of the cornea (~43 dioptries) and the crystalline lens (~20 dioptries for relaxed ciliary muscle), and there is continuous refraction in the lens, which is a gradient refractive index medium.

There are continuous changes in the dimensions and other physical parameters, with accompanying changes in the refractive index distribution throughout life, with most of these changes being largest in childhood.

Axial lengths (or separations of the optical components through change of surface curvatures) show approximately 10 percent variations between individuals (Charman, 2000) and small tilts, displacements or asymmetry of optical surfaces may also occur (Sorsby, 1956; Sorsby *et al.*, 1981).

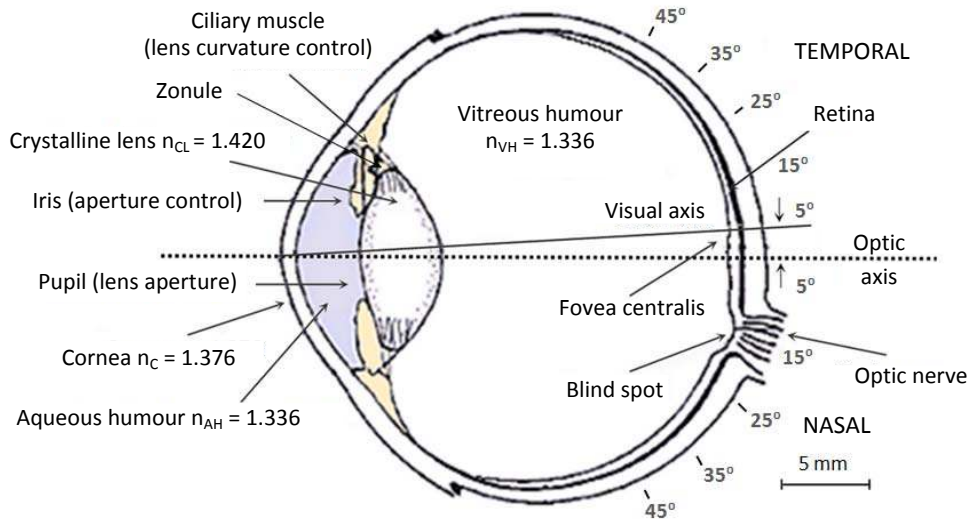


Fig. 2.1 Schematic representation of the human eye in cross-section

The figure shows the schematic horizontal section of the human eye with the values of refractive indices (for sodium D₂ line at 582.3 nm) of its optical elements. The blue shaded component indicates the anterior chamber; the yellow shaded part is the interface of the posterior chamber of the eye. For the light propagating in the ocular media, the iris becomes the entrance pupil, the size of which is controlled by pupillary response in diameter from 2 to 8 mm. The numerical aperture of the eye ranges between 0.06 and 0.25 (from Freeman *et al.*, 2003). The numerical values around the back of the eye correspond to the degrees of eccentricity; the bar gives the approximate scale.

The adult human eye varies 21-26 mm (averages 24 mm) in diameter which is characteristically smaller in hypermetropia and larger in myopia. At birth the size is about 13 mm in diameter and reaches its maximum by puberty. A detailed description of the human eye is discussed for example by (Tasman & Jaeger, 2006), (Kaufmann & Alm, 2003) and (Kanski, 2007); the physiological and functional optics is discussed in this chapter.

II.1.1 Physiological and functional optics of the main components

The cornea, more specifically the anterior tear film surface, provides the majority of the refractive power of the human eye. The air and tear film interface on the anterior cornea (Oshika *et al.*, 1998), where the light enters the eye, is the major refractive surface of the optics of the visual system, and is responsible for almost 70% of the overall refractive power. From an optical perspective, the cornea as a fixed focus lens must provide two functions: it must be transparent and must provide the proper curvature. It combines its optical properties with great tensile strength (Doutch *et al.*, 2008) to maintain the intraocular pressure of approximately 15 mmHg (this is the unit used in medical literature, and this value corresponds to about $2 \cdot 10^3$ Pa in SI units) and to hold its curvature of meniscus form stably. The remaining close to 30% focusing power of the eye, which is provided by the lens, is needed for focusing or accommodation.

The anterior cornea has microscopic irregularities forming roughness on the outer corneal surface which is smoothed by the precorneal tear film. The thickness of the film layer ranges from 6 to 20 μm and averages 7 μm (Mishima, 1965; Cavanagh, 1988); however, recent measurements from reflectance spectra support a value of approximately 3 μm (King-Smith *et al.*, 2000). The tear film distribution on the corneal surface continuously changes over time: after blinking, the tear film layer builds up (Németh *et al.*, 2002) and homogeneously smoothes surface irregularities (supposing the sufficient tear film formation of a normal subject), and through evaporation its thickness decreases and it finally breaks up. The assessment of tear film stability (Alonso-Caneiro, 2009), its dynamic change (Dubra, Paterson & Dainty, 2004; Gruppetta *et al.*, 2005a; Erdélyi *et al.*, 2006; Szczesna *et al.*, 2006; Zhu *et al.*, 2007; Erdélyi, 2007; Kosina-Hagyó, 2011) and understanding its effect on dynamic aberrations (Gruppetta *et al.*, 2005b; Li & Yoon, 2006) are essential since insufficient tear film distribution places a significant constraint on both retinal examination and visual quality (Li & Yoon, 2006). When aqueous deficiency occurs, this causes various problems, including blurred or fluctuating vision (Liu & Pflugfelder, 1999; Tutt *et al.*, 2000), as it causes significant changes in the optical characteristics of the cornea (Atchison & Smith, 2002) and the overall ocular aberration. The influence of the tear film layer on the optical quality of the eye (Li & Yoon, 2006) and physical properties of the tear film is given by Albarrán *et al.* (1997); the molecular basis of the corneal transparency (Freegard, 1997) is studied in detail by Hassel (2010).

Early studies explained corneal transparency by the oriented-lattice theory of Maurice (1954, 1957) and a recent study (Van Meter, 2006) has shown that beside physical factors, the hydration status of the cornea has influence on the corneal transparency, as has a study based on non-invasive OCT monitoring of optical and morphological changes after dehydration stress by Hosseini *et al.* (2004). Based on animal OCT assessment there is correlation between the corneal thickness and its hydration level (Kholodnykh *et al.*, 2003). Tear film break-up may lead to corneal dehydration (Tutt *et al.*, 2000) which may have an adverse influence on structural and optical changes of the cornea.

The average corneal diameter is 11.71 ± 0.42 mm (Rüfer *et al.*, 2005) of which the optical zone is about the central one-third in diameter (~3 mm according to Tabernero *et al.*, 2007). This zone is about 5-6% of the total corneal area and normally has a uniform spherical curvature but is slightly flattened at the periphery. The thickness of the cornea varies from 0.51 to 0.56 mm centrally to 0.62 to 0.67 mm peripherally (Rapuano *et al.*, 1993; Eysteinnsson *et al.*, 2002). These variations in the shape (Koch & Haft, 1993) of the anterior surface can significantly affect the optical performance by contributing to the spherical aberration of the eye; however, they are too small to be detected by conventional keratometers (Bennett & Rabbetts, 2007). A study by Bogan *et al.* (1990), that evaluated the topography of 399 normal corneas among 8 - 79 year olds, found that approximately 20% of the subjects were equally round and oval with the remaining having either irregular or regular astigmatic corneal shape. The evaluation of corneal surface regularities was studied in detail by Liu & Pflugfelder (1999), while the mechanical properties (McCally & Farrell, 1988; Patel & McGhee, 2007) and structure of the cornea are discussed in detail by Maurice (1988).

The cornea can be divided into several layers (detailed description by Snell & Lemp, 1989) from the front surface to the back surface: the epithelium, Bowman's membrane (Patel *et al.*, 1998), the stroma, Descemet's membrane and the endothelium. The thickest layer is the stroma, composed of collagen fibrils which are arranged in layers running parallel to each other and to the corneal surface. The collagen fibrils in the central cornea possess a highly uniform diameter (~32 nm in humans) and have a centre-to-centre spacing of ~62 nm.

The human endothelium is a layer of uniform cells with a characteristic hexagonal structure (Schmedt *et al.*, 2012) in the posterior cornea. The endothelial layer retains the

corneal clarity and provides a barrier between the stroma and the aqueous humour. This layer displays a high osmotic permeability supporting the transportation (Klyce & Bonanno, 1988) of nutrients into the stroma. Due to the avascular nature of this refractive medium, much of the oxygen for metabolic processes (Riley, 1988) comes directly from the atmosphere.

Light entering the cornea travels through up to approximately 100 layers of cells (McCally & Farrell, 1988). The refractive index of the fibres is about 1.47, while the surrounding substance is about 1.354 (Maurice, 1969). Scattering occurs due to this optical inhomogeneity but this structure and the local refractive index changes mitigate the scattering caused by the inhomogeneity (Atchison & Smith, 2002). The index of the multi-layered cornea and the tear film (detailed description in Holly *et al.*, 1986; Holly, 1988; Gilbard *et al.*, 1988) taken as a whole averages to about 1.376.

The anterior chamber is the cavity behind the cornea filled with liquid aqueous humour, with a water content of 98 percent. The circulating aqueous humour nourishes the cornea, giving a transparent and colourless medium with a refractive index of 1.336, and is an important component of the living optical system. In healthy eyes, the flow of aqueous humour against resistance generates an intraocular pressure (IOP), which is necessary for the proper shape and optical properties of the eye ball (Millar & Kaufmann, 1995). Interaction between systematic blood pressure and IOP was reported by Klein *et al.* (2005), Bakke *et al.* (2009) and He *et al.* (2012). The elevated intraocular pressure possibly reduces the nutrient availability and is also a risk factor for glaucoma development (He *et al.*, 2012).

The liquid media is secreted by the ciliary epithelium which enters the posterior chamber. The humour then flows around the lens through the pupil into the anterior chamber. There is convection flow in the aqueous humour, downward close to the cornea, where the temperature is cooler, and upward near the lens, where the temperature is warmer. A recent study by Ooi & Ng (2008) shows a two-dimensional temperature distribution model of the human eye (Schwartz & Feller, 1962; Tan *et al.*, 2009). Figure 2.2 shows the typical temperature distribution model when aqueous humour flow is presented; motion of fluid was considered only in the anterior chamber in this model, flow inside of the posterior chamber was neglected.

Aqueous humour formation is a compound physiological process (Millar & Kaufman, 1995) and moderate alterations in systematic blood pressure and blood flow determine the rate of its formation; in healthy eyes the aqueous humour formation rate is approximately 2.0 to $2.5 \mu\text{min}^{-1}$ (Johnson & Maurice, 1984; Caprioli, 1992).

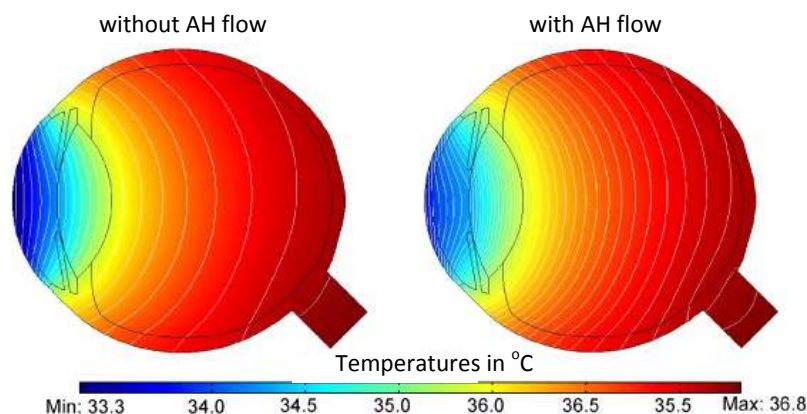


Fig. 2.2 Typical ocular temperature distribution

Figure shows the typical temperature distribution of the human eye with presence and without aqueous humour flow (vertical orientation). The ocular temperature measurement involved the use of non-contact and non-invasive infrared thermography. (Reprinted from *Computers in Biology and Medicine*, **38**(2), EH Ooi & EYK Ng, *Simulation of aqueous humor hydrodynamics in human eye heat transfer*, 252-262, Copyright (2008), with permission from Elsevier.)

The iris is a thin and contractile disc 12 mm diameter in size and lies in front of the crystalline lens. Analogous to the diaphragm of a camera the iris functions as the aperture stop of the eye separating the anterior and the posterior chambers. The opening of the iris is the pupil, through which the two chambers are in continuity. The pupil size may vary from 2-8 mm and a slight degree of asymmetry between the left and right eyes may occur in normal subjects (Forrester *et al.*, 2002). The pupil is under autonomic reflex control via intraocular muscles (detailed description by Atchison & Smith, 2002; Kardon, 2003; Patestas & Gartner, 2009).

The pupil diameter is dependent on the state of contraction of pupillary muscles, the sphincter and the dilator muscles which are located in the iris (Loewenfeld, 1993). The sphincter muscle is composed of a circular band of muscle fibres while the dilator muscle is arranged radially, and the balance between these two muscle groups determines the pupil size. Pupil size is also affected by changes in lens accommodation (Hunter *et al.*, 2000), respiration (Borgdorff, 1975; Daum & Fry, 1982; Yoshida *et al.*, 1994) and the effect of circadian pulse (Daum & Fry, 1982; Calcagnini *et al.*, 1997).

The term pupillary light reflex (PLR) refers to the changes of the pupil size which allows the eye to adjust the amount of light reaching the retinal cells and protects the photoreceptors from high exposure of light. The ability to change the diameter of the pupil has three major functions: optimizing retinal illumination to maximize visual perception, improving the image quality and changing the depth of focus of the eye. There are two mechanisms for pupil dilation (mydriasis): an active reflex due to the contraction of the dilator muscle, and a passive reflex due to the activity of the Edinger-Westphal nucleus (EWN) discussed in an early paper by Loewenfeld, 1958. When the pupil constricts (miosis) tension is increased in the sphincter muscle controlled by the parasympathetic nervous system and by the EWN located in the midbrain (a detailed description of the process is given for example by Milton, 2003 and Kozicz *et al.*, 2011). Some studies have found that pupil size decreases with age (Winn *et al.*, 1994) and that there is less pupil response according to Atchison & Smith (2002); physiology and dynamic behaviour of the pupil in common disorders are discussed for example by Kawasaki (1999).

The pupil of a real eye is usually shifted, often being displaced by about 0.5 mm nasally (Westheimer, 1970; Bradley & Thibos, 1995) but this varies between individuals. The position of the centre of the pupil can change with pupil diameter controlling the direction of the beam propagation, which affects the magnitude and type of ocular aberrations. However, for small pupil diameter (approximately 2-3 mm) around the optical axis and under good lighting condition the eye is capable of nearly diffraction-limited performance (Charman, 2000).

The size of the pupil fluctuates at an average temporal frequency of approximately 1.3 Hz at normal illumination (Clarke *et al.*, 2003) in healthy conditions and the normal pupil cannot respond to changes in light levels at frequencies above 4 Hz (Lowenstein & Loewenfeld, 1969; Kardon & Weinstein, 2006). The mechanism of accommodation is correlated with the pupillary reflex (Pokorny & Smith, 1997) and there is a pupillary latency (gap between the stimulus and response) which can be predicted in a model by Link & Stark (1988):

$$\tau(R, L_{fl}) = 253 - 14 \ln(L_{fl}) + 70R - 29R \ln(L_{fl}) , \quad (1.4)$$

where τ is the latency in milliseconds, L_{fl} is the luminance in foot-Lamberts, and R is the frequency in Hz.

Other models based on experimental data, for example by Moon & Spencer (1944), give estimation for the average pupil size:

$$D = 4.9 - 3 \tanh[0.4(\log_{10}(L_b) - 0.5)] , \quad (1.5)$$

where D is the pupil diameter in mm, the background luminance L_b is expressed in blondels (in the range from 10^5 in sunny and 10^{-5} in dark conditions); a unified formula for light-adapted pupil sizes is given by Watson & Yellott (2012). In recent studies, the latency of the PLR was found to be 280 ms for humans (Clarke *et al.*, 2003), and according to a study by Kardon & Weinstein (2006) the PLR was in range of 200-450 ms. The time delay cannot be explained by the speed of sensory processing alone; it may be partially explained by the axonal conduction and integration time, and the response of sphincter muscles (Clarke *et al.*, 2003); detailed physiological and anatomical descriptions remain to be determined.

The lens is a specialized avascular epithelial tissue that is responsible for fine-tuning the image that is formed on the retina. To perform this function, the lens must be transparent and have a higher refractive index than the media around the lens, and have refractive surfaces of proper curvature. The precise organisation of the structure of the cells and the use of ocular muscular power enables the lens to accommodate through controlled optical changes (Glasser & Kaufman, 1999). The focal length of the cornea-lens combination is adjusted by a change of the curvature of the lens surfaces (Dubbelman & van der Heijde, 2001) which is controlled by a ring muscle around the lens called the ciliary muscle. Changes in the shape of the lens are the result of tension on the zonules, the elasticity of the capsule, and the growth properties of the lens fibres. The change of the lens curvature leads to thickness changes of the lens as well as changes in the refractive surface placement relative to the retina, while the volume of the lens shows no significant change (Hermans *et al.*, 2007). This implies that the lens undergoes elastic deformation during accommodation and the lens material is assumed to be incompressible. According to other studies (Gerometta *et al.*, 2007; Sheppard *et al.*, 2011) accommodative process may involve 2-3% volumetric increase in humans (based on theoretical calculations) and 6-8% increase of volume in bovine eyes, thus opposing the theory that the crystalline lens is incompressible.

The human lens shows continuous growth intensively after birth and at a nearly linear rate later throughout life and there is a degradation of the optical quality of the lens with

ageing that is associated with morphological changes (Alio *et al.*, 2005). The loss of the accommodative mechanism is associated with the structural changes in the lens with age (Dubbelman *et al.*, 2003) and causes a loss in nearer focusing ability. In one study (Strenk *et al.*, 1999) magnetic resonance imaging was used to investigate the accommodative and aging properties of the lens in 10 young (22-30 years) and 15 older (37-82 years) volunteer subjects. The average change of the equatorial thickness of the lens was found to be $310 \pm 210 \mu\text{m}$ (estimated from the results by Strenk *et al.*, 1999) in agreement with (Kasthurirangan *et al.*, 2011). According to this study, the equatorial diameter of the lens showed no correlation with age, while the thickness of the lens under accommodative effort showed modest age-dependence.

To maintain transparency and a high refractive index, lens fibre cells are aligned with their neighbours and accumulate high concentration of proteins referred to as the crystalline proteins (Fagerholm, 1979; Wistow & Piatigorsky, 1988; Bloemendal & de Jong, 1991). This gradient in the refractive index (Hoshino *et al.*, 2011; Pierscionek & Regini, 2012) partially corrects the spherical aberrations of the crystalline lens (Smith & Atchison, 2001). The fibres, near the surface of the lens, have smoother membranes and are arranged in a hexagonal lattice. The lattice structure of the fibres acts as a diffraction grating, where the regular spacing of the scattering centres results in constructive interference and at other angles leads to destructive interference (Bassnett *et al.*, 2011). Scattering in biological tissues generally occurs at boundaries between the compartments where the cellular components have non-uniform refractive indices. However, in the lens, light scattering resulted from the fluctuation of the refractive index is compensated for by the high spatial order of the fibre structure with its narrow intercellular spacing. Besides effects from the high protein concentration of the fibre cells, the amount of light scattering is minimised due to the close matching of the refractive indices of the fibres and the cytoplasm (Michael *et al.*, 2003; Costello *et al.*, 2008). An adaptive model of the structure of the lens is given in detail by Navarro *et al.* (2007); the mechanical properties of human donor lenses were investigated for example by Krag & Andreassen (2003).

The vitreous humour contains more than 99% water; the rest, less than 1%, is composed of solids. The vitreous humour acts as a gel that surrounds and stabilizes a large amount of water. The gel structure results from the arrangement of long and thick collagen fibrils suspended in hyaluronic acid. This stabilizes the high water-content gel structure and the

conformation of the collagen fibrils. This arrangement of small, 10-20 nm diameter fibres permits the transmission of light to the retina with minimal scattering.

There has been extended research on building of schematic eye models based on anatomical and physiological findings to better understanding the role of the different optical components of the human eye. A theoretical eye model with aspherics (Lotmar, 1971), an accommodation-dependent model with aspherics (Navarro *et al.*, 1985), an anatomically accurate model (Liou & Brennan, 1997) and recently a gradient-index lens model by Goncharov & Dainty (2007) are just some examples. Since a model eye is a structural description of a real eye and averages the variation among subjects, it is also useful in predicting the visual performance of the overall eye for new imaging modalities.

II.1.2 Anatomical structures and physiology of the retina

Anatomically, the retina is a thin and intricate layer of cells in the back of the eye and an outgrowth of the nervous system (Tasman & Jaeger, 2006; Kolb, 2003) which is responsible for photodetection by acting like a fibre optics bundle (Enoch & Glisman, 1966; Enoch, 1967). The retina is a circular area in size of 30 to 40 mm in diameter (Polyak, 1941; Van Buren, 1963; Kolb 1991) consisting of several cell types of which five are neural classes; other cell types include glial cells and vascular endothelium. The retinal layer of predominantly neurons, thickness of around 0.5 mm on average (Kolb *et al.*, 2011), is located in the image surface of the ocular optics where the photons are absorbed by the visual pigment of the photosensitive cells to transduce information from an optical image into electrical signals. This process induces biochemical reactions in retinal cells and relays information to the brain via the optic nerve by converting light stimuli into neural impulses through a series of neurons.

The anatomical description of the retina and the neural circuitry are discussed by for example (Kaufman & Alm, 2003; Kolb *et al.*, 2011, Tasman & Jaeger, 2006). This section introduces the regional and topographical retinal structures and summarizes the physiological and biophysical aspects of the human retina (Tasman & Jaeger, 2006; Forrester *et al.*, 2002; Kaufman & Alm, 2003; Kolb *et al.*, 2011); the biochemistry (Whikehart, 2003; Kaufman & Alm, 2003; Forrester *et al.*, 2002) and mechanical inhomogeneity of the eye is given in (Franze *et al.*, 2011).

II.1.2.1 Regional and topographical variations of the retina

There is confusion regarding the terminology used to describe the regions of the retina by clinicians (Kaufman *et al.*, 2003; Tasman & Jaeger, 2006) and anatomists (Forrester *et al.*, 2002). The most often used terminologies and physical location of the structures are given in Table 1.1 for comparison; the locations of the retinal structures are shown in Figure 2.3 in an ophthalmoscopic view of the back of the eye. The table in Figure 2.3 refers to the terms and notations used in this thesis, following (Tasman & Jaeger, 2006) and in line with the recommendation of the American Academy of Ophthalmology (AAO, 1996).

Table 1.1 Clinical and anatomical terms for retinal regions

#	diameter (mm)	Tasman & Jaeger (2006) <i>clinical ophthalmology</i>	Forrester <i>et al.</i> (2002) <i>ophthalmic anatomy</i>		Kaufman <i>et al.</i> (2003) <i>clinical physiology</i>
		terminology	clinical term	anatomical term	terminology
1	0.35	foveola / fovea centralis	fovea centralis	foveola	-
2	1.50 - 1.85	fovea	macula lutea	fovea	fovea centralis
3	1.50 - 2.35*	parafovea (w: 0.5)	-	-	parafovea (w: 1.25)
4	2.35 - 2.75	parafovea/perifovea interface	-	-	parafovea/perifovea interface
5	2.35 - 4.25*	perifovea (w: 1.25)	-	-	perifovea (w: 2.75)
6	5.00 - 6.00	area centralis / macula (3-5 mm macula lutea)	posterior pole / central retina	area centralis	macula lutea

* The sizes for region (3) and (5) indicating ranges of retinal rings; widths of the ring structures are given in mm separately in brackets under the category 'terminology' in the table.

For descriptive purposes, the retina is divided into two halves, the nasal and temporal parts by a vertical line through the centre of the fovea (FC), while the optic disc (OPD) is often used as a reference for separation of the superior and inferior parts (Figure 2.3). The ability of the retina to distinguish detail reaches a maximum in the cone-dominated central region. The central region, around 5-6 mm in diameter located in between the inferior and superior arteries (Tasman & Jaeger, 2006), is the macula (anatomically, area centralis or centre of the retina).

The subdivision of this field is the macula lutea (anatomically, fovea) at about 3-5 mm lateral to the optic disc (measuring 2 mm horizontally by 0.88 mm vertically). The macula lutea is a yellow spot based on the anatomic appearance of the central retina due

to the presence of pigments in the cone axons which may function as a short wavelength filter, in addition to that provided by the lens (Rodieck, 1973; Forrester *et al.*, 2002).

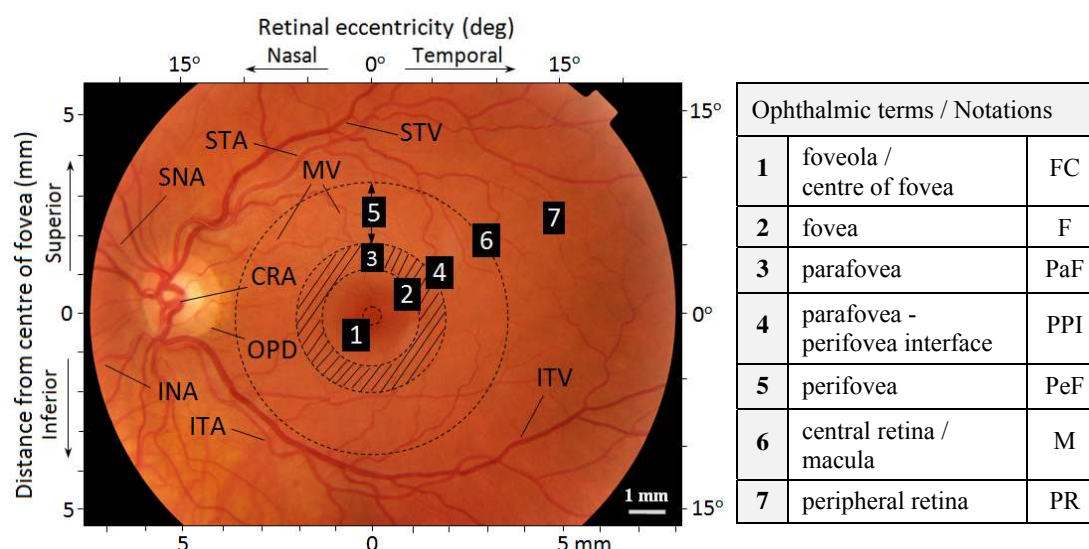


Fig. 2.3 Ophthalmoscopic view of a healthy retina and regional structures

This photograph was taken by a fundus camera (Nikon D90 attached to TOPCON TRC 50DX Retinal camera) showing the author's retina (OS) illustrating regional variations of a normal retina structure. During the examination procedure 1 drop of tropicamide 0.5% was applied for pupil dilation; IOP was measured as 16 mmHg. The main regions are shown in a simplified version with circles; from an anatomic viewpoint, the zones are in fact horizontally elliptical. The image is rescaled to average values of a normal retina. Main anatomical and clinical terms used to describe the regions: STA, superior temporal artery; STV, superior temporal vein; SNA, superior nasal artery; INA, inferior nasal artery; ITA, inferior temporal artery; CRA, central retinal artery; MV, macular vessels and OPD, optic disc. The macula (including regions number 1-6) is the central part of the retina which contains the highest concentration of the photosensitive receptors. (Fundus photo taken by Dr. Laszlo Szalay, courtesy of Department of Ophthalmology, University of Szeged; figure and annotation by the author, 2012.)

The almost circular area of diameter 1.5-1.85 mm at the edge and approximately 400 μm at the floor (Kaufman & Alm, 2003) in the yellow-zone comprises a smaller central region, the fovea; the central 0.35 mm wide region is the centre of the fovea (anatomically, foveola or fovea centralis). The structure of the retina is not uniform (Figure 2.4 showing the central field), and it varies in thickness ranging from 100-230 μm on average, from the periphery to locations near the optic nerve head (Forrester *et al.*, 2002), and it changes with age and heart rate (Kaufman & Alm, 2003; Stockman & Sharp, 2006; Kolb *et al.*, 2011).

The retina is an extremely metabolically active tissue having the highest oxygen consumption compared to other tissues in the human body (Forrester *et al.*, 2002). In general, the vascular system is hidden from non-invasive investigations; however, clarity

of the ocular media and transparency of tissues make the microcirculation an exception in the eye (Figure 2.3 and Figure 2.4).

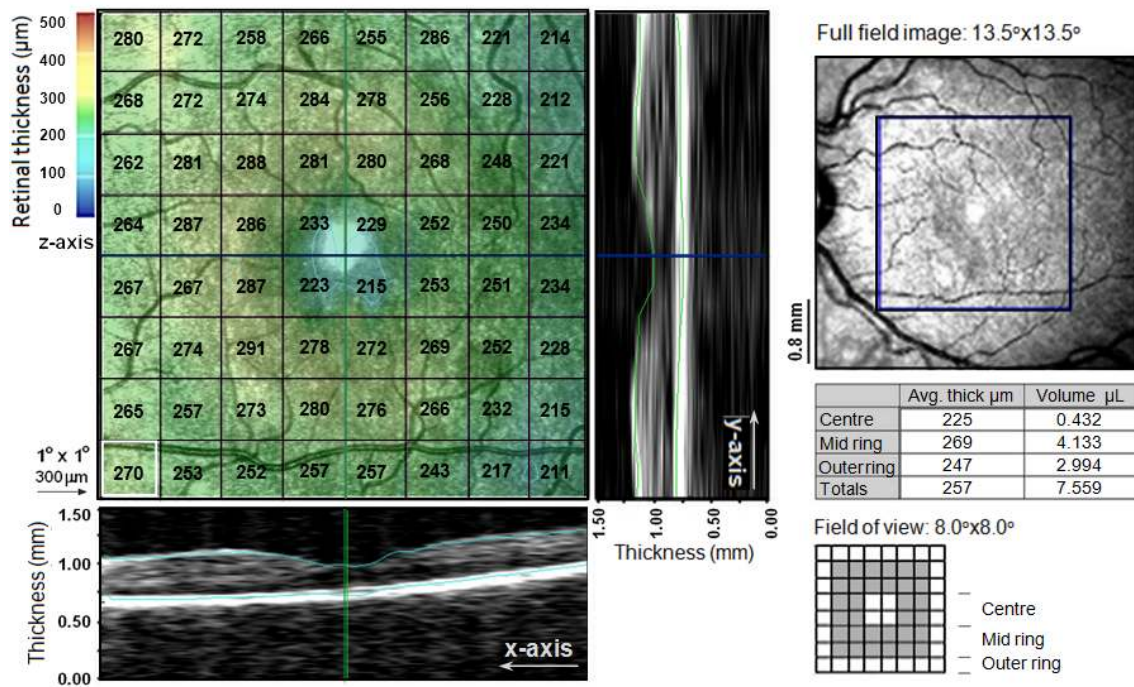


Fig. 2.4 Varying thickness of a healthy retina in central field

The figure shows images of the author's retina taken by a commercially available scanning laser ophthalmoscope and an optical coherence tomograph (OTI Ophthalmic Technology Inc. Imaging Instrumentation, OCT/SLO Combination Imaging System). Upper left colour image shows typical values for thickness of the retinal layers above the photoreceptors and the corresponding OCT scans from the same subject. (Images were taken by Dr Laszlo Szalay, courtesy of Department of Ophthalmology, University of Szeged; figure by the author, 2012.)

The eye has two sources of blood supply (detailed description for example by Elsner, 2006; Kolb *et al.*, 2011): the central retinal artery (CRA) and the choroidal blood vessels. The latter receives 65-85% of the blood flow (Henkind *et al.*, 1979) nourishing the outer retina, particularly the photoreceptors, the remaining 20-30% flows to the retina through CRA from the optic nerve head to maintain the inner layers.

The flow rate is 25 mm/s and 150 mm/s corresponding to retinal (high oxygen exchange) and choroidal (low oxygen exchange) circulation respectively (Kaufman & Alm, 2003; Forrester *et al.*, 2002). The CRA (0.3 mm in diameter) branches to form the arteries typically less than 100 μm in diameters which are around the macula branching into superior and inferior arteries, and subdivided into nasal and temporal parts, and even further into small capillaries.

Through the capillaries, usually less than 10 μm in diameter (Kaufman & Alm, 2003), the blood flows and meets to form larger vessels until it reaches the veins (around 140 μm in diameter or less), which leave the orbit via the optic nerve head. The density of the capillary network is greatest near the macula. A capillary-free zone is present in the central region, which extends roughly 400-500 μm in diameter (Forrester *et al.*, 2002) in most adults.

II.1.2.2 General organization of retinal layers and the photoreceptors

The retina has two main components, the neural retina and the retinal pigment epithelium (PE); considering the histological structure of the retina (Kolb *et al.*, 2011; Forrester *et al.*, 2002; AAO, 1996), it is arranged in an organized manner in eight distinct planar layers of cells (Figure 2.5 and 2.6) including three layers of nerve cells and two layers of synapses.

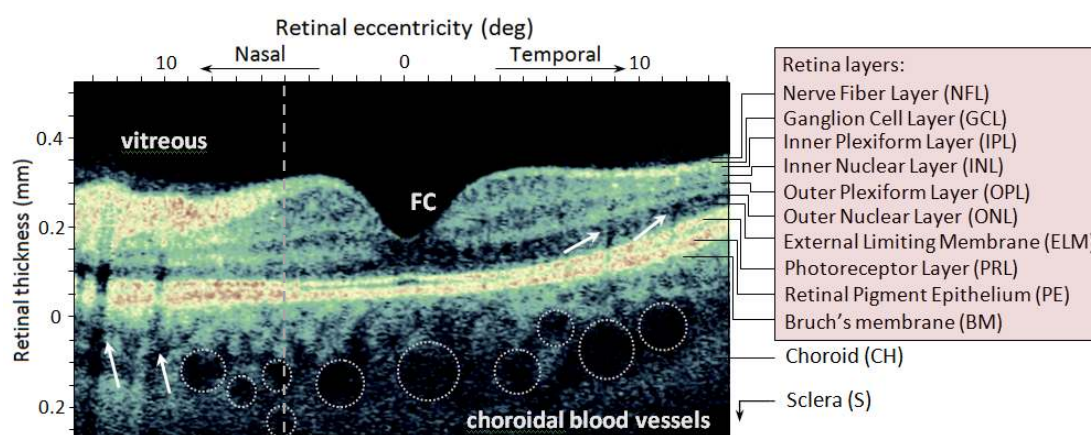


Fig. 2.5 Cross section of a healthy retina

The diagram shows the author's retina, illustrating the main layers in false colour (original OCT image taken by OTI Ophthalmic Technology Inc. Imaging Instrumentation, OCT/SLO Combination Imaging System, courtesy of Dr Laszlo Szalay and Department of Ophthalmology, University of Szeged). White arrows indicate shadows of blood vessels as dark vertical lines across the retina and the white circles (bottom of image) are blood vessels in the choroid, dashed line at 5° nasally indicates the location of Figure 2.6; FC refers to the location of the centre of the fovea. (Figure and annotation by the author, 2012)

The layer of the output neurons, (the nerve fibre layer (NFL)), lies closest to the crystalline lens and is formed by axons of ganglion cells and may also contain amacrine cells according to Kaufman & Alm (2003). The approximately 1.2 million axons of ganglion cells form bundles and leave the eye to form the optic nerve, which lies approximately 5 mm (about 15° of eccentricity) from the centre of the fovea. The size of

the optic disc is approximately 1.5 mm, while the nerve exiting the globe is around 2 to 4 mm in diameter. The ophthalmoscopic appearance of the optic disc (Figure 2.7) depends on several factors including the size of the ocular globe, the number of nerve fibres, the surrounding retinal and choroidal layers (Digre & Corbett, 2003).

The nuclei of the ganglion cells are in the ganglion cell layer (GCL), which is located between the NFL and the inner plexiform layer (IPL). The thickness of the GCL varies across the retina from 60-80 μm in the central retina to 10-20 μm at the periphery, and theoretically there are around 4-6 cones and 100 rods for each ganglion cell (Forrester *et al.*, 2002). Ganglion cells collect all the visual information and the cells of the IPL modulate and carry the signal towards the photoreceptor cells.

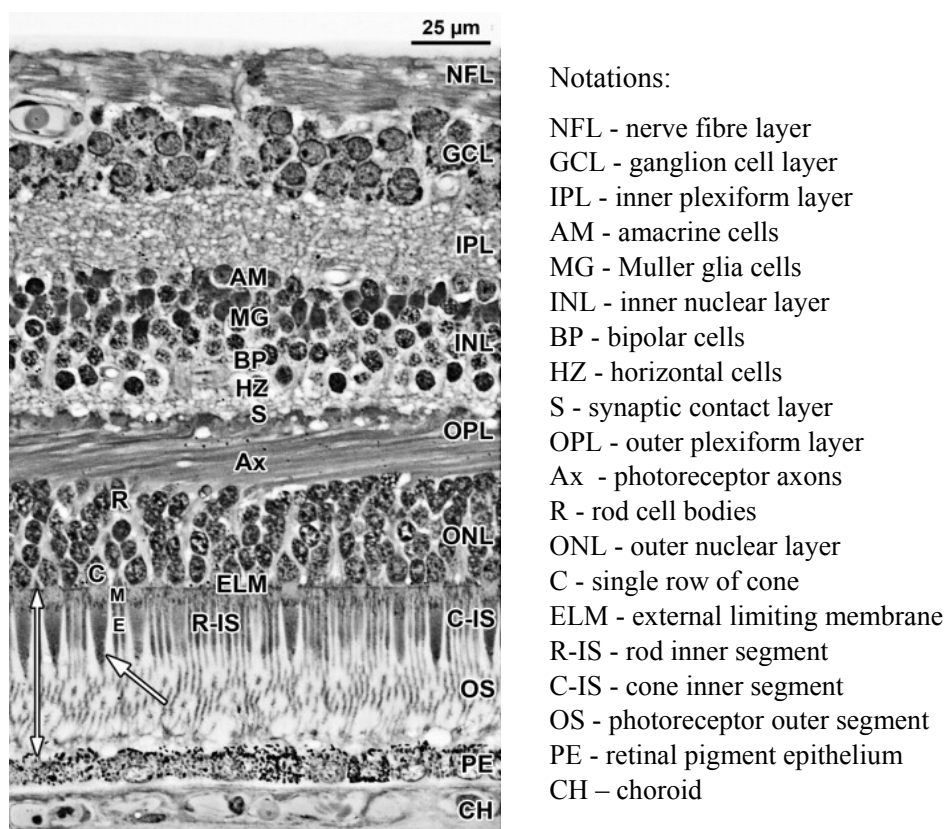


Fig. 2.6 Retinal layers and histology of normal adult human retina

Diagram showing *ex vivo* the layers of an adult human retina 2 mm nasal (the location at about 5° of eccentricity as indicated with dashed line in Fig. 2.5) from foveal centre (reprinted from Am. J. Ophthalmol. **154**(5), A Hendrickson *et al.*, *Histologic development of the human fovea from midgestation to maturity*, 767-778, Copyright (2012), with permission from Elsevier).

The photoreceptor cells usually consist of a nucleus, an outer and inner segment, and an inner fibre, the equivalent of an axon, which are located in different layers of the retina. The IPL serves as an interconnecting layer (with a thickness of 18-36 μm but it is absent

in the foveola), with the inner nuclear layer (INL) and the outer plexiform layer (about 50 μm in thickness in the macula and a few microns toward the periphery). These layers form a series of junctional complexes with the photoreceptors that allow electrical coupling in cells. The outer retinal layers absorb and scatter some of the light before it reaches the photoreceptors. These layers are displaced towards the edge of the foveal region at the foveal pit (Atchison & Smith, 2002).

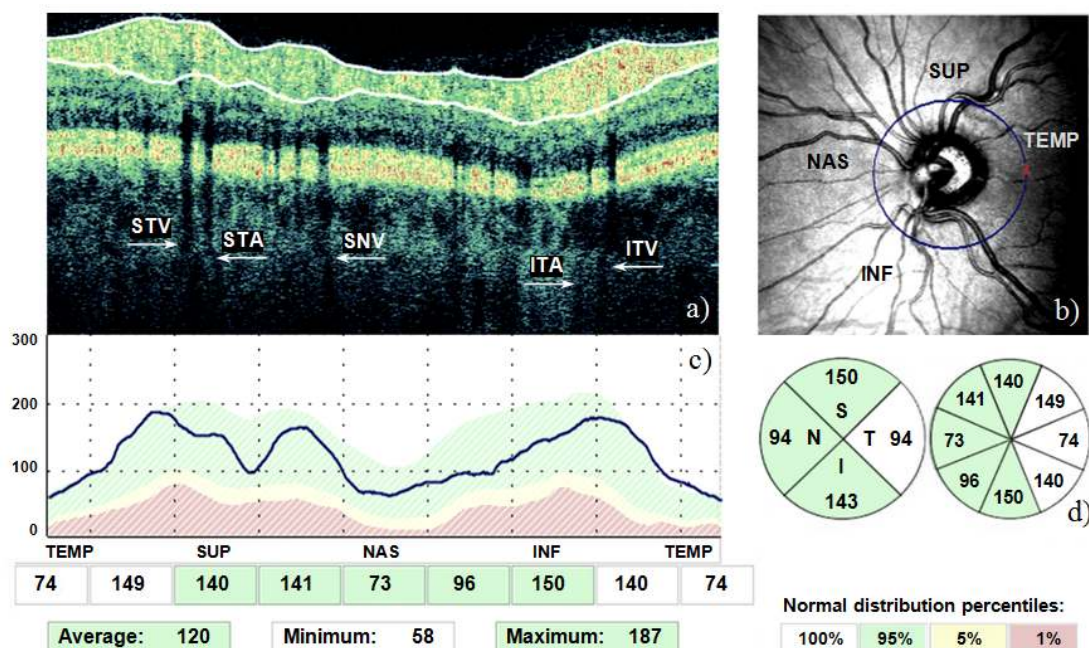


Fig. 2.7 Non-uniform structure of a healthy retina at the optic disc

This figure shows an OCT image (a) and a corresponding SLO image (b) of the author's retina in the optic disc region (OTI Ophthalmic Technology Inc. Imaging Instrumentation, OCT/SLO Combination Imaging System). The diagram (c) shows the thickness values for the nerve fibre layer highlighted in (a) by white curves. The blue curve in (c) is the result of the thickness measurement on a healthy subject point-by-point anticlockwise on the blue circle from temporal through nasal as indicated on (b) by a red arrow. The blue circle shows the optic disc region under investigation and the corresponding thickness values are on the diagram below in (d). Notations: STV, superior temporal vein; STA, superior temporal artery; SNV, superior nasal vein; ITA, inferior temporal artery; ITV, inferior temporal vein and NAS, nasal; TEMP, temporal; SUP, superior; INF, inferior for indicating the retinal subdivisions. (Images courtesy of Dr Laszlo Szalay and Department of Ophthalmology, University of Szeged; figure by the author, 2012.)

The photoreceptor nuclei are located in the outer nuclear layer (ONL); this layer is thickest in the foveal region and becomes progressively thinner toward the periphery. The last connecting layer is the external limiting membrane (ELM) which is not a true membrane, its membranous appearance through a microscope is an optical artefact (Kaufman & Alm, 2003). The photoreceptor layer (PRL) lies outermost in the retina against the retinal pigment epithelium and choroid compromising the outer and inner

segments of the photoreceptor cells. There are two types of photoreceptors, the rods (110-125 million) and the cones (6.3-6.8 million according to Tasman & Jaeger, 2006) and they are arranged in hexagonal mosaics; the cell size and density vary across the retina.

The cone photoreceptors (Roorda & Williams, 1999; Roorda *et al.*, 2001; Hofer *et al.*, 2005; Choi *et al.*, 2006, Roorda *et al.*, 2001) densely populate the fovea at 147,000/mm² and this is where their diameter is the smallest, varying between 1-4 μm , increasing to 4-10 μm extra-foveally. They are concentrated at maximum density, diameter of 1.6 to 2.2 μm with centre-to-centre spacing of 2.5 μm (Hirsch & Hylton, 1984), to the exclusion of rods in the centre of the fovea. The density of the photoreceptors significantly determines the resolving power of this region.

The first rods start to appear approximately 130 μm from the foveal centre (Tasman & Jaeger, 2006) or 1.25 to 2.5 degrees (equivalent to 370-750 μm) according to Hirsch & Miller (1987), while in a recent *non-invasive* AO study by Dubra *et al.* (2011) it was found to be 190 μm . The number of rods increases to about 100,000/mm² (corresponding to about 3-4 μm in diameter) and they are predominantly found in a ring at a distance of 1.2 to 1.7 mm from the centre of the fovea (Kaufman & Alm, 2003) and exceed a density of 30,000/mm² at the periphery; no photoreceptors are present at the optic nerve head. These values vary between individuals depending on age and the presence of disease.

The photoreceptors relay the electrical impulses generated in the ganglion cells, and their activity is modulated by other neural (horizontal and amacrine) cells. The rods are 100-120 μm long cells (Forrester *et al.*, 2002) containing the visual pigment rhodopsin (maximal spectral sensitivity at 496 nm) while the human cone cells (60-75 μm in length) contain three different opsins sensitive to different wavelength ranges of light. They have their peak absorptions at 420, 531 and 588 nm. The green and red sensitive cells are predominantly in the foveola, while this region is devoid of blue sensitive cells, probably as an adaptation to minimize the effects of chromatic aberration (Kaufman & Alm; 2003). Green and red sensitive cells are spaced evenly whereas blue sensitive cells are unevenly spaced throughout the retina. The arrangement of the three cone classes in the living human retina was first investigated by Roorda & Williams (1999).

The retinal pigment epithelium (PE) lies posterior to the neurosensory retina, providing a highly selectively permeable blood/retina barrier (Forrester *et al.*, 2002; Strauss, 2005). The cells in this layer are arranged in a hexagonal structure (Gray *et al.*, 2006; Morgan *et*

al., 2009); the shape and size of the cells is not uniform, and depends on age and location (Forrester *et al.*, 2002), measuring about 14 μm x 10 μm in the central retina. They are more flattened 10-14 μm x 60 μm , in the peripheral retina and lose their uniformity of size. The estimated number of PE cells in humans is 4.2-6.1 million (Forrester *et al.*, 2002; Kaufman & Alm, 2003). This layer structure enables the metabolically-active photosensitive receptors to lie adjacent to the nutrient supply from the choroidal blood vessels. The PE transports ions, glucose, fatty acids and water from the blood and delivers these nutrients to the photoreceptors. The PE is responsible for stray light absorption by melanin granules (which improves retinal image quality) and also for photoreceptor development during embryonic life (AAO, 1996).

Posterior to the PE is Bruch's membrane (BM), which separates the PE from the choroid. The main function of BM is supplying nutrients to the outer layers. Bruch's membrane consists of five layers 1-4 μm in thickness from periphery to the optic disc and the basement membrane of the PE forms Bruch's membrane's innermost layer.

The choroid (CH) is a thin, highly pigmented, vascular connective tissue in the posterior portion of the eye in between the retina and sclera. The layer thickness may depend on blood flow dynamics according to Forrester *et al.*, (2002) and is in the range from 100 μm anteriorly and 220 μm at the posterior pole; the regulation of blood flow may influence the IOP in the eye. The choroid is also a pigmented layer that absorbs the unwanted light from back reflections, analogously to the tapetum membrane in some species (Forrester *et al.*, 2002). Histologically, five different sublayers of this tissue can be distinguished, including Bruch's membrane, the choriocapillaris, two vessel-sized and medium-sized vessel layers. The sclera (S) is a 0.3-1.0 mm thick layer through which the axons of ganglion cells exit to form the optic nerve.

The light entering the eye has to pass through all these potentially light scattering layers of tissues to reach the photoreceptors, which is an advantage from a physiological point of view, as the pigments in the cells protect the neural cells against oxidative stress and reduce scattering (Kaufman & Alm, 2003). From an optical point of view this would be disadvantageous, as the amount of light is significantly decreased after propagating through this series of tissues, but specialized cell structures may improve light transmission. It was recently suggested by Franze *et al.* (2007) that Muller cells (type of supporting glial cells) may act as living waveguides, optimising the eye's sensitivity to

light. These funnel shaped cells lying in the direction of the photoreceptors have a higher refractive index than the surrounding medium, so that they act like tunnels collecting and guiding the light directly to the photoreceptors. Photoreceptors also contribute to the effective collection of photons with their specialized waveguiding properties (Stiles & Crawford, 1933; van Blockland; 1986, Gorrard & Delori; 1995, Burns *et al.*; 1995; Roorda & Williams, 2002). This effect is thought to be more significant for cone receptors and their directionality vary across the central retina (Burns *et al.*, 1997).

The means by which light is reflected back to the pupil is unclear; it may be scattered within the PE and choroid before the light is recaptured by the photoreceptors and then redirected to the pupil. Studies on retinal reflection (Delori & Pfibsen, 1989; van der Kraats *et al.*, 1996; Marcos *et al.*, 1996; van Blockland, 1986) suggest that the returned light from deeper layers (via multiple scatterings) is relatively small probably due to absorption by pigments present in the retinal cells (Kaufmann & Alm, 2003).

II.1.3 Change of optics with aging and abnormal ocular conditions

This section summarizes the main optical changes in different ophthalmic diseases and alterations that may occur, limiting image quality and decreasing the level of achievable resolution. The factors and structural changes presented in the ocular medium are discussed by Tasman & Jaeger (2006), Forrester *et al.* (2002), Kaufman & Alm (2003) and Kanski & Bowling (2011); the clinical and physiological characteristics of ocular abnormalities are given in (Eagle, 2011; Yanoff & Sassani, 2008; Purvin & Kawasaki, 2009; Schiefer *et al.*, 2007).

In spite of the progress in ophthalmic diagnosis and treatment, cataracts still remain the leading cause (47.9%) of visual impairment in almost all the world, except in developed countries, according to recently published statistics produced by the World Health Organization (WHO report, 2012). Cataract usually shows symptoms at an advanced stage and is the leading cause of reversible blindness. Other causes of severe loss of vision or blindness, when retinal layers are affected by irreversible alterations (WHO report, 2012), are glaucoma (12.3%), age-related macular degeneration (8.7%) and diabetic retinopathy (4.8%). Conventional ophthalmic diagnostic methods in screening (Shingleton & O'Donoghue, 2000; Staurengi *et al.*, 2007), generally consist of the

measurement of refractive power, visual field and intraocular pressure, viewing retinal structures and the optic nerve head. Future advances in clinical research to allow the design of new therapies will require a better understanding of the progress and pathophysiology of these ocular diseases, the majority of which cause blindness. A further goal in research and treatment is at least the partial restoration of vision in patients with advanced cell death and neovascularisation (Jager *et al.*, 2008).

Most ocular diseases are manifestations of aging effects which involve the reduction of blood flow or a disturbance to normal cellular functions in many individuals. Reduced transmission of light by the lens with age can occur when disruption of the organisation of fibre cells or damage to the proteins within the fibres destroys the transparency of the crystalline lens. This process is known as cataract formation and refers to an increase of the amount of yellow pigmentation and a disruption to order of the crystallines. The lens crystallines break down partly in response to light exposure, particularly to the shorter, more energetic wavelengths of light. The incident light is absorbed by the pigments present in the lens to protect the light sensitive cells from a high exposure of light in the retina. Any metabolic disturbances, such as diabetes may also potentially alter the maintenance of transparency of tissues, leading to lens opacification. An especially high concentration of pigmentation can reduce visual acuity through increased light absorbance; according to some studies (Kanski, 2007), oxidative modification of the proteins may play a significant role. Cataract formation (Michael & Born, 2011) is still an irreversible process and the only treatment is the replacement of the core of the crystalline lens by an artificial intraocular lens (IOL).

Glaucoma as a degenerative optic neuropathy (Tasman & Jaeger, 2006; Kaufman & Alm, 2003) is the second leading cause of blindness after cataract (Quigley, 1996). The primary site of injury in glaucoma is the ganglion cells (Kuehn *et al.*, 2005) resulting in thinning of the nerve fibre layer (Kanski, 2007; Tasman & Jaeger, 2006) with variable death rates for individual cells (Osborne *et al.*, 1999). Most forms of glaucoma are painless and detection is possible before significant vision loss occurs (Alward, 1998; Osborne *et al.*, 1999) by examining the characteristic appearance of the optic nerve in an ophthalmoscopic view of the retina. According to Nickells (1996) detection is possible (Doble, 2005), only after significant 50-60% loss of ganglion cells has already occurred. It is often difficult to identify and characterize NFL defects and the loss of ganglion cell

using conventional ophthalmic instruments in clinical practice (Tan *et al.*, 2009) and a significant loss of ganglion cells may occur before detectable visual field deficits. A recent *in-vivo* study by Choi *et al.* (2011) confirmed structural changes in cone photoreceptors in eyes with glaucomatous damage consistent with histological findings by Nork *et al.* (2000).

There is good evidence that older age and elevated IOP (normal value <20 mmHg in average) and myopia are risk factors in the development of glaucoma (Kaufman & Alm, 2003; Tasman & Jaeger, 2006; Kwon *et al.*, 2009); the elevated intraocular pressure results from reduced aqueous outflow. However, there is no proven treatment for optic neuropathy to date. Randomised clinical trials have shown that reducing IOP slows the progression of the disease (Kass *et al.*, 2002). Therefore, the current focus of treatment is mainly the medical control of the disease by lowering IOP (Alward, 1998).

Age related macular degeneration (AMD) occurs mainly in middle-aged people (de Jong, 2006; Jager *et al.*, 2008; Kanski, 2007; Congdon *et al.*, 2004; Ding *et al.*, 2009). AMD first manifests in deeper retinal layers (Figure 2.8), when Bruch's membrane becomes thicker, or yellow-white focal deposits, called drusen (Bressler *et al.*, 1988) develop between the PE and the basement membrane underneath.

Progression of the disease (Keane, 2012) is associated with changes in the aging retina and affects primarily the photoreceptor-, PE layers and the Bruch's membrane. Two types of AMD can be distinguished (Figure 2.8): the wet (or neovascular) AMD (Figure 2.8 a-b) develops when cells are damaged due to abnormal formation of blood vessels while the dry type (Figure 2.8 c-d) is formed when macular cells become damaged due to lack of nutrients, forming drusen from their waste products; wet AMD is the more serious form of the disease.

The first clinical findings of these alterations become visible by a standard clinically used ophthalmoscope only when the diameter of the alteration exceeds 25 μm (Sarks *et al.*, 1999). Drusen are formed as clusters in the macula and they vary in size, shape, colour and distribution, and tend to increase in number with age (Ding *et al.*, 2009). Loss of physiological function in PE with aging may also contribute to drusen formation.

In addition, there are also changes in pigmentation and localized detachments of the PE. As AMD progresses, the accumulation of drusen and PE abnormalities result in the

growth of new choroidal blood vessels which, early on, cannot be seen by conventional fundus imaging instruments. Despite intensive research (Green, 1999; Feher *et al.*, 2006; Gehrs *et al.*, 2006; Chen *et al.*, 2008; Coleman *et al.*, 2008; Ding *et al.*, 2009), our understanding of AMD pathogenesis is still incomplete and consequently the treatment options are limited in clinical practice.

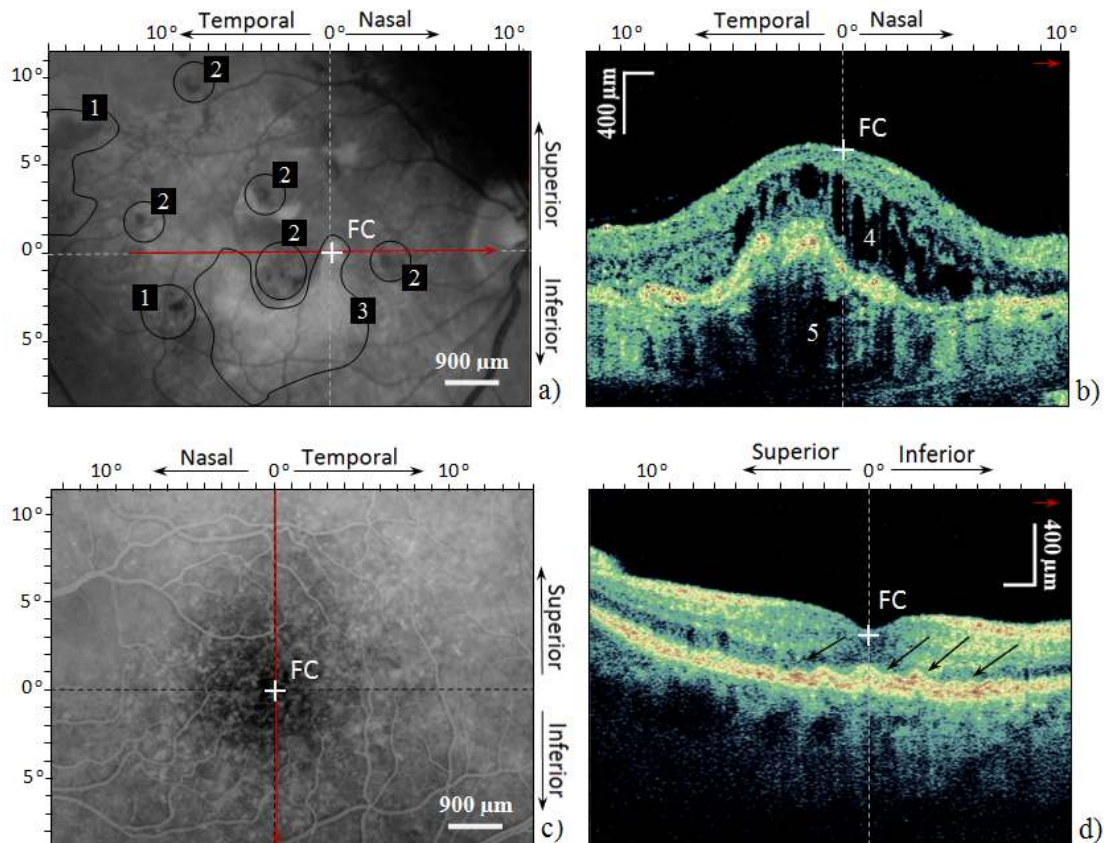


Fig. 2.8 Fundus photography and OCT images in dry and wet AMD

Characteristic examples of fundus angiography (a) and the corresponding OCT image (b) from wet age-related macular degeneration (OD), and angiography (c) and the corresponding OCT image of the macula (d) from dry AMD (OS) of the same 77-year-old male patient. Disruption of PRL is present in both eyes. Structural changes: haemorrhage (an area bleeding) formed (1) and (2); leakage, subretinal fluid (3) and (4); subfoveal choroidal neovascularisation (5). Disruption of Bruch's membrane is presented in (b). Small drusen (numerous small spots) in angiography (c) are formed as mild undulation of the PE in OCT image (d). (Images taken by OTI Ophthalmic Technology Inc. Imaging Instrumentation, OCT/SLO Combination Imaging System, courtesy of Dr Laszlo Szalay and Department of Ophthalmology, University of Szeged; figure by the author, 2012.)

Diabetic retinopathy (Tasman & Jaeger, 2006) is the most severe ocular complication of diabetes (Ferris *et al.*, 1999; Frank, 2004). The first clinical signs (Figure 2.9) of the ocular sequel of retinopathy are microaneurysms and small outpouchings from the capillaries (Frank, 2004). As the disease progresses, there is an increase in the number

and size of retinal haemorrhages and some signs indicating regional failure of the microvascular circulation.

Proliferative diabetic retinopathy involves the formation of new blood vessels when new vessels can extend even into the vitreous cavity. The formation of new vessels can damage the photoreceptor structure and allow haemorrhage into the vitreous humour, which decreases the transparency of the medium for the light entering the eye resulting in a loss of visual acuity. New vessels may form within the stroma of the iris blocking the outflow of the aqueous humour.

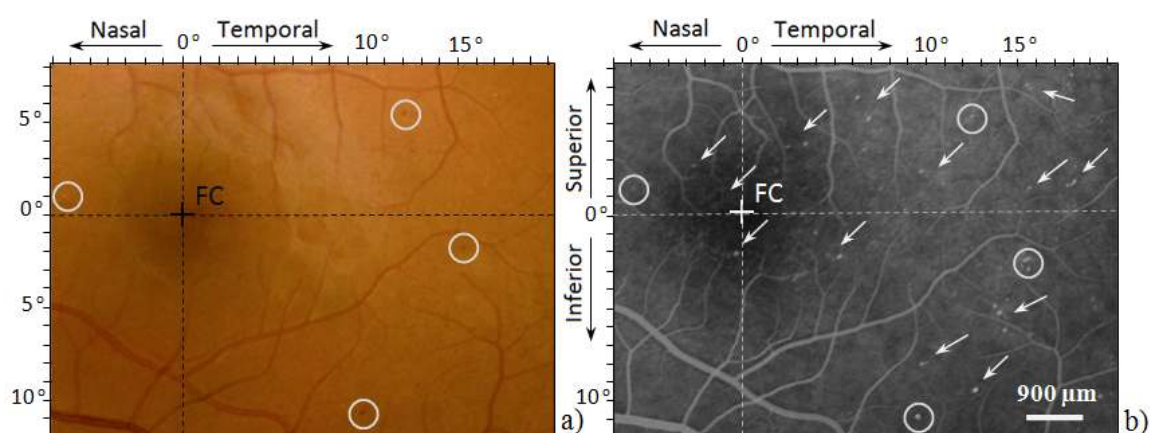


Fig. 2.9 Fundus photography in early phase of diabetic retinopathy

The photographs were taken by a fundus camera (Nikon D90 attached to TOPCON TRC 50DX Retinal camera) field of 27 degrees x 20 degrees showing the central field of the retina (OS) of a 37- year-old female patient diagnosed with diabetes (original fundus photos courtesy of Department of Ophthalmology, University of Szeged; annotation by the author). The images were taken using 1 drop of tropicamide 0.5% in both cases for pupil dilation and sodium-fluorescein 100 mg/ml in 5 ml dose intravenously in case (b) for fluorescein angiography. Image (b) shows the first detectable signs of a diabetic retina; microaneurysms are on the scale of around 40-50 μm diameter (groups of small white spots indicated by arrows). The areas circled in both images are the microaneurysm structures which can be detected with both techniques. FC shows the location of the fovea centralis.

The new blood vessel formation can cause neovascular glaucoma with increased intraocular pressure and change the overall optical performance of the eye. Several biochemical mechanisms have been proposed recently as explanations for the progress of these diseases and have led to extensive research on possible therapies (Frank, 2004); however, none have yet led to effective treatment.

Other laser treatments have also been successfully employed in reducing the progress of vision loss in vascular abnormality by the application of small laser burns (50-100 μm in

diameter). Since laser radiation does not directly photocoagulate the vessels there is no clear evidence that these therapies slow progression according to (Frank, 2004).

The current methods for the prevention of more severe complications and slowing the progression of retinopathy in diabetes and AMD involve Argon-Laser Photocoagulation Therapy. During therapy, multiple (1,000 to 2,000), large diameter (approximately 500 μm), scattered laser burns are placed around almost the whole retina except to the macula (Figure 2.10) resulting in regression of new blood vessels.

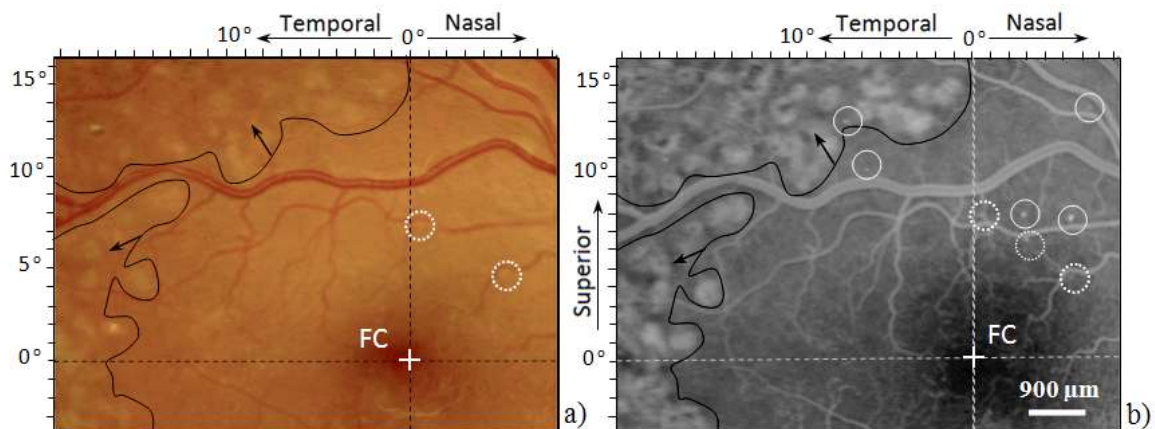


Fig. 2.10 Fundus photography in progressed diabetic retinopathy

The photographs were taken by a fundus camera (Nikon D90 attached to TOPCON TRC 50DX Retinal camera) field of 27 degrees x 20 degrees showing the central field of the retina (OD) of a 42-year-old female patient diagnosed with proliferative diabetic retinopathy (original fundus photos courtesy of Department of Ophthalmology, University of Szeged; annotation by the author). The images show microaneurysms size of about 90-100 μm in diameter (groups of small white spots indicated by dotted circles, while solid white circles indicate haemorrhages). The circled areas with black line at the mid-periphery (showing black arrows) are the locations of photocoagulation laser therapy (diameter of laser burns in the range from 300 to 450 μm). The patient underwent laser therapy at two different sessions (the second time after a 3-month healing period); these are the simple white spots with black centres and white spots respectively. FC is the location of fovea centralis.

Most of these diseases manifest themselves in various depths of the retinal layers, quite often in an irreversible way. Current examination techniques and diagnostic routine of the diseases, which are especially useful in the evaluation of the symptoms, are described in detail by Shingleton & O'Donoghue, 2000 or in more detail by Tasman & Jaeger (2006) and Kanski (2007) in the medical literature.

II.2 Ocular aberrations and dynamical effects performed in the eye

When light passes through multiple layers of cells, the projected image deteriorates, mainly due to scattering by optical and geometrical inhomogeneities (Tuchin, 2000). Optical inhomogeneities result from pathological changes to tissues (Tuchin, 1997) e.g. a local increase in the blood volume due to growing microvessels, or in a more serious form, haemorrhage into the vitreous humour, and varying crystalline distributions in the lens; refractive index changes also play a role. The geometrical inhomogeneities are associated with varying cell structure sizes and irregularities on the corneal surface. The image is also distorted by refraction and reflection. Distortion degrades the overall optical performance of the eye, which is compromised by aberrations that can be mathematically described by means of Zernike polynomials (Appendix A).

The overall ocular aberration contains aberration terms from each ocular surface in the eye. The quality of ophthalmic images depends mainly on the amount of optical aberrations present in the two main refractive components in the eye, the cornea and the lens. The aberrations in healthy eyes depend on several factors and conditions: pupil size (Campbell & Gubisch, 1966; Artal & Navarro, 1994; Schwiegerling, 2000; Donnelly & Roorda, 2003), age of the subject (Artal *et al.*, 1993; Guirao *et al.*, 1999, Oshika, 1999), retinal shape (Williams *et al.*, 1996; Guirao *et al.*, 1999), accommodation (He, Burns & Marcos, 2000) and the overall refractive state.

The most significant aberrations in human subjects are: defocus, astigmatism, spherical aberration, coma and trefoil (Artal *et al.*, 2006; Guirao & Artal, 1999). The distribution of the aberrations in the normal healthy human population is given in studies by Porter *et al.* (2001) and Thibos *et al.* (2002). The average root-mean-square (RMS)¹ aberration is around $\lambda/2$ (approximately 0.25 μm) for normal eyes at the fovea (for a 5-mm pupil diameter), equivalent to 0.25 dioptres (Artal *et al.*, 2006). The source of these aberrations can be estimated and localized by simultaneous measurement of the anterior cornea and the ocular aberrations, the latter based on wavefront sensing techniques. Corneal

¹ RMS, in statistics, the magnitude of a varying quantity which is calculated as the square root of the mean of the squared values. For example for a wave aberration described by Zernike polynomial, RMS wavefront error is the square root of the sum of the squares of a given number of Zernike coefficients (Porter *et al.*, 2006).

topography (Klyce & Dingeldein, 1988) measurements (Salmon, 1999; Mejía-Barbosa & Malacara-Hernández, 2001) with videokeratoscopes (Koch *et al.*, 1989) offer a means to compute and analyze the shape of the anterior surface of the cornea. Therefore, the aberration data associated with the posterior cornea and the crystalline lens can be separated from the total measurement data. This allows the determination of the relative contribution of each optical element to the total wavefront data.

The human eye has a remarkable feature in adapting for external forces, one example of this is the crystalline lens' characteristic that it is able to compensate (Tasman & Jaeger, 2006; Artal *et al.*, 2006) for some of the corneal aberrations (Artal *et al.*, 2001). It is well established that higher-order ocular aberrations fluctuate over a relatively short timescale and ocular aberrations vary with time due to dynamic effects in the eye. The reason for the change in the aberrations is due to the living tissue components and dynamic behaviour of the whole eye, but there is no conclusive evidence regarding the origin of the fluctuations yet. Blood glucose level changes may also be associated with fluctuations in high-order ocular aberrations (Shahidi *et al.*, 2004) in diabetic eyes. However, no confirmation was found for this effect in a study by Huntjens *et al.* (2012) and it is possible that other factors are responsible for the transient visual problems reported in diabetes. Better understanding of dynamic effects, especially ones that are associated with pathological change, is important in the design consideration of high-resolution ocular viewing instruments with adaptive optics.

Beside the mechanical and optical effects (Ethier *et al.*, 2004), the human eye as a living system has an active metabolism and flow supported by the temperature distribution (Shafahi & Vafai, 2011) present in the ocular globe. Mathematically the motion of the aqueous humour in the anterior chamber can be modelled (Ooi & Ng, 2008) by the Navier-Stokes equation (Kumar *et al.*, 2006):

$$\rho \left(\frac{\partial u}{\partial t} + u \frac{\partial u}{\partial x} + v \frac{\partial u}{\partial y} \right) = - \frac{\partial p}{\partial x} + \mu \left(\frac{\partial^2 u}{\partial x^2} + \frac{\partial^2 u}{\partial y^2} \right) + \rho g_x \quad (1.6)$$

$$\rho \left(\frac{\partial v}{\partial t} + u \frac{\partial v}{\partial x} + v \frac{\partial v}{\partial y} \right) = - \frac{\partial p}{\partial y} + \mu \left(\frac{\partial^2 v}{\partial x^2} + \frac{\partial^2 v}{\partial y^2} \right) + \rho g_y \quad (1.7)$$

where p is pressure and μ is the aqueous humour viscosity, ρ is its density, u and v are velocities in the x and y directions respectively; the variables g_x and g_y refer to gravitational acceleration. The effects of buoyancy can be estimated by using the

Boussinesq approximation (Incropera & DeWitt, 2002) that the density ρ slightly changes with temperature but negligible with pressure. Mathematically this can be expressed by $\rho = \rho_0[1 - \beta(T - T_{ref})]$, where ρ_0 is the reference density ($\rho_0 = 996 \text{ kg m}^{-3}$ for aqueous humour), β is the volume expansion coefficient and T_{ref} is the reference temperature which is considered in the model as 34°C . The central corneal temperature was found to be 33.72°C when aqueous humour flow (AHF) was present (and 33.0°C without AHF). According to this model (Ooi & Ng, 2008), the maximum velocity of the flow was $1.03 \times 10^{-4} \text{ ms}^{-1}$ that is $10.3 \text{ }\mu\text{m}$ displacement every 10 ms. There is convection flow in the aqueous humour (Canning *et al.*, 2002), downward close to the cornea (from right to left in the figure), where the temperature is cooler, and upward near the lens (from left to right here), where the temperature is warmer. The maximum velocity of the horizontal component of the flow was found to be $2.78 \times 10^{-5} \text{ ms}^{-1}$, which is equivalent to $27.8 \text{ }\mu\text{m s}^{-1}$. The primary source of the aqueous humour flow is the thermally induced buoyant forces; Figure 2.11 (reprinted from Villamarin *et al.*, 2012) shows the velocity distribution in the anterior chamber.

These forces are the result of the temperature gradients between the front surface of the anterior chamber (assumed to be 34°C) and surface of the lens and iris (generally 37°C). According to Ethier *et al.* (2004) the aqueous humour production rate corresponds to a turnover rate of 60% of the liquid volume per hour under healthy conditions. All the processes become more complex due to pathological changes when inhomogeneities become more significant in the ocular media, and the refractive elements are less transparent to visible radiation.

The most essential aberration changes are due to accommodation of the lens (Artal *et al.*, 2002). These changes can be measured with the use of real-time wavefront sensors (Hampson *et al.*, 2006, 2009). The effect is more significant on the anterior surface of the lens than on the posterior part. This process does not occur instantaneously since there is a short reaction time before the lens starts to change its shape. The process to change the shape of the crystalline lens typically takes 0.6 seconds, resulting in an overall response time of about 1.0 seconds, including 0.4 seconds of latency to complete the lens deformation process (Freeman *et al.*, 2003).

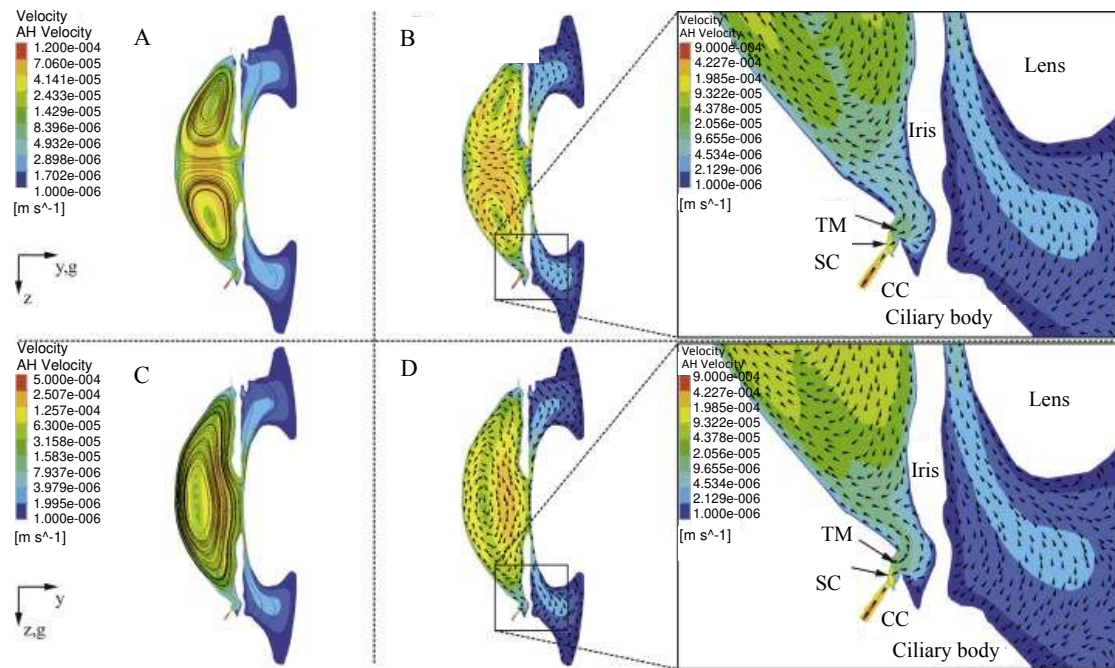


Fig. 2.11 Velocity distribution in anterior chamber when gravity is applied

Diagram A and B show contours of velocity magnitudes and velocity vectors in the anterior chamber with gravity in y and z , C and D when gravity is applied in the z direction, parallel to the iris; in this location $\Delta T=2^{\circ}\text{C}$ is present (Reprinted from Med. Eng. & Phys. **34**(10), Villamarin *et al.*, *3D simulation of the aqueous flow in the human eye*, 1462-1470, Copyright (2012), with permission of Elsevier). AH is secreted by the ciliary body and then flows through the pupil where the velocity increases up to $7 \times 10^{-2} \text{ mm s}^{-1}$. The velocity towards the cornea increases, the streamlines then descend along the cornea down and exit either through the trabecular meshwork (TM) or get mixed with the fluid entering the chamber; the highest velocities, 0.9 mm s^{-1} are present in Schlemm's canal (SC) and through the collecting channels (CC) and near the central iris with 0.2 mm s^{-1} .

It has been found that during steady-state observation of the ocular media, involuntary eye movements and small fluctuations known also as fixational instability or retinal jitter occur. Beside these effects, a number of other factors, such as head- and eye movements, the cooperation of the patient (Figure 2.12 shows a typical example of blinking during image acquisition) determine the quality of the ophthalmic image and the repeatability of a measurement. The timescale of these effects determines the required speed of the AO correction.

There are three categories of fixational eye movements (Zuber *et al.*, 1965): ocular microtremor, ocular drifts and microsaccades. Microfluctuations (rate of 1-2 Hz), first observed by (Collins, 1937) are correlated with the arterial pulse (Winn & Gilmartin, 1992; Collins *et al.*, 1995). The lower frequency components are thought to be under neurological control, in the range of 0 to less than 0.6 Hz. As a result of low luminance

with small pupils, low-frequency drifts arise. Drifts involve low-frequency movements with median amplitude of the order of 10 μm in magnitude.

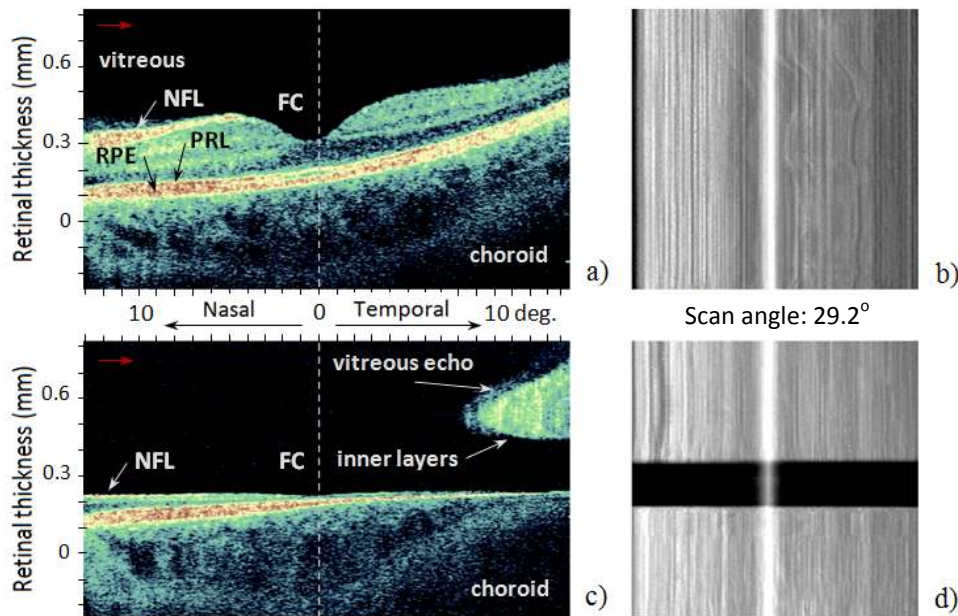


Fig. 2.12 Stable fixation and blinking during SLO/OCT image acquisition

Examples of OCT images (a) and (c) of the centre of the author's retina (OS) and the corresponding scanning sequences (b) and (d) when the subject is focusing stable (a) and blinking (c) during image acquisition. The red arrows in (a) and (c) show the section of the OCT sampling. Notation in the diagrams: FC foveola, NFL nerve fibre layer, PRL photoreceptor layer and PE retinal pigment epithelium. (Original photographs taken by OTI Ophthalmic Technology Inc. Imaging Instrumentation, OCT/SLO Combination Imaging System, courtesy of Dr Laszlo Szalay, Department of Ophthalmology, University of Szeged; annotation by the author, 2012.)

Microsaccades are similar to voluntary saccades and involve sudden shifts in eye positions of the same order of magnitude as ocular drifts (Zuber *et al.*, 1965). The ability to maintain steady fixation is limited by involuntary eye tremor. This is dependent on a balanced muscular system such as those responsible for the rotation of the eye. An early investigation, by Riggs *et al.* (1954), shows that the retina is virtually stationary for exposures up to 10 ms in duration. Longitudinal eye movements have also been investigated; recent studies (Iskander & Kasparzak, 2006) with a high-speed videokeratoscope (sampling frequency of 50 Hz) showed that the magnitude of the longitudinal corneal apex movement could be more than 200 μm .

Various events are associated with retinal vascular dynamics as described by Friedenwald (1934) including the change in axial length through the pulsation of the fundus, intraocular pressure (Namba *et al.*, 1989), pupillary movements (Daum & Fry, 1982) and microsaccades (Gros *et al.*, 1991; Eadie *et al.*, 1994).

A recent study by Hampson *et al.* in 2005 showed that the variability of the heartbeat and pulse account for 11% and 20% of the aberration dynamics respectively. Furthermore, pupil size fluctuations (Ohtsuka *et al.*, 1988) and microfluctuations in accommodation (Collins *et al.*, 1995) have been shown to be correlated with respiration.

A further complexity of imaging in the eye is the double-pass effect (Williams *et al.*, 1994) which results in a loss of phase information (Solomon & Dainty, 1992). The light entering the eye first travels through the perturbative ocular medium and the multiple layers of the retina, which scatters the incident wave. The ocular double-pass process is discussed in detail by Diaz-Santana & Dainty (2001), who state that the light travels through the same ocular medium twice, causing distortion of the wavefront on both the incoming and outgoing path.

II.3 The human eye as a biological sample

II.3.1 Radiation sensitivity of the ocular cells

Studies on the characteristics of transmittance of electromagnetic radiation in the eye have established a basis for the explanation of ocular photoeffects. In order to fully understand light propagation in biological tissues, knowledge of their optical properties is essential. Although some studies show similarities, others disagree, as most of the tests were carried out on donor samples. There has not yet been a full investigation as to how post-mortem changes affect ocular characteristics (Alguere *et al.*, 1993). Therefore, a more fundamental knowledge of the optical properties of the whole eye and ocular fundus is necessary to obtain correct parameters for instrumental design and applications.

Compared to other biological tissues, ocular tissues possess very peculiar optical properties (Svaasand *et al.*, 1989). However, a significant amount of the incident light is lost due to scattering caused by inhomogeneities on a cellular level, such as the membrane, nuclei or mitochondria and absorption in the constituents such as haemoglobin and water.

Some light is reflected at each major ocular interface and some light is scattered by the ocular media. These surfaces are smooth; therefore the specularly reflected light contributes to the image formation on the retina. According to a study by Boettner & Wolter (1962), the total transmittance of the ocular media in humans reaches its maximum of over 90% in the wavelength region from 630 to 730 nm (Alguere *et al.*, 1993) with no age dependency. A recent investigation by van den Berg & Tan (1994) found no age dependence of the corneal transmittance. The overall ocular transmittance depends upon the amount of scattered light; furthermore, while the transmission of ultraviolet radiation decreases with age, the transmission of infrared radiation is independent of age (Atchison & Smith, 2002).

Most investigations have found that the main reflection loss (estimated at 2%) is at the corneal-air interface. It is also well-known that the changes in the optics of the lens that come with age reduce transmittance. Furthermore, transmittance decreases with increasing absorption and scattering in the ocular media (Alguere *et al.*, 1993).

The cornea (and the high protein concentration lens) absorbs nearly all the optical radiation below 300 nm wavelength (Atchison & Smith, 2002). The absorbed ultraviolet radiation causes a photochemical reaction and damages the epithelial cells. While the retinal pigment epithelium and the choroid show strong absorption over the entire visible wavelength range, the optics of the sclera is dominated by scattering.

II.3.2 Ocular scattering and stray light

The retina acts like a diffuser (Campbell & Gubisch, 1966) and scattering in the ocular media is due to spatial variations in the refractive index and other factors such as microscopic scale irregularities mainly in the lens and cornea. These irregularities may change the direction of the incident light and scattered light can spread over a wide range of angles. We can distinguish between back-scattered light which never reaches the retina and forward-scattered light, which reduces the contrast of the image (Tuchin, 2007).

Light scattering and the resulting retinal stray light is the basis for retinal contrast reduction and subsequently glare. There are four main sources that contribute to the amount of stray light in normal healthy eyes: the iris, sclera, crystalline lens and fundus

(van den Berg *et al.*, 2007). In normal young eyes, approximately a quarter of the scattered light reaching the back of the eye comes from the cornea, another quarter from retinal reflection and most of the remaining 50% is from the lens (van den Berg *et al.*, 2007).

The overall scattering increases with age roughly by a factor of 2-3 in adult life, mainly due to the ageing effects in the lens and scattering is negligible in the high water-content chambers in healthy conditions; however, haemorrhages into the vitreous, for example, cause an increased amount of scattered light. Most corneal disturbances such as in corneal dystrophies and turbidity in the vitreous also cause a strong increase in stray light, often with significant effects on visual acuity. The iris and sclera transmit some of the light depending on the level of pigmentation; this is especially considerable for lightly-pigmented irises. With ageing comes the development of cataract, whose earliest sign is increased stray light (Waard *et al.*, 1992; van den Berg, 2007). The level of stray light depends strongly on the pigmentation of the eye (IJspert *et al.*, 1993; Coppens *et al.*, 2006) and changes with age according to IJspert *et al.* (1990) and van den Berg (2007); a clinical assessment of the intraocular stray light is given by (van den Berg & IJspert, 1992).

II.4 Summary and discussion

The eye is a self-adaptive optical system which consists of several refractive interfaces such as the cornea, the crystalline lens and the two chambers filled with turbid liquid. Each ocular surface contributes to the image quality through multiple layers of randomly oriented cells. The major factors that affect the amount of light reaching the retina are: pupil area, lens optical density and the optical density of the macular pigment which selectively filters the light arriving at the photoreceptor layer in the retina.

This chapter is focused on normal and diseased retina structure in adults; however, retinal development (Reese, 2011) is incomplete at the time of birth (Kaufman & Alm, 2003). The retinal layers undergo structural changes and cell structures are reorganised up to the age of 5. At birth, the cone density of the human fovea is only about 20% of the adult value, and the foveal pit is only fully formed (by migration of ganglion cells) by an age of about 11 to 15 months. Figure 2.13 shows a summary of the mean thickness of various retinal layers during human foveal development and maturation. The density of the cones reaches a maximum at an age of 4 to 5 years, and involves a change of cell shape, which is achieved through a decrease in the foveal area during development, producing a more compact structure. The development of the rod-free zone is poorly understood, and there is no evidence for programmed cell death as the tissues develop.

Aging effects (normal or cataract) and pathological changes (haemorrhage) cause difficulties when imaging the retina; the medium is often less transparent to applied radiation due to optical inhomogeneities. In adult life, some parameters of the ocular optics differ from normal values and this increases the level of scatter and stray light. These effects cannot be neglected and considerably degrade retinal image quality.

The ocular aberrations that cause distortion are present in the two main refractive media, the cornea and the lens. The most significant changes in aberration occur mainly due to accommodation and pupil size fluctuations. This can be cancelled by induced pupil dilatation, which maximises the size of the aperture stop of the eye, thus causing a dramatic increase in wavefront aberration. An increase in pupil diameter results in degraded image quality and the eye is no longer diffraction limited.

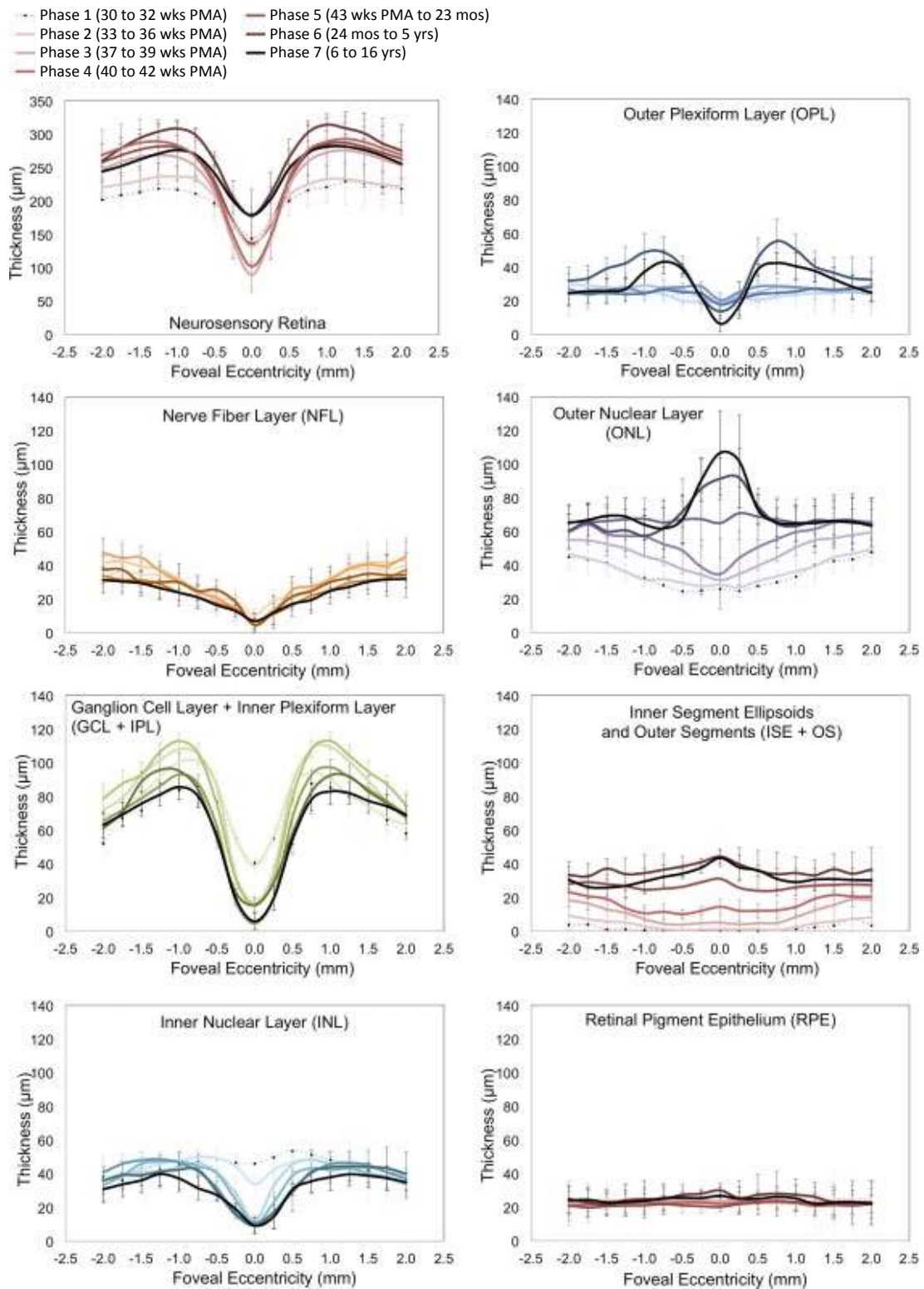


Fig. 2.13 Thickness of human retinal layers during development and maturation

This diagram shows a summary of the mean thickness of retinal layers from 20 weeks postmenstrual age (PMA) to 16 years in the following 6 phases of development, from premature infants (phase 1, 2, 3 and 4 including term birth) and children (phase 5-6). (Reprinted from *Am. J. Ophthalmol.* **154**(5), Vajzovic *et al.*, *Maturation of the human fovea: Correlation of spectral-domain optical coherence tomography findings with histology*, 779-789, Copyright (2012), with permission of Elsevier.)

The most significant aberrations in retinal imaging that require correction are defocus, astigmatism, spherical aberration, coma and trefoil. During steady-state observation of the retina, fixational instability and retinal jitter occur at a rate of approximately 1-2 Hz, which is a further constraint. Respiration, head- and eye movements and changes in tear film distribution also contribute to the aberration dynamics. The retina is considered to be stationary for exposures up to 10 ms in duration; however, imaging in the eye, both in normal conditions and in disease conditions is quite challenging due to the optical complexity of the eye and due to the associated safety hazards, low light level conditions and the low reflectance of the retina.

Chapter III

Technical issues in retinal imaging

III. Technical issues in retinal imaging

This chapter opens with a short overview of the main developments in retinal imaging and summarizes the technical issues in using confocal scanning laser ophthalmoscopy and adaptive optics as implemented in this thesis.

The construction of a cSLO as integrated in a commercially available ophthalmoscope; the modified Heidelberg Retina Tomograph (HRT) is discussed in the first section, including the principles of operation and its use in the current clinical diagnostic routine. The main components of an AO system and wavefront sensing methods are presented with the purpose of reducing the ocular and system aberrations which are the main concerns in any ophthalmic imaging instrument.

The method of achieving diffraction limited performance by the introduction of correcting devices to compensate for distortion effects is discussed. Finally, the limitations of wavefront sensing in a low illumination level AO ophthalmic system that can be used in the eye are considered.

III.1 HRT as a confocal scanning laser ophthalmoscope

Ophthalmic imaging has undergone a significant change as new technologies became available, and developments in ophthalmology have had effects on other fields in medicine, as the eye offers the only direct visual access to blood vessels for investigation of the mechanisms of blood flow regulation and neural reflex stimulation in a *non-invasive* manner.

This section gives an introduction to the operation of the Heidelberg Retina Tomograph (modified version for AO imaging). The retina tomograph (different from the one presented in this thesis) is a commercially available and widely used confocal laser scanning imaging system designed to use in clinical practice (Heidelberg Engineering, 2007) for the follow-up of topographic changes to ocular structures in the posterior segment of the eye. Figure 3.1 shows a schematic diagram of the optical layout of the modified HRT customized for high-resolution confocal laser scanning imaging development.

The modified HRT for adaptive optics development comprises four main components to acquire retinal images: light delivery, raster scanning, light detection and frame grabbing. The light source is a 5 mW diode laser operating at 670 nm, which when run at maximum output power provides 180 μ W at the pupil plane. According to the British Standard (BS-60825-8: 2006 and BS-60825-13: 2006) this light level in the visible range of radiation corresponds to a Class I laser equipment. The angular field of view is user controlled and can be manually set to $10^\circ \times 10^\circ$, $15^\circ \times 15^\circ$ or $20^\circ \times 20^\circ$. The focus of the optics can be changed ± 11 dioptres to compensate for spherical aberration in steps of a quarter dioptre on the controller board by changing the position of the non-condenser optics of the ophthalmoscope with a stepper motor, whilst the position of the condenser lens remains fixed.

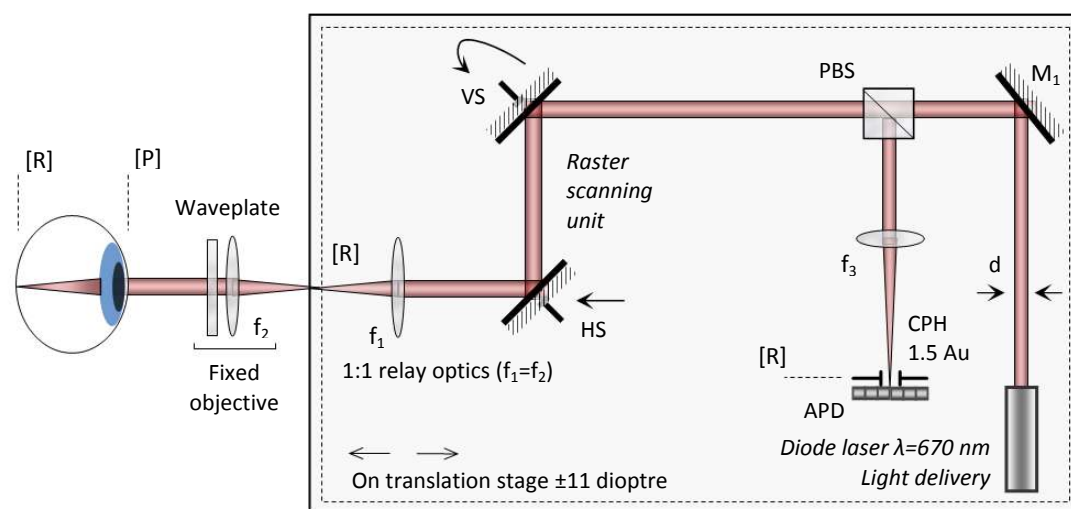


Fig. 3.1 Schematic optical layout of the modified HRT

Diagram showing the main components of a schematic confocal SLO arrangement of the HRT: lenses are labelled #, the mirror M_1 ; the retinal and pupil conjugate planes as [R] and [P] through the optical path. All lenses are achromatic doublets (ACDs), the mirror is flat and aluminium coated. Notations: HS, horizontal scanner; VS, vertical scanner; CPH, confocal pinhole; APD, avalanche photodiode and PBS, polarizing beamsplitter.

The laser beam (d) is collimated and passes through a polarising beam splitter (PBS) onto the vertical (VS) and horizontal (HS) scanners and finally through two achromatic lenses (f_1 and f_2) arranged in a relay lens arrangement on a translation stage, into the eye. A waveplate is placed after the last lens in the ophthalmoscope to allow for discrimination of the double-pass illumination later on in the beam path. The beam is scanned on the retina with a resonant scanner horizontally (HS) at 4 kHz in a sinusoidal pattern. A galvanometric scanner is coupled to the resonant scanner (VS) and operates in

a sawtooth pattern at 50 Hz. The light reflected from the retina is descanned and is focused onto the 1.5 Airy disc unit in confocal pinhole (CPH) in the detection arm (d exit beam, f_3 focal length collector lens). The confocal feature refers to an optical arrangement where a pinhole (CPH), which is optically conjugated to the focal plane of the laser illuminating system in the retina, is placed in front of the avalanche photodetector (APD). This optical arrangement allows the spatial filtering of out-of-focus light so that only light reflected at the focal plane of the retina can pass through the pinhole and be detected by the APD.

The image signal data is digitised in the range from 0 to 1 Volts. This input feeds into a frame grabber card on a computer capable of displaying 256x256 pixel live images. The topography image is red-and-black colour coded on the display with dark and light colours representing elevated and depressed structures respectively. To obtain a 3D dataset, the system acquires a series of two-dimensional images of the sample at multiple focal planes above, at and below the retinal focal plane by moving the position of focus. Each series consists of 32 confocally sectioned images from different depths. Each two-dimensional image section is acquired in 32 ms, with a repetition rate of 20 Hz. The total time acquisition to acquire one series of 32 images is 1.6 seconds.

The main advantages of this system are its flexibility and the fact that a small, 1-2 mm pupil diameter of the subject is sufficient to acquire good quality images; thus induced pupil dilation usually is not required. A detailed description of the standard HRT can be obtained from the website of the Heidelberg Engineering GmbH (HRT Tutorial and Manual 2007).

In its standard configuration, the HRT instrument is capable of achieving spatial resolutions on the order of ~ 10 μm laterally and ~ 200 μm axially. Although this is sufficient to pick up gross features on the retina, it would be desirable to obtain images at increased resolution, which may enable cellular-level information to be used in the diagnosis of various pathologies. A practical means of obtaining increased spatial resolution is the implementation of adaptive optics aberration compensation techniques, and this is discussed in the following section.

III.2 Wavefront sensing for ophthalmic application

Adaptive optics is used for real-time compensation for continuous fluctuations due to turbulence in the ocular media and correcting for dynamic change of the aberrations. The major components of an AO system are the wavefront sensor, the wavefront corrector and the control algorithm. The wavefront sensor makes measurements for determination of the incoming wavefront; the control algorithm uses this data in a calculation of the conjugate wavefront that is applied on the wavefront corrector.

The key requirements for an AO system include the frame rate and sensitivity of the detection camera and the stroke of the corrective element. The speed of the correction is usually in the range of Hz in ophthalmic applications depending on the dynamics of the aberrations (Hofer *et al.*, 2001b); generally the speed of correction has to be 5-10 times faster than the aberration (Murray, 2006). The change of aberrations includes the fluctuation of focus about its mean level with amplitudes of approximately 0.03-0.5 dioptres and with temporal frequencies up to 5 Hz during steady state accommodation (Charman & Heron, 1988). In retinal imaging, the time constraints are imposed by the movement of the subject, including voluntary and involuntary movements, partly due to pulse and respiration. For the proper real-time correction of the wavefront aberrations in the eye, the structure of the wavefront sensor and the correcting device must match that of the ocular aberration being corrected with sufficient spatial resolution (Geary, 1995).

Most sensors are improved versions of classical test devices (Malacara, 1992) used in optics. The most commonly used AO systems employ a Shack-Hartmann sensor (SHS); however, pyramid-type, curvature wavefront sensor (Gruppetta *et al.*, 2005a) and interferometric sensing (Love *et al.*, 2005) applications have also been tested. The SHS and pyramid wavefront sensing methods will be reviewed in the rest of this section.

III.2.1 Shack-Hartmann wavefront sensor

Of the existing wavefront sensors with widespread applications in adaptive optical systems, the most commonly used is the Shack-Hartmann type (Figure 3.2) sensor. This is due to its simplicity, high light efficiency and especially due to its flexibility in integration into optical systems (Irwan *et al.*, 1999). One of the most important advantages of this sensor is that it contains no moving optical elements (Geary, 1995). It is also fast, accurate and, in contrast to interferometers, is insensitive to vibrations (Neal *et al.*, 2002; Choo & Muller, 2004).

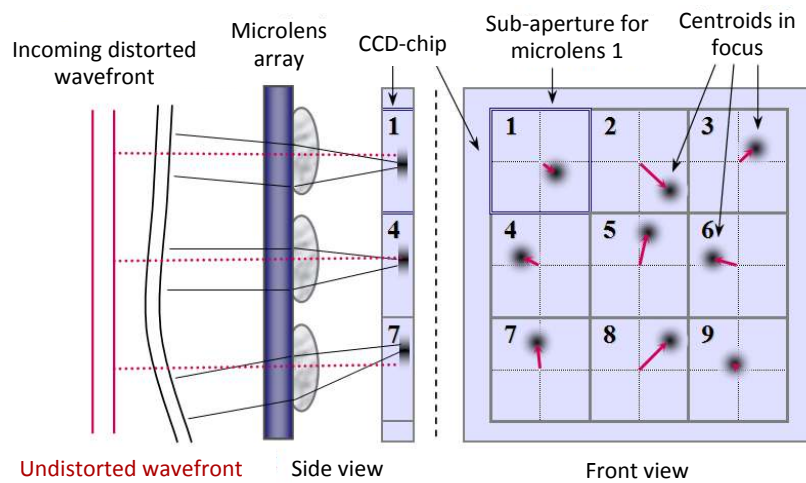


Fig. 3.2 Schematic representation of a SHS in geometrical optics approximation

Schematic representation of a SHS in a geometrical optics approximation (side view). In SH sensing the wavefront is spatially sampled by a microlens array of around 1x1cm in total size. The lenslets behave just like standard low NA spherical lenses, and they are usually diffraction limited (Paterson, 2006). Each microlens has its own detector subaperture divided into 4 quadrants (front view), (after Choo & Muller 2004). If the incoming wavefront is plane (red), the sampled parts would be focused at the centres of the quad cells (as reference points) by the lenslet array. If the plane wave is distorted (black), the centroids of the spots would spatially shift (indicated by red arrows on the right side) from the reference points depending on the average slope of the wavefront.

Shack-Hartmann sensing is the improved version of the Hartmann screen test (Platt & Shack, 2001; Malacara, 1992) from the early 1900s, originally developed to test the optics of a telescope. A simple array of holes in an opaque screen was placed over the aperture of the telescope, and on either side of the focus, photographic plates were inserted and exposed. The mask with holes effectively created a discrete set of ray bundles that passed through different entrance pupil locations. The exposed plates represented a spot diagram of the telescope for positions on both sides of the focus. If the parameters of the optical system are known, the concentration of rays can be determined

and therefore the wavefront distortion of the optical system can also be determined. The primary lens of the telescope could be refigured with this technique and the resolution of images taken can also be enhanced by use of adaptive optics.

The Hartmann test can be improved considerably (Pfund *et al.*, 1998) by replacing the series of holes on a mask with microlens arrays. Early sensors based on crude lenslet arrays were found to be sufficiently accurate to measure the distortions found in actual optical systems (Neal *et al.*, 2002). This led to the development of more sophisticated sensors based on CCD cameras and micro-optics.

The principle of a Shack-Hartmann sensor (Ares *et al.*, 2000; Primot, 2003; Roddier & Rigaut, 1999) is shown in Figure 3.2. The SHS is composed of two-dimensional lenslet elements of identical optical quality e.g. characterized by identical parameters such as focal lengths, refractive indices and diameters. First, the microlens array spatially samples the wavefront in a number of subapertures and produces a two-dimensional array of light spots, which are measured by a suitable detector.

A commonly used detection array for measuring the spot displacement and therefore the phase gradient associated with each subaperture is the quad cell (Milonni, 1999). This consists of four detectors forming the quadrants of a square. The different photon counts in the four quadrants provide the measure of the phase gradient (Fried, 1982). The digitally coded data comprises the characteristic features of the distorted wavefront which can be obtained by serial data processing.

Using the Shack-Hartmann technique in an AO system, aliasing can occur due to the sparse spatial sampling of phase by the microlens array (Poyneer & Machintosh, 2004). Aliasing (Roddier & Rigaut, 1999) is a distorting effect encountered when a continuous signal (wavefront) is sampled at a low resolution. Due to this effect, the performance of most AO systems is degraded and the original wavefront cannot be uniquely reconstructed from the sampled signal, just an approximation.

Aliasing can take place either in time (temporal aliasing), when the aberration induced by the distorting system fluctuates faster than the sampling time, or in space (spatial aliasing) (Poyneer & Machintosh, 2004). A simple solution to prevent spatial aliasing is to place a low-pass filter in the input wavefront before the samples are taken. Such a filter can be implemented by using a field stop at a focal plane before the wavefront sensor.

At high spatial frequencies, the spatial filter reduces the power in the wavefront and correspondingly reduces the error in the wavefront correction due to aliasing.

The intensity distribution in the given observational plane produced by each lenslet is an Airy disk (Wolf, 2002) if the compound optical system has circular apertures. The position of the centroid of each such disk indicates the local slope of the incoming wavefront, as previously discussed.

In practice, the shape of the subaperture is generally rectangular; however, there are also regular hexagonal shape lenslets (Moreno-Barriuso *et al.*, 2001). In practice, the light distribution on the sensor only approximates to a spot. The actual pattern formed is an Airy disk, which is a bright central spot surrounded by a number of fainter rings. Each Airy ring is separated from its neighbours by a circle of zero intensity. The effective area of each lenslet is around 75% of the total area of the lenslet, as estimated from the intensity distribution of the spot pattern (Yoon *et al.*, 1996).

The positions of the centroids of the focal spots are related to the average wavefront slope over each microlens aperture. Thus the pattern of spots at the focal plane contains information about the spatially-resolved waveform slope that can be integrated to reconstruct the wavefront. There are several algorithms to determine centroid spot positions, however, Noethe (2002), indicates that in general, for accurate centroiding the spot diameter has to be at least 1.5 times the pixel size.

One of the most important characteristics of a wavefront sensor is the dynamic range, the range of measurable slope or curvature. The dynamic range of a conventional SHS has some fundamental limits. One of these is the aperture size of the optical system, which puts a limit on the achievable resolution. The focal point of one microlens can be displaced onto an adjacent subaperture assigned to receive the focal point of another microlens (Figure 3.3). The limit can be reached if the light wave is significantly aberrated. Beside the astronomical and medical implementations of the SHS, one of the earliest applications was the measurement of high-speed dynamic phenomena such as the turbulence or fluid motion (Holohan & Dainty, 1997). Laser beam quality measurement (Hooker *et al.*, 1999) and control of high power laser systems (Kartz *et al.*, 1999) have also been implemented.

As a system requirement, in order to compensate for wavefront disturbances on timescales of tens of milliseconds (e.g. in atmospheric turbulence), the closed-loop

control which flattens the aberrated wavefront has to run at a frame rate of a few 100 Hz. As a consequence, the detector must be capable of capturing a few hundred images per second, in order for real time compensation and high-resolution image detection to occur.

In ophthalmologic wavefront sensing applications, the frame rate is much lower since the aberration effects occur on longer time scales (around hundreds of milliseconds). There is no significant temperature change in the living human body, which is one of the most common causes of refractive index fluctuation; this is a major reason why from an adaptive optics point of view this system can be considered more stable than an astronomical system. However, pressure gradients could appear between different sections of the eye in which the speed of fluid flow is different, a process described by Bernoulli's equation, and this can lead to a variation of the local index of refraction among other reasons. Refractive index fluctuations are related to also different optical characteristic of the cell structures present in the eye.

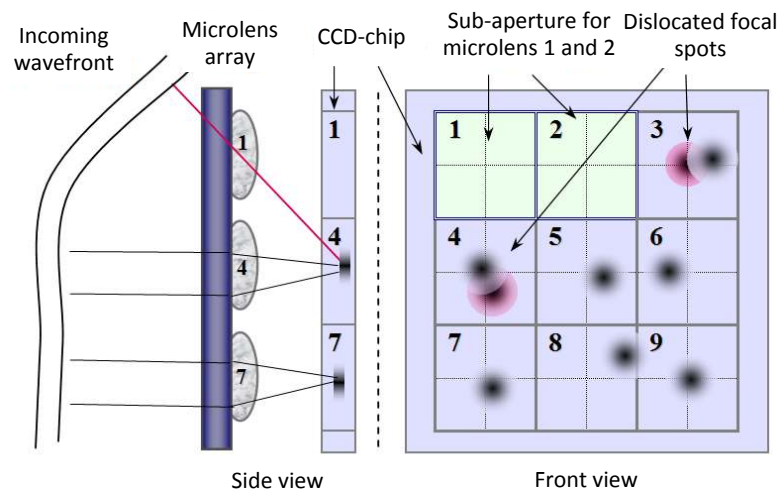


Fig. 3.3 Limited dynamic range of a conventional Shack-Hartmann sensor

A highly curved- or steeply sloped-wavefront results in focal point dislocations (after Choo & Muller, 2004). The green subapertures contain no centroids since the lenslet 1 and 2 form images into neighbouring lenslet locations as indicated by the red centroids.

The SHS for wavefront sensing technique provide a mechanically stable optical configuration, as it has no moving components, and it can be constructed in a compact and simple optical layout which makes this sensor suitable for integration in wide range of applications; it is the most often used wavefront sensor in ophthalmic applications.

III.2.2 Pyramid wavefront sensor

The pyramid wavefront sensor was recently tested for ophthalmic applications (Chamot & Dainty, 2006). This technique can be considered as a variant of the Foucault knife-edge test. The knife-edge test was suitable for testing the surface quality of the refractive elements of a telescope, of mirrors and later for other optical elements. However, when testing the elements of an optical system, this method (Ojeda-Costañeda, 1992) is suitable for only qualitative measurements.

For a perfect optical system, a knife edge placed so that it just touches the optic axis before the focal plane results in a half dark, half bright aperture distribution (Figure 3.4). When the knife-edge is moved to the focus, all rays are covered simultaneously, resulting in a uniformly dark aperture. For an aberrated optical system this is no longer the case as marginal- and paraxial rays intersect the optic axis at different locations and an uneven aperture distribution is observed.

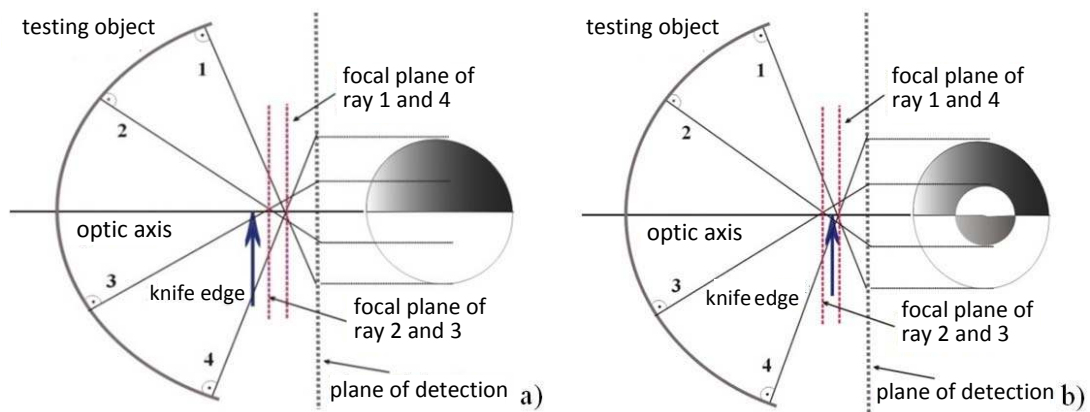


Fig. 3.4 Schematic representation of the knife edge test

Diagram showing (a) Narrow ellipsoid optical element under test. If the knife-edge is placed before the focal planes of the rays, dark and light half-circles can be seen in the plane of detection. (b) If the knife-edge is placed between the two focal planes, half dark and light circles can be seen in the plane of detection with different diameters (diagram redrawn after Ojeda-Costañeda, 1992).

For example, for a lens with spherical aberration, the focal point is shifted along the optical axis. Therefore the knife-edge will be “before the focal point” for some of the rays, and “after the focal point” for others. Hence an asymmetric distribution of light and dark patches can be observed on the image. The knife-edge test was also used to measure wavefront tilts (Babcock, 1953) in astronomy.

Pyramid sensing (Figure 3.5) is a more recent technique meant to compensate wavefront distortions. Ragazzoni (1996) first described the method in the framework of geometrical optics as slope sensing. As detailed in (Bauman, 2003; Feeney, 2001), the pyramid wavefront sensing technique can be thought of as a Foucault knife-edge test where two orthogonal knife-edges are implemented simultaneously. Ragazzoni developed this technique by placing a 4-faceted pyramid with its apex at the image plane. When the optical system has no aberration, all rays converge to the focal plane at the edge of the pyramid are split into two as indicated in Figure 3.5 (showing rays 1 and 2). The distance between the lens and the edge of the pyramid is the focal length of the lens.

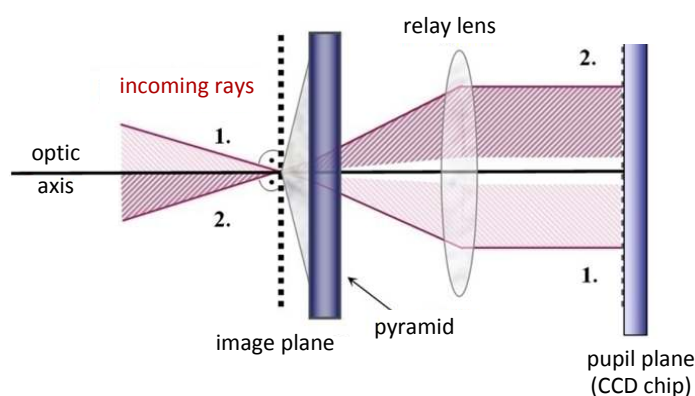


Fig. 3.5 Schematic representation of a pyramid sensor

The optical setup of a pyramid sensor is similar to Foucault knife-edge test but instead of the application of sharp-edge, a (rectangular-based) pyramid is placed into the focal plane with its apex. While the knife-edge selects certain parts of the incident light (since it is placed as a hindrance), the transparent pyramid dissects the beam into four parts. The beams are then deflected, and form four images on the same detector. Each pixel represents a subaperture on the chip, and each of the 4 images (2x2 pixels) of the pupil in a pyramid sensor corresponding to a quad cell in a SHS.

If the pyramid is moved along the optic axis, its edge is no longer in the focal plane and the pupil images are altered, similarly as shown in Figure 3.4a and two half illuminated pupil images will be detected on the CCD. In the original method, this sensor performs operations in a reverse order compared to a SHS. While a quad-cell type SHS first divides the pupil, via a lenslet array placed at the pupil, into subapertures, then divides the field into quadrants through the pixel boundaries on the CCD, the pyramid divides the beam into four quadrants, and the subsequent pupils are then divided into subapertures via the pixels of the imaging sensor (which is a CCD-chip in most applications). Hence, from a geometrical optics point of view, the information is similar to that obtained in SH wavefront sensing, but organised differently.

III.2.3 Centroiding at low light levels in AO systems

This section summarizes some of the problems of wavefront sensing using a Shack-Hartmann sensor in low light conditions for ophthalmic applications. The discussion of centroiding methods in this section is based on recently published studies by Vyas *et al.* (2009b) and Ma *et al.* (2009), which include the centre of gravity, weighted centre of gravity, iteratively weighted centre of gravity and a matched filtering based technique (Thomas *et al.*, 2006; Baker & Moallem, 2007; Poyneer *et al.*, 2005); some of these methods are discussed in this section.

When light is incident on the SHS, Gaussian-like spots are formed on the detector, and their position changes with the wavefront gradient. In AO systems applied to the eye, due to safety hazards and the optical characteristics of the ocular media, only a low level of light is feasible for both wavefront sensing and imaging.

Accurate calculation of centroid positions is one of the most important issues in wavefront reconstruction, and an insufficient light level is a common problem in centroiding. A number of methods (Southwell, 1980; Irwan & Lane, 1999; Ares *et al.*, 2000; van Dam & Lane, 2000; Arines & Ares, 2002) have been developed to determine the positions of Shack-Hartmann centroid spots formed by the lenslet array (Figure 3.6 shows the geometrical optics representation of this arrangement).

The wavefront sensor parameters affecting centroiding include the size of the pixels on the detector and the SHS spot and pitch size. Some external factors that may affect the centroid estimation accuracy are the photon flux, exposure time and the shift of a centroid from the centre of the subaperture. The detector pixel size and SHS pitch determine the number of pixels corresponding to a single aperture on the detector. Pitch size reduction decreases the available space for each subaperture on the detector; however, reducing the spot size may be beneficial in low light conditions since the reduced number of readout events reduces the level of camera read noise compared to the number of incident photons and improves centroiding accuracy. The number of photons received on a pixel with aperture diameter d can be given by

$$N_{ij} = Fd^2t, \quad (3.1)$$

where F is the photon flux in photons/m²/s, which is correlated to the exposure time (usually on the time scale of milliseconds); (i,j) refers to the coordinates, and t is time.

Centre of gravity (CoG) is the simplest method in the estimation of centroiding position, which gives the exact positions of the centroids in the absence of noise. The advantage of using this technique is its relatively short computing time, although it should be noted that it assumes that the spots are of a 2D Gaussian form. Iterative methods are more time consuming compared to CoG, especially as the number of iterations increases.

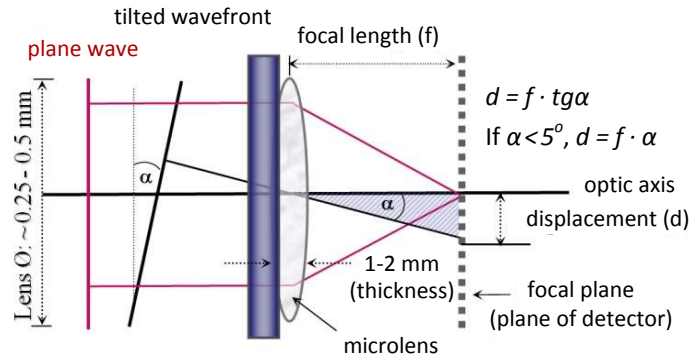


Fig. 3.6 Wavefront-slope measurement

Diagram showing wavefront-slope measurement using a microlens array in a Shack-Hartmann sensor in the geometrical approximation. Each lenslet produces a spot on a detector array in the focal plane. The Shack-Hartmann sensor transforms the local phase gradients into a matrix of focal-spot displacements.

The presence of noise determines the optimal technique to use, as each technique has advantages and disadvantages, depending on the boundary conditions, which is studied in detail in the literature (Vyas *et al.*, 2009a and 2009b). One solution to define the spot positions is the placing of a CCD camera in the focal plane of the lenslet array as a detector which in principle allows the determination of the intensity centroid of the spots with a large number of pixels per subaperture. CoG identifies the geometric centre of each spot through summing. A simple estimation of centroid positions can be given by the formula for x-coordinate (x_c) and y-coordinate (y_c) of the centroids

$$(x_c, y_c) = \frac{\sum_{ij}^M X_{ij} I_{ij}}{\sum_{ij}^M I_{ij}}, \quad (3.2)$$

where I_{ij} is the intensity of the signal, and $X_{ij} = (x_i, y_j)$ are the position coordinates of the pixels (i, j) with values 1,2 ... M.

Taking into account that a SHS centroid has the form of an Airy pattern and can be approximated by a Gaussian function, the centroiding formula can be expressed in the following weighted form

$$(x_c, y_c) = \frac{\sum_{ij} x_{ij} I_{ij} W_{ij}}{\sum_{ij} I_{ij}}, \quad (3.3)$$

where W_{ij} is the Gaussian weighting function given by σ

$$W(x, y) = \frac{1}{2\pi\sigma^2} \exp \left\{ -\frac{(x-x_c)^2}{2\sigma^2} - \frac{(y-y_c)^2}{2\sigma^2} \right\}, \quad (3.4)$$

Since the weighting function given in Eq. 3.3 depends on the centroid position and spot size, an iterative process may be applied (Baker & Moallem, 2007). Compared to CoG and weighted CoG, the iterative weighted centre of gravity (IWCoG) gives a more accurate estimation for the centroid position. Increasing the number of iterations may decrease the centroiding error and makes centroiding time consuming; however, the number of iterations can be optimised. Intensity weighted centroiding (IWC) is similar to the centroiding given in Eq. 3.3 except that the weighting function is intensity dependent:

$$W(x, y) = I^p(x, y), \quad (3.5)$$

where $p (\geq 1)$ is any real positive number; with $p=1$ in the absence of noise.

In a realistic environment, background noise and stray light are present in optical systems. Hence, the accuracy of the centroiding method depends on the following error sources: photon noise (caused by the illumination source), readout noise (circuit noise of CCD), background noise (scattered light or system light sources), background level (offset voltage of CCD), and sampling error (due to discrete sampling of spot). Table 3.1 gives a summary of the error sources and their distribution.

The following analysis of the error distribution and propagation in the rest of this section is based on the study by Ma *et al.* (2009). The centroiding formula (Eq. 3.2) on the x-axis can be expressed by

$$X_c = \frac{\sum_{ij}^{L,M} x_{ij} N_{ij}}{\sum_{ij}^{L,M} N_{ij}} = \frac{U}{V}. \quad (3.6)$$

The notation for the size of the aperture is $L \times M$; the computations in the rest of this section use the following expressions (as also in Eq. 3.6)

$$U = \sum_{ij}^{L,M} x_{ij} N_{ij} \quad V = \sum_{ij}^{L,M} N_{ij} \quad (3.7)$$

As the x-axis and y-axis are usually symmetrical since most cameras have square pixels, the centroiding error is analysed only on one axis here; an analysis for the other axis can be similarly computed.

Table 3.1 Error sources of CCD-based centroiding and their distribution

Error source	Distribution
Photon noise (signal light)	Poisson distribution, the variance σ_{pij}^2 is $\overline{N_{\text{sij}}}$
Photon noise (background light)	Poisson distribution, the variance σ_{bij}^2 is $\overline{N_b}$
Readout noise (CCD)	Gauss distribution, the mean is 0 and the variance is σ_r^2
Background level (CCD)	Without modulation, the variance σ_{dij}^2 is 0
Sampling error (CCD)	Correlated with the spot size in subaperture

Table adapted from Ma *et al.* (2009)

The error source can be classified in two categories, the first class sources equally affect each pixel including background photon noise, the readout noise and background level. Since the readout noise obeys Gaussian distribution with mean value 0 and the background level of the CCD can be considered constant, the error source on one pixel can be expressed by

$$N_{\text{Bijc}} = N_{\text{bij}} + N_{\text{dij}} + N_{\text{rij}} = \frac{U}{V}, \quad (3.8)$$

where N_{bij} is the background photon numbers of a pixel with coordinate (i, j), N_{rij} is the readout noise of a pixel with coordinate, and N_{dij} is the background level, indices (i, j) refer to the pixel coordinate.

The second class error sources affect the area of light spot and include the signal photon noise and the sampling error of the CCD. Using the definition of N_{ij} from Eq. 3.6 we get

$$N_{\text{ij}} = N_{\text{sij}} + N_{\text{bij}} + N_{\text{rij}} + N_{\text{dij}} = N_{\text{sij}} + N_{\text{Bijc}}, \quad (3.9)$$

where N_{sij} is the photon number of the signal.

The position of the detected centroid can be expressed as (Jiang *et al.*, 1997)

$$X_c = \frac{U}{V} = \frac{U_S + U_B}{V_S + V_B} = \frac{V_S}{V} X_S + \frac{V_B}{V} X_B, \quad (3.10)$$

where V_S is the number of signal photons collected by the CCD, V_B is the number of background noise photons collected by the CCD; X_S and X_B are the centroids without the presence of background and read noise, and centroid position of the first class error source respectively

$$X_S = \frac{U_S}{V_S}, \quad nX_B = \frac{U_B}{V_B} \quad (3.11)$$

$$U_S = \sum_{ij}^{L,M} X_i N_{Sij}, \quad U_B = \sum_{ij}^{L,M} X_i N_{Bij}. \quad (3.12)$$

Eq. 3.10 can be expressed in the following form

$$X_c = \frac{V_S}{V} (X_p + \sigma_S) + \frac{V_B}{V} X_B. \quad (3.13)$$

However, the centroid X_S in Eq 3.10 does not refer to the actual centroid position due to sampling error (σ_S); supposing that the detected centroid (X_p) with sampling error (σ_S) can be expressed by

$$X_S = X_p + \sigma_S. \quad (3.14)$$

Employing this expression to Eq. 3.10 we get

$$X_c = \frac{V_S}{V} (X_p + \sigma_S) + \frac{V_B}{V} X_B. \quad (3.15)$$

This equation shows that determination of the centroid position involves two main error sources, the displacement error (σ_p) which refers to the difference of the actual (X_p) and detected centroid (X_c), and the wobbling error. The displacement error can be given by

$$\sigma_p = X_p - X_c. \quad (3.16)$$

The wobbling error is defined as the variance of the detected centroid position caused by the read out noise (Genrui & Xin, 1994); signal photon noise also contributes to this error.

An understanding of the source of these errors in the process of wavefront reconstruction is important in designing an AO retinal imaging system and optimizing its performance in low light condition. Checking of the AO instrument accuracy and repeatability for detailed analysis of the aberration test results is usually complicated, as the temporal behaviour of the error sources is not known. A change in the reconstructed wavefront based on centroiding results can be induced either computationally, as discussed, or experimentally; Fig. 3.7 shows an illustration for the relative change of the wavefront when the system performance or the laboratory conditions are not optimized. The accuracy of the wavefront estimation can be improved by reducing the background noise, optimizing the search box area over which the centroid is estimated, and a clean optical environment free of back reflection minimizing speckle is also essential in optimal image processing; these procedures have also an impact on the imaging frame rate.

The most critical errors in retinal imaging and wavefront reconstruction include those associated with experimental factors. Thermally induced effects have the potential to affect alignment (Bauman & Eisenbies, 2005) when the instrument is operated at a temperature different than that during alignment and calibration of the system. This results in some degradation in the performance of the instrument (Fig. 3.7), especially when the temperature varies with time (Vukobratovich, 1993). The degradation of the system performance arises from issues that include changes in the relative positions of optical components and unstable behaviour of the membrane surface, which affects the accuracy of the centroiding method. Moving loads of the imaging system such as a focusing translation stage are further error sources, as bending of the support structure may occur, causing multiple misalignments.

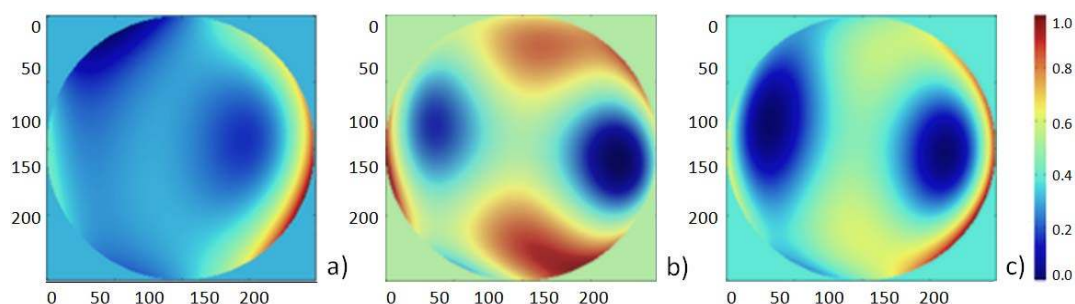


Fig. 3.7 Error propagation illustrating wavefront map changes in cAO-HRT

A series of measurements taken one after each other showing a change in wavefront maps as an illustration of the effect of temporally varying errors and error propagation in wavefront reconstruction.

Obtaining optimal performance of the AO instrument requires a careful characterization and calibration of the system in a controlled laboratory environment and mechanical isolation capable of damping out any external shock or vibration, which is essential for the precise measurement of ocular aberrations. The next chapter introduces the realisation of the instrument, the experimental setup and operation of the compact AO ophthalmoscope for the imaging of human subjects.

Chapter IV

The compact adaptive optics ophthalmoscope

IV. The compact adaptive optics ophthalmoscope

This chapter summarizes the main issues in retinal imaging using AO technology from a developmental viewpoint. The human eye as an integrated biological system is complex both in a physiological and an optical sense. In ocular imaging systems the human eye is necessarily part of the overall imaging system because its refractive elements are involved in focusing of the light onto the retina. In addition to its structural complexity, the eye as an imaging system has various components capable of adapting to environmental conditions, which results in a change in the aberrations present.

One of the first considerations in designing any imaging system is to ensure sufficient illumination of the object being observed. The amount of light entering the eye is controlled by the pupil, and the overall pupil area and its distance from the retina control the ratio of the incoming light to the backscattered light from the retina. Obtaining high resolution and sharp retinal images non-invasively from the eye is dependent upon various factors, including clarity of the ocular medium, pupil size and fixation ability. The parameters of these dynamical processes set important constraints for an AO imaging system to be suitable for correction of the temporally and spatially varying ocular aberrations.

The aim of this work was the investigation of the performance of confocal adaptive optics imaging systems, with a view towards providing a new diagnostic tool for high-resolution retinal imaging as an alternative approach to instruments currently used in clinical practice. The main results of this research, being discussed in the second part of the thesis, were the development of a compact adaptive optics Heidelberg Retina Tomograph (cAO-HRT) and the testing of the compact AO imaging system on human volunteers. The significant aspects of work in the development and construction of the ophthalmoscope, as well as the technical details of the compact system are summarized in this chapter; retinal imaging, the limitations of the system and its prospects for future clinical applications are presented in Chapter V and VI.

IV.1 Design consideration of an adaptive optics system

The primary goals of this research were the analysis and development of optical table based and compact adaptive optics imaging systems in order to compensate for aberrations, improve on previous models and reduce light loss. Specifically, this refers to the further optimisation and modification of the commercially available HRT imaging system in order to provide a functioning compact and low cost adaptive optics ophthalmoscope for clinical trials. This section summarizes the main aspects of the ophthalmic AO system design, which aims to resolve the cellular details of human retinal structures in the central field.

There are several factors determining the amount of light reaching various retinal layers (Figure 4.1), and the proportion of the light returned from the retina can be significantly increased by dilating the pupil to a diameter in the range of 2-8 mm at a safe level of 65 μW total illumination power (discussion of light level safety and method of calculation are given in the British Standard).

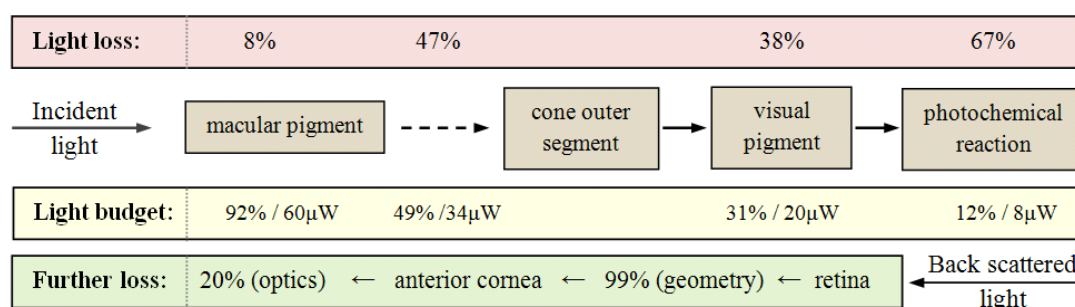


Fig. 4.1 Estimated light budget in the ocular media for imaging

Diagram showing the estimated light budget in the ocular media (brown cells) for imaging and wavefront sensing. Most of the light (70%) is absorbed by the macular pigment, the cone outer segment and the visual pigment; finally the 67% of the available 30% amount results in photochemical reaction (as shown in the red field). This model contains no spectral dependence of the absorption, and values are taken from (Atchison & Smith, 2002). The numerical percentage / power values in the yellow field indicate the available light if the incident power is 65 μW . In practice, due to the geometrical properties of the eye (shown in the green field), approximately 80 nW (maximum 0.001% of the incident light) exits the ocular globe.

According to the literature (Atchison & Smith, 2002; Porter *et al.*, 2006), the combination of the spectral properties of the ocular medium and the double-pass nature of the eye makes it an inefficient imaging system. Approximately 10^{-3} - 10^{-5} of the incident light is scattered back to be available for imaging and wavefront sensing, amounting to at most

tens of nanowatts; these estimations agree with a study by Delori *et al.* (1989). Therefore, in designing an ocular imaging system, the light budget needs to be carefully considered since the ocular hazards place restriction on the amount of light that can be put into the human eye.

Although dilation is inconvenient, it is one of the best ways to maximize the photon count on the detector in high-resolution imaging systems, corresponding to an increase in NA. Most subjects can be imaged without dilation under dark laboratory conditions when the AO loop is off, if pupil size is in the range from 3 to 4 mm.

When the AO loop is open, there is no dynamic correction of the ocular aberrations, so that undilated pupil size is satisfactory and paralysation of the ciliary muscle to inhibit accommodation of the lens is unnecessary for imaging. However, if the AO loop is closed and the ciliary muscle is unparalysed, the subject accommodates for all changes the AO system applies. In certain pathological cases, for example individuals with cataracts, dilation of the pupil is more likely to be needed to achieve higher quality ocular observations. The poor tear film secretion that is characteristic of dry-eye syndrome also diminishes the image quality, and ring-type artifacts can become distinguishable as the eye remains open during image acquisition (Fingeret, 2009).

The optical setup must be precisely aligned by adjusting the positions of all the optical elements and detectors since the goal is to obtain diffraction limited performance of the imaging system. AO systems use several relay optics to image the retina; therefore, the collimation of each relay block is essential, and can be checked by testing it in an interferometer. Human factors, such as fixation and stability are an important part of the alignment procedure. In addition to the precise alignment of the optical setup, the location of the image is highly dependent on the orientation of the subject, the proper positioning of the patient is imperative, being achieved by the use of a headrest and chinrest on a positioning translation stage.

IV.2 Construction of a compact adaptive optics system

In recent years, adaptive optics has been widely used in *in-vivo* imaging to compensate for the higher-order aberrations in tabletop experiments; however, these systems are used and tested mainly in research laboratory conditions. The concept of a compact high-resolution ophthalmoscope was based on research conducted in collaboration with Heidelberg Engineering Inc., Germany. The compact adaptive optics Heidelberg Retina Tomograph (cAO-HRT) was based on an HRT instrument (originally designed by Dr Gordon T Kennedy) which was modified by the addition of adaptive optics to give a compact scanning laser ophthalmoscope in a confocal arrangement.

The compact AO-HRT system had been trialled on test objects before; however, it was unable to produce images in the human eye. The design and construction of the ophthalmoscope was reconsidered; wavefront sensing and correction was optimized for *in vivo* eye measurements, which included the optimization of the optical set-up by reducing the existing light loss for retinal imaging through improved alignment and coating of optical surfaces. The development process included the calibration of the compact system for *in vivo* eye tests, which is summarized in this section of the thesis.

IV.2.1 Light delivery and optical layout of the system

IV.2.1.1 Optical components and operation of the ophthalmoscope

This section presents results from the development of an AO ophthalmoscope with features that differ from the standard HRT instrument in some parameters. The standard HRT ophthalmoscope was modified in a manner that allowed the base structure of the instrument to be kept as similar as possible to the original whilst remaining compact, providing a more applicable and deployable ophthalmoscope in a general clinical environment. Figure 4.2 shows the optical layout of the cAO-HRT ophthalmoscope.

Adaptive Optics Ophthalmoscope (cAO-HRT)

Notations on HRT block:

BSP: beamsplitter plate (10%)
 cP: antireflection coated prism (>99.9%)
 OPC: optical connector
 CPH: confocal pinhole
 f_x : achromatic doublet lenses ($x=3$)
 M_1 : Al-coated mirror
 PBS: polarizing beamsplitter
 VS: vertical scanner
 HS: horizontal scanner

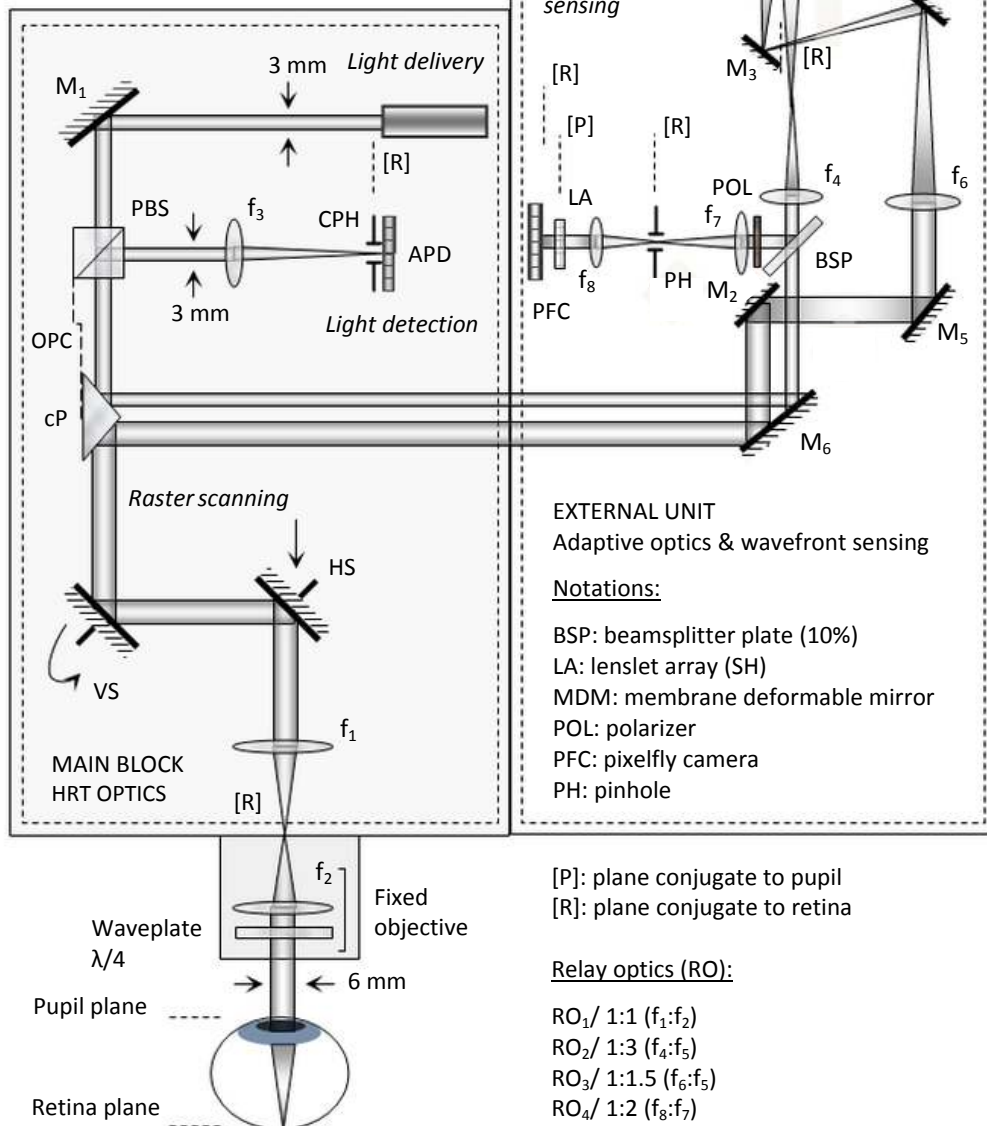


Fig. 4.2 Optical layout of the compact AO scanning laser ophthalmoscope

The AO ophthalmoscope uses the original optics (f_{1-3} lenses and M_1 mirror) and detector (APD) such that confocal microscopy and adaptive optics were combined in a compact system mounted on the base structure of the HRT. The output power of the system was significantly increased by using a class 3A laser source (Toshiba TLD-9231, operating at 670 nm) while the size of the pinhole was reduced from 2.0 Airy disc units to a 1.5 Airy pinhole size.

The ophthalmoscope comprises two attached blocks: the main block (on the left) with the basic HRT optics, and the external unit (on the right) with the adaptive optics components. As the optical layout of the imaging system shows, a mirror-surfaced 45 degree prism (cP) was integrated into the optical setup behind the polarizing beamsplitter (PBS) to direct the beam to the external adaptive optics unit.

The cP (MellesGriot LDM-670-RAP-050-UV-45, reflectivity >99.9%) was a replacement of a low reflectivity ($\sim R=80\%$) aluminium coated prism to minimize the light loss. This modification of the optics resulted in a more than 50% reduction in the total light loss compared to the previous optical arrangement, where an aluminium coated prism was employed. The prism acts as an optical ‘connector’ in between the main HRT block and the external unit. The adaptive optics subsystem picks off the beam and returns it to the same optics but doubles the optical pupil at the cornea in the following way: the incoming beam reflects off the deformable mirror (37-channel OKO MDM) after going through the RO_2 relay optics (lenses f_4 and f_5) and is relayed back onto the built-in vertical (VS) and horizontal (HS) scanners. Figure 4.3 illustrates the scan pattern of the focused spot as is moved in a rectangular raster on the retina.

The light is focused by the human eye (which acts as a compound objective lens) after passing through the RO_1 relay optics (f_2 and f_1 lenses), and the backscattered light from the retina goes through the same optical components as the incident beam on its way back. To maximize the amount of light available for imaging on the detector, a beamsplitter plate (BSP) of split ratio 10:90 at a 45° incidence angle was placed in the system to take some of the light reflected back from the retina for imaging and wavefront sensing. The BSP reflects 10% of the beam into the SHS and the remaining transmitted 90% is focused on the confocal pinhole (CPH=1.5 Airy disc pinhole size) in front of the detector (APD), from which the signal is taken to the A/D converter for digitisation.

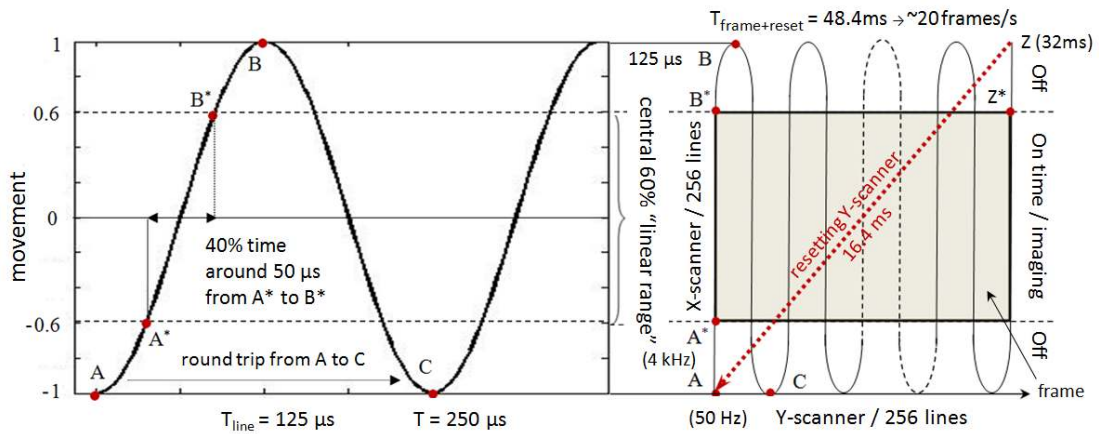


Fig. 4.3 The movement of the scanners as they cross the field

Figure showing the movement of the scanners (horizontal and vertical) as they cross the field. The velocity changes at the edges due to the sinusoidal pattern. The incident beam acquires image only during the forward part of the scans which is ~40% of the time corresponding to 50 μs (from A* to B*). The nonlinear parts of the scan (from A to A* and B* to B) and the flyback movement are dead time. The two-dimensional image sections (256x256 pixels) are acquired over a period of 32 ms (until the position Z is reached) with a repetition rate of 20 Hz. The total acquisition time to take one series of 32 images is around 1.6 seconds.

The two attached units, the HRT optics and the AO external unit, can be positioned together on a single translation stage, while the position of the condenser lens (f_2) is kept fixed; this optical arrangement allows compensation for spherical aberration in the range +/- 11 dioptres in steps of 0.25 dioptre. The field of view was reduced and the scanning angle was altered to 1°-10° (in steps of 1, 2 and 10 degrees) as opposed to the original set of three fields - 10° x 10°, 15° x 15° or 20° x 20°. In an optical system with a single optical element, the light loss may be small; however, the cumulative loss can be considerable with a large number of elements such as in the cAO-HRT. The reason for integration of a number of lenses in the cAO-HRT is that both the deformable mirror and the wavefront sensor must be placed in conjugate planes to the entrance pupil, and the requirements for diameter sizes on their surfaces differ. This required the integration of relay lenses (RO₁-RO₄) in the external AO block. To minimize the light loss in the optical system, highly reflective mirrors and antireflective coated achromatic doublet lenses were employed.

IV.2.1.2 Alignment of the system

The system uses LINOS and Thorlabs mechanics in most of its components, providing high mechanical stability and well defined reference points for the alignment of the optical relay system. This is especially important since in this compact version of the ophthalmoscope, the basic HRT optics cannot be modified, and most of the optical elements are inaccessible when the external AO unit is attached.

The current construction of the optical connector between the main HRT block and the external unit does not allow for modification of the orientation and position of the beamsplitter separately from the prism (cP), see Figure 4.5. The prism is glued using optical wax onto a thin metal plate which is mechanically attached to the kinematic base (indicated with dashed line in Figure 4.2) of the beamsplitter (PBS). This arrangement of the optical elements causes severe misalignment of the beam on the confocal pinhole (CPH) each time when the prism is inserted or removed during development. Access from the outside of the enclosure to this part of the system is physically limited.

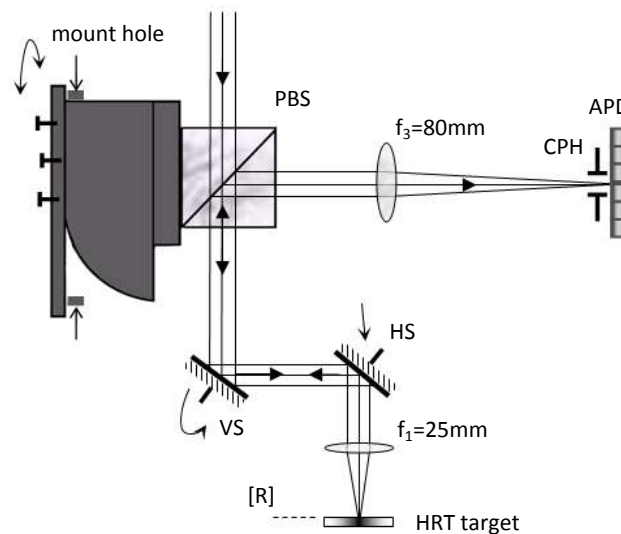


Fig. 4.4 Schematic of the HRT for beam alignment of the pinhole

Notations: polarizing beamsplitter (PBS), confocal pinhole (CPH), avalanche photodiode (APD) vertical scanner (VS), horizontal scanner (HS) and [R] the plane conjugate to the retina.

There were two different procedures to align the system; one was for the basic construction of the HRT (Figure 4.4) and the other method was for the AO modified version (Figure 4.5) of the ophthalmoscope. The alignment of beam on the confocal pinhole in the HRT optical setup can be done by replacing the fixed condenser lens (f_2 on Figure 4.2) with a microscopic target in the plane conjugate to the retina (Figure 4.4).

In this setup, the angle of the beam is modified by a change in the beamsplitter (PBS) position, and alignment is achieved by maximizing the signal on the detector and providing a sharp image of the target. In the second case, the precise “blind” alignment of the confocal pinhole was carried out with a retro-reflector (Figure 4.5) in the cAO-HRT optical arrangement. The retro-reflector comprised of an $f_R=60$ mm achromatic doublet lens and a mirror (M_R) in its focal plane placed directly after the prism, separate from the main block.

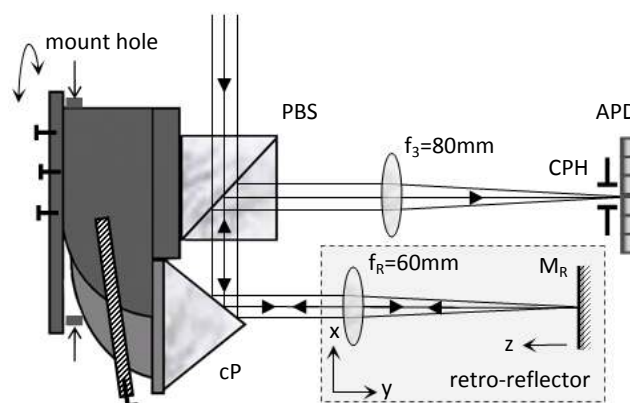


Fig. 4.5 Schematic diagram of the cAO-HRT for beam alignment of the pinhole

Notations: polarizing beamsplitter (PBS), confocal pinhole (CPH), avalanche photodetector (APD), coated prism (cP) and mirror on kinematic mount (M_R). In this setup the lens (f_R) is on an x-y translation stage and the position of the mirror (M_R) in z direction can be changed.

The beam was aligned on the pinhole when the signal on the detector was maximized. The alignment of the rest of the optics in the cAO-HRT system was similar to that of the basic HRT optics: the HRT alignment target (replacing f_2) was used to direct the beam on-axis on the optics of the external AO unit in the pupil plane through adjustments of M_2 - M_6 , while the optics of the main HRT block remained unchanged.

IV.2.2 Wavefront sensor and deformable mirror

The compact AO-HRT has been discussed in the first part of this chapter in terms of the general arrangement of the ophthalmoscope and the optical layout of the imaging system; this section focuses on the adaptive optics components and gives a summary of the operation of the wavefront sensor and the deformable mirror for the precise measurement of phase changes and compensation for the optical distortion effects present both in the imaging instrument and the ocular media.

IV.2.2.1 Wavefront sensing with SHS

The cAO-HRT uses a SHS for wavefront sensing due to its mechanical stability, as it contains no moving parts, and its compactness and simplicity make it suitable for integration in a portable optical system. The arrangement of the sensor is shown in Figure 4.2 which consists of a pixelfly camera (PFC) coupled with a WelchAllyn square based lenslet array made up of 7 mm focal length lenslets, with an actual centre-centre pitch size of 200 μm . This value corresponds to a 46 μm spot size on the pixelfly camera, which has 9.9 μm x 9.9 μm pixels. In the current configuration, the wavefront sensor has 11 lenslets across the beam diameter; in total 95 lenslets are usable, corresponding to a \sim 6 mm pupil at the cornea. The beam is relayed by two more lenses (f_7 and f_8 in Figure 4.2) providing a magnification of 3.38x between the pupil of the eye and the SH sensor.

If a plane wave propagating along the optic axis is incident on the sensor, it produces an array of spots along the optical axes of the corresponding lenslets. This central position of the focal spots is the reference position and search boxes can be constructed around these positions. Alignment of all spots on-axis can be achieved when the optical performance of the system is optimized and the static aberrations are compensated. When the incident wavefront is distorted, the spots (D_1 and D_2 in Figure 4.6) of each lenslet are shifted from their reference positions. These shifts are proportional to the local slope (σ) of the distorted wavefront. By use of a centroiding algorithm, the shift of these focal spots from the reference can be determined. The estimation of the phase in the subaperture locations is provided by the shift in focal position from the reference.

The centroiding operation is dependent on the signal-to-noise ratio at the focal plane of the lenslets. The light loss and absorption in the optics determines the exposure time for SHS slope measurements (typically 300-400 ms in human subjects). To eliminate the unwanted back reflections and stray light and to reduce the noise on the sensor, a 150 μm pinhole was integrated in the relay optics and a polariser is placed in front of the relay (see Figure 4.2).

There are two main parameters that characterize a wavefront sensor; the minimum measurable phase, which is determined by the sensitivity (Figure 4.6), and the maximum phase that can be measured defines the dynamic range (Figure 4.7). These are well-defined parameters based on the sensor geometry, including the focal length of the lenslet

array, and their validity for ophthalmic applications on normal eyes has been examined in the literature for example by Porter *et al.* (2006).

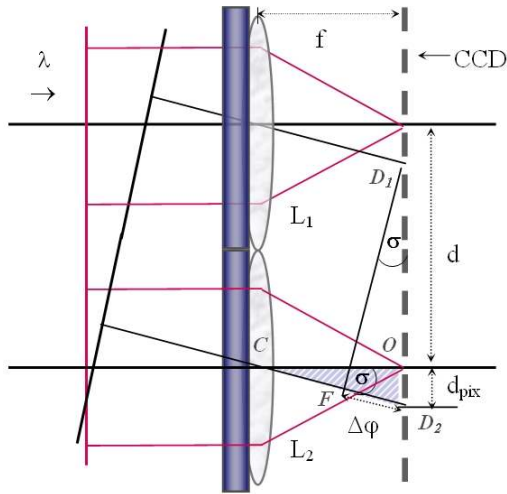


Fig. 4.6 Schematic for the sensitivity of a Shack-Hartmann sensor

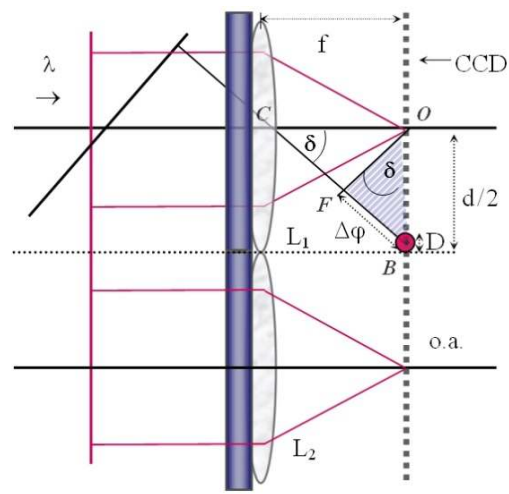


Fig. 4.7 Schematic for the dynamic range of a Shack-Hartmann sensor

Diagram in Figure 4.6 showing the sensitivity of a Shack-Hartmann sensor which is the minimum slope of the incident wavefront that can be measured with the given lenslet array and CCD camera. Red lines correspond to a plane wave along the optic axis, while the black is the distorted wavefront: focal length (f), pitch size (d), camera pixel size (d_{pix}). Figure 4.7 showing the schematic for the illustration of the dynamic range of a SH sensor which is the maximum slope of the incident wavefront that can be measured with a lenslet array and CCD camera. Focal spot (O) on optical axis (o.a.), boundary position (B), lenslet diameter (D) and lenslets (L_1 and L_2).

According to the definition by Yoon (2006) the sensitivity is a measure of the smallest slope of the distorted wavefront that can be measured with a lenslet array and a CCD camera. The relationship between the local slope of the aberrated wavefront and the focal spot shift can be estimated from the optical features and geometry of the lenslet array. In the cAO-HRT system the parameters of the CCD camera are a pixel count of 640 (horizontal) x 480 (vertical) and a corresponding pixel size of $9.9\mu\text{m} \times 9.9\mu\text{m}$ (d_{pix}), so that the sensitivity of the SHS is 1.41 mrad/pixel. If centroiding is used to define the shifts of the focal spots, the centroid will be shifted in its position by one pixel when the corresponding wavefront is tilted by 1.41 mrad (calculated from d_{pix}/f as shown in the figure). When two parallel rays (drawn in black) reach two neighbouring lenslets (L_1 and L_2 in Figure 4.6), the one produced by L_2 will be delayed by a phase difference $\Delta\phi$ relative to the one produced by L_1 , the distance between F and D_2 .

Figure 4.7 shows the dynamic range change in the lenslet array parameters. The maximum measurable wavefront slope (δ) will occur when the focal spot is on the

boundary (B) of the two lenslets (L_1 and L_2). The spot size (D), produced by a square-based subaperture at a wavelength of 670 nm, is calculated to be 45.77 μm (4.62 pixels in this configuration). For the given sensor parameters and from the two similar triangles (OBC and OBF), the maximum phase difference that can be measured by each subapertures is 0.85 μm (corresponding to $\sim 1.27\lambda$ at 670 nm).

There is some degree of freedom in determining the sensor parameters (focal length, pitch size) which satisfy the requirements. According to Yoon (2006), a smaller lenslet diameter requires a shorter focal length during wavefront sampling to cover the same fraction of subjects (tested on over 300 human subjects for lenslet diameters of 200 μm and 400 μm). When the lenslet diameter was 200 μm and the focal length was 7 mm, the measurable fraction of subjects was $\sim 20\%$ and $\sim 95\%$ for uncorrected and defocus-only corrected cases respectively.

IV.2.2.2 Wavefront correction using MDM

Adaptive mirrors are capable of phase corrections for different types of ocular aberrations during retinal imaging. Local variations of the refractive indices in the eye that give rise to ocular aberrations can be conjugated to provide correction for the wavefront changes. Corrective static ocular lenses, for example, use the same principle, and usually correct for defocus and astigmatism but have no active adaptive capability; similarly, the crystalline lens uses a dynamic shape change for fixation.

This section discusses the principles of operation of a membrane deformable mirror (MDM) as an active wavefront corrector in the compact AO-HRT imaging system. One of the key components of the adaptive optics imaging system is the wavefront sensor (in this compact system, an SHS) which is coupled with an OKO membrane deformable mirror (TU Delft) which has 37 close-packed hexagonal electrodes of spacing 1.75 mm, which is used as a wavefront corrector in a closed loop configuration. The electrode pattern for the 37-actuator mirror is shown in Figure 4.8. Specific parameters such as the membrane thickness (typical values are in the range from 0.5-10 μm), the gap between the electrodes (usually 75 μm) and the membrane material vary from device to device. These parameters can be all unified in one scaling parameter, knowing that the maximum

deflection the membrane can reach is 9 microns when all actuators have the maximum voltage applied (Loktev *et al.*, 2006).

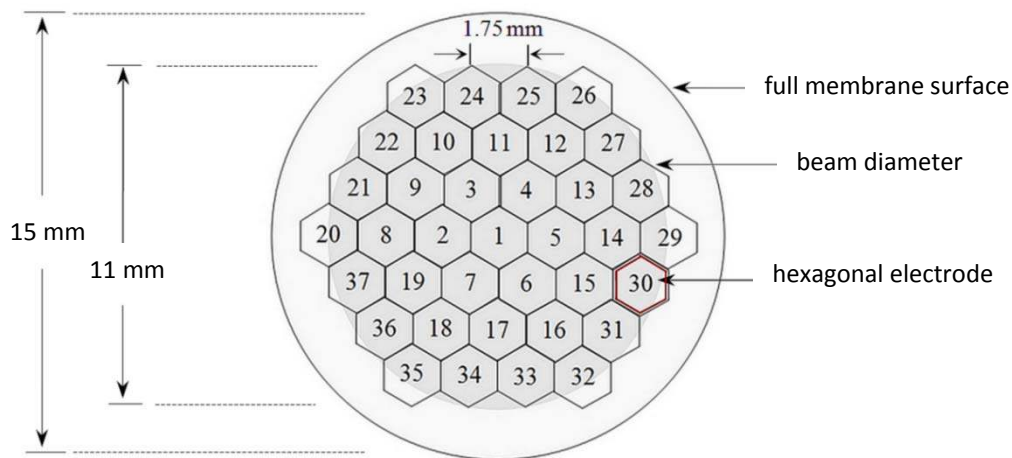


Fig. 4.8 Schematic representation of the 37 channel OKO membrane mirror

Diagram showing the schematic representation of the 37 channel OKO electrostatic membrane mirror (after OKO Technology, 2005) for wavefront correction. The mirror has a diameter of 15 mm with 37 closely packed hexagonal electrodes with a 1.75 mm centre to centre spacing. The 70% of the full membrane surface (11 mm in diameter, gray circle) was covered by the incoming beam.

The basic structure of a membrane deformable mirror consists of a silicon chip attached to a printed circuit board. The chip has on one face a silicon nitride composite membrane which is coated with metal or metal-dielectric material to make the membrane surface reflective and conductive. Optimally designed membrane mirror surfaces are able to produce a reflectivity of better than 99.8% (Vdovin & Kiyko, 2001). Although, the membrane has a diameter of 15 mm, the electrode structure covers only the central ~70% of the full membrane surface. As the circumference of the MDM is fixed to the edges of the circular aperture, only the central 9-12 mm is used for aberration compensation (Vdovin & Sarro, 1995). In the compact AO ophthalmoscope, the beam diameter on the MDM surface is 9 mm, and the mirror is mounted on a Newport tip-tilt mechanical stage. Due to the small size and light weight of the MDM, it was mounted directly to the stage of the HRT in the external AO unit, on the open side of the ophthalmoscope, conjugated to the pupil plane, as in the optical arrangement given in Figure 4.2. This mechanical setup allowed off-loading of tip and tilt control of the mirror without a tip-and-tilt aberration compensation loop which was essential to consider in the design, since the amount of correction for these parameters achievable using this mirror alone may not be sufficient (Paterson *et al.*, 2000) in ophthalmic applications.

The shape of the MDM surface is controlled by electrostatic forces that result from the potential difference applied between the electrodes and the mirror surface. The electrodes produce a potential difference of 0V to 180V relative to the mirror, which is grounded. Any potential applied between the membrane and the electrodes results in deformation of the membrane centered around the electrode. Since the electrostatic forces are attractive, the membrane can produce only concave shapes by moving in the direction of the electrodes. To permit the movement of the mirror surface in both directions, a constant offset (bias voltage) was applied to all electrodes; the state of the membrane at this offset is taken as a reference. The voltage applied to an electrode essentially controls the curvature of the membrane surface in the vicinity of the given electrode; the deflection of the membrane surface is proportional to the square of the applied voltage (Booth *et al.*, 2005). Modeling the mirror deformation modes requires a mathematical description of the membrane behaviour, as discussed in detail by Paterson *et al.* (2000). The behaviour of the membrane can be estimated from the membrane equation (Grosso & Yellin, 1977):

$$\nabla^2 z(x, y) = -P(x, y)/T = -\epsilon_0 V^2 / T d^2 , \quad (4.1)$$

where z is the membrane deformation, T the membrane tension and P the electrostatic pressure due to the voltage V across the gap d between the membrane and the electrode, $z=0$ at the clamped edge of the membrane. Singular Value Decomposition (SVD) gives (Press *et al.*, 1992) a quantitative estimation of the mirror's ability to correct for static aberrations. The linear approximation of Eq. 4.1 can be used to calculate the influence functions of the mirror in order to obtain a characterisation of the mirror. Each influence function shows the shape of the surface when a potential is applied to a single electrode. The effect of the resulting mirror deformation on the wavefront is given by:

$$\Phi_m = \mathbf{A}_m \mathbf{x}_m , \quad (4.2)$$

where \mathbf{A}_m is the influence matrix of the mirror, and vector \mathbf{x}_m represents the set of actuator signals. The actuator signals for a required wavefront correction (Φ_0) are given by

$$\mathbf{x}_0 = \mathbf{A}_m^{-1} \Phi_0 , \quad (4.3)$$

where \mathbf{A}_m^{-1} is the pseudo-inverse of \mathbf{A} and can be expressed in the following form:

$$\mathbf{A}_m^{-1} = \mathbf{V}\mathbf{S}^{-1}\mathbf{U}^T, \quad (4.4)$$

where \mathbf{U} (orthonormal sets of the mirror deformation), \mathbf{S} (singular values representing the gain of different modes) and \mathbf{V} (actuator signal spaces) are the SVD of \mathbf{A}_m such that $\mathbf{A}_m = \mathbf{V}\mathbf{S}^{-1}\mathbf{U}^T$. The ratio of the smallest to the largest value gives the condition factor giving the measure of the controllability of the DM.

The next section of the thesis shows how this technology and wavefront sensing can be integrated into the ophthalmoscope. It discusses also the operation of the compact AO-HRT instrument and highlights the main problems in design of ophthalmic imaging systems associated with their use in clinical environment.

IV.3 Operation of the adaptive optics ophthalmoscope

The successful operation of an adaptive optics system results in the significant reduction of aberrations by correction of phase distortions. When an imaging system experiences aberrations, the result is degraded image quality, giving a blurred image with reduced sharpness and low contrast (Fienup & Miller, 2003). The required corrections are determined by a wavefront sensor in most AO imaging systems (Fernandez *et al.*, 2001; Roorda *et al.*, 2002; Hampson *et al.*, 2005; Romero-Boorja *et al.*, 2005, Vogel *et al.*, 2005) and are translated to deformable mirror commands for the correction of the aberrated wavefront. This adaptive method was first proposed by Babcock in 1953 while the first wavefront sensorless method was introduced by Muller & Buffington (1974). Wavefront sensorless methods have been implemented in ophthalmic imaging systems by Murray (2006) and Sredar *et al.* (2010).

The wavefront sensorless imaging systems use only corrective elements with adjustable segments to maximise a metric correlating to the image quality (Murray *et al.*, 2005). The original paper (Muller & Buffington, 1974) presented computer simulations in which active optical elements maximised the image sharpness by correcting atmospheric distortions for telescope systems (Roddier, 1999). In order to optimise the image quality, search algorithms have been employed to find the optimal set of actuator voltages on the DM maximising the sharpness metric and thus the peak of the point spread function on the detection camera (Zhang *et al.*, 2006).

In some conventional AO imaging systems, either the optics are not the same for wavefront sensing and detection (Bauman & Eisenbies, 2006), or the system contains moving optics (Hofer *et al.*, 2006) and non-common path aberrations change occur. In order to obtain the best possible wavefront at the detector, the performance of the system has to be optimized by correcting aberrations which are undetectable by the wavefront sensing camera. The wavefront correction process is based on a wavefront sensorless method, and employs an image sharpness metric. This is one of the critical issues in achieving the best optical performance of an imaging system by correcting of non-common path errors (Fusco *et al.*, 2005).

IV.3.1 Optimization of the system

IV.3.1.1 Image sharpening

The benefit of using a wavefront sensing technique is the direct determination of close conjugation of the aberrations for phase corrections, which requires wavefront reconstruction from the wavefront sensing measurements. In adaptive optics systems, the image sharpening method refers to the wavefront-sensorless compensation of fixed aberrations which degrade the image quality. Calculations for sharpness maximisation are generally straightforward and based on the intensities measured at the CCD camera while the image sharpness is maximised by a series of deformable mirror commands, as was recently studied in detail by Murray (2005).

This section presents the suitability of various metrics by application of mirror modes through different sets of voltages in the cAO-HRT ophthalmoscope and enables calibration for non-common path errors, a limitation of many adaptive optics retinal imaging instruments. The aim is to provide the optimal shape of the deformable mirror to minimise the non-common path error.

When the signal is weak and there is little information about the object, such as in ophthalmic applications, processing can be very slow (Tyson, 1997) and image sharpening becomes a time-consuming process so that this technique is useful in compensation of slow varying or static aberrations when the wavefront sensor cannot be applied. The image sharpening method applies trial phase corrections using an iterative

approach using different sets of actuator voltages on the DM, and the resulting image is evaluated to produce a sharpness metric which is to be maximised.

In the cAO-HRT system (Figure 4.2), the optics are not the same for wavefront sensing and detection. The non-common path aberrations occur between the wavefront sensor beamsplitter plate (BSP) to the pixelfly camera (PFC) and from the BSP to the detector (APD). Therefore, any non-common path aberrations are not detected by the WFS, providing a false reference. Sharpness maximisation, by pre-compensating and correcting these errors, can minimise the aberrations and restoring the Airy rings and a true reference can be provided for the wavefront sensor (Murray *et al.*, 2005). These optical components are part of the two main adjustable blocks (the main HRT unit and the external AO block), and the non-common path is unaffected during spherical aberration compensation in real eye imaging. Manual focusing correction of the system only affects the common path, from the block to the fixed objective (f_2), by altering the path length.

The measure of the image quality is defined as sharpness (S); generally the higher the metric, the better the image quality (Murray *et al.*, 2005). Sharpening metrics are widely used in image processing (Russ, 2011) discussed for example by (Seul *et al.*, 2000) but in recent years there have also been introduced in vision science (US Patent 7077522 – Williams *et al.*, 2006) to control eye surgery or the fabrication of artificial eye lenses in cataract.

The simplest method used is to maximize the intensity at one point (Muller & Buffington, 1974; Tyson, 1997; Murray, 2006) by the manipulation of the phase-correcting elements. This method ($S_0 = I(x_0, y_0)$) is simple, and is achieved by changing the phase by adjusting one element at a time while observing the sharpness metric of the image at one point. However, due to the poor use of photon-counting statistics, this sharpness metric is satisfactory only for bright objects (Muller & Buffington, 1974).

Removing or minimizing the aberrations relies on the definition of the sharpness metric and the sample or phantom applied. During the cAO-HRT optimization tests, 4 sharpness metrics (Equations 4.5 - 4.8) as defined in Table 4.1 were tested on 3 fake eye models using 10 different optical characteristic samples.

The compact AO-HRT system uses a 37-actuator OKO DM (operating at a maximum 180 volts) as a phase correcting device to be driven to the optimal shape of its membrane in image sharpening maximisation (Murray, 2006). A standard actuator numbering

scheme is employed (Figure 4.8), with mirror actuator signals being normalised in the range from -1 to +1. The 0 level signals in the normalised range correspond to the bias position of the mirror that is the halfway point of its travel. It can be seen from the equation which describes the membrane behaviour that if the same voltage is applied to all actuators, the mirror surface will adopt a form of constant curvature, introducing defocus.

Table 4.1 Definition of image sharpness metrics

Definition of sharpness	Description or reference of metrics	
$S_1 = \int I(x, y) dx dy$	The simplest metric is the integral of the intensity across the image plane.	(4.5)
$S_2 = \int I^2(x, y) dx dy$	Sharpness metric (S_2) according to the definition by (Muller & Buffington, 1974).	(4.6)
$S_3 = \frac{\int I^2(x, y) dx dy}{\int I(x, y) dx dy}$	Improved definition of sharpness S_2 by normalisation. This metrics was used in either for the whole (256x256 pixels) field or for the central 100x100 pixel area (S_{3M}).	(4.7)
$S_4 = \frac{\int I^2(x, y) dx dy}{\int (I(x, y) dx dy)^2}$	Improved definition of sharpness metric S_2 .	(4.8)

Table showing the definition of image sharpness metrics (S_z where $z=1, 2, 3, 4$) which are employed to minimize the non-common path aberrations of the cAO-HRT system where x and y denote the coordinates in the image plane and $I(x, y)$ is the image irradiance.

To find the best set of actuator voltages there are 37 degrees of freedom (DoF) for the search algorithm to determine the global minimum of the system. According to (Doble, 2000), the Nelder-Mead simplex algorithm gives a good solution, and this method is employed in the cAO-HRT optimization routine.

The simplex proposed by Nelder & Mead (1965) is for finding a local minimum of a function of several variables which later was tested by Olsson & Nelson (1975) in terms of its applicability for general function minimisation. This simplex method is a black-box optimization method that operates on a set of solution points discussed in detail by Hansen (2009). The simplex itself is a geometrical figure comprising $n+1$ vertices, where n is the degree of freedom. For two variables, a simplex is a triangle and the method is to search a pattern that compares function values at the three vertices of a triangle (Mathews & Fink, 2004). The worst vertex is rejected and replaced with a new vertex, forming a new triangle, and the search is continued. This generates a sequence of triangles during the search process (Matthews & Fink, 2004; Murray, 2006) during which the function

values get smaller. The process results in a reduced triangle size and gives the coordinates of the minimum point, which is the global minimum. This is done through a series of operations such as reflection, expansion and contraction which is an effective and computationally compact method (Matthews & Fink, 2004).

In the cAO-HRT experiments similar to those carried out by Murray (2006), the simplex has a complex figure with 38 vertices, each of them representing a set of mirror voltages. First, 38 (n+1) sets of voltages are generated and the corresponding sharpness values are calculated with the aim of contracting to the global minimum. The simplex stops when it has met a termination criterion or the global minimum cannot be determined within the defined maximum number of iterations.

According to a paper published by Fusco *et al.* (2005), although pre-compensation methods result in increased image quality, some significant aberrations may be uncorrected and some metrics are object dependant (Fienup & Miller, 2003). However, when the object is known, the method can be suitable for compensating for slowly varying turbulent effects (Tyson, 2000). A further goal of this work was to find a suitable phantom retina sample for non-common path error compensation without the direct knowledge of the error sources of aberration differences in wavefront sensing and in imaging optics; tests on fake eye models using image sharpening metrics is discussed in the next section.

IV.3.1.2 Fake eye models

In image sharpening, the use of the human eye as a calibration target for imaging is not possible since there is uncertainty due to the time and space varying effects performed in the ocular medium. Optimization and calibration of imaging systems require a static and stable fake eye object (FEO) or an artificial eye (AE). The literature describes the construction of sophisticated eye models (Harvey *et al.*, 2010; US Patent 6485142 – Sheehy, 2002) for specific applications such as measuring the oxygen saturation within the retinal vasculature (Mordant *et al.*, 2010) or testing the effectiveness of protection shielding the human eye against radiation (US Patent 6485142 – Sheehy *et al.*, 2002). However, these are often systems designed for either primates (monkeys) or for rodents. The design of these systems is different from those for humans since small animals have a smaller pupil, larger lens and poorer ocular medium (Hammer *et al.*, 2010).

The Harvey AE-model closely replicates the fine layer structure of the retina: it comprises an ocular chamber filled with saline consisting of synthetic blood vessels on its “retina” through which known oxygenated blood can be pumped, and three other layers of the retina, the PE, choroid and sclera. This AE model has potential in retinal imaging including OCT or SLO testing and safety assessment. The Sheehy AE-model includes a spherically shaped container including a hemispherical posterior portion and some functional counterparts to the two chambers of the human eye. These chambers are filled with fluids mimicking the characteristics of the aqueous and vitreous humours.

In most AO imaging systems less sophisticated eye models are used for testing. For example, a simple FE model (Bao-Guang, 2008) is composed of a white piece of paper with carbon granules measuring 4-10 μm in diameter (comparable in size to the cones), on its surface and an achromatic lens of 25 mm focal length with an adjustable pupil size of 3-7 mm. However, in most cases a simple piece of card is used to act as the retina, for example in a system designed by (Hampson, 2004).

The optimization of the cAO-HRT system to minimize the non-common path errors does not require a model as sophisticated as the Harvey or Sheehy models. However, the optical characteristics of the artificial eye (Baumann & Eisenbies, 2006) retina object have to be similar to that of the human retina (Harvey *et al.*, 2010). The ideal artificial retina is a diffusely scattering object placed at the focal plane of the focusing lens. Table 4.2 summarizes the materials which were employed to construct fake eye models for the optimization routine testing.

Compact fake eye models were constructed from Linos microbenches for their ease of operation and high mechanical stability. The basic components were connected by four rods to create compact, three-dimensional artificial eye structures. The optics of the fake eyes contain a Linos achromatic doublet of $f=25$ mm (in some cases 35 mm or 50 mm depending on the structure and thickness of the sample), an iris having adjustable diameter in the range from 1-8 mm and the target. The target was placed at the focal plane of the lens and was attached to a Linos centring mounting plate. The position and angle of the mounts were adjustable, perpendicular to the surface of the target in x - y translation.

Table 4.2 Selection of list of targets used as artificial retina samples

	Target (Reference#)	Description / physical parameters	Optical feature
[1]	Silicon test specimen - STS (EMS 79502-01)	5mmx5mm square single crystal silicon specimen. Squares repeat every 10 μ m; the dividing lines are 1.9 μ m wide. Broader line is written every 500 μ m. Suitable for assessing distortion in the image field.	specular reflector (highly)
[2]	HRT calibration target	2 mm thickness of crossed scale graticule	specular reflector
[3]	Microscope slide – MT	2mm thickness of glass slide Lily anther with pollen	specular reflector
[4]	Photographic film / regular – PFR	film thickness of approx. 130-150 μ m line thickness of 10 μ m 35mmx40mm negative film (matt side)	specular reflector (moderate)
[5a]	Gilder grid, mesh (hex.) (EMS T600H-Cu)	copper grids of 3.05mm overall diameter, 2.05mm mesh area diameter; one side being shiny, the other matt. pitch 37 μ m, hole 29 μ m, bar 8 μ m	specular reflector (moderate)
[5b]	Gilder grid, mesh (hex.) (EMS T601H-Cu)	pitch 42 μ m, hole 37 μ m, bar 5 μ m	specular reflector (moderate)
[5c]	Gilder grid, mesh (square) (EMS T2000-Cu)	pitch 12.5 μ m, hole 7.5 μ m, bar 5 μ m	specular reflector (moderate)
[6]	Photographic film / irregular – PFIR	thickness of approx. 100 μ m Thin film with carbon granule contamination (matt side).	Scatterer
[7]	Resolution test target RTT (NP:USAF-1951 target)	clear line on opaque chrome background (2.0 OD), optical glass substrate 50x50x1.5mm.	specular reflector (moderate)
[8]	Sand paper P800 / P1200 (ISO 6344-3:1998)	super fine, average particle diameter of 21.8 / 15.3 μ m	diffuse scatterer
[9]	Sellotape	thickness of approx. 2-5 μ m one side being matt, the other sticky	diffuse scatterer
[10]	Graph paper	paper thickness of approx. 5-7 μ m line spacing of 1mm	diffuse scatterer

Table showing the selection of list of targets used as artificial retina samples in the compact fake eye models to test the optimization routines.

To compare the effectiveness of the correction algorithms approximately 100 optimization tests were carried out and several targets having different optical characteristics were tested. A selection of the results, a comparison of the sharpness metrics and targets, is discussed in the next section.

IV.3.1.3 Optimization test results

The purpose of the tests was to determine the characteristics of a suitable target and to minimize the non-common path errors in the system. Calculation of the sharpness values is generally a straightforward operation since the intensities are measured on the detector. The system uses an Intel(R) Xeon(TM) CPU 2.40 GHz processor running on Linux OS; the search and control algorithms were written in Python programming language.

If the target is a specular reflector, some of the aberrations described by odd function such as coma or distortions may be cancelled due to the double-path effect. The images in Figure 4.9 illustrate that some of the aberrations may not be corrected after optimization. The wider horizontal line is brighter than the vertical line and the finer structure was resolved for only the horizontal lines indicating the presence of astigmatism.

This target is suitable for testing sharpness metrics but not suitable for use in determining the set of actuator positions for removal of non-common path errors. These targets have smooth and highly reflective surfaces, so odd aberrations may be cancelled; similarly specular reflective targets include the hexagonal Gilder grids (Table 4.2 /#5a-c) and the HRT calibration target (Figure 4.10). The advantage of using the hexagonal Gilder grids is that the structure of a similar size to the photoreceptor cells on the retina.

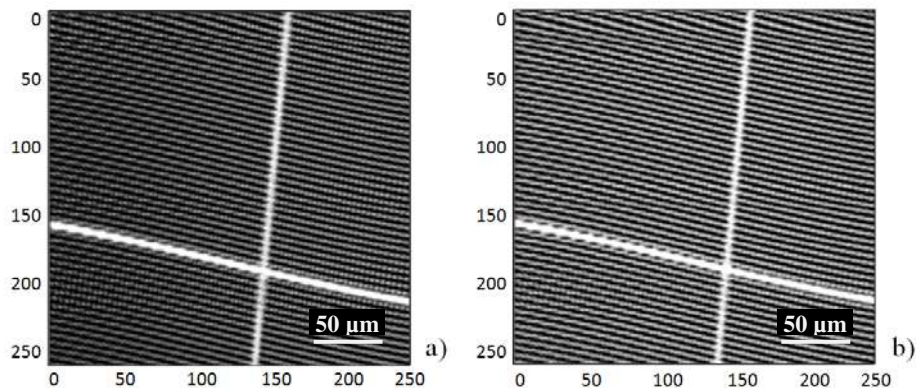


Fig. 4.9 Aberrated and corrected images using a microscope target

Figures showing aberrated (on bias) and corrected images after optimization employing sharpness metric 3. The fake eye consisted of a 25 mm focal length achromatic doublet with pupil diameter of 7 mm and the target is silicon test specimen (Table 4.2 /#1).

The HRT target (2 mm in thickness) is a transparent sample, and during optimization the system attempted to focus on different layers axially, resulting in a loop of an uncompleted process after reaching a maximum number of iterations without finding a global minimum.

Figure 4.11 shows tests on normal photographic films in fake eye models. The sample (Table 4.2 /#4) was a negative film on which parallel lines, thickness and separation of 10 μm , were exposed. Photographic films (Figure 4.11-4.12) are good samples as they are thin (50-100 μm) with some high contrast structures, while some parts are transparent. They have no surface structures at different depths to cause false results in sharpness optimization. However, these samples are shiny and act as highly reflective specular reflectors.

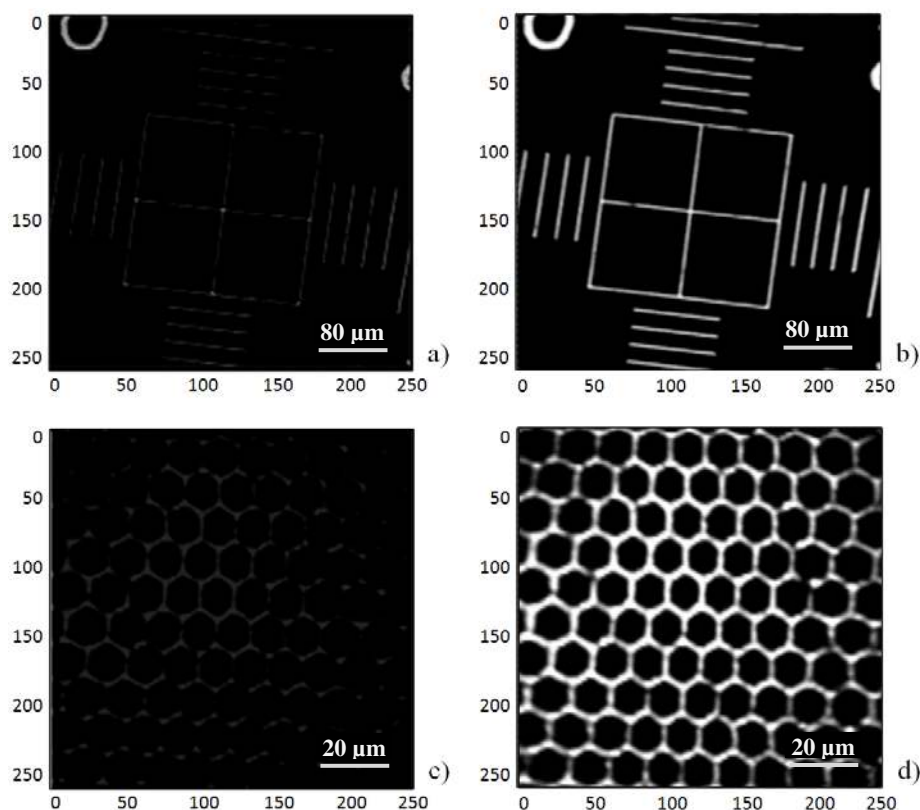


Fig. 4.10 Corrected images after optimization using highly reflective samples

Uncorrected (left) and corrected (right) images employing sharpness metric 3. The fake eye consisted of 35 mm and 25 mm focal length achromatic doublet with a pupil diameter of 7 mm for imaging the HRT target (Table 4.2 /#5a) upper row and a hexagonal copper mesh (Table 4.2 /#2) bottom row.

The results from 10 series of measurements show some increase in the sharpness values after compensating for aberrations, but if the sample is a specular reflector it may cancel out some system aberrations. The measurements were repeatable with an average variation of 3.8% on a pixel-by-pixel basis.

If the image is saturated before it is fully corrected (Figure 4.12) it results in a false sharpness value that limits the achievable correction by the active element. Optimization

was often terminated when these targets were tested and a real global minimum could not be determined. This issue can be remedied by the use of a lower illumination power.

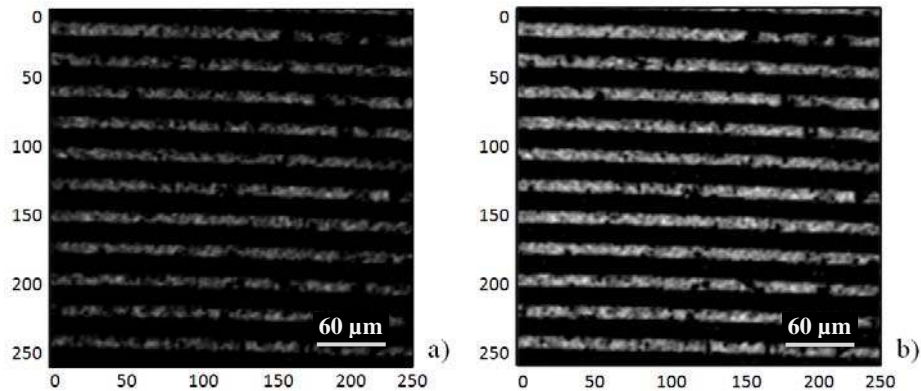


Fig. 4.11 Aberrated and corrected images using thin film with regular structure

Aberrated and corrected images after optimization employing sharpness metric 3. The fake eye consisted of a 30 mm focal length, achromatic doublet with a pupil diameter of 7 mm and the target is a photographic film with regular structure (Table 2 /#4).

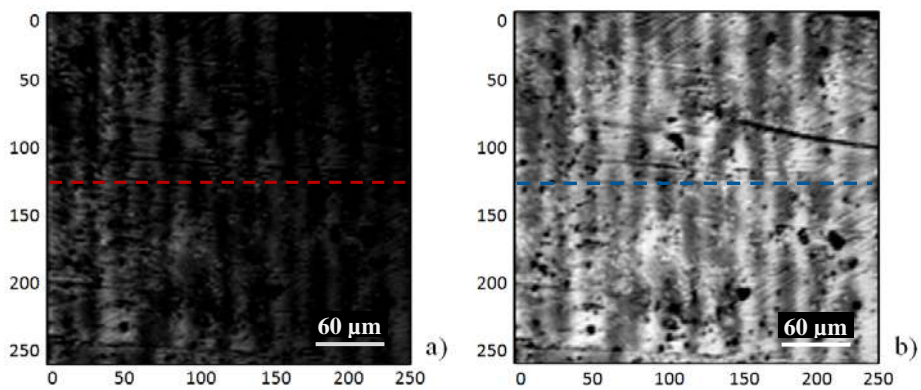


Fig. 4.12 Aberrated and corrected images using photographic film

Aberrated and corrected images after optimization employing sharpness metric 3. The fake eye consisted of a 35 mm focal length acromatic doublet with pupil diameter of 7 mm and the target is a photographic film with carbon granule contamination (Table 4.2 /#6).

To compare the correction of system aberrations and find the best set of actuator settings, a photographic thin film was used to show the measure of the improvement of the image quality. Figure 4.13-15 are a series of intensity profiles to illustrate the effect of noise on the sharpness metric optimization. Two parameters were manually changed on the HRT board, the incident power at the artificial corneal level of the model eye and the gain, in a manner that image quality before optimization on the display was comparable in all cases (Figure 4.10-12, images in left columns showing examples for uncorrected cases, before optimization). The gain values were in the range from 3-7 and the power level incident on the fake eye cornea was from 4-11 μW .

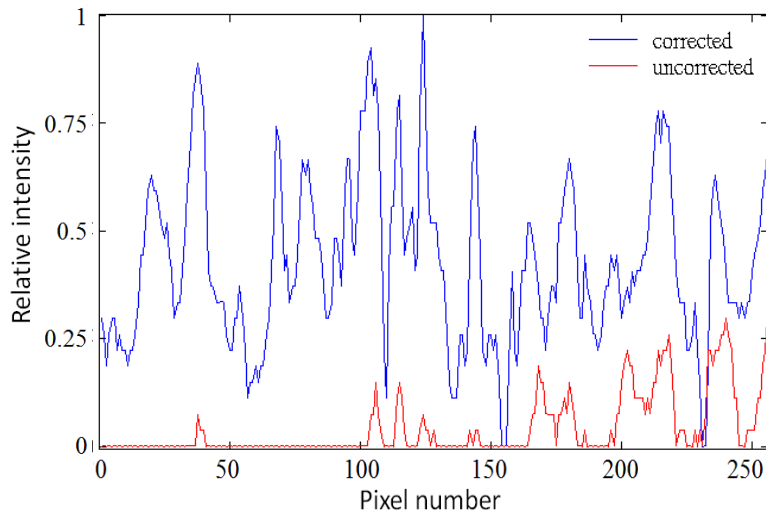


Fig. 4.13 Intensity profile for sharpness metric (low gain) in photographic film

Intensity profile (row 125 as shown in Figure 4.12) through corrected and uncorrected photographic film (Table 4.2 /#6) used sharpness metric S_3 at power level $11\mu\text{W}$ and gain 3.

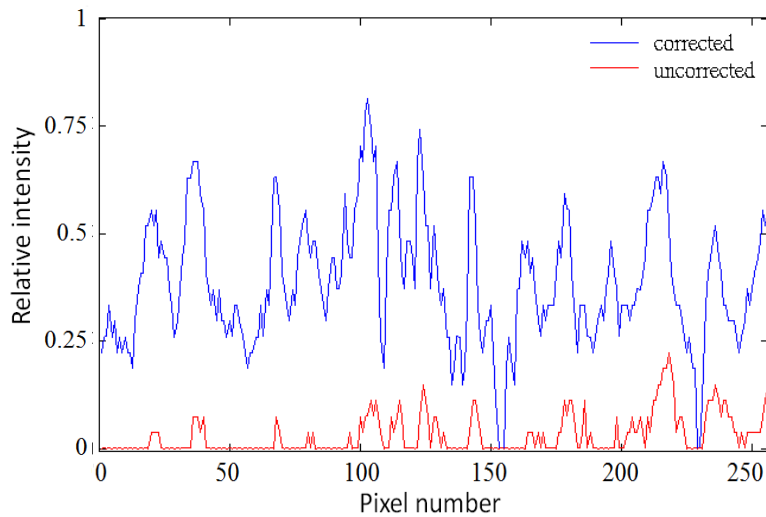


Fig. 4.14 Intensity profile for sharpness metric (medium gain) in photographic film

Intensity profile (row 125) through corrected and uncorrected photographic film (Table 4.2 /#6) used sharpness metric S_3 at power level $7\mu\text{W}$ measured at the sample and gain 5.

To demonstrate the reduction of aberration, an intensity profile was taken through the centre line of the image (row 125) as indicated (red and blue dashed lines) in Figure 4.12. As the signal-to-noise ratio decreased, the sharpness metric optimization was less successful and the average relative intensity value dropped from 0.65 to 0.40 au. As can be seen (Figure 4.12-15), significant improvement in the image quality employing the sharpness metric is achievable, corresponding to an increased contrast if the artificial retina is a scatterer object. All the sets of actuator settings described in this section were tested on real eyes;

however, sometimes these optimization results were not satisfactory, with the mirror on its bias position showing better resolution on human samples.

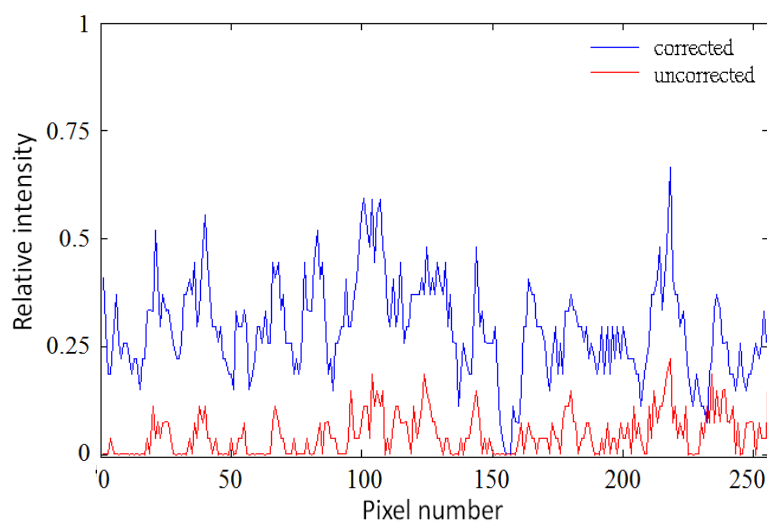


Fig. 4.15 Intensity profile for sharpness metric (high gain) in photographic film

Intensity profile (row 125) through corrected and uncorrected photographic film (Table 4.2 /#6) used sharpness metric S_3 at power level $4\mu\text{W}$ measured at the sample and gain 7.

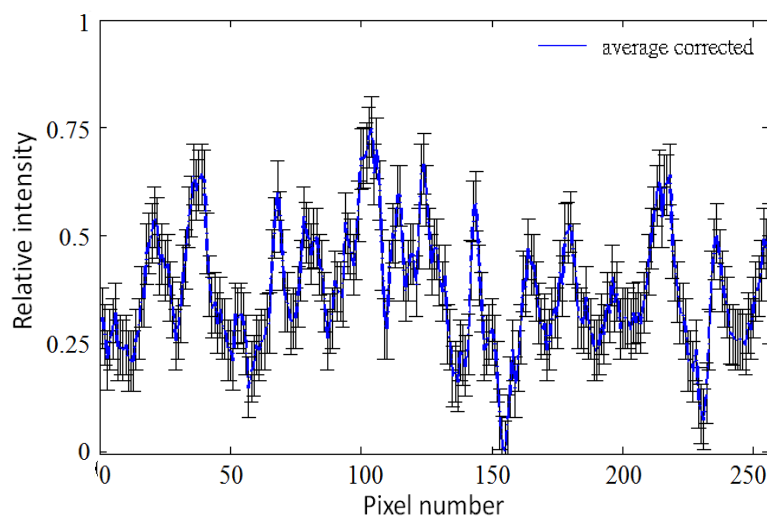


Fig. 4.16 Relative intensity taken through corrected images with optimization

The optimization results of the compact AO-HRT using a sharpness metric (Figure 4.16 and Figure 4.17 showing examples for corrected and uncorrected cases) are in agreement with other studies (Murray *et al.*, 2005) using various optical samples for compensating aberrations in a wavefront sensorless imaging system. The improvement in image quality was significant in all cases (Figure 4.13-15) but the correction was not optimal since the deformable mirror reached its limit in deformation capability to correct the aberrations or the simplex fell into a local minimum.

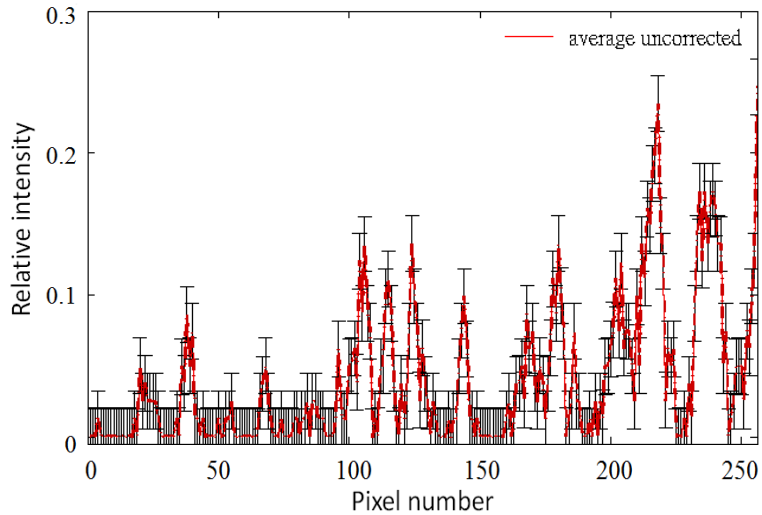


Fig. 4.17 Relative intensity taken through uncorrected values

Average intensity values of 10 series of uncorrected images when the mirror actuators were all on bias.

Figure 4.18 shows comparison examples for correcting the system aberrations using metrics S_1 - S_3 ; the most effective sharpness metric resulted in the best contrast and the highest resolution was achievable by using metric S_3 as demonstrated in the diagram (Figure 4.18c). The intensity profiles through images show increase in contrast with corrections and the image resolution has also increased which is demonstrated on the Lilly anther microscopic sample in increased level of clarity of the finer cell structures.

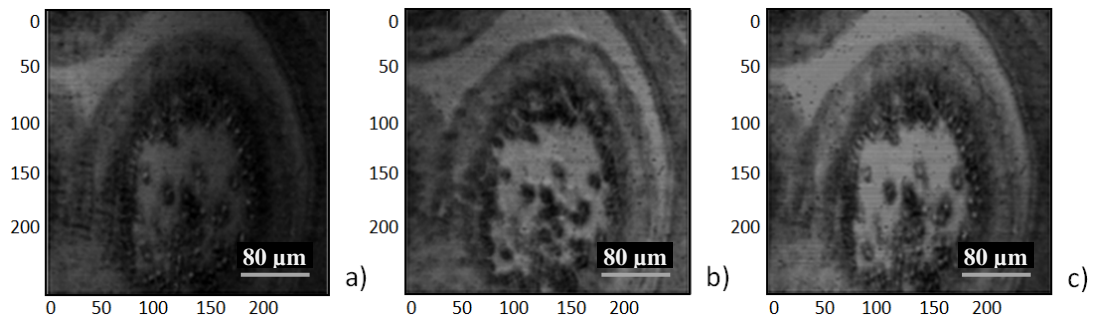


Fig. 4.18 Comparison of metrics for removal of non-common path errors

Comparison of different metrics (a) S_1 , (b) S_2 and (c) S_3 in the figure on a Lilly anther sample. Optimisations were performed in an optical setup using sand paper p/1200 as a sample in the model eye to obtain set of actuator voltages for system aberration correction. The set of voltages were applied to compare the image quality. Sharpness metric S_3 provided the best contrast and the finest cellular level details can be distinguished.

The sharpness metric results in optimization of the imaging system to remove non-common path errors shows that in finding the global minimum (Figure 4.19 and Figure 4.20), which is a randomised process often results in completely different sets of actuator settings when run on the same sample. The reason for the differences in the optimisation

tests is the change in noise level and fluctuations in the power of the laser source during optimisations, which are random processes.

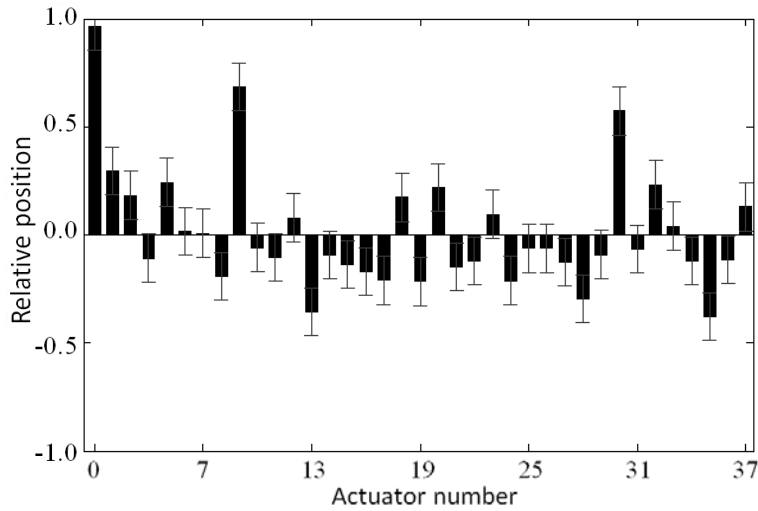


Fig. 4.19 Average actuator arrays using metric S_3 for photographic film

Average actuator arrays of 10 measurement series from sharpness metric (S_3) optimization. The target is a photographic thin film.

Figure 4.20 shows an example for a set of actuator settings used to remove the non-common path errors of the AO retinal imaging system.

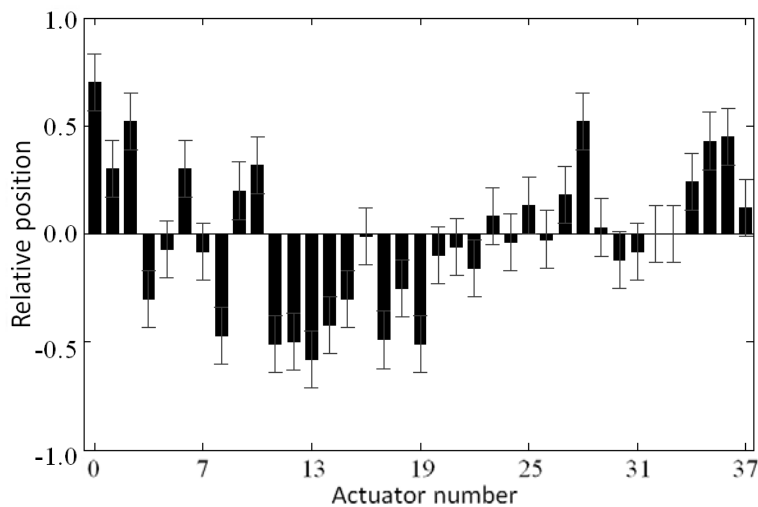


Fig. 4.20 Average actuator arrays metric S_3 for sand paper sample

Average actuator arrays of 10 measurement series from sharpness metric (S_3) optimization. The target is sand paper p/1200.

The best set of actuator settings (based on objective comparison in real eye tests) for providing a reference for real eye imaging was based on the S_3 sharpness metric optimisation with sandpaper (p/1200 object in Table 4.2) used as the artificial retina.

To conclude, image sharpening is a useful method to correct for the optical path which is undetectable by the wavefront sensor in adaptive optics systems. The optimal set of actuator settings can be achieved by imaging a diffusely scattering object which has similar optical characteristic that of the real retina during *in vivo* measurements. The optimal actuator positions are highly dependent on the optical quality of the sample and are also limited by the boundary conditions such as the gain and power level.

IV.3.2 Summary and discussion

This work confirmed that search algorithms can be successfully used to maximise sharpness metric through finding the optimal shape of the deformable mirror for adaptive corrections. Aberrations were corrected by using the simplex in a slow process even when static samples were analysed. The typical time required to perform an algorithm was ~8-12 minutes in about 500-600 iterations in average, even higher number of iterations and more time consuming cases have been also reported depending on the sample. Hence, this method can be used only in compensation of slow varying or static aberrations, and the results performed in this thesis suggest that it is a possible approach for the removal of non-common path errors in lens based designed adaptive optics imaging systems.

Chapter V

Retinal imaging with the compact AO ophthalmoscope

V. Retinal imaging with the compact AO ophthalmoscope

The main goal of this chapter is to demonstrate the effectiveness of high-resolution retinal imaging as a quantitative method, image sharpening methods for removal of non-common path error and to show the usefulness of this technique in photoreceptor diseases as a new diagnostic tool in a future clinical investigation. As part of development of the compact AO imaging system, this chapter presents the first results from the compact AO-HRT ophthalmoscope (cAO-HRT) using a membrane deformable mirror as a corrective device on healthy human volunteer subjects.

The chapter opens with a section on the objective of retinal imaging tests and discusses the imaging protocol on human subjects. One of the main goals in this study was to examine the human retina at cellular level in the central field. The next section discusses the method of retinal imaging and introduces the first results taken from the high-resolution compact AO ophthalmoscope. Finally, comparison of imaging results to previously reported histological data is present including photoreceptor counting at different fields of the human macula.

V.1 Objective of non-invasive retinal investigations

The aim of the experimental study and test of the cAO-HRT imaging system were the real-time observation of the centre of the human retina correcting the dynamic ocular aberrations in real-time. The retinal images in Figure 5.1 shows the focus of our interest for *in vivo* study the cellular level details using the high-resolution imaging method with adaptive optics.

The focus of the cAO-HRT investigation is the photoreceptor layer (blue shaded band on OCT image) in the central field (yellow circle on fundus image) at about 1-5° of eccentricities; the numerical values in the SLO image indicate the thickness of the retina in microns. The central gray field is the centre of the fovea, about 350 μm in diameter corresponding to about 1° field of view where the thickness of the retina is about 250 μm in average (Figure 5.1). The quadrants around the centre of the fovea refer (anticlockwise from left to right) to the superior, temporal, inferior and nasal parts of the central retina.

The retina has increased thickness, ~320-340 μm in the fovea and ~270-310 μm in the parafoveal location; the photoreceptors are about 50-70 μm long in average (longest in the foveola). The light used for illumination has to go through several layers of cells to reach the photoreceptor level (R/C-IS - rod/cone inner segment, I/OPJ - inner/outer photoreceptor junction, POS - photoreceptor outer segment) in deeper depths of the retina.

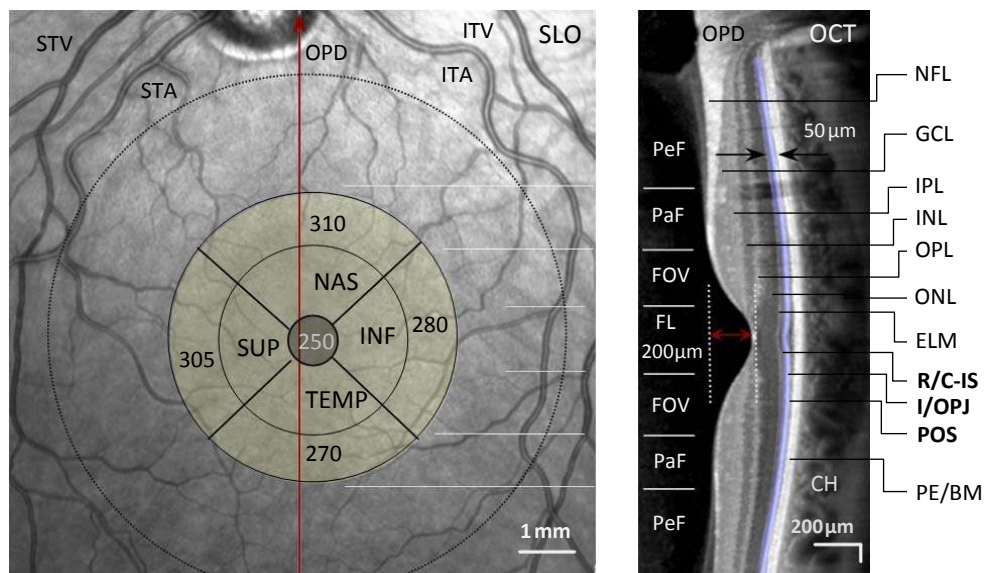


Fig. 5.1 Surface and cross section of fundal locations under investigation

Diagram (the author's retina) showing the morphology of the centre field (OD) obtained with HRA+OCT spectralis (IR) diagnostic instrument (images courtesy of Dr Kester Nahen, Heidelberg Engineering, annotations by the author): cSLO (left, rotated 90° anticlockwise) and OCT (right) as an illustration of the locations where the AO imaging tests were performed. Notations /their diameters (data from literature) but vary between individuals: foveola (FL/350 μm), fovea (FOV/1.85 mm) and parafovea (PaF/2.85 mm); numerical values in the cSLO diagram indicate the estimated retinal thickness in microns.

V.1.1 Retinal imaging protocol

In ophthalmic application of AO modalities, the eye must be prepared for imaging in order to maximise the photon count on the detector in high-resolution *in vivo* retinal imaging studies, which requires pupil dilation of the subject. When the AO loop is closed, the ocular aberrations are dynamically corrected, but paralysation of the ciliary muscle to inhibit the accommodation action of the eye is necessary for imaging. Table 5.1 summarizes the most commonly used eye drops and their effects (Shah *et al.*, 1989; Huber *et al.*, 1985; Paediatric Glaucoma & Cataract Family Association (PGCFA), 2008;

Clinician's Ultimate Reference (CUR), 2011; Taneri *et al.*, 2011; Pi *et al.*, 2011; Bartlett & Jaanus, 2008; Duvall & Kershner, 2006).

Table 5.1 Summary of the eye drops used in eye examinations

	Eye drop	Dose	Effect	Employed in AO
1	Atropine / Isopto Atropine	1-2 drops 0.5 or 1.2%	up to 6 hrs or 1-2 weeks	-
	Cycloplegic eye drop in a series of administrations, 2-3 times daily 1-3 days a week before examination.			
2	Cyclopentolate / Cyclogyl	1-2 drops 0.5% 1% or 2%	Cycloplegia: 6-24hrs Mydriasis: complete recovery usually occurs in 24 hrs	-
	Anticholinergic preparation blocks the responses of the sphincter muscle of the iris and the accommodative muscle of the ciliary body, producing pupil dilation (mydriasis) and paralysis of accommodation (cycloplegia). Should not be used when untreated glaucoma.			
3	Homatropine / Isopto Homatropine	1-2 drops 2% or 5%	2-3 days	-
	Pupil dilation; there is little if any effect on accommodation (similar effect as 2.5% Phenylephrine)			
4	Tropicamide / Mydracil	1-2 drops 0.5 or 1%	4-8 hrs, complete recovery in 24 hrs	Liang <i>et al.</i> (1997); Roorda <i>et al.</i> (2002)
	Anticholinergic preparation blocks the responses of the sphincter muscle of the iris and the ciliary muscle to cholinergic stimulation, dilating the pupil (mydriasis); 1% also paralyzes accommodation.			
5	Phenylephrine / Mydfrin	1-2 drops	4-6 hrs	-
	Mydriasis only, stimulates pupil dilation			
6	Tropicamide 1%+phenylephrine 2.5%	1-2 drops	n.a.	Choi <i>et al.</i> (2011); Wolfing <i>et al.</i> , (2006); Romero-Borja <i>et al.</i> , (2005); Bessho <i>et al.</i> (2009); Dubra <i>et al.</i> (2011)

Tropicamide, eye drop no. 4 (highlighted) indicates the medication that was administered during high-resolution imaging using the cAO-HRT since this eye drop has low risk for complications according to the medical literature. The eye drop was tested by the College ophthalmologist for allergy and side effects on the volunteer eyes before its administration in the pilot studies.

The mydriatic drops exert their effect on the sphincter muscle to dilate the pupil. The dilating drops can work either by temporarily paralysing the muscle that keeps control of the size of the pupil, or by stimulating the dilator muscle of the iris. Some of the mydriatics relax the focusing muscle of the lens which allows more accurate measurements and high-resolution visualisation of the retina.

The duration of the effect of dilating drops (Table 5.1) depends on the particular eye drop being used. Ophthalmic medications may result in side effects as a result of their

absorption into the bloodstream through the blood vessels in the eye. These side effects include flushing of the face, warm sensation of the skin and sweating, which mean that lower dose of the medication should be considered. Other, but rare, side effects are increased blood pressure, confusion and seizures. Most of these side effects can be avoided when a weaker concentration of medication is administered.

There are two main groups of dilating drops, of which some are listed in the table. The parasympathetic antagonists (eye drops no. 1-4 in Table 5.1) which paralyse the sphincter muscle. This category of medicines dilates the pupil and paralyse the muscle involved in focusing. The other type of sympathetic agonist acts by stimulating the iris dilator muscle (phenylephrine eye drop 5 in Table 5.1). The advantage of using this eye drop is that it does not cause blurring of vision. In clinical practice, the two types of drops are often mixed in one bottle (for example, see eye drop 6). Mydriatics may have little or no effect on the accommodative mechanism, instead stimulating the muscle of the iris. In ophthalmic practice *scopolomine* and *hydroxyamphetamine* eye drops are also used. During the pilot studies, tropicamide 1% was administered in volunteer eyes since this eye drop has low risk for complications. The allergic and side effects of the eye drops must be tested all time by an ophthalmologist before administration in eyes for AO imaging tests.

The ophthalmoscope was tested in different accommodative states employing no medication in the eye and after pupil dilation during reduced paralysation of the ciliary muscle by employing 1 drop of tropicamide 1% so that a continuous series of images could be taken without the active accommodative mechanism of the crystalline lens in action. Preliminary measurements were taken to ensure that reduction of lens accommodation was maintained. The optics of the eye focused the incoming laser beam onto the retina and the beam was aligned by translating the head of the subject along the optical axis.

V.1.2 Method and subjects

V.1.2.1 Subjects and retinal locations

The compact AO-HRT was tested on 7 eyes of 4 human volunteer subjects (1 female, 3 males), with an average age of 39 years, diagnosed with no ophthalmic diseases. They are referred to as normal healthy subjects in the rest of this chapter. The central retina at 1-5° was the image target in most individuals which provided an *in vivo* study of the photoreceptors and the nerve fibre layer; some imaging tests were taken at a far field of view to investigate other cell structures such as the optic disc.

V.1.2.2 Head- and eye movements / Image registration

A forehead rest and a chinrest attached to the housing of the standard HRT instrument were used for head stabilisation, and the translation stage of the ophthalmoscope was used for pupil centring and alignment. During image acquisition, the eye usually moves due to voluntary and involuntary eye movements, and each image in the series is randomly translated with respect to each of the others. Image registration was used for retinal motion analysis by building a mosaic image from different retinal photographs. This method resulted in reduced noise with increased signal-to-noise ratio and image stabilisation. Detailed description of this technique was recently published by Faisan, Lara & Paterson, (2011); the method was tested in the high-resolution retinal imaging series with the cAO-HRT.

V.1.3 High-resolution retinal imaging with adaptive optics

V.1.3.1 Retinal locations under high-resolution investigation

The cAO-HRT was tested on a limited number of human volunteer subjects with no diagnosed retinal disease. Figure 5.2 shows the normal healthy retina of a 32-year-old male volunteer at 11.4° x 8.6° field of view. The incident power at the corneal level was 65 μ W; this exposure is safe for long exposure of retinal investigation according to British Standard (BS-60825-8 and BS-60825-13).

The central, approximately $3.5^\circ \times 3.5^\circ$ region (dark gray circle, ~ 1 mm in radius) is the fovea; the smaller $\sim 1.5^\circ \times 1.5^\circ$ black circle (~ 0.4 mm in radius) in its centre is the foveola. The small red squares in the figure correspond to $300 \times 300 \mu\text{m}$ locations (equivalent to $1^\circ \times 1^\circ$ fields) of the retina which were under cAO-HRT investigation.

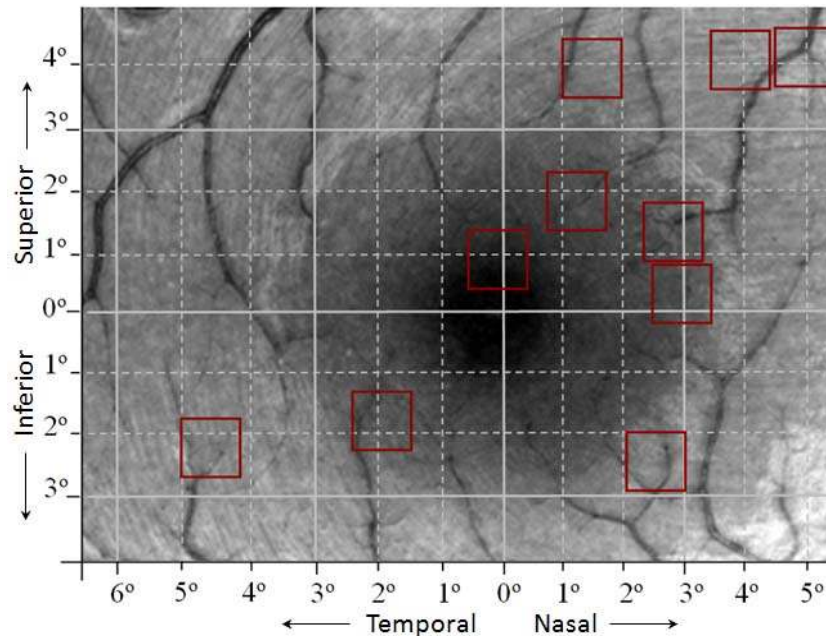


Fig. 5.2 Location of high-resolution images on the centre of the retina

Image of the centre of the retina (OD) of a 32 year-old male subject obtained with Zeiss FF450^{plus} fundus camera. The main image (courtesy of Dr David Lara, annotation by the author) shows the field $11.4^\circ \times 8.6^\circ$; the grid scale ($1^\circ \times 1^\circ$ equivalent to a unit of a red square), is around $300\mu\text{m} \times 300\mu\text{m}$.

The next section shows the preliminary high-resolution retinal imaging results using the cAO-HRT on human volunteer eyes in some of the locations of interest in the central retina as indicated in Figure 5.2.

V.1.3.2 Imaging the photoreceptors in the central field

The first images were obtained with the cAO-HRT ophthalmoscope when the non-common path error was removed using eyes at a normal pupil size - about 3-4 mm in diameter (no dilation). Photoreceptors could have been successfully resolved in the range of $2.5\text{-}4.0 \mu\text{m}$ in diameter in over 90% of the volunteer subjects in this pilot retinal imaging study. Figure 5.3 shows images at a 1.5° field of view (in the superior nasal quadrant) taken by a fundus camera (left) and cAO-HRT (right).

Photoreceptors were resolved within $\sim 0.5^\circ$ (about 0.15 mm) of the centre of the fovea in one individual. This part of the fovea contains the highest density of cone photoreceptors (Curcio *et al.*, 1991) in the retina (about $>190,000/\text{mm}^2$) and their numbers drop by about 50% at 500 μm from the foveal centre and down to less than 5% of that density at about ~ 4 mm eccentricity.

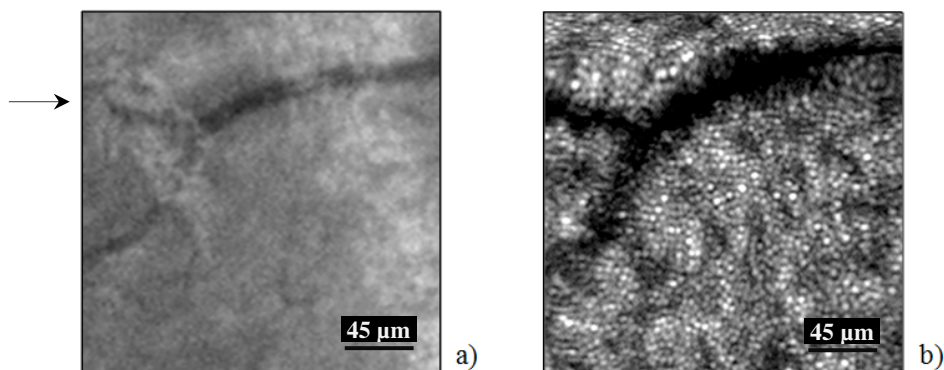


Fig. 5.3 Images of the macula obtained with a fundus camera and cAO-HRT

Images showing the macula (OD) at about 1.5° (superior-nasal quadrant) taken by (a) Zeiss FF450^{plus} fundus camera (courtesy of Dr David Lara) and (b) cAO-HRT. The bright spots are photoreceptors and the Y-shaped structure is the shadow of a blood vessel. The diameter of the photoreceptors is $\sim 4.0 \mu\text{m}$ in this field, corresponding to a density of $62,500/\text{mm}^2$.

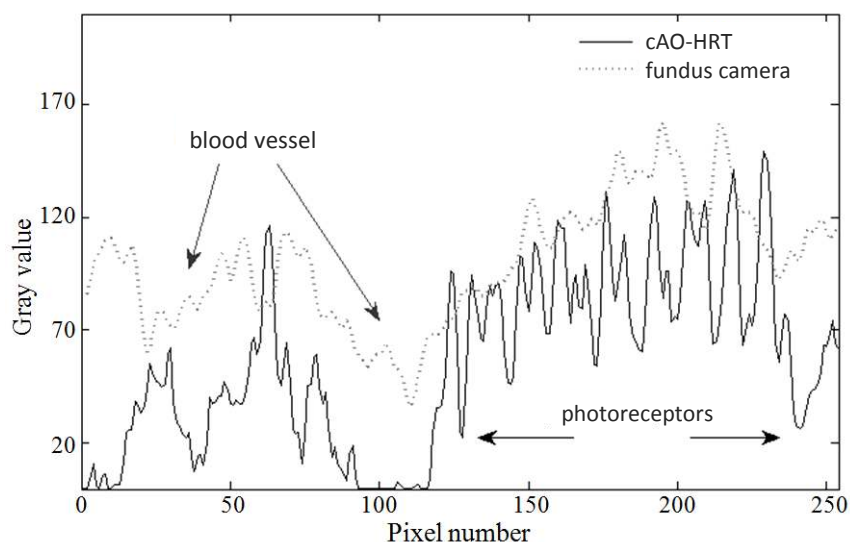


Fig. 5.4 Plot profile taken from Figure 5.3 at $\sim 1.5^\circ$ field of view

Figure showing the plot profile at a row as indicated (by black arrow) in Figure 5.3 taken by the Zeiss fundus camera and the cAO-HRT as a comparison for the image contrast.

According to histological data (Curcio *et al.*, 1991), the size of one cone photoreceptor is equivalent to about one pixel in diameter at this location of the retina. After the removal of the non-common path error from the ophthalmoscope, finer details of cells were

distinguishable. Figure 5.5 shows an image at 4.5° of retinal eccentricity when dynamic correction of the ocular aberration was applied (a), and the image was registered (b).

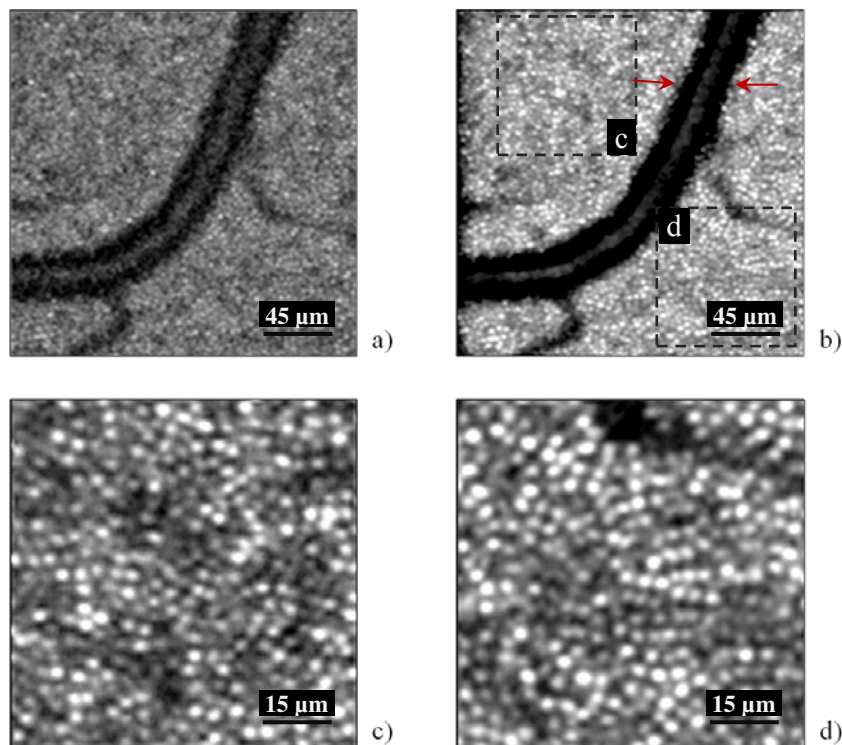


Fig. 5.5 Retinal image at about 4.5° from the centre of the fovea

Diagram showing cAO-HRT images of the centre of the retina (OD) at about 4.5° (superior-nasal quadrant): (a) raw image, (b) registered AO image; (c) and (d) are magnified regions from (b) when the plane of the blood vessel is in focus.

The diameter of the blood vessel, indicated by red arrows in image (b), is $\sim 20 \mu\text{m}$, the diameter of the photoreceptor is $\sim 4.5 \mu\text{m}$ corresponding to the density of $49,300/\text{mm}^2$. In image (d) the capillary appears dark because scattered light from the surface of the capillary is blocked by the confocal pinhole of the ophthalmoscope.

Photoreceptors were studied in more subjects, and image sequences of 32 static frames (per second) were acquired across the central field which allows the real-time observation of the dynamic changes in the retina such as the study of blood flow. In a series of static frames taken by the cAO-HRT the movement of leukocytes (whose size vary from approximately 6 to $12 \mu\text{m}$ in diameter according to Bruil *et al.*, 1991) was non-invasively observable in the capillaries without the use of fluorescein dye and their flowing speed could be estimated. In one case, other cell structures were observed in the macular area and beside the *in vivo* study of blood flow and dynamic behaviour of the retina, the nerve fibre layer could also be visualised in real time.

V.1.3.3 In-vivo imaging of nerve fibre layer

The retina is composed of several layers linked to each other by complex synaptic connections. The examination of one of these layers, the NFL, is essential for detecting and managing glaucoma, which is a progressive disease characterized by a thickening of the NFL due to the loss of ganglion cells. The early change of this layer composed of ganglion cell axons is difficult to detect, especially when the background reflection is high since ganglion cells are transparent and reflect more than 60% less light back compared to the reflectivity of the PRL (Miller, 2005) resulted in images of low contrast. Figure 5.6 shows images of this layer taken by the cAO-HRT.

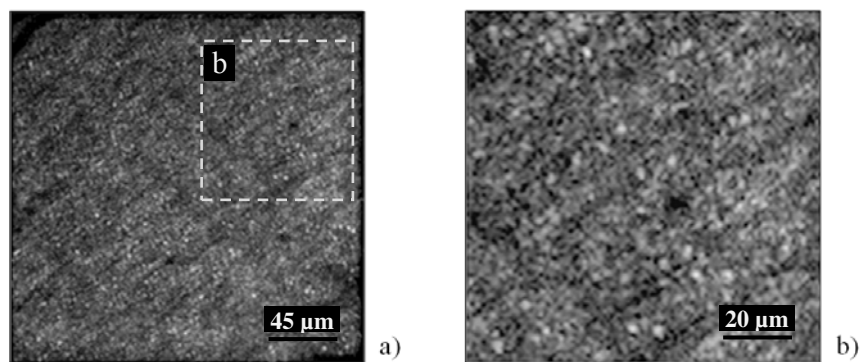


Fig. 5.6 Non-invasive images of the nerve fibre layer of a human volunteer

Images of the nerve fiber layer (OD): (a) AO on registered image, field of $1^\circ \times 1^\circ$; (b) taken from (a), field of $0.5^\circ \times 0.5^\circ$.

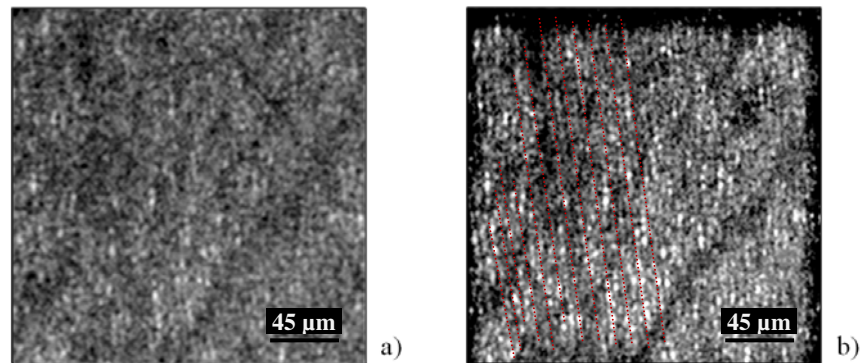


Fig. 5.7 Retinal image at about 4.5° from the centre of the fovea

Image from a location 4.5° (inferior-temporal quadrant) in the centre of the retina (OD). In this image the focal plane is at the surface of the nerve fiber layer (parallel vertical structures, some of them are shown by red dashed lines on the left side of image (b): (a) AO on raw, (b) registered image. The centre-to-centre distance of structures is around $5.6 \mu\text{m}$ (Figure 5.7b).

The images in Figure 5.7 show the individual nerve fibre bundles as they are structured parallel to each other. In clinical OCT study, sufficiently clear images of individual nerve fibre bundles have not yet been achieved for investigation of specific structural abnormalities.

V.2 Morphology of human photoreceptor populations

V.2.1 Mosaic structure of the photoreceptors in the central field

In one individual, a series of images were taken in the central field to compare the structure of the photoreceptor hexagonal mosaic packing and to count their size and density as a function of retinal eccentricity. Figure 5.8 shows images taken at 3.5° of retinal eccentricity, where the average diameter of an individual photoreceptor is estimated as $\sim 3.5\text{-}4.0\ \mu\text{m}$ corresponding to the density of $>70,000/\text{mm}^2$.

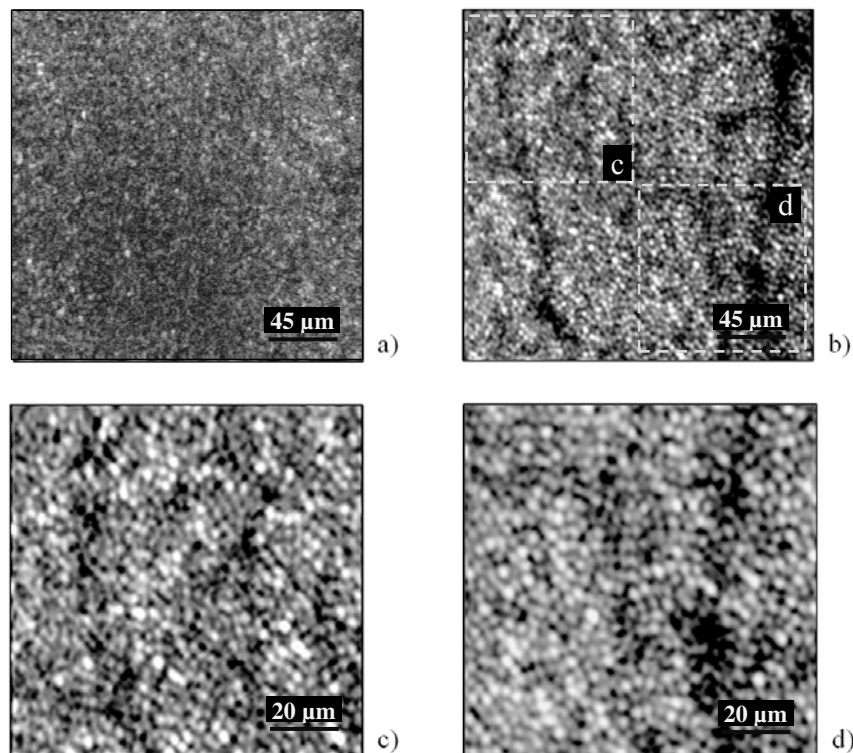


Fig. 5.8 Image of the macula at about 3.5° from the centre of the fovea

Images from the centre of the retina (OD) at about 3.5° (inferior-nasal quadrant) showing: (a) AO off raw image, (b) AO on registered image; (c) and (d) are taken from (b). The diameter of the photoreceptors is around $3.7\ \mu\text{m}$, corresponding to a density of $73,000/\text{mm}^2$. The capillaries ($\sim 6\text{-}7\ \mu\text{m}$ in diameter) appear dark as they are out of focus.

The mosaic formed by the photoreceptors initiates the visual process by converting the image formed by the ocular optics to a discrete array of signals. This structure thus provides all the spatial information of visual processing and imposes some fundamental limitations.

V.2.2 Photoreceptor mosaic regularity

In the central field the density of the photoreceptors reached its maximum, estimated at $>170,000/\text{mm}^2$ (Figure 5.9 - 5.10) and the structure of the mosaic in this field showed a highly regular form.

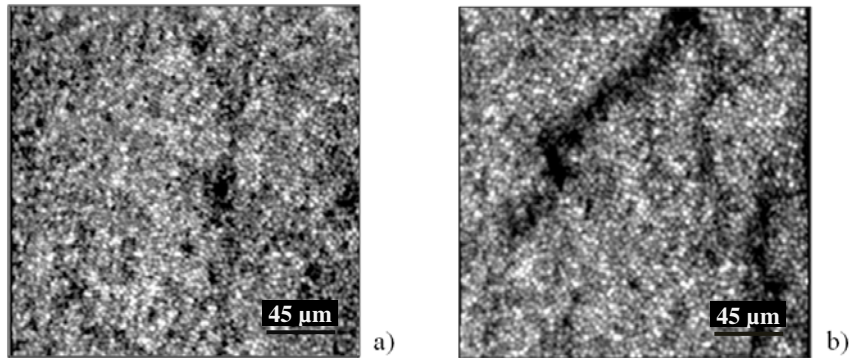


Fig. 5.9 Images of the fovea in the central field

AO image of the centre of the fovea (OD) in the superior-nasal quadrant showing: (a) at about 0.5° and (b) 2.0° field of view. Diameter of the photoreceptors (Fig. 5.9a) is $\sim 2.4 \mu\text{m}$ corresponding to a density of $174,000/\text{mm}^2$.

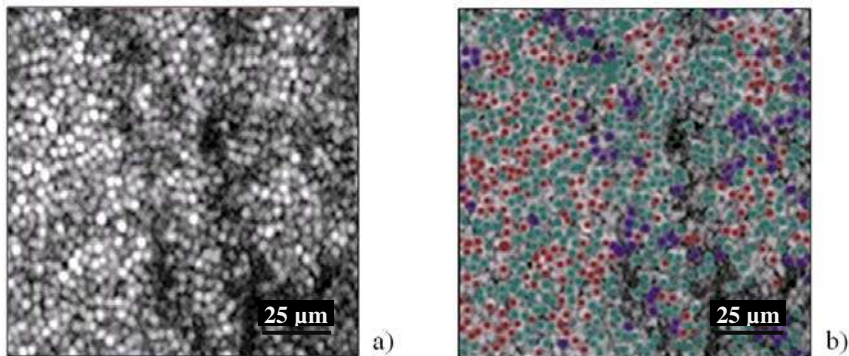


Fig. 5.10 Images of the centre of the retina; gray scale and color coded

Images of the centre of the retina (OD) at around 2° (inferior-nasal quadrant) from the fovea showing: (a) AO on registered gray scale image, (b) color coded image of (a) showing different cell structures.

The density and distribution of the different types of photoreceptors determine the resolving capability of the eye and the spectral sensitivity of the visual process in different lighting conditions. The remaining challenge that high-resolution imaging modalities, including the use of state-of-the-art OCT instruments, can be applied to, is the investigation of the effect of cell death in various retinal diseases and monitoring of effectiveness of retinal stem cell therapy (Baker & Brown, 2009) including migration, differentiation, integration of cells in restoring partial sight to blind people.

V.2.3 Discontinuities in photoreceptor mosaic structure

In one case, the photoreceptor structure showed irregular forms (Figure 5.11) where 10-15 individual photoreceptors bundled together and separated from their surroundings. Similar types of structures have been reported in histological studies (Luthert, 2011), referring to drusen formation underneath the layer of photoreceptors. The early pathologic change (Johnson *et al.*, 2005) becomes detectable at an intermediate stage of progression (Chiu *et al.*, 2012) when secondary change occurs in PE (normal values are $4,200 \pm 727$ cells/mm² in the fovea according to Panda-Jonas *et al.*, 1996) and CNV.

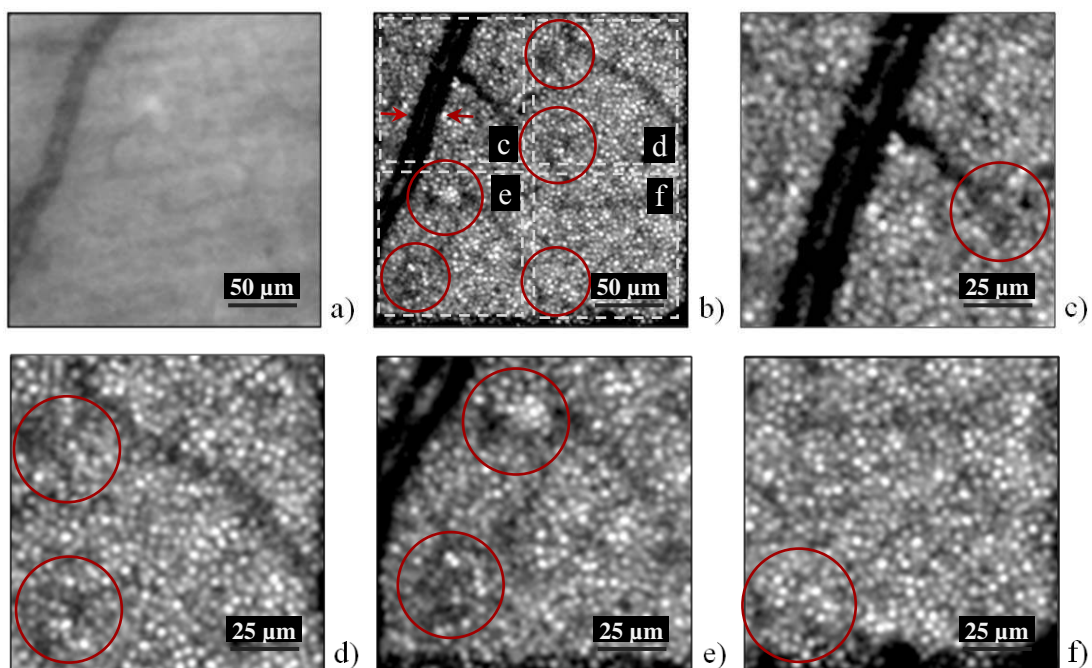


Fig. 5.11 Image of the macula at about 2° from the centre of the fovea

cAO-HRT images (OD) at about 2° in the superior-nasal quadrant: (a) fundus camera image (courtesy of Dr David Lara), (b) AO registered image; (c)-(f) are taken from (b). The diameter of the blood vessel (at red arrows) is ~12 µm and the diameter of the photoreceptors is 3.0 µm corresponding to the density of 111,000/mm² (~20-30 receptors / PE cell); red circles indicate the locations of abnormalities.

Drusen are associated with deflection and shortening of photoreceptor outer segment and cell death (Johnson *et al.*, 2003). Smith *et al.* (1998) reported correlation between macular changes and Stiles-Crawford effect, slower rates of dark adaptation (Eisner *et al.*, 1987) before clinical diagnosis. The presence of a few small drusen is considered to be normal in the peripheral retina (Ding *et al.*, 2009), yet little is known about their role and early development in the central field. According to the author's knowledge, similar morphological change of photoreceptor populations such as in Figure 5.11 has not yet been investigated *in vivo* at this level of resolution.

V.2.4 Comparison of cAO-HRT imaging results with histological data

In one individual, a series of images were taken in the central field at 1-5° of eccentricity and were analysed and compared to previously published histological data (Curcio *et al.*, 1987; Jonas, 1992; Oyster, 1999). The density and distribution of photoreceptors are known from only a few histological studies and these show large variability between individuals, depending on also the age of the donor sample and the size of the counting field (Figure 5.12).

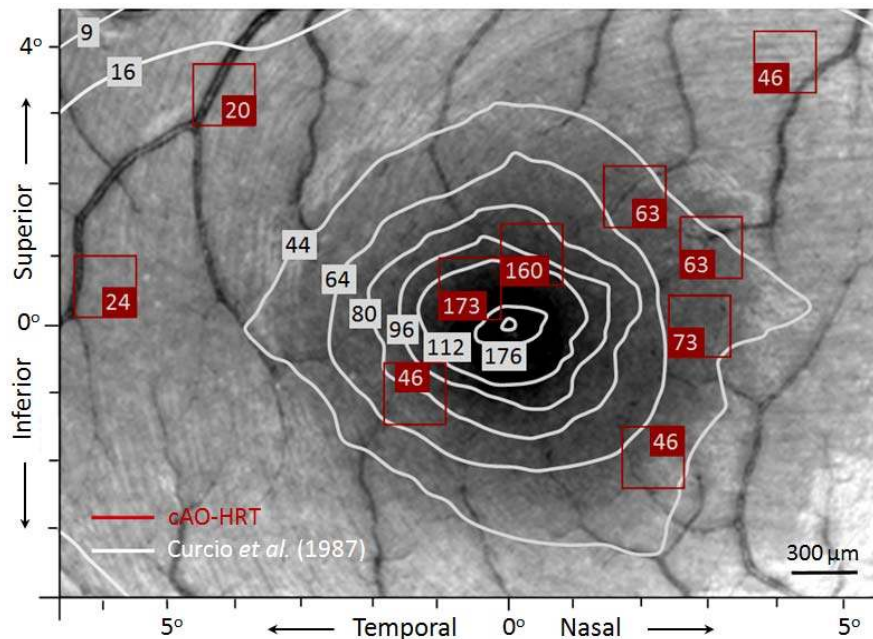


Fig. 5.12 Cone density map in comparison to histological study

Figure showing the distribution of cone photoreceptors (in units of $\times 1,000/\text{mm}^2$) adapted after Curcio *et al.*'s histological data (1987) in white circles; the data in red is manually counted from the *in vivo* images (OD of a 34-year-old healthy male volunteer) taken by the cAO-HRT. The main image (courtesy of Dr David Lara, annotation by the author, 2011) was obtained with Zeiss FF450^{plus} fundus camera.

Higher densities were reported in the nasal and superior retinal quadrants (Osterberg, 1935; Curcio *et al.*, 1987) and the cone distribution is radially asymmetrical about the central retinal field. The photoreceptor distribution (Figure 5.13) varies significantly with retinal eccentricity (Curcio *et al.*, 1987 and 1990): the peak photoreceptor densities showed less variability in the centre of the fovea, and the cone density may increase slightly in the nasal retina (right-hand side of the figure), which is confirmed by this high-resolution retinal imaging study. The diameters of the photoreceptors were estimated as shown in Figure 5.13.

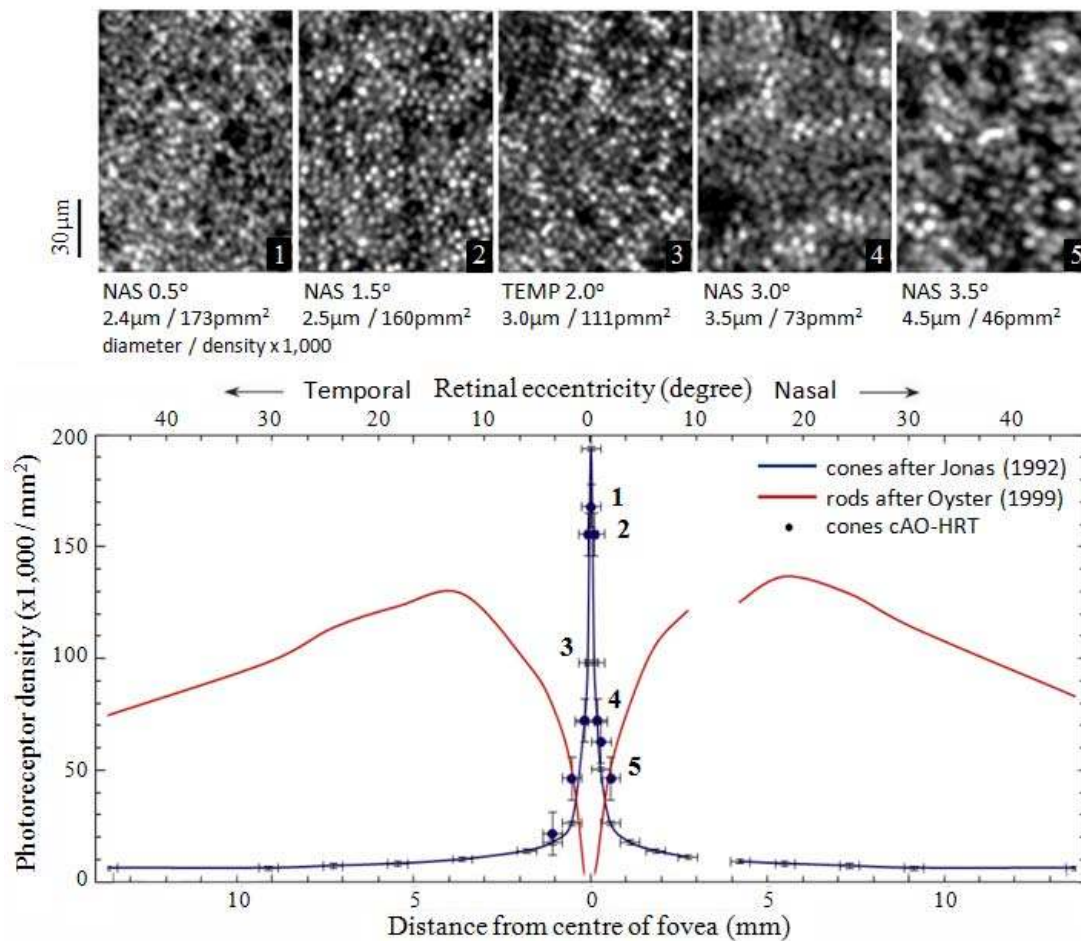


Fig. 5.13 Photoreceptor densities in comparison to histological data

Figure shows cAO-HRT images at 0.5-3.5° of retinal eccentricities (OD) of a 35 year-old male subject (using 1 drop of tropicamide 1%): the images were analysed via counting of photoreceptors, the numerical values (photoreceptor diameters and corresponding densities) are the results of manual counting. The smallest photoreceptor was $\sim 2.4 \mu\text{m}$ in diameter, corresponding to a peak density of $173,000/\text{mm}^2$; this location was found at 0.5° field of view (nasal) in the centre of fovea (image no. 1). The numbers (1-5) on the blue curve of cone density refer to the numbers of the high-resolution images taken by the cAO-HRT (attached above the graph).

The highest density $173,000/\text{mm}^2$ was measured at $\sim 0.5^\circ$ of eccentricity compared to the histological finding of $>170,000/\text{mm}^2$ in the same location of the retina. The smallest photoreceptor, the cAO-HRT was able to resolve, is estimated to be $\sim 2.4 \mu\text{m}$ in diameter, which corresponds to roughly the diffraction limited performance of the imaging system.

V.3 Limits of the current configuration

Discussion

In the last two chapters of this thesis, design considerations of a compact and low cost AO system, optimization methods and control have been investigated, followed by experimental results and implications for non-invasive retinal imaging supported by adaptive optics.

The first trials for in-vivo imaging in the eye with the compact system were successful and cellular structures were investigated in more detail, including the dynamic behaviour of the retina. Finer details of the cell structures were successfully resolved: the retinal image quality was equally good in both cases when the ocular aberrations were dynamically corrected, and when only the non-common path errors were removed. The reasons for comparable image quality could be the limited stroke of the membrane deformable mirror and the insufficient ciliary muscle paralysation using tropicamide 1%.

The characteristics of the membrane mirrors are discussed by (Paterson *et al.*, 2000) in detail and a comparative analysis of the deformable mirrors for medical applications is given in (Dalmier & Dainty, 2005). According to this paper, the best suited AO device is the AOptix bimorph mirror for ocular adaptive optics and the 37-actuator OKO deformable mirror has showed limited correction. It has been demonstrated by the authors that a larger stroke is necessary. However, the relatively low cost of optical systems using these mirrors with sufficient spatial correction is feasible for ophthalmic applications (Paterson *et al.*, 2000). Beside the higher cost, a further disadvantage of the use of a higher-stroke deformable mirror, would be its much heavier weight on the device since in the current construction, the stepper motor carries the whole optical block, including the external adaptive optics unit and the wavefront sensing optical bench. Furthermore, while the main advantage of the system is its compactness from a practical point of view for clinical trials, during the developmental work it has proved to be difficult to modify, and most parts of the system are not accessible during operation.

A further limitation of the system is the method used to measure the system aberrations. The Shack-Hartmann wavefront sensing technique has proven a useful technique; however, it has also limitations. If the system introduces large aberrations, this can result

in large displacements of the focal spots on the detector. In some cases, it can produce overlapping of spots, making the wavefront estimation impossible. Another problem is that if the displacement is smaller than the accuracy of the centroiding algorithm, scattering can cause false results in the wavefront sensor measurements; therefore the compensation of the aberrations may not be correct.

Beside the analysis of the code architecture and optimization of the system one may consider the effectiveness of the running and calculation time (cost efficiency) of the algorithms used (Sommerville, 2000) in the future development. When the AO loop is off, the system is able to produce images at around 20-30 fps. However, during real-time correction when the loop is closed, this value is only 8-15 fps, which is low compared with the time scale of ocular dynamics.

The cAO-HRT optimization algorithms are implemented in the Python programming language. Python (Lutz, 2010) is an interpreted high-level programming language which supports object oriented (OO) development and implementation. It is important to know how many correction steps can be calculated in a single time and how much time needed to run the control algorithms; these determine the performance of the imaging system and its capability to compensate for the dynamic ocular aberrations. For this reason, the running time of the algorithms has to be considered. One possibility is the analysis of efficiency and choice of language that the algorithms are created in i.e. with the same implementation of the algorithms in other programming languages. For this comparison Java (Knudsen & Niemeyer, 2009; Cadenhead & Lemay, 2007) was chosen as a "low-level" programming language; the processor of the computer being tested and used in system control was an Intel(R) Xeon(TM) CPU running at 2.40 GHz.

The Java implementations are compiled to byte code (class file) that runs on a Java Virtual Machine. This virtual machine can be run on various operating system architectures, usually Windows or Unix. The cAO-HRT control and image processing require array operations (initialization-, copy operations). In the optimization of the algorithms, efficient sorting is essential and the copy operation was timed in a series of tests using bubble sorting algorithm (Chang, 2003; Ullenboom, 2010).

The worst-case performance of the sorting algorithm is $O(n^2)$. For the time measurement of the initialization and copy-operations in different languages, programs were written in

Java (Appendix B) and Python (Appendix C). These results show (Table 5.2) that the array initialization is progressively more time consuming in Python as the array size increases and the bubble sorting algorithm shows significantly better performance in its Java implementation.

Table 5.2 Running times of algorithms

Array initialization in Python (running time in ms)								Bubble sort in Python (running time in ms)			
Array size	4096	16384	65536	262144	1048576	4194304	1.7E+07	Elements	64	128	256
Integer	0	0	0	24	38	78	531	Integer	148	3336	65888
Flow	0	0	2	22	33	81	537	Flow	177	5416	88102
Long	0	1	1	26	322	412	1037	Long	176	5742	93038

Array initialization in Java (running time in ms)								Bubble sort in Java (running time in ms)			
Array size	4096	16384	65536	262144	1048576	4194304	1.7E+07	Elements	64	128	256
Integer	0	0	0.02	0.11	0.44	1.74	7.04	Integer	28	458	6742
Flow	0.01	0.01	0.04	0.12	0.5	1.98	7.98	Flow	27	449	8898
Long	0	0.01	0.04	0.17	0.66	2.64	10.69	Long	28	455	6901

The cAO-HRT development and trials were carried out in ‘real’ laboratory conditions, similarly to a clinical environment; the tests were performed in a non-air conditioned laboratory and the ophthalmoscope was placed on a standard non-isolated table. This research did not consider the temperature tolerance of the AO system, approximately 10 degree Celsius of temperature variation was noticed between daytime and at night, but according to the literature (Porter *et al.*, 2006) only a few degrees Celsius of temperature change can cause misalignment of optical systems and instability in their operation.

Based on these results (Table 5.2), optimisation of the calculation time and further tests in different programming languages are required. Languages more closely related to the underlying hardware of the computer, such as C or C++ may be necessary to the optimization of the cAO-HRT control to reduce the running times and make the control algorithms faster.

Chapter VI

Progress for non-invasive cellular imaging

VI. Progress for non-invasive cellular imaging

Summary and conclusion

Ophthalmic imaging has become a major clinical tool in routine diagnosis of ocular diseases; however, it presents particular challenges (Roorda & Williams, 1997; Kaufman & Alm, 2003; Podoleanu & Rosen, 2008). Evolution has created sophisticated adaptive optical components out of biological materials in the eye for self-protective purposes against external injuries, including high exposures, and shaped the ocular optics into an appropriate complex image forming system by optimizing their properties. Aside from the human eye providing our first primary sense, it also allows the *in vivo* study of the nervous system (Doble, 2005).

The human eye is a sophisticated detector, sampling an image with about 5 million cone and 100 million rod photoreceptors. Each photoreceptor acts as a waveguide with different spectral properties, funnelling the light into a narrow tube which makes them easier to visualize with high-resolution ophthalmic imaging systems (Carroll *et al.*, 2005). The eye offers a small entrance and exit aperture through the pupil, which can vary in size between 2-8 mm in diameter depending on the background illumination (Kaufman & Alm, 2003; Sharp *et al.*, 2004). The fundus reflectance in the direction of the exit pupil is dependent on wavelength, and in the range from 400 nm to 700 nm this varies from 0.1% to 10% (Delori & Pflibsen, 1989). The main difficulty of *in vivo* observation is that the eye undergoes rapid saccadic movements (about 6 per second), which requires any imaging technique to have short exposure times.

Laser scanning ophthalmoscopes (Webb *et al.*, 1987; Sharp & Manivannan, 1997, US Patent 5892569 - Van de Velde, 1998; Hammer *et al.*, 2003; van de Velde, 2006; Hunter *et al.*, 2007; US Patent 7794081 – Fujishiro & Akita, 2008) offer a number of solutions to achieve high-resolution retinal imaging. Image acquisition times are typically a few tens of milliseconds, so to minimise degradation from saccadic movement. Recently some hybrid applications of ophthalmoscopes and adaptive optics technology (US Patent 20080218694 – Chen, Olivier and Jones, 2008) including wavefront sensing methods (US Patent 11/200457 – Feierabend, Ruckel and Denk, 2005) have been used in order to improve the resolution of ophthalmic imaging techniques (Roorda *et al.*, 2002; Grieve *et al.*, 2006; Vogel *et al.*, 2005; Hammer *et al.*, 2006).

Recent developments in ophthalmic imaging supported by new technologies provide new means for the real-time study of the finer cell structures in the eye. These developments will help to resolve some fundamental questions about the healthy retina and will provide a new tool for the early diagnosis of retinal diseases (& Williams, 1997; Carroll *et al.*, 2005) and an effective tool for the monitoring of treatments. Many retinal diseases are characterized by the degradation of the photosensitive receptors, so the main challenge in research and development in the field of retinal imaging has been the visualization of these cells in recent years. Several groups have demonstrated techniques and imaging systems for visualizing the cone photoreceptors; the first systems were introduced by for example Liang *et al.* (1997), Roorda & Campbell (1997), Roorda & Williams (1999) and Roorda *et al.* (2002).

The *in vivo* ophthalmic diagnostic instruments image living tissues through intervening aberrated optical components which degrade the image quality and reduce the ability to visualize the finer structures. The ocular media suffers from higher order aberrations, induced mainly by the crystalline lens and the cornea, limiting the spatial vision and degrading the retinal image quality. There are several research institutes and consortia, including the Centre for Adaptive optics (CfAO) in the US and the Sharp Eye and the Smart Optics Faraday Partnership in Europe that have the goal of developing improved adaptive optics systems for ophthalmic applications; however, most of the high-resolution adaptive imaging systems produced to date are large, and confined to research laboratory conditions.

The aim of this research was the investigation of the performance of a compact and low cost adaptive optics ophthalmoscope suitable for future clinical trials and the visualization of retinal cell structures. The ability of the cAO-HRT has been investigated to correct for static aberrations and non-common path errors using image sharpness metric optimization and showed that a true reference can be provided for adaptive optics closed loop operations. The thesis has discussed the performance of the first compact Heidelberg Retina Tomograph supported by adaptive optics according to the author's knowledge for correcting the ocular aberrations. The imaging system has been tested on limited numbers of human subjects and the investigations have also highlighted some weakness of the instrument, which requires further tests to fully characterize. In conclusion, the preliminary results show that the AO ophthalmoscope is able to resolve cell structures about 2.5 μm in diameter (this corresponds to roughly the diffraction limited performance

of the cAO-HRT); the potential of the high-resolution imaging device (Figure 6.1) was verified in Chapter V of this thesis.

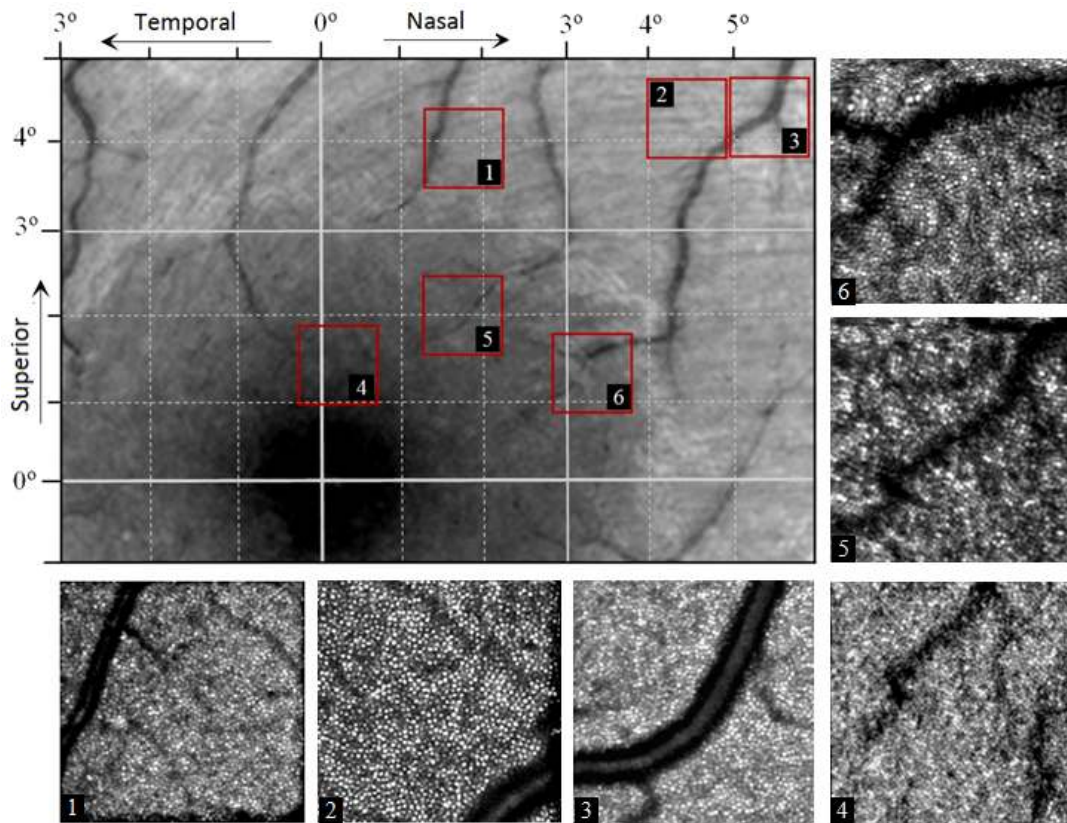


Fig. 6.1 Comparison of retinal images taken by a fundus camera and cAO-HRT

Image of the central field of the retina (OD) obtained with Zeiss FF450^{plus} fundus camera (upper left) showing the field $9^\circ \times 6^\circ$ of view (equivalent to ~ 2.7 mm by 1.8 mm); the grid scale ($1^\circ \times 1^\circ$ equivalent to a unit of a red square) is around $300 \mu\text{m} \times 300 \mu\text{m}$ (annotation by the author, 2011). The central, approximately $3.5^\circ \times 3.5^\circ$ part (dark gray circle) is the fovea; the smaller $1.5^\circ \times 1.5^\circ$ black circle (bottom of the main image) in its centre is the foveola. The smaller images, around the main image, are registered high-resolution images taken by the cAO-HRT corresponding to the image parts in red squares (field of $1^\circ \times 1^\circ$) in the main image (numbered from 1 to 6).

The first generation of high-resolution imaging instruments with adaptive optics, including the cAO-HRT, has achieved success in a number of developments in ophthalmology (Dreher, Bille & Weinreb, 1989; Liang, Williams & Miller, 1997; Roorda *et al.*, 2002; Hermann *et al.*, 2004; Zawadzki *et al.*, 2005; Zhang *et al.*, 2006; Burns *et al.*, 2007; Bigelow *et al.*, 2007): AO has been integrated into flood illumination retinal cameras, confocal SLOs and OCT instruments for high-resolution reflectance imaging of the retina. An AO system with a closed loop bandwidth of 1-2 Hz is able to correct for ocular aberrations (Hofer *et al.*, 2001a) providing a valuable diagnostic modality for early diagnosis of retinal diseases. The recent developments of imaging systems in ophthalmology, a newer generation of advanced ophthalmic instruments with high-

resolution capabilities with adaptive optics has dramatically revolutionized the future prospective for retinal imaging in evaluating retinal abnormalities (Tojo *et al.*, 2013; Lombardo *et al.*, 2012a-c; Sahin *et al.*, 2012; Viard *et al.*, 2011; Godara *et al.*, 2010a-b and 2012; Rosolen *et al.*, 2010; Zacharria, 2008). Most of the imaging systems are research laboratory based instruments, but the first compact and portable systems in line scanning ophthalmoscopy (Mujat *et al.*, 2009) and OCT instruments (Bigelow *et al.*, 2007) have been introduced. According to the author's knowledge, the cAO-HRT is the first compact system (Kepiro, Kennedy & Paterson, 2008) as presented in this thesis in scanning laser ophthalmoscopy with adaptive optics (Kepiro & Paterson, 2013a-c).

It has been demonstrated that with this compact system the *in vivo* study of the photoreceptors and the dynamic behaviour of the retina is possible; retinal blood flow measurements of individual cells such as leukocytes have been successfully made without using fluorescence dye. The pilot studies from the compact adaptive optics scanning laser ophthalmoscope using a membrane deformable mirror for correcting the aberrations showed great promise for the use of a new generation of imaging instruments in early diagnosis of retinal diseases.

Ophthalmic devices that have produced high-resolution images so far have included systems based on biomorph mirrors, membrane mirrors, liquid-crystal spatial light modulators and microelectromechanical mirror systems (Carroll *et al.*, 2005). For widespread adoption of this technology in ophthalmic applications (Godara *et al.*, 2010a-b; Michaelides *et al.*, 2011; Dubra *et al.*, 2011; Godara *et al.*, 2012 ; Carroll *et al.*, 2012; Yanni *et al.*, 2012), the cost of the adaptive optics devices have to be reduced for general clinical applications, particularly in terms of the cost of the corrective elements. In the next few years, alternate corrective adaptive optics elements and advances in wavefront sensing will play an important role in development of a new generation of retinal imaging instruments.

The remaining research challenges in retinal imaging are primarily: image stabilization methods to remove artifacts due to eye movements, image post processing to improve the image quality and visualization of other retinal cell types in deeper layers, for example PE or choroidal layers. Future developments that provide sub-micrometer imaging of cells using nanoscopy in examining the prevention of cell death, precise focusing for individual cells in laser therapy and cellular level examination of stem cell transplants are expected to lead to breakthroughs in clinical research.

Bibliography

1. AAO, *Fundamentals and principles of ophthalmology* Eds. GW Cibis, RE Anderson, WY Chew *et al.*, American Academy of Ophthalmology (1996)
2. C Albarrán, AM Pons, A Lorente, R Montés and JM Artigas, *Influence of the tear film on optical quality of the eye*, Contact Lens and Anterior Eye **20**(4), 129-135 (1997)
3. PV Alguere, PAL Torstensson and BM Tengroth, *Light transmittance of ocular media in living rabbit eyes*. Inv. Opht. Vis. Sci. **34**, 349-354 (1993)
4. JL Alio, P Schimchak, HP Negri and R Montés-Micó, *Crystalline lens optical dysfunction through aging*. Ophthalmology **112**(11), 2022-2029 (2005)
5. D Alonso-Caneiro, DR Iskander and MJ Collins, *Assessment of tear film surface quality using dynamic-area high-speed videokeratoscopy*. IEEE Transaction on Biomedical Engineering **56**(5), 1473-1482 (2009)
6. WLM Alward, *Medical management of glaucoma*. Published in Drug Therapy, edited by AJJ Wood, New Engl. J. Med. **339**(18), 1298-1307 (1998)
7. J Ares, T Manceb and S Bará, *Position and displacement sensing with Shack-Hartmann wavefront-sensors*. Appl. Opt. **39** (10), 1511-1520 (2000)
8. J Arines & J Ares, *Minimum variance centroid thresholding*. Opt. Lett. **27** (7), 497 (2002)
9. P Artal, M Ferro, I Miranda, R Navarro, *Effects of aging in retinal image quality*. J. Soc. Am. A **10**, 1656-1662 (1993)
10. P Artal & R Navarro, *Monochromatic modulation transfer function of the eye for different pupil diameters: an analytical expression*. J. Opt. Soc. Am A **11**, 246-249 (1994)
11. P Artal, A Guirao, E Berrio and DR Williams, *Compensation of corneal aberrations by the internal optics in the human eye*. J. Vision **1**, 1-8 (2001)
12. P Artal, EJ Fernandez, S Manzanera, *Are optical aberration during accommodation a significant problem for refractive surgery?* J. Refract. Surg. **18**, S563-566 (2002)
13. P Artal, JM Bueno, A Guirao and PM Prieto, *Aberration structure of the human eye*. Published in “Adaptive optics for vision science”, edited by J Porter, H Queener, J Lin, K Thorn and A Awwal. John Wiley & Sons (2006)
14. DA Atchison & G Smith, *Optics of the human eye*. Butterworth-Heinemann, imprint of Elsevier (2002)
15. HW Babcock, *The possibility of compensating astronomical seeing*, Publ. Astr. Soc. Pac. **65**, 229-236 (1953)
16. KL Baker and MM Moallem, *Iteratively weighted centroiding for Shack- Hartmann wave-front sensors*, Opt. Exp. **15**, 5147-5159 (2007)

17. PS Baker & GC Brown, *Stem-cell therapy in retinal disease*. Curr. Opin. Ophthalmol. **20**, 175-181 (2009)
18. EF Bakke, J Hisdal and SO Semb, *Intraocular pressure increases in parallel with systematic blood pressure during isometric exercise*. Invest. Ophthalmol. Vis. Sci. **50**(2), 760-764 (2009)
19. J Bao-Guang, C Zhao-Liang, M Quan-Quan, H Li-Fa, L Chao and X Li, *Simulated human eye retina adaptive optics system based on a liquid crystal on silicon device*. Chinese Physics B **17**(12), 4529-4532 (2008)
20. RC Baraas, J Carroll *et al.*, *Adaptive optics retinal imaging reveals S-cone dystrophy in tritan color-deficiency*. J. Opt. Soc. Am. A **24**(5), 1438-1447 (2007)
21. JD Bartlett & SD Jaanus, *Clinical ocular pharmacology*. Elsevier (2008)
22. S Bassnett, Y Shi, GFJM Vrensen, *Biological glass: structural determinants of eye transparency*. Phil. Trans. R. Soc. **366**(1568), 1250-1264 (2011)
23. BJ Bauman, *Optical design for extremely large telescope adaptive optics systems*. PhD thesis, University of Arizona (2003)
24. BJ Bauman & SK Eisenbies, *Adaptive optics system assembly and integration*. In: Adaptive optics for vision science (Ch. 7), eds. by Porter *et al.* (2006)
25. AG Bennett & RB Rabbetts, *Clinical visual optics* (Ed. 4th). Butterworth-Heinemann, imprint of Elsevier (2007)
26. K Bessho, DUG Bartsch, L Gomez, L Cheng *et al.*, *Ocular wavefront aberrations in patient with macular diseases*. Retina **29**(9), 1356-1363 (2009)
27. CE Bigelow, NC Iftimia, RD Ferguson, TE Ustun, B Bloom, DX Hammer, *Compact multimodal adaptive optics spectral domain optical coherence tomography instrument for retinal imaging*. J. Opt. Soc. Am A **24**, 1327-1336 (2007)
28. H Bloemendal & WW de Jong, *Lens proteins and their genes*. Prog. Nucleic Acid Res. Mol. Biol. **41**, 259-81 (1991)
29. EA Boettner & JR Wolter, *Transmission of the ocular media*. Invest. Ophthalmol. Vis. Sci. **1**(6), 776-783 (1962)
30. SJ Bogan, GO Waring, O Ibrahim, C Drews and L Curtis, *Classification of normal corneal topography based on computer-assisted videokeratography*. Arch. Opht. **108**, 945-949 (1990)
31. M Booth, T Wilson, HB Sun, T Ota, S Kawata, *Methods for the characterization of deformable membrane mirrors*. Appl. Opt. **44**(24), 5131-5139 (2005)
32. P Borgdorff, *Respiratory fluctuations in pupil size*. Am. J. Physiol. **228**(4), 1094-1102 (1975)
33. M Born & E Wolf, *Principles of optics – Electromagnetic theory of propagation, interference and diffraction of light*. 7th Ed. Cambridge University Press (2003)

34. A Bradley & LN Thibos, *Modeling off-axis vision - I, The optical effects of decentering visual targets or the eye's entrance pupil.* p.313-337 in: E Peli (Ed.), *Vision Models for Target Detection and Resolution*, Singapore: WSP (1995)
35. NM Bressler, SB Bressler, JM Seddon, ES Gragoudas, LP Jacobsen, *Drusen characteristics in patient with exudative versus nonexudative age-related macular degeneration.* *Retina* **8**(2), 109-114 (1988)
36. M Brezinski, *Optical coherence tomography - Principles and applications.* Elsevier Academic Press (2006)
37. A Bruil, WG van Aken, T Beugeling, J Feijen, I Stenker, JG Guisman, HK Prins, *Asymmetric membrane filters for the removal of leukocytes from blood.* *J. Biomed. Mat. Res.* **25**, 1459-1480 (1991)
38. BS-60825-8: 2006: *Safety of laser products. Guidelines for the safe use of laser beams on humans.* PD IEC/TR 60825-8:2006 (2007)
39. BS-60825-13:2006: *Safety of laser products. Measurements for classification of laser products.* (2006)
40. SA Burns, S Wu, FC Delori and AE Elsner, *Direct measurement of human cone photoreceptor alignment.* *J. Opt. Soc. Am. A* **12**(10), 2329-2338 (1995)
41. SA Burns, S Wu, J He, AE Elsner, *Variations in photoreceptor directionality across the central retina.* *J. Opt. Soc. Am. A* **14**, 2033-2040 (1997)
42. SA Burns, R Tumbar, AE Elsner, RD Ferguson and DX Hammer, *Large field of view modular stabilized, adaptive-optics-based scanning laser ophthalmoscope.* *J. Opt. Soc. Am. A* **24**, 1313-1326 (2007)
43. R Cadenhead & L Lemay, *Sams teach yourself Java 6 in 21 days.* Sams (2007)
44. G Calcagnini, S Lino, F Censi and S Cerutti, *Cardiovascular autonomic rhythms in spontaneous pupil fluctuations.* *Comp. Cardiology* p.133-136 (1997)
45. FW Campbell and RW Gubisch, *Optical quality of the human eye.* *J. Physiol.* **186**, 558-578 (1966)
46. CR Canning, MJ Greaney, JN Dewynne and AD Fitt, *Fluid flow in the anterior chamber of a human eye.* *Math. Med. Biol.* **19**(1), 31-60 (2002)
47. J Caprioli, *The ciliary epithelia and aqueous humor.* In WM Hart (ed): *Adler's Physiology of the Eye: Clinical Application*, Mosby (1992)
48. J Carroll, M Neitz, H Hofer and DR Williams, *Functional photoreceptor loss revealed with adaptive optics: an alternate cause of color blindness.* *Proc. Natl. Acad. Sci.* **101**(22), 8461-8466 (2004)
49. J Carroll, DC Gray, A Roorda and DR Williams, *Recent advances in retinal imaging with adaptive optics.* *Opt. Phot. News* (2005)

50. J Carroll, A Dubra, JC Gardner, L Mizrahi-Meissonnier, RF Cooper, AM Dubis, R Nordgren, M Genead, TB Connor, KE Stepien, D Sharon, DM Hunt, E Banin, AJ Hardcastle, AT Moore, DR Williams, G Fishman, J Neitz, M Neitz, M Michaelides, *The effect of cone opsin mutation on retinal structure and the integrity of the photoreceptor mosaic*. Invest. Ophthalmol. Vis. Sci. **53**(13), 8006-8015 (2012)
51. HD Cavanagh (ed.), *The cornea - Transactions of the World Congress on the Cornea III*. Raven Press, New York (1988)
52. SR Chamot & C Dainty, *Adaptive optics for ophthalmic applications using a pyramid wavefront sensor*. Opt. Exp. **14** (2) 518-526 (2006)
53. SK Chang, *Data structures and algorithms* (Series on Software Engineering and Knowledge Engineering). World Scientific Publishing (2003)
54. WN Charman & G Heron, *Fluctuations in accommodation: a review*. Ophthalmol. Physiol. Opt. **8**, 153-163 (1988)
55. WN Charman, *Optics of the eye*. In: Handbook of Optics (by M Bass, C Decusatis, JM Enoch *et al.*) - Vision, part 7, McGraw-Hill Professional (2000)
56. DC Chen, SS Olivier, SM Jones, *High-resolution adaptive optics scanning laser ophthalmoscope with multiple deformable mirrors - US Patent 20080218694* (2008)
57. H Chen, B Liu, TJ Lukas and AH Neufeld, *The aged retinal pigment epithelium/choroid: a potential substratum for the pathogenesis of age-related macular degeneration*. PLoS ONE **3**, e2339 (2008)
58. SJ Chiu, JA Izatt, RV O'Connell, KP Winter, CA Toth, S Farsiu, *Validated automatic segmentation of AMD pathology including drusen and geographic atrophy in SD-OCT images*. Invest. Ophthalmol. Vis. Sci. **53**(1), 53-62 (2012)
59. SS Choi, N Doble, JL Hardy *et al.*, *In vivo imaging of the photoreceptor mosaic in retinal dystrophies and correlation with visual function*. Invest. Ophthalmol. Vis. Sci. **47**(5), 2080-2092 (2006)
60. SS Choi, RJ Zawadzki, MC Lim, JD Brandt, JL Keltner, N Noble and JS Werner, *Evidence of outer retinal changes in glaucoma patients as revealed by ultrahigh-resolution in vivo retinal imaging*. Br. J. Ophthalmol. **95**(1), 131-141 (2011)
61. H Choo and RS Muller, *Addressable microlens array to improve dynamic range of Shack-Hartmann sensors Solid-State Sensor. Actuator and Microsystems Workshop 79* (2004)
62. RJ Clarke, H Zhang and PDR Gamlin, *Characteristics of pupillary light reflex in the alert rhesus monkey*. J. Neurophysiol. **89**, 3170-3189 (2003)
63. Clinician's Ultimate Reference (CUR). Accessed (March, 2012) at: http://www.globalrph.com/ophthalmic_mydratics.htm
64. CJ Cogswell & KG Larkin, *The specimen illumination path and its effect on image quality*. In: Handbook of biological confocal microscopy, ed. by JB Pawley (ed.) Plenum Press, New York (1995)

65. HR Coleman, CC Chan, FL Ferris III, EY Chew, *Age-related macular degeneration*. Lancet. **372**, 1835–1845 (2008)
66. G Collins, *The electronic refractometer*. Br. J. Physiol. Opt. **1**, 30-40 (1937)
67. M Collins, B Davis and J Wood, *Microfluctuations of steady-state accommodation and the cardiopulmonary system*. Vision Res. **35**, 2491-2502 (1995)
68. N Congdon, B O’Colmain *et al.*, *Causes and prevalence of visual impairment among adults in the United States*. Arch Ophthalmol. **122**, 477-485 (2004)
69. JE Coppens, L Franssen, TJTP van den Berg, *Wavelength dependence of intraocular straylight*. Exp. Eye Res. **82**(4), 688-692 (2006)
70. MJ Costello, S Johnsen, S Metlapally, K Gilliland, *et al.*, *Ultrastructural analysis of damage to nuclear fibre cell membranes in advanced age-related cataract from India*. Exp. Eye Res. **87**, 147-158 (2008)
71. CA Curcio, KR Sloan, O Packer, AE Hendrickson, RE Kalina, *Distribution of cones in human and monkey retina: individual variability and radial asymmetry*. Science **236**, 579-582 (1987)
72. CA Curcio, KR Sloan, RE Kalina, AE Hendrickson, *Human photoreceptor topography*. J. Comp. Neurol. **292**, 497-523 (1990)
73. CA Curcio, AA Kimberly, KR Sloan, CL Lerea, JB Hurley, IB Klkock, AH Milam, *Distribution and morphology of human cone photoreceptors stained with anti-blue opsin*. J. Comp. Neurol. **312**, 610-624 (1991)
74. E Dalmier & C Dainty, *Comparative analysis of deformable mirrors for ocular optics*. Opt. Exp. **13**(11), 4275-4285 (2005)
75. KM Daum & GA Fry, *Pupillary micro movements apparently related to pulse frequency*. Vision Res. **22**, 173-177 (1982)
76. PTWM de Jong, *Mechanisms of disease: Age related macular degeneration* (Review article). N. Engl. J. Med. **355**(14), 1474-1485 (2006)
77. PW de Waard, JK IJspert, TJ van den Berg and PT de Jong, *Intraocular light scattering in age-related cataract*. Invest. Opht. Vis. Sci. **33**(3), 618-625 (1992)
78. FC Delori & and KP Pflibsen, *Spectral reflectance of the human ocular fundus*. Appl. Opt. **28**,1061-1077 (1989)
79. FC Delori, ES Gragoudas, R Francisco, RC Pruett, *Monochromatic ophthalmoscopy and fundus photography: the normal fundus*. Arch. Ophthalmol. **95**, 861-868 (1977)
80. L Diaz-Santana & JC Dainty, *Effect of retinal scattering in the ocular double-pass process*. J. Opt. Soc. Am. A **18**(17), 1437-1444 (2001)
81. KB Digre & JJ Corbett, *Practical viewing of the optic disc*. Elsevier (2003)
82. X Ding, M Patel and CC Chan, *Molecular pathology of age-related macular degeneration*. Prog. Retina Eye Res. **28**(1), 1-18 (2009)
83. N Doble, *Image sharpening metrics and search strategies for indirect adaptive optics*. PhD thesis, University of Durham (2000)

84. N Doble, *High-resolution, in-vivo retinal imaging using adaptive optics and its future role in ophthalmology*. *Expert. Rev. Med. Devices* **2**(2), 205-216 (2005)
85. N Doble, D Miller, H Zhao, G Yoon, DW Williams, *Deformable mirror requirements for adaptive correction of the population of normal eyes*. *Invest. Ophthalmol. Vis. Sci.* **44**, E-Abs. 999 (2003)
86. N Doble, G Yoon, L Chen *et al.*, *Use of micromechanical mirror for adaptive optics in the human eye*. *Opt. Lett.* **27**, 1537-1539 (2002)
87. WJ Donnelly III & A Roorda, *Optimal pupil size in the human eye for axial resolution*. *J. Opt. Soc. Am. A* **20**(11), 2010-2-15 (2003)
88. J Douth, AJ Quantock, VA Smith and KM Meek, *Light transmission in the human cornea as a function of position across the ocular surface: Theoretical and experimental aspects*. *Biophys. Journal* **95**(11), 5092-5099 (2008)
89. AW Dreher, JF Bille, RN Weinreb, *Active optical depth resolution improvement of the laser tomographic scanner*. *Appl. Opt.* **28**, 804-808 (1989)
90. W Drexler, U Morgner, FX Cartner *et al.*, *In vivo ultrahigh-resolution optical coherence tomography*. *Opt. Lett.* **24**(17), 1221-1223 (1999)
91. M Dubbelman & van der Heijde, *The shape of the aging human lens: curvature, equivalent refractive index and the lens paradox*. *Vision Res.* **41**(14), 1867-1877 (2001)
92. M Dubbelman, van der Heijde, HA Weeber and GF Vrensen, *Changes in the internal structure of the human crystalline lens with age and accommodation*. *Vision Res.* **43**(22), 2362-2375 (2003)
93. A Dubra, C Paterson and C Dainty, *Study of tear topography dynamics using lateral shearing interferometer*. *Opt. Exp.* **12**(25), 6278-6288 (2004)
94. A Dubra, Y Sulai, JL Norris, RF Cooper, AM Dubis, DR Williams, J Carroll, *Noninvasive, imaging of the human rod photoreceptors mosaic using a confocal adaptive optics ophthalmoscope*. *Biomed. Opt. Exp.* **2**(7), 1864-1876 (2011)
95. NM Ducrey, FC Delori, ES Gragoudas, *Monochromatic ophthalmoscopy and fundus photography II. The pathological fundus*. *Arch. Ophthalmol.* **97**, 188-193 (1979)
96. JL Duncan, Y Zhang, J Gandhi, C Nakanishi, M Othman, KEH Branham, A Swaroop and A Roorda, *High-resolution imaging with adaptive optics in patients with inherited retinal degeneration*. *Invest. Ophthalmol. Vis. Sci.* **48**(7), 3283-3291 (2007)
97. B Duvall & RM Kershner, *Ophthalmic medications and pharmacology*. Slack Inc. (2006)
98. AS Eadie, B Winn and JR Pugh, *The influence of arterial pulse on miniature eye movements*. *Invest. Opht. Vis. Sci.* **35**, 2037 (1994)
99. EC Eagle, *Eye pathology: An atlas and text*. Lippincott Williams and Wilkins (2011)

100. A Eisner, SA Fleming, ML Klein, WM Mauldin, *Sensitivities in older eyes with good acuity: eyes whose fellow eye has exudative AMD*. Invest. Ophthalmol. Vis. Sci. **28**, 1832-1837 (1987)
101. AE Elsner, SA Burns, MR Kreitz, MR Weiter, *New views of the retina/RPE complex: quantifying sub-retinal pathology. Non invasive assessment of the visual system*. Opt. Soc. Am. Tech. Dig. **1**, 150-153 (1991)
102. AE Elsner, AE Jalkh, JJ Weiter, *New devices in retinal imaging and functional evaluation*. In: W Freeman (ed.) Practical atlas of retinal disease therapy. Raven, New York, 19-35 (1993)
103. AE Elsner, SA Burn, JJ Weiter, ME Hartnett, *Diagnostic applications of near infrared solid-state lasers in the eye*. Lasers and Electro-Optics Soc. Ann. Meeting, LEOS Conf. Proc. **1**, 14-15 (1994)
104. AE Elsner, SA Burns, JJ Weiter *et al.*, *Infrared imaging of sub-retinal structures in the human ocular fundus*. Vision Res. **36**, 191-195 (1996)
105. AE Elsner, *Fundamental properties of the retina*. Published in “Adaptive optics for vision Science”, edited by J Porter, H Queener, J Lin, K Thorn and A Awwal. John Wiley & Sons (2006)
106. EMS *microscopic targets and samples* (2007), from: <http://www.emsdiasum.com>
107. JM Enoch & LE Glismann, *Physical and optical changes in excised retinal tissue: Resolution of retinal receptors as a fibre optic bundle*. Invest. Ophth. 209-222 (1966)
108. JM Enoch, *The retina as a fiber optics bundle*, Appendix B. Published in “Fiber optics: Principles and applications” edited by NS Kapany, Academic Press (1967)
109. B Erdélyi, B Csákány, G Rödönyi, A Soumelidis, Z Lang, J Németh, *Dynamics of ocular surface topography in healthy subjects*. Ophthalmic Physiol. Opt. **26**(4), 419-425 (2006)
110. B Erdélyi, *The effects of the tear-film dynamics in healthy subject and dry eye patients*. Semmelweis University, PhD Thesis (2007)
111. CR Ethier, M Johnson and J Ruberti, *Ocular biomechanics and biotransport*. Annu. Rev. Biomed. Eng. **6**, 249-273 (2004)
112. T Eysteinnsson, F Jonasson, H Sasaki *et al.*, *Reykjavik Eye Study Group: Central corneal thickness, radius of the corneal curvature and intraocular pressure in normal subjects using non-contact techniques: Reykjavik Eye Study*. Acta Ophthalmol. Scand. **80**(11), 2002
113. PP Fagerholm, *The influence of calcium on lens protein*. Exp. Eye Research **28**(2), 211-222 (1979)
114. S Faisan, D Lara, C Paterson, *Scanning ophthalmoscope retinal image registration using one-dimensional deformation fields*. Opt. Exp. **19**(5), 4157-4169 (2011)
115. O Feeney, *Theory and Laboratory Characterisation of Novel Wavefront Sensors for Adaptive Optics Systems*. PhD thesis, National University of Ireland, Galway (2001)

116. J Feher J, I Kovacs, M Artico M, C Cavallotti, A Papale A, GC Balaco-Gabrieli, *Mitochondrial alterations of retinal pigment epithelium in age-related macular degeneration*. Neurobiol. Aging. **27**, 983–993 (2006)
117. M Feierabend, M Ruckel and W Denk, *Method and device for wave-front sensing*. US Patent 11/200457 (2005)
118. AF Fercher, K Mengedoht, W Werner, *Eye-length measurement by interferometry with partially coherent light*. Optics Letters **13**(3), 186-188 (1988)
119. EJ Fernandez, I Igleasias, P Artal, *Closed loop adaptive optics in the human eye*. Opt. Letters **26**(10), 746-748 (2001)
120. EJ Fernandez, L Vabre, B Hermann, *Adaptive optics with a magnetic deformable mirror: applications in the human eye*. Opt. Exp. **14**, 8900-8917 (2006)
121. EJ Fernandez, B Hermann, B Povazay, A Unterhuber, H Sattmann, B Hofer, PK Anheld and W Drexler, *Ultrahigh resolution optical coherence tomography and pancorrection for cellular imaging of the living human retina*. Opt. Exp. **16**, 11083-11094 (2008)
122. FL Ferris, MD Davis and LM Aiello, *Treatment of diabetic retinopathy*. In Drug Therapy, ed. by AJJ Wood, New Engl. J. Med. **341**(9), 667-678 (1999)
123. JR Fienup & JJ Miller, *Aberration correction by maximizing generalised sharpness metrics*. J. Opt. Soc. Am. A **20**(4), 609-620 (2003)
124. HF Fine, JL Prenner and D Roth, *Fluorescein angiography*. FG Holz & RF Spaide (eds.), *Medical retina - Essentials in Ophthalmology Series* (eds. GK Kriegelstein and RN Weinreb), Springer 19-27 (2007)
125. M Fingeret, *Using the Heidelberg Retina Tomograph II (HRT): Image acquisition and accessing the data*. In: The essential HRT primer chapters (Ch. 2). Accessed at: <http://www.heidelbergengineering.com/us/academy-education/quick-guides> (2009)
126. JV Forrester, AD Dick, PG McMenemy and WR Lee, *The Eye: Basic sciences in practice*. Saunders (2002)
127. RN Frank, *Diabetic retinopathy*. Published in Medical Progress, New. Engl. J. Med. **350**(1), 48-58 (2004)
128. K Franze, J Grosche, SN Skathkov, S Schinkinger, C Foja, D Schild, O Uckermann, K Travis, A Reichenbach and J Guck, *Müller cells are living optical fibres in the vertebrate retina*. PNAS **104**(2), 8287-8292 (2007)
129. K Franze, M Francke, K Gunter, AF Christ, N Kober, A Reichenbach and J Guck, *Spatial mapping of the mechanical properties of the scanning force microscopy*. Soft Matter **7**, 3147-3154 (2011)
130. TJ Freegard, *The physical basis of transparency of the normal cornea*. Eye **11**, 465-471 (1997)
131. MH Freeman, CC Hull and WN Charman, *Optics* (Ed. 11th). Butterworth-Heinemann, imprint of Elsevier (2003)

132. T Friberg & LT Labriola, *Wide-field imaging and angiography*. FG Holz & RF Spaide (eds.), *Medical retina - Essentials in Ophthalmology Series* (eds. GK Kriegelstein and RN Weinreb), Springer (2007)
133. DL Fried, *Anisoplanatism in adaptive optics*. J. Opt. Soc. Am. **72**(1), 52 (1982)
134. JS Friedenwald, *Retinal vascular dynamics*. Am. J. Ophthalmol. **17**(5) (1934)
135. A Fujishiro & J Akita, *Scanning laser ophthalmoscope* - US Patent 7794081 (2008)
136. T Fusco, C Petit, G Rousset, JF Sauvage, JM Conan, *et al.*, *Optimization of the pre-compensation of non-common path aberrations for adaptive optics systems*. Adaptive Optics: Methods, Analysis and Applications paper AWB2 (2005)
137. JM Geary, *Introduction to wavefront sensors*. SPIE (1995)
138. KM Gehrs, DH Anderson, LV Johnson and GS Hageman, *Age-related macular degeneration-emerging pathogenetic and therapeutic concepts*. Ann. Med. **38**, 450–471 (2006)
139. C Genrui & Y Xin, *Accuracy analysis of a Hartmann-Shack wave-front sensor operated with a faint object*. Opt. Eng. **33**, 2331-2335 (1994)
140. R Gerometta, AC Zamudio, DP Escobar, OA Candida, *Volume change of the ocular lens during accommodation*. Am. J. Physiol. Cell Physiol. **293**(2), C797-804 (2007)
141. JP Gilbard, SR Rossi and KL Gray, *Mechanisms for increased tear film osmolarity*. In: *The cornea: Transaction of the World Congress III*, ed. by HD Cavanagh, Raven Press, New York p.5-7 (1988)
142. A Glasser & PL Kaufman, *The mechanism of accommodation in primates*. Ophthalmology **106**, 863–872 (1999)
143. P Godara, AM Dubis, A Roorda, JL Duncan and J Carroll, *Adaptive optics retinal imaging: emerging clinical applications*. Optom. Vis. Sci. **87**(12), 930-941 (2010a)
144. P Godara, C Siebe, J Rha, M Michaelides and J Carroll, *Assessing the photoreceptor mosaic over drusen using adaptive optics and spectral domain optical coherence tomography*. Ophthalm. Surg. Las. Imaging **41**(6), S104-S108 (2010b)
145. P Godara, RF Cooper, PI Sergouniotis, MA Diederichs, MR Streb, MA Genead, JJ McAnany, AR Webster, AT Moore, AM Dubis, M Neitz, A Dubra, EM Stone, GA Fishman, DP Han, M Michaelides, J Carroll, *Assessing retinal structure in complete congenital stationary night blindness and Oguchi disease*. Am. J. Ophthalmol. **154**(6), 9878-1001 (2012)
146. AV Goncharov & C Dainty, *Wide-field schematic eye model with gradient-index lens*. J. Opt. Soc. Am. A **24**(8), 2157-2174 (2007)
147. JM Gorrand & FC Delori, *A reflectometric technique for assessing photoreceptor alignment*. Vision Res. **35**, 999-1010 (1995)
148. DC Gray, W Merigan, JI Wolfing, *In vivo fluorescence imaging of primate retinal ganglion cells and retinal pigment epithelial cells*. Opt. Exp. **14**(16), 7144-7158 (2006)

149. WR Green, *Histopathology of age-related macular degeneration*. Mol. Vision **5**, 27 (1999)
150. K Grieve, P Tiruveedhula, Y Zhang and A Roorda, *Multi-wavelength imaging with the adaptive optics laser ophthalmoscope*. Opt. Exp. **14**(25), 12230-12242 (2006)
151. B Gros, D Pope and T Cohn, *Involuntary oculomotor events time-locked to the arterial pulse*. Invest. Ophth. Vis. Sci. **32**, 895 (1991)
152. RP Grosso & M Yellin, *The membrane mirror as an adaptive optical element*. J. Opt. Soc. Am. **67**(3), 399-406 (1977)
153. S Gruppeta, L Koechlin, F Lacombe, P Puget, *Curvature sensor for the measurement of the static corneal topography and the dynamic tear film topography in the human eye*. Opt. Lett. **30**(20), 2757-2759 (2005a)
154. S Gruppeta, F Lacombe and P Puget, *Study of the dynamic aberrations of the human tear film*. Opt. Exp. **13**(9), 7631-7636 (2005b)
155. A Guirao & P Artal, *Off-axis monochromatic aberration estimated from double pass measurements in the human eye*. Vision Res. **39**, 207-217 (1999)
156. A Guirao, C Gonzalez, M Redondo, *Average optical performance of the human eye as a function of age in normal population*. Invest. Ophth. Vis. Sci. **40**, 203-213 (1999)
157. DX Hammer, RD Ferguson, JC Magill, MA White, AE Elsner and RH Webb, *Compact laser scanning ophthalmoscope with high-speed retinal tracker*. Appl. Opt. **42**(22), 4621-4632 (2003)
158. DX Hammer, RD Ferguson, CE Bigelow, NV Ifitima, TE Ustun and SA Burns, *Adaptive optics scanner laser ophthalmoscope for stabilized retinal imaging*. Opt. Exp. **14**(8), 3354-3367 (2006)
159. DX Hammer, RD Fergusson, M Mujat, AH Patel, N Iftima, TYP Chui, JD Akula and AB Fulton, *Multifunctional imaging device for adaptive optics compensation in humans and small animals*. Front. Opt. FTuB1 (2010)
160. KM Hampson, *The higher-order aberrations of the human eye relation to the pulse and effect on vision*. PhD thesis, Imperial College London (2004)
161. KM Hampson, I Munro, C Paterson and C Dainty, *Weak correlation between the aberration dynamics of the human eye and the cardiopulmonary system*. J. Opt. Soc. Am. A **22**(7), 1241-1250 (2005)
162. KM Hampson, C Paterson, C Dainty and EAH Mallen, *Adaptive optics system for investigation of the effect of the aberration dynamics of the human eye on steady-state accommodation control*. J. Opt. Soc. Am. A **23**(5), 1082-1088 (2006)
163. KM Hampson, SS Chin, EAH Mallen, *Dual wavefront sensing channel monocular adaptive optics system for accommodation studies*. Opt. Exp. **17**(20), 18229-18240 (2009)
164. N Hansen, *Benchmarking the Nelder-Mead downhill simplex algorithm with many local restarts*. GECCO '09, ACM 978-1 (2009)

165. JW Hardy, *Adaptive optics for astronomical telescopes*. Oxford University Press (1998)
166. AR Harvey, I Al-Abboud, G Muyo, A Gorman, DJ Mordant and AI McNaught, *An artificial eye with compound retina for rigorous validation of retinal chemical imaging*. IoP Topical Meeting; Imaging in the eye V: Technologies and clinical applications. <http://www.eps.hw.ac.uk/~ceearh2/IoP/ImagingInTheEye10.pdf> (2010)
167. JR Hassel, *The molecular basis of corneal transparency*. Exp. Eye. Res. **91**(3), 326-335 (2010)
168. JC He, SA Burns, S Marcos, *Monochromatic aberration in the accommodated human eye*. Vision Res. **40**, 41-48 (2000)
169. Z He, CTO Nguyen, JA Armitage, AJ Vingrys, BV Bui, *Blood pressure modifies retinal susceptibility to intraocular pressure elevation*. PLoSONE **7**(2), e31104 p9 (2012)
170. Heidelberg Engineering: <http://www.heidelbergengineering.com> (2007)
171. A Hendrickson, D Possin, L Vajzovic and CA Toth, *Histologic development of the human fovea from midgestation to maturity*. Am. J. Ophthalmol. **154**(5), 767-778 (2012), Figure 1 from page 768 was reprinted in this thesis with permission of Elsevier under license number 3103610897153 to reuse in the thesis/dissertation both in electronic and printed format.
172. P Henkind, RI Hansen and J Szalay, *Ocular circulation*. In: *Physiology of the human eye and visual system*. p. 98-155. Harper & Row, New York (1979)
173. B Hermann, EJ Fernandez, A Unterhuber, H Sattmann, AF Fercher, W Drexler, PM Prieto and P Artal, *Adaptive-optics ultrahigh-resolution optical coherence tomography*. Opt. Lett. **29**, 2142-2144 (2004)
174. E Hermans, M Dubbelman, R van der Heijde and R Heethaar, *The shape of the human lens nucleus with accommodation*. J. Vision **7**(10), 1-10 (2007)
175. J Hirsch & R Hylton, *Quality of the primate photoreceptor lattice and limits of spatial vision*. Vision Res. **24**(4), 347-355 (1984)
176. J Hirsch & WH Miller, *Does cone positional disorder limit resolution?* J. Opt. Soc. Am. **4**(8), 1482-1492 (1987)
177. H Hofer, L Chen, G Yoon *et al.*, *Improvement in retinal image quality with dynamic correction of the eye's aberrations*. Opt. Exp. **8**(11), 631-643 (2001a)
178. H Hofer, P Artal, B Singer, JL Aragon, DR Williams, *Dynamics of the eye's wave aberration*. J. Opt. Soc. Am. A **18**(3), 497-506 (2001b)
179. H Hofer, B Singer, DR Williams, *Different sensations from cones with the same photopigment*. J. Vision **5**(5), 444-454 (2005)
180. H Hofer, J Porter, G Yoon, L Chen, B Singer, DR Willilams, *Rochester adaptive optics ophthalmoscope*. In: *Adaptive optics for vision science* (Ch. 16), eds. by Porter *et al.* (2006)

181. FJ Holly (ed.) *et al.*, *The preocular tear film in health, disease and contact lens wear*. Lubbock, Texas by Dry Eye Institute Inc. (1986)
182. FJ Holly, *Basic factor underlying the formation and stability of the preocular tear film*. In “The cornea: Transaction of the World Congress III” edited by HD Cavanagh, Raven Press, New York p.1-4 (1988)
183. ML Holohan & Dainty, *Low-order adaptive optics: a possible use in underwater imaging?* Opt. Las. Techn. **29**(1), 51-55 (1997)
184. FG Holz & RF Spaide (eds.), *Medical retina - Essentials in Ophthalmology Series* (eds. GK Kriegelstein and RN Weinreb), Springer (2007)
185. Hooker CJ, Divall EJ, Lester WJ, Moutzouris K, Reason CJ, Ross IN, *A low-cost adaptive optical system for laser wavefront control*. Proceedings of the 2nd International Workshop on Adaptive optics for industry and medicine (ed. by Love GD, World Scientific), 3-8 (1999)
186. M Hoshino, K Uesugi, N Yagi, S Mohri, J Regini and B Pierscionek, *Optical properties of in situ eye lenses measured with interferometry: A novel measure of growth processes*. PLoS ONE **6**(9), e25140 (2011)
187. K Hosseini, AI Kholodnykh, IY Petrova, RO Esenaliev, F Hendrikse and M Motamedi, *Monitoring of rabbit cornea response to dehydration stress by optical coherence tomography*. Invest. Ophthalmol. Vis. Sci. **45**, 2555-2562 (2004)
188. HRT Tutorial & Manual: <http://www.heidelbergengineering.co.uk/products> (2007)
189. MJ Huber, SA Smith and SE Smith, *Mydriatic drugs for diabetic patients*. Br. J. Ophthalmol. **69**, 425-427 (1985)
190. JD Hunter, JG Milton, H Lüdtke, B Wilhelm, H Wilhelm, *Spontaneous fluctuations in pupil size are not triggered by lens accommodation*. Vis. Res. **40**, 567-673 (2000)
191. JJ Hunter, CJ Cookson, ML Kisilak, JM Bueno and MCW Campbell, *Characterizing image quality in a scanning laser ophthalmoscope with differing pinholes and induced scattered light*. J. Opt. Soc. Am A **24**(5), 1284-1295 (2007)
192. JJ Hunter, B Masella, S Dubra *et al.*, *Images of photoreceptors in living primate eyes using adaptive optics two-photon ophthalmoscopy*. Biomed. Exp. **2**(1), 139-148 (2010)
193. B Huntjens, WN Charman, H Workman, SL Hosking and C O'Donnell, *Short-term stability in refractive status despite large fluctuations in glucose levels in diabetes mellitus type 1 and 2*. PLoS ONE **7**(12), e52947 (2012)
194. JK IJspert, PWT de Waard, TJTP van den Berg and PTVM de Jong, *The intraocular straylight function in 129 healthy volunteers - Dependence on angle, age and pigmentation*. Vision Res. **30**(5), 699-707 (1990)
195. JK IJspert, TJTP van den Berg and H Spekreijse, *An improved mathematical description of the foveal visual point spread function with parameters for age, pupil size and pigmentation*. Vision Res. **33**(1), 15-20 (1993)

196. F Incropera & DP De Witt, *Fundamental of heat and mass transfer*. Wiley, New Jersey 5th Ed. (2002)
197. R Irwan and RG Lane, *Analysis of optimal centroid estimation applied to Shack-Hartmann sensing*. Appl. Opt. **38**(2), 6737 (1999)
198. DR Iskander & HT Kasparzak, *Dynamics in longitudinal eye movements and corneal shape*. Opht. Physiol. Opt. **26**(6), 572-579 (2006)
199. ISO 6344-3:1998, available at: <http://www.iso.org> (2011)
200. PC Issa, M Flackenstein, HM Helb, HPN Scholl, S Schmitz-Valckenberg and FG Holz, *Simultaneous SD-OCT and confocal SLO-imaging*. In: *Medical retina – Essentials in Ophthalmology Series* (eds. GK Kriegelstein and RN Weinreb), Springer edited by FG Holz & RF Spaide (2007)
201. RD Jager, WF Mieler and JW Miller, *Medical progress: Age-related macular degeneration* (Review article). N. Engl. J. Med. **358**(24), 2606-2617 (2008)
202. W Jiang, H Xian, S Feng, *Detecting error of Shack-Hartmann wavefront sensor*. Proc. SPIE **3126**, 534-544 (1997)
203. A Johansson, K Kromer, R Sroka and H Stepp, *Clinical optical diagnostic – Status perspectives*. Med. Laser Appl. **23** 155-174 (2008)
204. F Johnson & D Maurice, *A simple method of measuring aqueous humor flow with intravitreal fluoresceinated dextrans*. Exp Eye Res **39**,791 (1984)
205. PT Johnson, GP Lewis, KC Talaga *et al.*, *Drusen-associated degeneration in the retina*. Invest. Ophthalmol. Vis. Sci. **44**, 4481-4488 (2003)
206. PT Johnson, MN Brown, NC Pulliamm DH Anferon, LV Johnson, *Synaptic pathology, altered gene expression, and degeneration in photoreceptors impacted by drusen*. Invest. Ophthalmol. Vis. Sci. **46**(12), 4788-4795 (2005)
207. JB Jonas, U Schneider, GOH Naumann, *Count and density of human retinal photoreceptors*. Graefe's Arch. Clin. Exp. Ophthalmol. **230**, 505-510 (1992)
208. JJ Kanski, *Clinical ophthalmology: A systematic approach*, (Ed. 6th). Butterworth-Heinemann (2007)
209. JJ Kanski & B Bowling, *Clinical ophthalmology: A systematic approach - Expert Consult* 7th ed. Saunders (2011)
210. R Kardon, *Pupil* Vol. 3 Ch. 32 in *Adler's Physiology of the eye*, Clinical application (Eds. PL Kaufman and A Alm), Mosby (2003)
211. R Kardon & J Weinstein, *The iris and the pupil*. Duane's Ophthalmology CD ROM (2006)
212. MW Kartz, SS Olivier, K Avicola, J Brase, C Carrano, D Silva, D Pennington, C Brown, *High resolution wavefront control of high-power laser systems*. Proceedings of the 2nd International Workshop on Adaptive optics for industry and medicine (ed. by Love GD, World Scientific), 16-21 (1999)

213. MA Kass, DK Heuer, EJ Higginbotham *et al.*, *The ocular hypertension treatment study: A randomized trial determines that topical ocular hypotensive medication delays or prevents the onset of primary open-angle glaucoma*. Arch Ophthalmol. **120**, 701-712 (2002)
214. S Kasthurirangan, AL Markwell, DA Atchison and JM Pope, *MRI study of the changes in crystalline lens shape with accommodation and aging in humans*. J. Vis. **11**(3), 1-16 (2011)
215. PL Kaufmann & A Alm, *Adler's physiology of the eye* (Ed. 10th). St. Louis, Mosby (2003)
216. A Kawasaki, *Physiology, assessment, and disorder of the pupil*. Curr. Opinion Ophthalmol. **10**(6), 394-400 (1999)
217. PA Keane, PJ Patel, S Liakopoulos, FM Heussen, SR Sadda and A Tufail, *Evaluation of age-related macular degeneration with optical coherence tomography*. Surv. Ophthalmol. **57**(5), 389-414 (2012)
218. IE Kepiro, GT Kennedy and C Paterson, *A compact scanning laser ophthalmoscope with adaptive optics*,. 4th European Meeting in Visual and Physiological Optics, Greece (2008)
219. IE Kepiro & C Paterson, *Adaptive optics ophthalmoscope findings in photoreceptor loss*, (2013a, in preparation)
220. IE Kepiro & C Paterson, *Progress for early diagnosis of ophthalmic diseases: Improved non-invasive evaluation of human retina structures using a compact adaptive optics ophthalmoscope*, (2013b, in preparation)
221. IE Kepiro & C Paterson, *Characterization of phantom retina samples for optimization in adaptive optics ophthalmoscopy*, (2013c, in preparation)
222. AI Kholodnykh, K Hosseini, P Kamran *et. al.*, *In-vivo OCT assessment of rabbit corneal hydration and dehydration*. SPIE Proc. **4956**, 295-298 (2003)
223. PE King-Smith, BA Fink, N Fogt, Kelly K Nichols, RM Hill and GS Wilson, *The thickness of the human precorneal tear film: evidence from reflection spectra*. Inv. Opht. Vis. Sci. **41**(11), 3348-3359 (2000)
224. BEK Klein, R Klein and MD Knudtson, *Intraocular pressure and systematic blood pressure: longitudinal perspective - the Beaver Dam Eye Study*. Br. J. Ophthalmol. **89**, 284-287 (2005)
225. SD Klyce & JA Bonanno, *Role of epithelium in corneal hydration*. Published in "The cornea: Transaction of the World Congress III" ed. By HD Cavanagh, Raven Press, New York p.159-164 (1988)
226. SD Klyce & SA Dingeldein, *Corneal topography*. In *Corneal topography*, p. 61-77 (1988)
227. J Knudsen & P Niemeyer, *Learning Java*. 3rd Edition, O'Reilly Media (2009)

228. DD Koch, GN Fovles, T Moran and JS Wakil, *The corneal EyeSys System: Accuracy analysis and reproducibility of first-generation prototype*. *Refract. & Corneal Surg.* **5** 424-429 (1989)
229. DD Koch & EA Haft, *Introduction to corneal topography*. In DR Sanders, DD Koch (eds): *An Atlas of Corneal Topography*. Thorofare, NJ, SLACK Inc. (1993)
230. H Kolb, *The neural organization of the human retina - principles and practices of clinical electrophysiology of vision* (Eds. Heckenlively, J.R. and Arden, G.B.) Mosby St. Louis, 25-52 (1991)
231. H Kolb, H Ripps and S Wu, *Concepts and challenges in retinal biology* (Progress in brain research). Elsevier (2003)
232. H Kolb, R Nelson, E Fernandez and B Jones, *The organizations of the retina and visual system*. Available at: <http://www.webvision.med.utah.edu>. (August 2011)
233. K Kosina-Hagyó, *Examination of tear film and its dynamics using ophthalmological imaging methods*. Semmelweis University, PhD Thesis (2011)
234. T Kozicz, JC Brittencourt, PJ May, A Reiner, PDR Gamlin, M Palkovits, AKE Horn, CAB Toledo, AW Ryabinin, *The Edinger-Westphal nucleus: A historical, structural, and functional prospective on a dichotomous terminology*. *J. Comp. Neurol.* **519**, 1413-1434 (2011)
235. S Krag & TT Andreassen, *Mechanical properties of the human posterior lens capsule*. *Inv. Ophth. Vis. Sci.* **44**(2), 691-696 (2003)
236. RR Krueger, RA Applegate, SM MacRae eds., *Wavefront customized visual correction: The quest for super vision II*. Slack (2004)
237. MH Kuehn, JH Fingert and YH Kwon, *Retinal ganglion cell death in glaucoma: Mechanisms and neuroprotective strategies*. *Ophthalmol. Clin. N. Am.* **18**, 383-395 (2005)
238. S Kumar, S Acharya, R Beuerman, A. Palkama, *Numerical solution of ocular fluid dynamics in a rabbit eye: parametric effects*, *Ann. Biomed. Eng.* **34**, 530-544 (2006)
239. YH Kwon, JH Fingert, MH Kuehn and WLM Alward, *Primary open-angle glaucoma*. *New Engl. J Med.* **360**, 1113-1124 (2009)
240. H Leibowitz, DE Kruger, *et al.*, *The Framingham eye study monograph: An ophthalmological, diabetic retinopathy, macular degeneration, and visual acuity on general population of 2361 adults*. *Surv. Ophthalmol.* **24**, 335-610 (1980)
241. KY Li & G Yoon, *Changes in aberrations and retinal image quality due to tear film dynamics*. *Opt. Exp.* **14**(25), 12552-12559 (2006)
242. J Liang, B Grimm, S Goelz, JF Bille, *Objective measurement of wave aberrations of the human eye with use of a Shack-Hartmann wavefront-sensor*. *J. Opt. Soc. Am A* **11**, 1949-1957 (1994)
243. J Liang, DR Williams and T Miller, *Supernormal vision and high-resolution retinal imaging through adaptive optics*. *J. Opt. Soc. Am. A* **14**, 2882-2892 (1997)

244. N Lindqvist, Q Liu, J Zajadacz, K Franze and A Reichenbach, *Retinal glial (Muller) cells: Sensing and responding to tissue stretch*. Invest. Opht. Vis. Sci. **51**(3), 1683-1690 (2010)
245. N Link & L Stark, *Latency of the pupillary response*. Biomed Eng. IEE Trans. **35**(3), 214-218 (1988)
246. HL Liou & NA Brennan, *Anatomically accurate, finite model eye for optical modelling*. J. Opt. Soc. Am A **14**(14), 1684-1695 (1997)
247. Z Liu & SC Pflugfelder, *Corneal surface regularity and the effect of artificial tears in aqueous tear deficiency*. Ophthalmology **106**(5), 939-943 (1999)
248. IE Loewenfeld, *Mechanisms of reflex dilatation of the pupil - historical review and experimental analysis*. Doc. Ophthalmol. **12**, 185-448 (1958)
249. IE Loewenfeld, *The pupil: anatomy, physiology and clinical applications*. Ames, Iowa State University Press (1993)
250. M Loktev, O Soloviev, G Vdovin eds., *Adaptive optics product guide*. OKO Technologies 2nd ed. (2006)
251. M Lombardo, G Lombardo, P Ducoli and G Lombardo, *Adaptive optics photoreceptor imaging*. Ophthalmol. **119**(7), 1498-1498 (2012a)
252. M Lombardo, S Serrao, N Devaney, M Parravano and G Lombardo, *Adaptive optics technology for high-resolution retinal imaging*. Sensors 2013 **13**(1) 334-366 (2012b)
253. M Lombardo, S Serrao, P Duccoli and G Lombardo, *Variations in image optical quality of the eye and the sampling limit of resolution of the cone mosaic with axial length in young adults*. J. Cataract & Refract. Surg. **38**(7) 1147-1155 (2012c)
254. W Lotmar, *Theoretical eye model with aspherics*. J. Opt. Soc. Am. **61**(11), 1522-1529 (1971)
255. H Love, T Oag, A Kirby, *Common path interferometric wavefront sensor for extreme adaptive optics*. Opt. Exp. **13**(9), 3491-3499 (2005)
256. O Lowenstein & IE Loewenfeld, *The Pupil, The Eye*, vol. 3, H Davson (ed.), Academic Press, New York, Ch. 9, p.255-337 (1969)
257. PJ Luthert, *personal communication* (2011)
258. M Lutz, *Programming Python*. 4th Edition, O'Reilly Media (2010)
259. X Ma, C Rao and H Zhen, *Error analysis of CCD-based point source centroid computation under background light*. Opt. Exp. **17**(10), 8525-8540 (2009)
260. D Malacara (ed.), *Optical shop testing* John Wiley and Sons, Series in pure and applied optics (1992)
261. S Marcos, R Navarro and P Artal, *Coherent imaging of the cone mosaic in the living human eye*, J. Opt. Soc. Am A **13**, 897-905 (1996)
262. JA Martin & A Roorda, *Direct and noninvasive assessment of parafoveal capillary leukocyte velocity*. Ophthalmol. **112**, 2219-2224 (2005)

263. JA Martin & A Roorda, *Pulsatility of parafoveal capillary leukocytes*. Exp. Eye Res. **88**(3),356-360 (2009)
264. JH Mathews and KD Fink, *Numerical methods using Matlab*. Prentice-Hall Inc., 4th edition (2004)
265. DM Maurice, *The physical basis of corneal transparency*. In: XVII Council Ophthalmology, 465-469. New York (1954)
266. DM Maurice, *The structure and transparency of the cornea*. J. Physiol. **136**, 263-286 (1957)
267. DM Maurice, *The cornea and the sclera*. In: “The eye” edited by H Davson, Academic Press (1969)
268. DM Maurice, *Mechanics of the cornea*. In: “The cornea: Transaction of the World Congress III” ed. By HD Cavanagh, Raven Press, New York p.187-193 (1988)
269. R McCally & RA Farrell, *Interaction of light and the cornea: Light scattering versus transparency*. Published in “The cornea: Transaction of the World Congress III” edited by HD Cavanagh, Raven Press, New York p.165-171 (1988)
270. Y Mejía-Barbosa & D Malacara-Hernández, *A review of methods for measuring the corneal topography*. Optom. Vis. Sci. **78**(4), 240-253 (2001)
271. R Michael, J van Marle, G Vrensen, TJTP van den Berg, *Changes in the refractive index of the lens fibre membrane during maturation – impact on lens transparency*. Exp. Eye. Res. **77**, 93-99 (2003)
272. R Michael & AJ Bron, *The aging lens and cataract: a model of normal and pathological ageing*. Phil. Trans. R. Soc. B **366**, 1278-1292 (2011)
273. M Michaelides, J Rha, EW Dees, RC Baraas, M Wagner-Schuman, JD Mollon, AM Dubis, M Anderson, T Rosenberg, M Larsen, A Moore, J Carroll, *Integrity of the cone photoreceptor mosaic in oligocone trichromacy*. Invest. Ophthalmol. Vis. Sci. **52**(7), 4757-4764 (2011)
274. C Millar & PL Kaufman, *Aqueous humor: secretion and dynamics*. In: W Tasman, EA Jaeger, *Duane's foundations of clinical ophthalmology*. Philadelphia, Lippincott-Raven (1995)
275. DT Miller (2005) *of ganglion cell reflectivity*, cited as 'personal communication'. In: DR Williams & J Porter, *Development of adaptive optics in vision science and ophthalmology* (Chapter 1 in J Porter *et al.* eds., Adaptive optics for vision science. Wiley, 2006)
276. PW Milonni, *Adaptive optics for astronomy*. Am. J. Phys. **67**(6), 476-485 (1999)
277. J Milton, *Pupil light reflex: delays and oscillations*, Ch. 9, p. 271-301 published in *Nonlinear Dynamics in Physiology and Medicine* (Eds. A Beuter, L Glass, MC Mackey, MS Titcombe) Springer (2003)
278. S Mishima, *Some physiologic aspects of the precorneal tear film*. Arch. Ophthalmol. **73**, 233 (1965)

279. P Moon & D Spencer, *On the Stiles-Crawford Effect*. J. Opt. Soc. Am. **34**, 319-329 (1944)
280. E Moreno-Barriuso, S Marcos, R Navarro, SA Burns, *Comparing laser ray tracing, the spatially resolved refractometer, and the Hartmann-Shack sensor to measure the ocular wave aberration*. Optom. Vis. Sci. **78**(3), 152-156 (2001)
281. JIW Morgan, A Dubra, R Wolfe, *In vivo autofluorescence imaging of the human and macaque retinal pigment epithelial cell mosaic*. Invest. Ophthalmol. Vis. Sci. **50**(3), 1350-1359 (2009)
282. M Mujat, RD Fergusson, N Ifitima, DX Hammer, *Compact adaptive optics line scanning ophthalmoscope*. Opt. Exp. **17**, 10242-10258 (2009)
283. RA Muller & A Buffington, *Real-time correction of atmospherically degraded telescope images through image sharpening*. J. Opt. Soc. Am. **64**(9), 1200-1210 (1974)
284. LP Murray, JC Dainty, J Coignus and Felberer, *Wavefront correction of extended objects through image sharpness maximisation*. Proc. of SPIE Vol. **6018** 60281A-1 (2005)
285. LP Murray, *Smart optics: Wavefront sensorless adaptive optics – image correction through sharpness maximisation*. PhD thesis, National University of Ireland, Galway (2006)
286. K Nanba Nakayama and K Iwata, *Variation of intraocular pressure by non-contact tonometry and cardiac pulse wave*. Nippon Ganka Gakkai Zassi **93**, 155-160 (1989)
287. R Navarro, J Santamaría and J Bescós, *Accommodation-dependent model of the human eye with aspherics*. J. Opt. Soc. Am. A **2**(8), 1273-1281 (1985)
288. R Navarro, F Palos, LM Gonzalez, *Adaptive model of the gradient index of the human lens. II. Optics of the accomodating lens*. J. Opt. Soc. Am. A Opt. Image Sci. Vis. **24**(9), 2911-2920 (2007)
289. DR Neal, J Copland, D Neal, *Shack-Hartmann wavefront sensor precision and accuracy*, Proc. SPIE **4779**, 148 (2002)
290. DR Neal, *Ophthalmic Shack-Hartmann wavefront sensor applications*. In: Adaptive optics for Industry and Medicine, Imperial College Press, 219-226 (2007)
291. JA Nelder & R Mead, *A simplex method for function minimization*. Comp. J. **7**, 308-313 (1965)
292. J Németh, B Erdélyi, B Csákánz, P Gáspár, A Soumelidis, F Kahlesz and Z Lang, *High speed videokeratometric measurements of tear film build-up time*. Invest. Ophthalmol. Vis. Sci. **43**(6), 1783-1790 (2002)
293. RW Nickells, *Retinal ganglion cell death in glaucoma: the how, the why, and the maybe*. J. Glaucoma **5**(5), 345-356 (1996)
294. L Noethe, *Active optics in modern large optical telescopes* in Progress in Optics **43** (ed. Wolf E, Elsevier Science), 1-69 (2002)

295. RJ Noll, *Zernike polynomials and atmospheric turbulence*. J. Opt. Soc. Am. **66**(3), 207-211 (1976)
296. TM Nork, JN ver Hoeve, GL Poulsen *et al.*, *Swelling and loss of photoreceptors in chronic and experimental glaucomas*. Arch. Ophthalmol. **118**(2), 235-235 (2000)
297. NP:USAF-1951 target, available at: <http://www.newport.com> (2009)
298. K Ohtsuka, K Asakura⁷, H Kawasaki and M Sawa, *Respiratory fluctuations of the human pupil*. Exp. Brain Res. **71**, 215-217 (1988)
299. J Ojeda-Costañeda, *Optical Shop Testing*. John Wiley and Sons (ed. by Malacara), 265-321 (1992)
300. DM Olsson & LS Nelson, *The Nelder-Mead simplex procedure for function minimization*. Technomet. **17**(1), 45-51 (1975)
301. EH Ooi & EYK Ng, *Simulation of aqueous humour hydrodynamics in human eye heat transfer*. Comp. Biol. Med. **38**, 252-262 (2008); Figure 4 from page 256 was reprinted in this thesis with permission of Elsevier under the number 3103610306634 to reuse in a thesis/dissertation both in electronic and printed format.
302. S Ooto, M Hangai, K Takayama, A Sakamoto, A Tsujikawa, S Oshima, T Inoue, N Yoshimura, *Photoreceptor layer in epiretinal membrane using adaptive optics scanning laser ophthalmoscopy*. Ophthalmol. **118**, 873-881 (2011)
303. T Oshika, A Tomidokoro and H Tsuji, *Regular and irregular refractive powers of the front and back surface of the cornea*. Exp. Eye Research **67**, 443-447 (1998)
304. T Oshika, S Klyce, RA Applegate and HC Howland, *Changes in corneal wavefront aberrations with aging*. Invest. Ophth. Vis. Sci. **40**(7), 1351-1355 (1999)
305. NN Osborne, JPM Wood, G Childlow, JH Bae, J Melena and MS Nash, *Ganglion cell death in glaucoma: what do we really know?* Br. J. Ophthalmol. **83**, 980-986 (1999)
306. GA Osterberg, *Topography of the layer of rods and cones in the human retina*. Acta Ophthalmol. **13** (Suppl. **6**), 1-97 (1935)
307. CW Oyster, *The Human Eye: Structure and Function*. Sinauer Associates Inc, Sunderland, Massachusetts (1999)
308. Paediatric Glaucoma & Cataract Family Association (PGCFA), 2008 (accessed in 2012): <http://www.pgcf.org/kb/entry/166>
309. S Panda-Jonas, JB Jonas, M Jakobczyk-Zmija, *Retinal pigment epithelial count, distribution, and correlations in normal human eyes*. Am. J. Ophthalmol. **121**(2), 181-189 (1996)
310. S Patel, DZ Reinstein, RH Silverman and DJ Coleman, *The shape of the Bowman's layer in the human cornea*. J. Ref. Surg. **14**, 636-640 (1998)
311. DV Patel & CNJ McGhee, *Contemporary in vivo confocal microscopy of the living human cornea using white light and laser scanning techniques: a major review*. Clin. Exp. Opht. **35**, 71-78 (2007)

312. C Paterson, I Munro and C Dainty, *A low cost adaptive optics system using a membrane mirror*. Opt. Exp. **6**(9), 175-185 (2000)
313. C Paterson (2006) *of diffraction limited performance of lenslet array* (personal communication)
314. M Patestas & LP Gartner, *A textbook of neuroanatomy*. John Wiley & Sons (2009)
315. JB Pawley, *Handbook of biological confocal microscopy*. Plenum Press (1995)
316. J Pfund, N Lindlein, J Schwider, *Misalignment effects of the Shack–Hartmann sensor*, Appl. Opt. **37**, 22–27 (1998)
317. LH Pi, JL Zhao, Q Liu, L Chen, J Fang, N KE, Y Xiong *et al.*, *Comparison of cycloplegic retinoscopy using cyclopentolate or tropicamide eye drops in an epidemiologic study of paediatric refraction among 1907 school-ages children*. Sci. Res. Essay **6**(3), 635-640 (2011)
318. BK Pierscionek & JW Regini, *The gradient index lens of the eye: an opto-biological synchrony*. Prog. Retina Eye Res. **31**(4) (2012)
319. BC Platt & R Shack, *History and principles of Shack-Hartmann wavefront sensing*. J. Refr. Surg. **17**, S573 (2001)
320. AGh Podoleanu & RB Rosen, *Combinations of techniques in imaging the retina with high-resolution*. Prog. Retina Res. **27**, 464-499 (2008)
321. J Pokorny & VC Smith, *How much light reaches the retina?* In CR Cavonius (ed), *Colour Vision Deficiencies XIII*. Documenta Ophthalmologica Proc. Series **59**, 491-511 (1997)
322. SL Polyak, *The retina*. University of Chicago Press (1941)
323. J Porter, A Guirao, IG Cox, DR Williams, *Monochromatic aberrations of the human eye in large population*. J. Opt. Soc. Am A Opt. Image Sci. Vis. **18**(8), 1793-1803 (2001)
324. J Porter, H Queener, J Lin, K Thorn and A Awwal eds., *Adaptive optics for vision science*. John Wiley & Sons (2006)
325. LS Poyneer, Macintosh B, *Spatially filtered wave-front sensor for higher-order adaptive optics*. J. Opt. Soc Am. A **21**(5), 810-819 (2004)
326. LA Poyneer, DW Palmer, KN LaFortune and B Bauman, *Experimental results for correlation-based wave-front sensing*. Opt. Exp. **15**, 5147-5159 (2005)
327. WH Press, BP Flannery, SA Teukolsky, WT Vetterling, *Singular value decomposition*. In: Numerical recipes in Fortran – the art of scientific computing 2nd ed., 51-63 (1992)
328. PM Prieto, F Vargas-Martin, S Goelz, *Analysis of the performance of the Hartman-Shack sensor in the human eye*. J. Opt. Soc. Am. A **17**, 1388-1398 (2000)
329. J Primot, *Theoretical description of Shack-Hartmann wavefront sensor*. Opt. Comm. **222**, 81 (2003)

330. VA Purvin & A Kawasaki, *Common neuro-ophthalmic pitfalls: Case-based teaching*. Cambridge University Press (2009)
331. HA Quigley, *Number of people with glaucoma worldwide*. Br. J. Ophthalmol. **80**, 389-393 (1996)
332. R Ragazzoni, *Pupil plane wavefront sensing with an oscillating prism*. J. Mod. Opt. **43**, 289-293 (1996)
333. CJ Rapuano, JA Fishbaugh and DJ Strike, *Nine point corneal thickness measurements and keratometry readings in normal corneas using ultrasound pachymetry*. Insight **18**, 16 (1993)
334. BE Reese, *Development of the retina and optic pathway*. Vision Res. **51**(7), 613-632 (2011)
335. LA Riggs, JC Armington and F Ratliff, *Motions of the retinal image during fixation*. J. Opt. Soc. Am **44**(4), 315-321 (1954)
336. MV Riley, *Oxygen requirements of the cornea*. Published in "The cornea: Transaction of the World Congress III" ed. by HD Cavanagh, Raven Press, New York p.207-210 (1988)
337. F Roddier, *Imaging through atmospheric turbulence*, Cambridge University Press , Adaptive optics in astronomy, edited by Roddier, 2-22 (1999)
338. F Roddier, R Rigaut, *The UH-CFHT systems: Adaptive optics in astronomy* (edited by F Roddier, Cambridge University Press), 205-235 (1999)
339. RW Rodieck, *The vertebrate retina: principles of structure and function*. Freeman, San Francisco (1973)
340. F Romero-Borja, K Venkateswaran, A Roorda and T Hebert, *Optical slicing of human retinal tissue in vivo with the adaptive optics scanning laser ophthalmoscope*. Appl. Opt. **44**(19) (2005)
341. A Roorda & MCW Campbell, *Confocal scanning laser ophthalmoscope for real-time photoreceptor imaging in the human eye*. Vision Science and its applications: Technical digest OSA **1**, 90-93 (1997)
342. A Roorda & DR Williams, *New direction in imaging the retina*. Opt. Phot. News, 23-29 (February 1997)
343. A Roorda & DR Williams, *The arrangement of the three cone classes in the living human eye*. Nature **397**, 520-522 (1999)
344. A Roorda, *Adaptive optics ophthalmoscopy*. J. Refr. Surg. **16**, S602-S607 (2000)
345. A Roorda, A Metha, P Lennie, DR Williams, *Packing arrangement of the three cone classes in the primate retina*. Vision Res. **41**(12), 1291-1306 (2001)
346. A Roorda, F Romero-Borja, WJ Donnelly III, H Queener *et al.*, *Adaptive optics scanning laser ophthalmoscopy*. Opt. Exp. **10**(9), 405-412 (2002)
347. A Roorda & DR Williams, *Optical fiber properties of individual human cones*. J. Vis. **2**, 404-412 (2002)

348. A Roorda, CA Garcia, JA Martin, S Poonja, H Queener, F Romero-Borja, R Sepulveda, K Venkateswaran and Y Zhang, *What can adaptive optics do for a scanning laser ophthalmoscope*, Bull. Soc. belge Ophthalmol. **302**, 231-244 (2006)
349. A Roorda, YH Zhang, JL Duncan, *High-resolution in vivo imaging of the RPE mosaic in eyes with retinal disease*. Invest. Ophthalmol. Vis. Sci. **48**, 2297-2303 (2007)
350. A Roorda, *Applications of adaptive optics scanning laser ophthalmoscopy*. Optom. Vis. Sci. **87**(4), 260-268 (2010)
351. SG Rosolen, B Lamory, F Harms, J-A Sahel, S Picaud and J-F LeGargasson, *Cellular-resolution in vivo imaging of the feline retina using adaptive optics: preliminary results*. Vet. Ophthalmol. **13**(6), 369-376 (2010)
352. F Rüfer, A Schröder and C Erb, *White-to-white corneal diameter: normal values in healthy humans obtained with the Orbscan II topography system*. Cornea **24**(3), 259-261 (2005)
353. JC Russ, *The image processing handbook*. 6th ed. CRC Press (2011)
354. Sahin, B Lamory, X Levecq, F Harms *et al.*, *Adaptive optics with pupil tracking for high-resolution retinal imaging*. Biomed. Opt. Exp. **3**(2), 225-239 (2012)
355. TO Salmon, *Corneal contribution to the wavefront aberration of the eye*. PhD thesis, Indiana University (1999)
356. SH Sarks, JJ Arnold, MC Killingsworth and JP Sarks, *Early formation in the normal and aging eye and their relation to age related maculopathy: clinicopathological study*. Br. J. Ophthalmol. **83**, 358-368 (1999)
357. U Schiefer, H Wilhelm, W Hart, *Clinical Neuro-Ophthalmology*. Springer (2007)
358. T Schmedt, Y Chen, TT Nguyen, S Li. JA Bonanno *et al.*, *Telomerase immortalization of human corneal endothelial cells yields functional hexagonal monolayers*. PLoS ONE **7**(12), e51427 (2012)
359. B Schwartz and MR Feller, *Temperature gradient in the rabbit eye*. Inv. Opht. **1**(4), 513-521 (1962)
360. J Schwiegerling, *Theoretical limits to visual performance*. "Refraction and reflections", ed. by JM Miller, Surv. Ophthalmology **45**(2), 139-146 (2000)
361. M Seul *et al.*, *Practical algorithms for image analysis*. Cambridge University Press (2000)
362. M Shafahi & K Vafai, *Human eye response to thermal disturbances*. J. Heat Trans. **133**, 011009-1-7 (2011)
363. B Shah, B Hubbard, JH Stewart-jones, DF Edgar *et al.*, *Influence of thymoxamine eye-drops on the effect on the mydriatic effect of tropicamide and phenylephrine alone and in combination*. Ophthalmic Physiol. Opt. **9**(2), 153-155 (1989)
364. M Shahidi, NP Blair, M Mori, R Zelka, *Optical section retinal imaging and wavefront sensing in diabetes*. Optom. Vis. Sci. **81**(10), 778-784 (2004)

365. PF Sharp & A Manivannan, *The scanning laser ophthalmoscope*. Phys. Med. Biol. **42**, 951-966 (1997)
366. PF Sharp, A Manivannan, H Xu, JV Forrester, *The scanning laser ophthalmoscope – a review of its role in bioscience and medicine*. Phys. Med. Biol. **49**, 1085-1096 (2004)
367. JB Sheehy, KW Gish, JJ Sprenger, *Artificial human eye and test apparatus* - US Patent 6485142 (2002)
368. AL Sheppard, CJ Evans, KD Singh, JS Wolffsohn, MC Dunne and LN Davies, *Three-dimensional magnetic resonance imaging of the phakic crystalline lens during accommodation*. Invest. Ophthalmol. Vis. Sci. **52**, 3689–3697 (2011)
369. CJR Sheppard & KG Larkin, *Optimal concentration of electromagnetic radiation*. J. Mod. Phys. **41**, 1495-1505 (1994)
370. BJ Shingleton & MW O’Donoghue, *Primary care: Blurred vision* (Review article). N. Engl. J. Med. **343**(8), 556-562 (2000)
371. T Shirai, *Liquid-crystal adaptive optics based on feedback interferometry for high-resolution retinal imaging*. Appl. Opt. **41**, 4013-4023, (2002)
372. WC Smith, J Pokorny, KR Diddie, *Color matching and the Stiles-Crawford effect in observers with early age-related macular changes*. J. Opt. Soc. Am. A **5**, 2113 (1998)
373. G Smith & Atchison, *The gradient index and spherical aberration of the lens of the human eye*. Ophthal. Physiol. Opt. **21**(4), 317-326 (2001)
374. RS Snell & MA Lemp, *Clinical Anatomy of the Eye*. Blackwell Scientific Publications, Cambridge (1989)
375. DM Snodderly, PPL Brown, FC Delori, JD Auran, *The macular pigment. I. Absorbance spectra, localization and discrimination from other yellow pigments in primate retinas*. Invest. Ophthalmol. Vis. Sci. **25**, 600-673 (1984)
376. CJ Solomon & JC Dainty, *Imaging a coherently illuminated object through a random screen using a dilute aperture*. J. Opt. Soc. Am A **9**, 1385-1390 (1992)
377. I Sommerville, *Software engineering* (International Computer Science Series). 6th Edition, Addison Wesley (2000)
378. A Sorsby, *Emmetropia and its aberrations*. Trans. Ophthalmol. Soc. **76**, 167-169 (1956)
379. A Sorsby, B Benjamin and AG Bennett, *Steiger on refraction: a reappraisal*. Br. J. Ophthalmol. **65**, 805-811 (1981)
380. WH Southwell, *Wave-front estimation from wave-slope measurements*. J. Opt. Soc. Am. **70**(8), 998-1006 (1980)
381. N Sredar, H Queener, C Li, C Ting, H Hofer, J Porter, *Wavefront sensorless confocal adaptive optics scanning laser ophthalmoscopy in the human eye*. J Vision **10**(15), 14160-14171 (2010)

382. G Staurengi, G Levi, S Pedenovi and C Veronese, *New developments in cSLO fundus imaging*. In: Medical retina – Essentials in Ophthalmology Series (eds. GK Kriegelstein and RN Weinreb), Springer (2007) edited by FG Holz & RF Spaide
383. WS Stiles & BH Crawford, *The luminous efficiency of rays entering the eye pupil at different points*. Vision Res. **35**, 999-1010 (1933)
384. A Stockman & LT Sharp, *Color and vision database at Institute of Ophthalmology, London*. <http://www.cvrl.ioo.ucl.ac.uk>. (September, 2006)
385. O Strauss, *The retinal pigment epithelium in visual function*. Physiol. Rev. **85**, 845-881 (2005)
386. SA Strenk, JL Semmlov, LM Strenk, P Munoz, J Gronlund-Jacob and JK DeMarco, *Age-related changes in human ciliary muscle and lens: A Magnetic Resonance Imaging study*. Invest. Ophthalmol. Vis. Sci **40**, 1162-1169 (1999)
387. LO Svaasand, CJ Gomer and AE Profio, *Laser-induced hyperthermia of ocular tumors*. Appl. Opt. **28**(12), 2280-2287 (1989)
388. DH Szczesna, J Jaronski, HT Kasprzak, U Stenevi, *Interferometric measurement of dynamic changes of tear film*. J. Biomed. Opt. **11**(3), 034028-1-8 (2006)
389. J Tabernero, SD Klyce, EJ Sarver, P Artal, *Functional optical zone of the cornea*. Invest. Ophthalmol. Vis. Sci. **48**(3), 1053-1060 (2007)
390. K Takayama, S Ooto, M Hangai, N Arakawa, S Oshima, N Shibata *et al.*, *High-resolution imaging of the retinal nerve fiber layer in normal eye using adaptive optics scanning laser ophthalmoscopy*. PLoS ONE **7**(3), e33158 (2012)
391. JH Tan, EYK Ng, UR Acharya, C Chee, *Infrared thermography on ocular surface temperature: A review*. Infr. Phys. Techn. **52**, 97-108 (2009)
392. S Taneri, S Oehler, DT Azar, *Influence of mydriatic eye drops on wavefront sensing with the Zywave aberrometer*. J. Refract. Surg. **27**(9), 678-685 (2011)
393. W Tasman & EA Jaeger, eds. *Duane's Ophthalmology* on CD-ROM. JB Lippincott Company (2006)
394. LN Thibos, A Bradley, X Hong, *A statistical model of the aberration structure of normal, well-corrected eyes*. Ophthalmol. Physiol. Opt. **22**(5), 427-433 (2002)
395. LN Thibos, RA Applegate, JT Schwiegerling, R Webb, VSIA, *Standards for reporting the optical aberrations of eyes*. J. Refract. Surg. **18**(5), S652-660 (2002)
396. S Thomas, T Fusco, A Tokovinin, M Nicolle, V Michau, and G Rousset, *Comparison of centroid computation algorithms in a Shack-Hartmann sensor*. Month. Not. Royal Astronom. Soc. **371**, 323-336 (2006)
397. N Tojo, T Nakamura, C Fuchizawa, T Oiwake, A Hayashi, *Adaptive optics fundus images of cone photoreceptors in the macula of patients with retinitis pigmentosa*. Clin. Ophthalmol. **7**, 203-210 (2013)
398. C Torti, B Povazay, B Hofer *et al.*, *Adaptive optics optical coherence tomography at 120,000 depth scans/s for non-invasive cellular phenotyping of the living human retina*. Opt. Exp. **17**(22), 19382-19400 (2009)

399. VV Tuchin, *Light scattering study of tissues, review of topical problems*. Physics - Uspekhi **40**, 495-515 (1997)
400. VV Tuchin, *Optical clearing of tissues and blood*. SPIE Press (2000)
401. V Tuchin, *Tissue optics: Light scattering methods and instruments for medical diagnosis*. 2nd edition SPIE Press (2007)
402. R Tutt, A Bradely, C Begley and LN Thibos, *Optical and visual impact of tear break-up in human eyes*. Invest. Ophthalmol. Vis. Sci. **41**, 4117-4123 (2000)
403. RK Tyson, *Principles of adaptive optics*. 2nd ed., Academic Press (1997)
404. RK Tyson, *Introduction of adaptive optics*. SPIE Press (2000)
405. C Ullenboom, *Java ist auch eine Insel: Das umfassende Handbuch*. Galileo Press Gmbh (2010)
406. SE Yanni, J Wang, M Chan, J Carroll, S Farsiu, JN Leffler, R Spencer, EE Birch, *Foveal avascular zone and foveal pit formation after preterm birth*. Br. J. Ophthalmol. **96**(7), 961-966 (2012)
407. M Yanoff & JW Sassani, *Ocular pathology*, Mosby 6th Ed. (2008)
408. GY Yoon, T Jitsuno, M Nakatsuka, S Nakai, *Shack-Hartmann wave-front measurement with a large F-number plastic microlens array*. Appl. Opt. **35**(1), 188-192 (1996)
409. G Yoon, *Wavefront sensing and diagnostic uses*. In: J Porter, H Queener, J Lin, K Thorn and A Awwal eds., Adaptive optics for vision science (Ch. 3). John Wiley & Sons (2006)
410. MK Yoon, A Roorda, Y Zhang *et al.*, *Adaptive optics scanning laser ophthalmoscopy images in family with the mitochondrial DNA T8993C mutation*. Vis. Sci. **50**(4), 1838-1847 (2009)
411. H Yoshida, K Yana, F Okuyama and T Tokoro, *Time-varying properties of respiratory fluctuations in pupil diameter of human eyes*. Methods Inf. Med. **33**(1), 46-48 (1994)
412. JG van Blockland, *Directionality and alignment of the foveal receptors, assessed with light scattered from the human fundus in vivo*. Vision Res. **26**, 495-500 (1986)
413. JM Van Buren, *The retinal ganglion cell layer*. CC Thomas, Springfield (1963)
414. WS Van Meter, WB Lee, DG Katz, *Corneal edema*. In: W Tasman & EA Jaeger, eds. *Duane's Ophthalmology* on CD-ROM, Vol. **4** (Ch.16). JB Lippincott Company (2006)
415. D Van Norren & LF Tiemeijer, *Spectral reflectance of the human eye*. Vision Res. **26**(2), 313-320 (1986)
416. MA van Dam & RG Lane, *Wavefront slope estimation* J. Opt. Soc. Am A **17**(7), 1319 (2000)
417. Van de Velde, *Scanning laser ophthalmoscope optimized for retinal microphotocoagulation* - US Patent 5892569 (1998)

418. FJ van de Velde, *The relaxed confocal scanning laser ophthalmoscope*. Bull. Soc. Belge Ophthalmol. **302**, 25-35 (2006)
419. TJTP van den Berg & JK IJspert, *Clinical assessment of intraocular stray light*. Appl. Opt. **31**(19), 3694-3696 (1992)
420. TJTP van den Berg & KEWP Tan, *Light transmittance of the human cornea from 320 to 700 nm for different ages*. Vision Res. **34**(11), 1453-1456 (1994)
421. TJTP van den Berg, LJ van Rijn, R Michael *et al.*, *Straylight effects with aging and lens extraction*. Am. J. Ophthalmol. **144**(3), 358-363 (2007)
422. J van der Kraats, TT Berendschot, and D van Norren, *The pathways of light measured in fundus reflectometry*. Vision Res. **15**, 2229-2247 (1996)
423. L Vajzovic, A Hendrikson, R O'Connell, LA Clark, D Tran-Viet, D Possin, SJ Chiu, S Farsiou and SA Toth, *Maturation of the human fovea: Correlation of Spectral-domain optical coherence tomography findings with histology*. Am. J. Ophthalmol. **154**(5), 779-789 (2012); Figure 2 from page 782 was reprinted in this thesis with permission of Elsevier under license number 3103601279189 to reuse in the thesis/dissertation both in electronic and printed format.
424. F Vargas-Martin, PM Prieto, P Partal, *Correction of the aberrations in the human eye with liquid-crystal spatial modulator: limits to performance*. J. Opt. Soc. Am. A **15**, 2552-2562 (1998)
425. G Vdovin & PM Sarro, *Flexible mirror micromachined in silicon*. Appl. Opt. **34**(16), 2968-2972 (1995)
426. G Vdovin & V Kiyko, *Intracavity control of a 200-W continuous-wave Nd:YAG laser by a micromachined deformable mirror*. Opt. Lett. **26**(22), 798-800 (2001)
427. G Vdovin, O Soloviev, A Samokhin and M Loktev, *Correction of low order aberrations using deformable mirrors*. Opt. Exp. **16**(5), 2859-2866 (2008)
428. C Viard, K Nakashima, B Lamory, M Paques, X Levecq and N Chateau, *Imaging microscopic structures in pathological retinas using a flood-illumination adaptive optics retinal camera*. Biomed. Opt. (BiOS) **7885** SPIE 788 509 (2011)
429. A Villamarin, S Roy, R Hasballa, O Vardoulis, P Reymond and N Stergiopoulos, *3D simulation of the aqueous flow in the human eye*. Med. Eng. & Phys. **34**(10), 1462-1470 (2012); Figure 2 from page 1465 was reprinted in this thesis with permission of Elsevier under license number 3111151315545 to reuse in the thesis/dissertation both in electronic and printed format.
430. CR Vogel, DW Arathorn, A Roorda and A Parker, *Retinal motion estimation in adaptive optics laser scanning ophthalmoscopy*. Opt. Exp. **14**(2), 487-497 (2005)
431. D Vukobratovich, *Introduction to opto-mechanical design – video short course notes*. Bellingham, WA, SPIE Opt. Eng. (1993)
432. A Vyas, MB Roopashree, BR Prasad, *Optimization of existing centroiding algorithms for a Shack Hartmann sensor*. NAC-CISS, Salem (2009a)

433. A Vyas, Roopashree, BR Prasad, *Performance of centroiding algorithms at low light level conditions in adaptive optics*. International conference on advances in recent technologies in communication and computing, 366-369 (2009b)
434. G Walsh, WN Charman and HC Howland, *Objective technique for the determination of monochromatic aberrations of the human eye*. J Opt Soc Am A **1**, 987-992 (1984)
435. AB Watson & Jli Yellott, *A unified formula for light-adapted pupil size*. J. Vision **12**(10), 1-16 (2012)
436. RH Webb and GW Hughes, *Scanning laser ophthalmoscope*. Biomed. Eng. IEEE Trans. **28**(7), 488-492 (1981)
437. RH Webb, GW Hughes and FC Delori, *Confocal scanning laser ophthalmoscope*. Appl. Opt. **26**(8), 1492-1499 (1987)
438. RH Webb & FC Delori, *How we see the retina*. In: J Marshall (ed.), *Laser technology in ophthalmology*. Kugler and Ghedini, 2-14 (1988)
439. RH Webb, *Scanning laser ophthalmoscope*. In: RR Masters (ed.), *Noninvasive diagnostic techniques in Ophthalmology* Springer, 438-450 (1990)
440. G Westheimer, *Image quality in the human eye*. Optica Acta. **17**, 541-658 (1970)
441. DR Whikehart, *Biochemistry of the eye*. Butterworth-Heinemann (2003)
442. WHO, *Vision 2020 Priority eye diseases report*: Accessed (2012) at: http://www.who.int/ncd/vision2020_actionplan/documents/V2020priorities.pdf
443. DR Williams, DH Brainard, MJ McMahon, R Navarro, *Double-pass and interferometric measures of the optical quality of the eye*. J. Opt. Soc. Am. A **11**(12), 3123-3135 (1994)
444. DR Williams, P Artal, R Navarro, *Off-axis optical quality and retinal sampling in the human eye*. Vision Res. **36**, 1103-1114 (1996)
445. DR Williams, J Liang, D Miller, A Roorda, *Wavefront sensing and compensation for the human eye*. In: Tyson, adaptive optics engineering handbook. Marcel Dekker, 187-310 (1999)
446. DR Williams, *Sharpness metric for vision quality* - US patent 7077522 (2006)
447. DR Williams, *Imaging single cells in the living retina*. Vision Res. **51**(13), 1379-1396 (2011)
448. B Winn & B Gilmartin, *Current perspective on microfluctuations of accommodation*. Ophthalmic Physiol. Opt. **12**(2), 252-256 (1992)
449. B Winn, D Whitaker, DB Elliott, NJ Phillips, *Factors affecting light-adapted pupil size in normal human subjects*. Invest. Ophthalmol. Vis. Sci. **35**, 1132-1137 (1994)
450. GJ Wistow & J Piatigorsky, *Lens crystalline: the evolution and expression of proteins for a highly specialized tissue*. Annu. Rev. Biochem. **57**, 479-504 (1988)
451. E Wolf (editor), *"Progress in Optics" Vol. 43*. Elsevier Science (2002)

452. JI Wolfing, M Chung, J Carroll, A Roorda, DR Williams, *High-resolution retinal imaging of cone-rod dystrophy*. *Ophthalmol.* **113**(6), 1014-1019 (2006)
453. L Wu & T Evans, *Common pitfalls in the use of optical coherence tomography for macular diseases*. FG Holz & RF Spaide (eds.), *Medical retina - Essentials in Ophthalmology Series* (eds. GK Kriegelstein and RN Weinreb), Springer (2007)
454. JC Wyant & K Creath, *Basic wavefront aberration theory for optical metrology*. *Applied optics and optical engineering Vol. XI. Ch. 1*, Academic Press (1992)
455. G Wyszecki & WS Stiles, *Color science: Concepts and methods, quantitative data and formulae*. New York, Wiley (1982)
456. M Zacharria, *The eyes have it – adaptive optics approaches clinical ophthalmology*. *BioOpt. World* **1**(6), 22-26 (2008)
457. RJ Zawadzki, SM Jones, SS Olivier, M Zhao, BA Bower, JA Izatt, S Choi, S Laut and JS Werner, *Adaptive-optics optical coherence tomography for high-resolution and high-speed 3D retinal in vivo imaging*. *Opt. Exp.* **13**, 8532-8546 (2005)
458. Y Zhang, B Cense, J Rha, RS Jonnal, W Gao, RJ Zawadzki, JS Werner, S Jones, S Olivier, DT Miller, *High-speed volumetric imaging of cone photoreceptors with adaptive optics spectral-domain optical coherence tomography*. *Opt. Exp.* **14**, 4380-4394 (2006)
459. ZY Zhong, BL Petrig, XF Qi and SA Burn, *In vivo measurement of erythrocyte velocity and retinal blood flow using adaptive optics scanning laser ophthalmoscopy*. *Opt. Exp.* **16**, 12746-12756 (2008)
460. M Zhu, MJ Collins, DR Iskander, *Dynamics of ocular surface topography*. *Eye* **21**(5), 624-632 (2007)
461. BL Zuber, L Stark and G Cook, *Microsaccades and the velocity-amplitude relationship for saccadic eye movements*. *Science* **150**(3702), 1459-1460 (1965)

APPENDIX

Appendix A:

The decomposition of the waveform into Zernike polynomials

I. Zernike Polynomials

1. Definition

The complex Zernike polynomials of order n and azimuthal frequency $|m| \leq n$ (the positive integers n and $|m|$ being restricted by $n - m = \text{even}$) is defined as

$$Z_n^m(\rho, \theta) = N_n^m R_n^{|m|} e^{im\theta}, \quad (\text{A.1})$$

Where

$$N_n^m = \sqrt{\frac{2(n+1)}{1 + \delta_{m0}}} \quad (\text{A.2})$$

is a normalization factor (Noll, 1976; Thibos, Applegate, Schwiegerling, Webb & VSIA, 2002),

$$R_n^{|m|} = \sum_{k=0}^{(n-|m|)/2} \frac{(-1)^k (n-k)! \rho^{n-2k}}{k! \left[\frac{n+m}{2} - k\right]! \left[\frac{n-m}{2} - k\right]!} \quad (\text{A.3})$$

is a radial polynomial (a special case of the Jacobi polynomials) of the radial variable ρ , and θ is the polar angle.

2. Orthogonality

The radial polynomial $R_n^{|m|}$ are normalized in such a manner $R_n^{|m|}(1) = 1$ to satisfy the orthogonality condition (Born & Wolf, 2003; Wyant & Creath, 1992) over the radial interval $[0,1]$:

$$\int_0^1 d\rho \rho R_n^{|m|}(\rho) R_{n'}^{|m'|}(\rho) = \frac{1}{2(n+1)} \delta_{mm'} . \quad (\text{A.4})$$

The exponentials from the Zernike polynomials also satisfy an orthogonality relation over the unit circle:

$$\int_0^{2\pi} d\theta \exp(im\theta) [\exp(im\theta)]^* = 2\pi \delta_{mm'} . \quad (\text{A.5})$$

Therefore the complex Zernike polynomials form an orthogonal set of functions over the unit disk:

$$\int_0^1 \rho d\rho \int_0^{2\pi} d\theta Z_n^m(\rho, \theta) [Z_{n'}^{m'}(\rho, \theta)]^* = \frac{2\pi}{1+\delta_{m0}} \delta_{nn'} \delta_{mm'} . \quad (\text{A.6})$$

3. Even and odd real Zernike polynomials

The complex Zernike polynomials $Z_n^m = Z_n^m \pm iZ_n^{-m}$ can be decomposed into even and odd type real Zernike polynomials Z_n^m and Z_n^{-m} as:

$$Z_n^m(\rho, \theta) = N_n^m R_n^{|m|} \cos(m\theta) , \quad (\text{A.7})$$

$$Z_n^{-m}(\rho, \theta) = N_n^m R_n^{|m|} \sin(m\theta) . \quad (\text{A.8})$$

The orthogonal property (5), applied to the index pairs (m, m') , and $(m, -m')$, by adding and subtracting the real and imaginary parts are:

$$\int_0^{2\pi} d\theta \cos(m\theta) \cos(m'\theta) = \pi(\delta_{mm'} + \delta_{m,-m'}), \quad (\text{A.9})$$

$$\int_0^{2\pi} d\theta \sin(m\theta) \sin(m'\theta) = \pi(\delta_{mm'} - \delta_{m,-m'}). \quad (\text{A.10})$$

Employing trigonometric identities on the sums and differences of sine and cosine functions we find the orthogonal property of the sine and cosine functions:

$$\int_0^{2\pi} d\theta \sin(m\theta) \cos(m'\theta) = 0. \quad (\text{A.11})$$

These further imply the orthogonality of the even and odd Zernike polynomials:

$$\int_0^1 d\rho \rho \int_0^{2\pi} d\theta Z_n^m(\rho, \theta) Z_{n'}^{m'}(\rho, \theta) = \pi \delta_{nn'} \delta_{|m|, |-m'|}, \quad (\text{A.12})$$

$$\int_0^1 d\rho \rho \int_0^{2\pi} d\theta Z_n^m(\rho, \theta) Z_{n'}^{-m'}(\rho, \theta) = 0, \quad (\text{A.13})$$

$$\int_0^1 d\rho \rho \int_0^{2\pi} d\theta Z_n^m(\rho, \theta) Z_{n'}^{-m'}(\rho, \theta) = \pi \delta_{nn'} (\delta_{mm'} - \delta_{m,-m'}). \quad (\text{A.14})$$

Due to known parity properties of both Z_n^m and Z_n^{-m} we can choose as a basis the limited subset of even and odd Zernike polynomials with either $m > 0$ or $m < 0$, the most common choice being the first one³. Then Eqs. (A.12) and (A.14) simplify to

$$\int_0^1 d\rho \rho \int_0^{2\pi} d\theta Z_n^{\pm m}(\rho, \theta) Z_{n'}^{\pm m'}(\rho, \theta) = \pi \delta_{nn'} \delta_{mm'}. \quad (\text{A.15})$$

³ An alternative definition of the odd Zernike polynomials (A.8) is also widespread in the literature (Thibos, Applegate, Schwiegerling, Webb, & VSIA, 2002). This is achieved by denoting the superscript $-m$ in the odd polynomials by a new integer, which by abuse of notation is also m , such that the odd Zernike polynomial becomes $Z_n^m(\rho, \theta) = -N_n^m R_n^{|m|} \sin(m\theta)$. Then a basis is formed the even Zernike polynomials with $m > 0$ and the above defined odd Zernike polynomials with $m < 0$.

II. Description of a waveform in terms of the Zernike polynomials

The phase Φ of a generic waveform can be given either in terms of the polar coordinates (ρ, θ) or Cartesian coordinates $(X = \rho \cos \theta, Y = \rho \sin \theta)$. The former is suitable for writing it up as a linear combination of the orthogonal set of Zernike polynomials. This combination may be taken for the real set of Zernike polynomials:

$$\Phi(\rho, \theta) = \sum_{n=0}^{\infty} \sum_{\substack{m=0 \text{ or } 1 \\ n-m=\text{even}}}^n [W_n^m Z_n^m(\rho, \theta) + W_n^{-m} Z_n^{-m}(\rho, \theta)]. \quad (\text{A.16})$$

The individual coefficients $W_n^{\pm m}$ can be considered to vanish for $n - m = \text{odd}$ while if the condition $n - m = \text{even}$ holds, they can be expressed

$$W_n^{\pm m} = \frac{1}{\pi} \int_0^1 d\rho \rho \int_0^{2\pi} d\theta \Phi(\rho, \theta) Z_n^{\pm m}(\rho, \theta). \quad (\text{A.17})$$

The set of coefficients $W_n^{\pm m}$ (possibly ordered in a column matrix) are equivalent with the phase of the wave front.

III. Details of computation

1. The orthogonality of the complex exponentials

$$\begin{aligned} \int_0^{2\pi} d\theta \exp(im\theta) [\exp(im'\theta)]^* &= \int_0^{2\pi} d\theta \exp(im\theta) \exp(-im'\theta) \\ &= \int_0^{2\pi} d\theta \exp[i(m-m')\theta] \\ &= \begin{cases} \frac{\exp[i(m-m')\theta]_0^{2\pi}}{i(m-m')} \text{ for } m' \neq m \\ 2\pi \text{ for } m' = m \end{cases} \\ &= \begin{cases} 0 \text{ for } m' \neq m \\ 2\pi \text{ for } m' = m \end{cases} = 2\pi \delta_{mm'} \end{aligned} \quad (\text{A.18})$$

Its real and imaginary parts give:

$$\int_0^{2\pi} d\theta \cos[(m - m')\theta] = 2\pi\delta_{mm'} , \quad (\text{A.19})$$

$$\int_0^{2\pi} d\theta \sin[(m - m')\theta] = 0 . \quad (\text{A.20})$$

The orthogonality of the complex exponentials, but with $-m'$ in place of m gives

$$\int_0^{2\pi} d\theta \exp(im\theta)[\exp(-im'\theta)]^* = 2\pi\delta_{m,-m'} , \quad (\text{A.21})$$

With the real and imaginary parts:

$$\int_0^{2\pi} d\theta \cos[(m + m')\theta] = 2\pi\delta_{m,-m'} , \quad (\text{A.22})$$

$$\int_0^{2\pi} d\theta \sin[(m + m')\theta] = 0 . \quad (\text{A.23})$$

By adding and subtracting Eqs. (A.19) and (A.22), also adding Eqs. (A.20) and (A.23), we obtain:

$$\int_0^{2\pi} d\theta \{\cos[(m - m')\theta] + \cos[(m + m')\theta]\} = 2\pi(\delta_{mm'} + \delta_{m,-m'}) , \quad (\text{A.24})$$

$$\int_0^{2\pi} d\theta \{\cos[(m - m')\theta] - \cos[(m + m')\theta]\} = 2\pi(\delta_{mm'} - \delta_{m,-m'}) , \quad (\text{A.25})$$

$$\int_0^{2\pi} d\theta \{\sin[(m - m')\theta] + \sin[(m + m')\theta]\} = 0 \quad (\text{A.26})$$

Then we employ trigonometric identities on the sums and differences of *sin* and *cos* functions and we find the orthogonality property of the *sin* and *cos* functions:

$$\int_0^{2\pi} d\theta \cos(m\theta) \cos(m'\theta) = \pi(\delta_{mm'} + \delta_{m,-m'}) , \quad (\text{A.27})$$

$$\int_0^{2\pi} d\theta \sin(m\theta) \sin(m'\theta) = \pi(\delta_{mm'} - \delta_{m,-m'}) , \quad (\text{A.28})$$

$$\int_0^{2\pi} d\theta \sin(m\theta) \cos(m'\theta) = 0 \quad (\text{A.29})$$

2. The orthogonality of the complex Zernike polynomials

$$\begin{aligned}
\int_0^1 \rho d\rho \int_0^{2\pi} d\theta Z_n^m(\rho, \theta) Z_{n'}^{m'}(\rho, \theta) &= N_n^m N_{n'}^{m'} \int_0^1 d\rho \rho R_n^{|m|} R_{n'}^{|m'|} \int_0^{2\pi} d\theta \cos(m\theta) \cos(m'\theta) \\
&= \sqrt{\frac{2(n+1)}{1+\delta_{m0}}} \sqrt{\frac{2(n'+1)}{1+\delta_{m'0}}} \frac{1}{2(n+1)} \delta_{nn'} \cdot \pi(\delta_{mm'} \\
&\quad + \delta_{m,-m'}) \\
&= \frac{2\pi}{1+\delta_{m0}} \delta_{nn'} \delta_{mm'} \tag{A.30}
\end{aligned}$$

3. The orthogonality of the even and odd Zernike polynomials

$$\begin{aligned}
\int_0^1 \rho d\rho \int_0^{2\pi} d\theta Z_n^m(\rho, \theta) Z_{n'}^{m'}(\rho, \theta) &= \int_0^1 \rho d\rho \int_0^{2\pi} d\theta N_n^m R_n^{|m|} \cos(m\theta) N_{n'}^{m'} R_{n'}^{|m'|} \cos(m'\theta) \\
&= N_n^m N_{n'}^{m'} \frac{1}{2(n+1)} \delta_{nn'} 2\pi \delta_{mm'} \\
&= \sqrt{\frac{2(n+1)}{1+\delta_{m0}}} \sqrt{\frac{2(n'+1)}{1+\delta_{m'0}}} \frac{1}{2(n+1)} \delta_{nn'} 2\pi \delta_{mm'} \\
&= 2\pi \sqrt{\frac{2(n+1)}{1+\delta_{m0}}} \sqrt{\frac{2(n'+1)}{1+\delta_{m'0}}} \frac{1}{2(n+1)} \delta_{nn'} \delta_{mm'} \\
&= \frac{\pi \delta_{nn'} (\delta_{mm'} + \delta_{m,-m'})}{\sqrt{(1+\delta_{m0}) + (1+\delta_{m'0})}} \delta_{nn'} \delta_{mm'} \\
&= \pi \delta_{nn'} \frac{\delta_{mm'} + \delta_{m,-m'}}{1+\delta_{m0}} \\
&= \pi \delta_{nn'} \cdot \begin{cases} 1, \text{ for } m = m' = 0 \\ 1, \text{ for } m = m' \neq 0 \\ 1, \text{ for } m = -m' \neq 0 \\ 0, \text{ for } m \neq \pm m' \end{cases} \\
&= \pi \delta_{nn'} \delta_{|m|, |m'|} \tag{A.31}
\end{aligned}$$

$$\begin{aligned}
\int_0^1 \rho d\rho \int_0^{2\pi} d\theta Z_n^m(\rho, \theta) Z_{n'}^{-m'}(\rho, \theta) &= \int_0^1 \rho d\rho \int_0^{2\pi} d\theta N_n^m R_n^{|m|} \cos(m\theta) N_{n'}^{m'} R_{n'}^{|m'|} \sin(m'\theta) \\
&= N_n^m N_{n'}^{m'} \int_0^1 d\rho \rho R_n^{|m|} R_{n'}^{|m'|} \int_0^{2\pi} d\theta \cos(m\theta) \sin(m'\theta) \\
&= \sqrt{\frac{2(n+1)}{1+\delta_{m0}}} \sqrt{\frac{2(n'+1)}{1+\delta_{m'0}}} \frac{1}{2(n+1)} \delta_{nn'} \cdot 0 \\
&= 0, \tag{A.32}
\end{aligned}$$

$$\begin{aligned}
\int_0^1 \rho d\rho \int_0^{2\pi} d\theta Z_n^m(\rho, \theta) Z_{n'}^{-m'}(\rho, \theta) &= \int_0^1 \rho d\rho \int_0^{2\pi} d\theta N_n^m R_n^{|m|} \sin(m\theta) N_{n'}^{m'} R_{n'}^{|m'|} \sin(m'\theta) \\
&= N_n^m N_{n'}^{m'} \int_0^1 d\rho \rho R_n^{|m|} R_{n'}^{|m'|} \int_0^{2\pi} d\theta \sin(m\theta) \sin(m'\theta) \\
&= \sqrt{\frac{2(n+1)}{1+\delta_{m0}}} \sqrt{\frac{2(n'+1)}{1+\delta_{m'0}}} \frac{1}{2(n+1)} \delta_{nn'} \cdot \pi(\delta_{mm'} \\
&\quad - \delta_{m,-m'}) \\
&= \frac{\pi \delta_{nn'} (\delta_{mm'} - \delta_{m,-m'})}{\sqrt{(1+\delta_{m0})(1+\delta_{m'0})}} = \pi \delta_{nn'} \frac{\delta_{mm'} - \delta_{m,-m'}}{1+\delta_{m0}} \\
&= \pi \delta_{nn'} \cdot \begin{cases} 0, \text{ for } m = m' = 0 \\ 1, \text{ for } m = m' \neq 0 \\ -1, \text{ for } m = -m' \neq 0 \\ 0, \text{ for } m \neq \pm m' \end{cases} \\
&= \pi \delta_{nn'} (\delta_{mm'} - \delta_{m,-m'}) \tag{A.33}
\end{aligned}$$

4. Additional check

The following expresses the direct consequences of the orthogonality of the complex Zernike polynomials:

$$\begin{aligned}
\frac{2\pi}{1 + \delta_{m0}} \delta_{nn'} \delta_{mm'} &= \int_0^1 \rho d\rho \int_0^{2\pi} d\theta Z_n^m \pm (Z_{n'}^{-m'})^* \\
&= \int_0^1 \rho d\rho \int_0^{2\pi} d\theta (Z_n^m \pm i Z_n^{-m})(Z_{n'}^{m'} \pm i Z_{n'}^{-m'})^* \\
&= \int_0^1 \rho d\rho \int_0^{2\pi} d\theta (Z_n^m \pm i Z_n^{-m})(Z_{n'}^{m'} \mp i Z_{n'}^{-m'}) \\
&= \int_0^1 \rho d\rho \int_0^{2\pi} d\theta [Z_n^m Z_{n'}^{m'} + Z_n^{-m} Z_{n'}^{-m'} \mp i(Z_n^m Z_{n'}^{-m'} - Z_n^{-m} Z_{n'}^{m'})] \\
&= \int_0^1 \rho d\rho \int_0^{2\pi} d\theta (Z_n^m Z_{n'}^{m'} + Z_n^{-m} Z_{n'}^{-m'}) \mp i \int_0^1 \rho d\rho \int_0^{2\pi} d\theta (Z_n^m Z_{n'}^{-m'} - Z_n^{-m} Z_{n'}^{m'}) \\
\begin{aligned} \xrightarrow{\text{yields}} & \left\{ \begin{aligned} \int_0^1 \rho d\rho \int_0^{2\pi} d\theta (Z_n^m Z_{n'}^{m'} + Z_n^{-m} Z_{n'}^{-m'}) &= \frac{2\pi}{1 + \delta_{m0}} \delta_{nn'} \delta_{mm'} \\ \int_0^1 \rho d\rho \int_0^{2\pi} d\theta (Z_n^m Z_{n'}^{-m'} - Z_n^{-m} Z_{n'}^{m'}) &= 0 \end{aligned} \right. \\ \\ \xrightarrow{\text{yields}} & \left\{ \begin{aligned} N_n^m N_{n'}^{m'} \int_0^1 \rho d\rho R_n^m R_{n'}^{m'} \int_0^{2\pi} d\theta \cos(m\theta) \cos(m'\theta) + \sin(m\theta) \sin(m'\theta) &= \frac{2\pi}{1 + \delta_{m0}} \delta_{nn'} \delta_{mm'} \\ N_n^m N_{n'}^{m'} \int_0^1 \rho d\rho R_n^m R_{n'}^{m'} \int_0^{2\pi} d\theta \cos(m\theta) \cos(m'\theta) - \sin(m\theta) \sin(m'\theta) &= 0 \end{aligned} \right. \\ \\ \xrightarrow{\text{yields}} & \left\{ \begin{aligned} \sqrt{\frac{2(n+1)}{1 + \delta_{m0}}} \sqrt{\frac{2(n'+1)}{1 + \delta_{m'0}}} \frac{1}{2(n+1)} \delta_{nn'} \int_0^{2\pi} d\theta \cos[(m - m')\theta] &= \frac{2\pi}{1 + \delta_{m0}} \delta_{nn'} \delta_{mm'} \\ \sqrt{\frac{2(n+1)}{1 + \delta_{m0}}} \sqrt{\frac{2(n'+1)}{1 + \delta_{m'0}}} \frac{1}{2(n+1)} \delta_{nn'} \int_0^{2\pi} d\theta \sin[(m - m')\theta] &= 0 \end{aligned} \right. \\ \\ \xrightarrow{\text{yields}} & \left\{ \begin{aligned} \sqrt{\frac{1}{1 + \delta_{m0}}} \sqrt{\frac{1}{1 + \delta_{m'0}}} \int_0^{2\pi} d\theta \cos[(m - m')\theta] &= \frac{2\pi}{1 + \delta_{m0}} \delta_{nn'} \delta_{mm'}, \text{ide} \\ \delta_{nn'} \int_0^{2\pi} d\theta \sin[(m - m')\theta] &= 0, \text{identity} \end{aligned} \right. \quad (\text{A.34})
\end{aligned}$$

Appendix B: Java Codes

```
public class TimeCalculation {
    private static int TYP_INT = 0;
    private static int TYP_FLOAT = 1;
    private static int TYP_LONG = 2;

    private static void calcArrayInitialization(int typ, int size){
        Date d = new Date();
        long timeStart =d.getTime();
        String typS="";

        if(typ==TYP_INT){
            int[] array = new int[size*size];
            for (int i = 0; i < size*size; i++) {
                array[i] = 111;
            }
            typS="Int";
        }else if(typ==TYP_FLOAT){
            float[] array = new float[size*size];
            for (int i = 0; i < size*size; i++) {
                array[i] = 111;
            }
            typS="Float";
        }else if(typ==TYP_LONG){
            long[] array = new long[size*size];
            for (int i = 0; i < size*size; i++) {
                array[i] = 111;
            }
            typS="Long";
        }

        Date dEnd = new Date();
        long timeFinish =dEnd.getTime();

        System.out.println(typS+(size*size)+": " + (timeFinish-timeStart));
    }

    private static void calcSimpleInitialization(){
        System.out.println("---TEST ARRAY INITIALIZATION---");
        int n = 64;
        for (int i = 1; i < 9; i++) {
            calcArrayInitialization(TYP_INT,n);
            calcArrayInitialization(TYP_FLOAT,n);
            calcArrayInitialization(TYP_LONG,n);
            System.out.println(" ");
            n *=2;
        }
    }
}
```

Appendix C: Python Codes

```
import numpy
from time import *
import random

TYP_INT = 0
TYP_FLOAT = 1
TYP_LONG = 2

def calcArrayInitialization( typ, size):
    timeStart = clock()
    typS=''
    if(typ==TYP_INT):
        array = numpy.zeros([size * size],int)
        for i in range(0, size*size):
            array[i] = 111;
        typS="Int";
    if(typ==TYP_FLOAT):
        array = numpy.zeros([size * size],float)
        for j in range(0, size*size):
            array[j] = 111;
        typS="Float";
    if(typ==TYP_LONG):
        array = numpy.zeros([size * size],long)
        for k in range(0, size*size):
            array[k] = 111;
        typS="Long";
    timeFinish = clock()
    print typS+str((size*size))+": " + str((timeFinish-timeStart))

def calcSimpleInitialization():
    print "----TEST ARRAY INITIALIZATION----"
    n = 64
    for k in range(1, 8):
        calcArrayInitialization(TYP_INT,n)
        calcArrayInitialization(TYP_FLOAT,n)
        calcArrayInitialization(TYP_LONG,n)
    print " "
    n *=2;

def calcBubbleSort(size):

    sizeA = size*size;
    arrayI = numpy.zeros([size * size],int)
    arrayF = numpy.zeros([size * size],float)
    arrayL = numpy.zeros([size * size],long)
    for i in range(0, sizeA):
        rI=random.randint(0, 10000)
        arrayI[i] = rI
        arrayF[i] = rI
        arrayL[i] = rI

    print " "
    print "Sort int"+str(sizeA)+" arrays..."
    timeStart = clock()
```

```

sortiere(arrayI)
timeFinish = clock()
print str(timeFinish-timeStart)+"s"

print " "
print "Sort float"+str(sizeA)+" arrays..."
timeStart = clock()
sortiere(arrayF)
timeFinish = clock()
print str(timeFinish-timeStart)+"s"

print " "
print "Sort long"+str(sizeA)+" arrays..."
timeStart = clock()
sortiere(arrayL)
timeFinish = clock()
print str(timeFinish-timeStart)+"s"

def sortiere(x):
    unsortiert=1;
    temp = 0;
    while (unsortiert==1):
        unsortiert = 0;
        for i in range(0, x.size-1):
            if(x[i] > x[i+1]):
                temp = x[i]
                x[i] = x[i+1]
                x[i+1] = temp
                unsortiert = 1

```

Copies of permission documents

Copies of permission documents showing that the author has permission to republish all the third party copyrighted works in the thesis.

ELSEVIER LICENCE DETAILS I.

Fig. 2.2 on typical ocular temperature distribution is reprinted with permission (Fig. 4 in the paper):

This is a License Agreement between Ibolya Kepiro and Elsevier provided by Copyright Clearance Centre. The license consists of the order details, the terms and conditions provided by Elsevier, and the payment terms and conditions.

Supplier	Elsevier Limited, The Boulevard, Langford Lane Kidlington, Oxford, OX5 1GB, UK
Registered Company Number	1982084
Customer name	Ibolya Kepiro
Customer address	Prince Consort Rd, London, SW7 2BW
License number	3103610306634
License date	Mar 07, 2013
Licensed content publisher	Elsevier
Licensed content publication	Computers in Biology and Medicine
Licensed content title	<i>Simulation of aqueous humor hydrodynamics in human eye heat transfer</i>
Licensed content author	Ean-Hin Ooi, Eddie Yin-Kwee Ng
Licensed content date	February 2008
Licensed content volume number	38
Licensed content issue number	2
Number of pages	11
Start Page	252
End Page	262
Type of Use	reuse in a thesis/dissertation
Intended publisher of new work	Other
Portion	figures/tables/illustrations
Number of figures/tables/illustrations	4
Format	both print and electronic
Are you the author of this Elsevier article?	No
Will you be translating?	No
Order reference number	
Title of your thesis/dissertation	<i>High-resolution retinal imaging with a compact adaptive optics ophthalmoscope</i>
Expected completion date	Mar 2013
Estimated size (number of pages)	
Elsevier VAT number	GB 494 6272 12
Permissions price	0.00 GBP
VAT/Local Sales Tax	0.0 USD / 0.0 GBP
Total	0.00 GBP

ELSEVIER LICENCE DETAILS II.

Fig. 2.6 on histology of the normal human retina is reprinted with permission (Fig. 1 in the paper):

This is a License Agreement between Ibolya Kepiro and Elsevier provided by Copyright Clearance Centre. The license consists of the order details, the terms and conditions provided by Elsevier, and the payment terms and conditions.

Supplier	Elsevier Limited, The Boulevard, Langford Lane Kidlington, Oxford, OX5 1GB, UK
Registered Company Number	1982084
Customer name	Ibolya Kepiro
Customer address	Prince Consort Rd, London, SW7 2BW
License number	3103610897153
License date	Mar 07, 2013
Licensed content publisher	Elsevier
Licensed content publication	American Journal of Ophthalmology
Licensed content title	<i>Histologic Development of the Human Fovea From Midgestation to Maturity</i>
Licensed content author	Anita Hendrickson, Daniel Possin, Lejla Vajzovic, Cynthia A. Toth
Licensed content date	November 2012
Licensed content volume number	154
Licensed content issue number	5
Number of pages	14
Start Page	767
End Page	778.e2
Type of Use	reuse in a thesis/dissertation
Intended publisher of new work	Other
Portion	figures/tables/illustrations
Number of figures/tables/illustrations	1
Format	both print and electronic
Are you the author of this Elsevier article?	No
Will you be translating?	No
Order reference number	
Title of your thesis/dissertation	<i>High-resolution retinal imaging with a compact adaptive optics ophthalmoscope</i>
Expected completion date	Mar 2013
Estimated size (number of pages)	
Elsevier VAT number	GB 494 6272 12
Permissions price	0.00 GBP
VAT/Local Sales Tax	0.0 USD / 0.0 GBP
Total	0.00 GBP

ELSEVIER LICENCE DETAILS III.

Fig. 2.11 on velocity distribution in AH is reprinted with permission (Fig. 2 in the paper):

This is a License Agreement between Ibolya Kepiro and Elsevier provided by Copyright Clearance Centre. The license consists of the order details, the terms and conditions provided by Elsevier, and the payment terms and conditions.

Supplier	Elsevier Limited, The Boulevard, Langford Lane Kidlington, Oxford, OX5 1GB, UK
Registered Company Number	1982084
Customer name	Ibolya Kepiro
Customer address	Prince Consort Rd, London, SW7 2BW
License number	3111151315545
License date	Mar 17, 2013
Licensed content publisher	Elsevier
Licensed content publication	Medical Engineering & Physics
Licensed content title	<i>3D simulation of the aqueous flow in the human eye</i>
Licensed content author	Adan Villamarin, Sylvain Roy, Reda Hasballa, Orestis Vardoulis, Philippe Reymond, Nikolaos Stergiopoulos
Licensed content date	December 2012
Licensed content volume number	34
Licensed content issue number	10
Number of pages	9
Start Page	1462
End Page	1470
Type of Use	reuse in a thesis/dissertation
Intended publisher of new work	Other
Portion	figures/tables/illustrations
Number of figures/tables/illustrations	2
Format	both print and electronic
Are you the author of this Elsevier article?	No
Will you be translating?	No
Order reference number	None
Title of your thesis/dissertation	<i>High-resolution retinal imaging with a compact adaptive optics ophthalmoscope</i>
Expected completion date	Mar 2013
Estimated size (number of pages)	
Elsevier VAT number	GB 494 6272 12
Permissions price	0.00 GBP
VAT/Local Sales Tax	0.0 USD / 0.0 GBP
Total	0.00 GBP

ELSEVIER LICENCE DETAILS IV.

Fig. 2.13 on foveal development is reprinted with permission (Fig. 2 in the paper):

This is a License Agreement between Ibolya Kepiro and Elsevier provided by Copyright Clearance Centre. The license consists of the order details, the terms and conditions provided by Elsevier, and the payment terms and conditions.

Supplier	Elsevier Limited, The Boulevard, Langford Lane Kidlington, Oxford, OX5 1GB, UK
Registered Company Number	1982084
Customer name	Ibolya Kepiro
Customer address	Prince Consort Rd, London, SW7 2BW
License number	3103601279189
License date	Mar 07, 2013
Licensed content publisher	Elsevier
Licensed content publication	American Journal of Ophthalmology
Licensed content title	<i>Maturation of the Human Fovea: Correlation of Spectral-Domain Optical Coherence Tomography Findings With Histology</i>
Licensed content author	Lejla Vajzovic, Anita E. Hendrickson, Rachelle V. O'Connell, Laura A. Clark, Du Tran-Viet, Daniel Possin, Stephanie J. Chiu, Sina Farsiu, Cynthia A. Toth
Licensed content date	November 2012
Licensed content volume number	154
Licensed content issue number	5
Number of pages	13
Start Page	779
End Page	789.e2
Type of Use	reuse in a thesis/dissertation
Intended publisher of new work	Other
Portion	figures/tables/illustrations
Number of figures/tables/illustrations	2
Format	both print and electronic
Are you the author of this Elsevier article?	No
Will you be translating?	No
Order reference number	
Title of your thesis/dissertation	<i>High-resolution retinal imaging with a compact adaptive optics ophthalmoscope</i>
Expected completion date	Mar 2013
Estimated size (number of pages)	
Elsevier VAT number	GB 494 6272 12
Permissions price	0.00 GBP
VAT/Local Sales Tax	0.0 USD / 0.0 GBP
Total	0.00 GBP